AN INVESTIGATION OF PROCESSING TECHNIQUES AND CHARACTERISATION METHODS FOR 3D DIAMOND DETECTORS

A thesis submitted to the University of Manchester
for the degree of Doctor of Philosophy
in the Faculty of Science and Engineering

2018

Steven Alexander Murphy
School of Physics and Astronomy

Contents

Word count 44000

List of Figures

The University of Manchester

Steven Alexander Murphy
Doctor of Philosophy
An Investigation of Processing Techniques and Characterisation Methods for 3D Diamond Detectors
March 29, 2018

In this thesis 3D diamond detectors were fabricated using an ultrafast femtosecond (120 fs) pulse length laser, with a 800 nm wavelength, to induce a phase change of diamond to graphite to form electrodes in the diamond bulk. Graphitic electrodes, with diameters of O(μm), were fabricated using a known processing technique and were enhanced further through the use of a Spatial Light Modulator (SLM), which is a new technology in this field. These detectors were subsequently characterised through the use of particle beams, and this work also presents methods for characterising such detectors: A pair of crossed polarisers to determine the stress induced by the electrodes on the diamond bulk; Raman spectroscopy to assess the relative quantity of diamond:graphite formed; Scanning Electron Microscopy (SEM) to image the starting (seed) and finishing (exit) sides of electrode formation; and current-voltage (I-V) measurements to calculate the electrical properties of the electrodes. These characterisation methods (alongside the use of particle beams) serve as a means to compare the two fabrication techniques and to determine the optimum fabrication parameters to produce 3D diamond detectors for use as tracking detectors in high luminosity environments such as those in the Large Hadron Collider (LHC).

This work shows that using a higher beam energy and translation speed of the focal spot results in electrodes of lower electrical resistivity, which is an ideal characteristic for a tracking detector. These higher processing parameters also result in more graphitic structure on the seed and exit sides of the diamond, determined separately via Raman spectroscopy and SEM. An increased beam energy also results in larger electrode diameters, reducing the active area of the detector and inducing more stress in the diamond bulk. These measurements therefore indicate an upper limit on the fabrication parameters. A further study into these processing parameters shows the translation speed scales with the pulse repetition rate of the laser and allows for fast fabrication of 3D diamond detectors.

Two devices were fabricated with and without the use of an SLM, with a more uniform detector response (through characterisation by particle beams), lower electrical resistivity, and more graphitic material observed for SLM-fabricated electrodes. The benefits of square and hexagonal cell structures were also investigated with both structures showing a similar response to particle beams. A lower charge sharing region is observed in hexagonal cells and indicates potentially different applications for these cell geometries. Transient Current Technique (TCT) measurements were also taken on both detectors, where faster charge collection and higher quality data were seen for the SLM-fabricated device. These measurements indicate a preference in the use of an SLM for the future fabrication of 3D diamond tracking detectors. These TCT measurements were then compared to simulations to extract the charge carrier properties in diamond. Only qualitative agreement was obtained, motivating further work in this area to fully understand the charge carrier dynamics and demonstrate the future viability of 3D diamond detectors.

Declaration

No portion of the work referred to in the thesis has been submitted in support of an application for another degree or qualification of this or any other university or other institute of learning.

Copyright Statement

i. The author of this thesis (including any appendices and/or schedules to this thesis) owns certain copyright or related rights in it (the "Copyright") and s/he has given The University of Manchester certain rights to use such Copyright, including for administrative purposes.

ii. Copies of this thesis, either in full or in extracts and whether in hard or electronic copy, may be made **only** in accordance with the Copyright, Designs and Patents Act 1988 (as amended) and regulations issued under it or, where appropriate, in accordance with licensing agreements which the University has from time to time. This page must form part of any such copies made.

iii. The ownership of certain Copyright, patents, designs, trade marks and other intellectual property (the "Intellectual Property") and any reproductions of copyright works in the thesis, for example graphs and tables ("Reproductions"), which may be described in this thesis, may not be owned by the author and may be owned by third parties. Such Intellectual Property and Reproductions cannot and must not be made available for use without the prior written permission of the owner(s) of the relevant Intellectual Property and/or Reproductions.

iv. Further information on the conditions under which disclosure, publication and commercialisation of this thesis, the Copyright and any Intellectual Property and/or Reproductions described in it may take place is available in the University IP Policy (see http://documents.manchester.ac.uk/DocuInfo.aspx?DocID=24420), in any relevant Thesis restriction declarations deposited in the University Library, The University Library's regulations (see http://www.library.manchester.ac.uk/about/regulations/) and in The University's Policy on Presentation of Theses.

Acknowledgements

"A diamond cannot be polished without friction, nor a man perfected without trials" - Paraphrased Chinese proverb.

As with any long term project of any kind, there are always people who will have helped you both directly and indirectly. From the academic side, all my thanks go to my supervisor. You always remind me that "it's trivial, no?" whenever I encounter something for the first time and struggled to grasp the concept, which is an attitude I've come to adopt.

From the non-academic side, I would like to thank my friends who somehow put up with my idiosyncrasies and helped me stay sane. Everyone in their own way helped me through my PhD, from helping me make sense of work and getting the best out of it, to allowing me to unwind with copious amounts of wine vent my frustration. Without a doubt my life is richer with them in it.

I also want to thank my family; my mother managed to raise two boys to become great physicists and receives nowhere near enough praise for everything she has done. My brother provided me with a source of inspiration and gave me far more time and patience than I deserved, yet never questioned me and always believed in me.

I would like to dedicate my thesis in its entirety to my late father. Although he is not around to witness everything I have accomplished, he would certainly be proud.

Chapter 1

Introduction

Collider experiments are crucial in aiding the understanding of the interactions with, and the properties of, matter, which are described by the four fundamental forces of the "Standard Model" [1]: the electromagnetic force; the strong nuclear force, which dictates the bonding of nuclei; the weak nuclear force, which governs nuclear reactions; and gravity. It is these experiments that discover the missing components in our understanding of the universe as it existed today and in the universe at the time of the Big Bang.

However, knowledge of the early universe in particular is still incomplete; the discovery of the Higgs boson in 2012 [2] proved the proposed mechanism by Higgs et al [3–5]. for the origin of mass and was considered a breakthrough in the field of particle physics, yet even this adds to the list of several important, unanswered questions: "Are there more particles that exhibit Higgs-like behaviour?" "Does a true Grand Unified Theory (GUT) from which the four fundamental forces can be derived exist?" Questions like these can only be answered by constructing experiments which operate at such high energies and have such volatile conditions at the interaction point of the collided particles that they can emulate the conditions of the early universe.

In experiments such as those at the Large Hadron Collider (LHC) particles which form from such collisions are the key to aiding our understanding. These particles may occur very rarely and exist for a very short time before decaying, such as the Higgs boson, so it is crucial to reliably identify the primary vertex (the point of collision) and where possible the secondary vertex, where particles with a short lifetime decay into other, well-known particles. Detectors capable of doing this need to identify these

vertexes to within micrometre precision and must be able to tolerate the large number of particles produced in these collision before experiencing permanent damage, which would reduce its detection efficiency.

These detectors were originally planar silicon detectors, where electrodes are implanted within the top and bottom of the substrate bulk. Such detectors were simple to fabricate though suffered from so called "radiation damage" as mentioned previously. In the 1990s a new "3D" detector architecture was proposed by Parker et al. [6], where instead electrodes penetrate through the bulk material, perpendicular to the substrate surface. This ground-breaking work showed an improved performance in 3D detectors over the existing planar detectors and predicted that this geometry would be more radiation hard, which was later confirmed by Da Via and Watts [7].

Despite the needed improvement in the radiation hardness for use as tracking detectors in the LHC, 3D silicon detectors still experience high levels of radiation damage ($O(10^{15}\,\mathrm{cm}^{-2}$ 1 MeV-equivalent neutron fluence [8])), where silicon was used due to its cost and reliability. The LHC is currently in "Phase 1" of its operation after completing its initial run in 2009-2013 (run 1) and the first long shutdown[1] (LS1) between 2013-2015. Phase 1 is currently running with an operating beam energy of 6.5 TeV (a 13 TeV collision energy) until 2018 (known as run 2), at which point a second long shutdown (LS2) occurs [9]. The final run of the LHC (run 3) will occur from 2021-2023, at which point the LHC enters a third long shutdown (LS3) until 2026. At this point, the commissioning of the high luminosity LHC (HL-LHC) [10] will occur, where the luminosity will be increased beyond the LHC's initial design to $O(10^{35}\,\mathrm{cm}^{-2}\mathrm{s}^{-1})$, and the experiment is expected to run until 2038. The expected radiation damage is $\geq O(10^{16}\,\mathrm{cm}^{-2})$ 1 MeV-equivalent neutron fluence [11], necessitating radiation hard detectors.

Additionally, there is also a proposal for a successor to the LHC known as the Future Circular Collider (FCC) [12], designed to achieve collision energies of up to 100 TeV to uncover new physics. It is expected that the FCC will require a significant luminosity increase, up to $O(10^{36}\,\mathrm{cm}^{-2}\mathrm{s}^{-1})$[2]. Due to the impact of radiation damage

[1] For every shutdown any damaged components are replaced, including tracking detectors, which have experienced significant radiation damage and provides the motivation for this thesis

[2] This is for one specific variation of the FCC, known as the FCC-ee, which collides electrons and positrons.

on the (currently) silicon tracker detectors there are some doubts as to the future of silicon, particularly in the HL-LHC and the proposed FCC (the expected radiation damage is $O(10^{18}\,cm^{-2})$ 1 MeV-equivalent neutron fluence [13]), so alternative detector materials are being considered that would be able to withstand this environment for a longer time period before replacement becomes necessary. One such material is synthetic diamond.

Diamond is a very robust and versatile material with a high radiation hardness. That is, diamond is able to tolerate high radiation conditions more easily than silicon in that diamond exhibits lower leakage current. This trait has been investigated and confirmed using alpha particles [14], beta particles [15], high energy protons [16], and neutron irradiation [17], and using the 3D architecture further improves the radiation hardness of diamond [18]. However, one of the first uses of diamond as a detector material was in 1999 [19], so it is a relatively new technology and thus less understood than silicon. While the principles of particle detection in silicon are applicable to diamond there are still areas of improvement required for diamond to be the successor to silicon, ranging from the manufacture of the synthetic diamond via chemical vapour deposition (CVD) to the formation of the electrodes within the diamond bulk.

The focus of this thesis is to investigate the viability of 3D diamond as a tracking detector, which is split into two key areas: the response of a 3D diamond detector to incident particles, and the processes involved in the manufacture of a 3D diamond detector. An overview of detector principles is described in Chapter 2, which includes the physical processes governing signal generation. Chapter 3 discusses the steps required to manufacture a 3D diamond detector with emphasis on the formation of the electrodes within the diamond bulk. Greater focus is given to the formation of the graphitic electrodes, which is part of the work in this thesis. Methods of characterising the detector fabrication are discussed in Chapter 4, including a novel characterisation using crossed polarisers to determine relative stress in the diamond. The characterisation of fully-functioning 3D diamond detectors using those methods is shown in Chapter 5. The results of characterisation by particle beams are shown in Chapter 6, providing new insight into the effects of different cell geometries. These characterisation results are summarised in Chapter 7, with an outlook towards the future applications of 3D diamond and its place within the LHC.

Chapter 2

Particle Detection

2.1 Introduction to Particle Detectors

A schematic for a planar detector[1] is shown in Figure 2.1. An incident charged particle (green in Figure 2.1) with sufficiently high energy will interact with the detector medium through one of three ways: ionisation; Cherenkov radiation, where particles travelling faster than the local phase velocity of the medium emit Cherenkov photons; and transition radiation, where photons are emitted as high energy particles cross a boundary between two different materials [20]. For an incident uncharged particle (specifically photons) there are also three possible interactions with the detector medium (which are all forms of indirect ionisation): the photoelectric effect (at energies $E \leq 100\,\text{keV}$)[2], where the photon is absorbed by an atomically-bound electron; Compton scattering (at $100\,\text{keV} \leq E \leq 10\,\text{MeV}$), where the photon collides and transfers some of its energy to an electron; and pair production (at $E \geq 10\,\text{MeV}$), where the photon is converted into an electron-positron pair. Ionisation of the detector material is the key interaction for the purposes of tracker detectors [20]. Applying a potential difference across the detector causes the charge carriers liberated by ionisation to drift in a direction defined by the applied field. The charge carriers are then collected by the electrodes and a signal is induced corresponding to their number.

Gases were used initially for the detector medium as this was the first developed

[1] A second detector architecture, 3D detectors, is discussed later in Section 2.5.

[2] The exact energies at which the processes dominate is strongly dependent on the atomic number of the material [21].

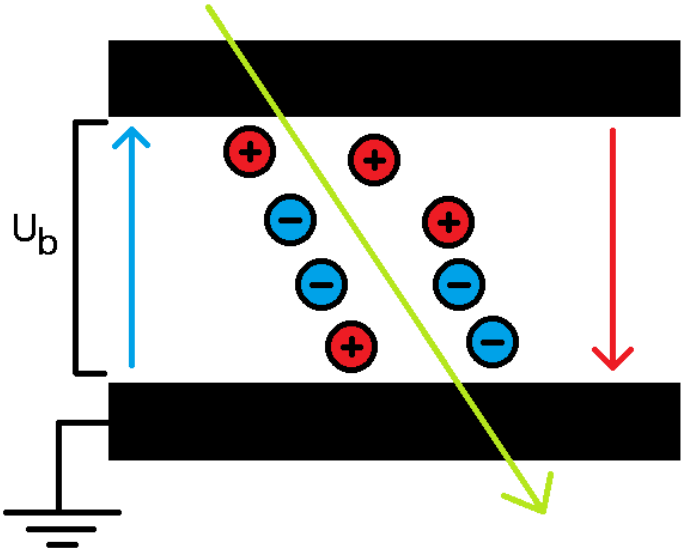

Figure 2.1: Schematic of how a planar detector collects charge induced by an incident particle. The particle (green) traverses the detector and ionises the detector. The charge (red and blue for positive and negative charge respectively) move to the electrodes (black) with a potential difference of U_b applied between them.

technology [22], though such detectors were phased out with the advent of semiconductor technology for the inner tracker detectors at the LHC. One reason why semiconductor detectors are preferable is due to the energy to create an electron-hole pair (explained in Section 2.6), which is typically lower for semiconductors (3.6 eV and 13 eV for silicon and diamond, respectively) versus gases (23.6 eV for solid argon [23]). The number of charge carriers induced can be approximated[3] by the ratio of the incident particle energy to the electron-hole pair energy, therefore more charge carriers implies a larger collected signal with the corollary that semiconductors have a higher energy resolution. Additionally, the density of semiconductors is higher than gases so the energy lost by an incident particle through ionisation may be localised to a smaller area in semiconductors. While gas detectors can provide excellent spatial resolutions by using time information, such as the Monitored Drift Tubes (MDT) in the ATLAS experiment at the Large Hadron Collider [24], the rate of particles per unit time per unit area is low. This implies that semiconductor detectors usually have greater spatial resolution than gaseous detectors. The movement of charge in semiconductors is also fast compared to gases so the charge is collected quickly, allowing for more accurate

[3]This assumes the particle stops within the detector medium, that is, it deposits all of its energy into the medium. A proper treatment of the energy loss of incident particles is discussed in Section 2.2.

timing measurements. All of these properties alone are desirable characteristics for a tracking detector.

There are considerable downsides to semiconductor detectors: cost, which scales with the detector area required; leakage current from thermal effects (see Section 2.4) that is mitigated only with constant cooling (adding to their cost); size, whereby material due to services, such as the support material and all electronics, as well as the sensitive detector substrate are all required in the tracking volume, which results in multiple scattering of the incident particle; and radiation damage, which negatively impacts the detector and is the biggest problem affecting semiconductor detectors. The mechanism for this is explained in more detail in Section 2.4.1.

2.2 Energy Loss of Particles

The number of charge carriers induced in the detector medium is proportional to the energy deposited by the incident particle. The method by which this occurs is dependent on the incident particle, that is, whether the incident particle has charge. In this thesis, the response of detectors to two different particle beams (photons and protons) was investigated (see Chapter 6), and the energy loss of these particles is discussed separately. The impact of this energy loss in terms of the generation of charge carriers in the detector medium (specifically in semiconductors) is discussed in Sections 2.3 and 2.4.

2.2.1 Energy Loss of Photons

Photons lose energy by one of three processes, the first of which is the photoelectric effect. In this case, photons incident to a material may be absorbed by electrons, thus transferring the energy to the electron. The electron may then be emitted from the material (thereby becoming a free electron) if the photon energy, hf, is greater than the work function, hf_0, of the material, such that the kinetic energy, E_K, of the emitted electron is given by $E_K = h(f - f_0)$, where h is the Planck constant. The energy range of this process is typically for low energy photons ($E << 1\,\text{MeV}$, typically O(keV)).

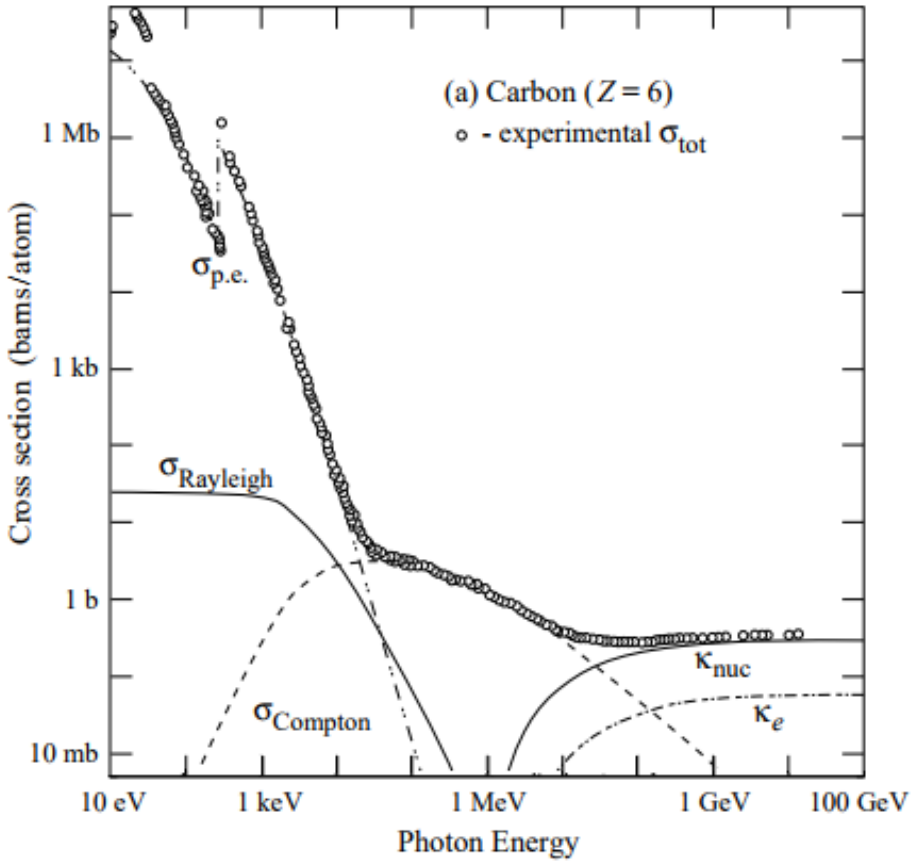

Figure 2.2: Cross sections of the processes by which photons lose energy in carbon. The processes are as follows: $\sigma_{p.e}$, the atomic photoelectric effect; $\sigma_{Rayleigh}$, Rayleigh scattering; $\sigma_{Compton}$, Compton scattering; κ_{nuc}, pair production in the nuclear field; κ_e, pair production in the electron field. Figure taken from reference [25].

The second process by which photons lose energy is scattering, which can be coherent/elastic ("Rayleigh" or "Thompson" scattering) or incoherent/inelastic ("Compton" scattering). Rayleigh scattering typically occurs when the incident photon energy is much less than the rest-mass energy of the particle by which it was scattered. In this case, there is no change to the energies of the scattering particle and the photon, and the energy range for this process is also for low energy photons ($E < 1\,\text{MeV}$). Compton scattering, in contrast to Rayleigh scattering, occurs when the incident photon is a significant fraction of the rest-mass energy of the scattering particle. In this case, some energy is transferred to the scattering particle from the incident photon, and so the energy range for this process is for higher energy photons (O(10 keV-10 MeV)).

The final process by which photons lose energy is pair production, where bombardment of a nucleus by an incident photon results in the production of an electron-positron pair. This process can occur in either the nuclear field or the electron field, whereby the cross section of the process is higher in the nuclear field. The energy range for this process is the highest, requiring a minimum energy above the sum of the two rest-mass energies of the resulting particles ($E >$ few MeV). These three processes and their cross sections are shown in Figure 2.2.

2.2.2 Energy Loss of Protons

The average energy loss of charged particles per unit length, $-\langle dE/dx \rangle$, in a material (also called the Stopping Power), with speed v, charge z, and energy E, is given by the Bethe formula (Equation 2.1), where m_e is the electron rest mass, c is the speed of light, n is the electron number density of the target, $\beta = v/c$, e is the electron charge, ϵ_0 is the vacuum permittivity, I is the mean excitation potential, and $\gamma = 1/(1-\beta^2)$. The classical form of Equation 2.1, which details the origin of some of the terms, is given in reference [26]. It should be noted that there are other corrections to be taken into account for highly relativistic particles, such as the density effect correction and the shell correction [26], which are not present in Equation 2.1. While such terms are important in experiments such as ATLAS at the Large Hadron Collider, the energies of the incident protons used in this thesis (O(MeV), see Chapter 6) are such that they are non-relativistic, so these effects are negligible.

$$-\left\langle \frac{dE}{dx} \right\rangle = \frac{4\pi}{m_e c^2} \frac{nz^2}{\beta^2} \left(\frac{e^2}{4\pi\epsilon_0} \right)^2 \left[\ln\left(\frac{2m_e c^2 \beta^2 \gamma^2}{I} \right) - \beta^2 \right] \tag{2.1}$$

In essence, Equation 2.1 describes how charged particles lose energy in their target by ionisation, which is the primary reason for energy losses in protons at the energies probed in this thesis. Charged particles may also lose energy by three other means: Bremsstrahlung, where charged particles may radiate photons in the Coulomb field of atomic nuclei; Cherenkov radiation, where charged particles travelling faster than the speed of light in a dielectric medium will emit radiation; and transition radiation, where charged particles crossing a boundary between two media with different dielectric constants will emit radiation. However, all three of these energy loss processes

primarily occur for high energy particles (O(GeV)), so for the energy range probed in this thesis, these processes are negligible.

The variation in the stopping power of protons in a material is shown in Figure 2.3a. In the context of this work, the stopping power is high enough that it is useful to define the range of protons in the target material. This is determined by integrating Equation 2.1, and the result is called the Bragg curve (shown in Figure 2.3b). In this case, if the range is less than the target thickness, then the incident particle will not pass through the target and all of its energy will be lost.

2.3 Semiconductor Physics

In solids electrons occupy eigenstates in bands of energy and are classed in one of three ways: a metal, a semiconductor, and an insulator. These classifications are based on the position of the Fermi level (and hence the Fermi energy) within such materials and is shown in Figure 2.4. The distribution of electron states is defined by the Fermi-Dirac distribution (Equation 2.2) and dictates the probability that a state of energy ϵ is occupied by an electron, where k is the Boltzmann constant, T is the temperature, and μ is the Fermi level. Hence, any state lying exactly at the Fermi level will have a 50% chance of being occupied. From Figure 2.4 the Fermi level lies within an energy band for a metal, whereas it lies between two bands (inside a band gap) for an insulator. A semiconductor is thus defined as a material whose Fermi level is also in a band gap (like an insulator), but whose band gap is small (typically O(eV)).

$$f(\epsilon) = \frac{1}{\exp\left[\frac{\epsilon-\mu}{kT}\right]+1} \tag{2.2}$$

Bands within a solid which are completely full of electrons are referred to as valence bands, whereas those completely devoid of electrons are called conduction bands. The excitation of an electron from the valence band to the conduction band allows for the free movement of that electron in the conduction band (due to the vast number of empty states). This also leaves an empty state within the valence band. This empty state can be thought of as a positively charged particle in a band of empty states, referred to as a hole. Holes will then move in the top of the valence band analogously to electrons in the bottom of the conduction band. In metals these bands completely

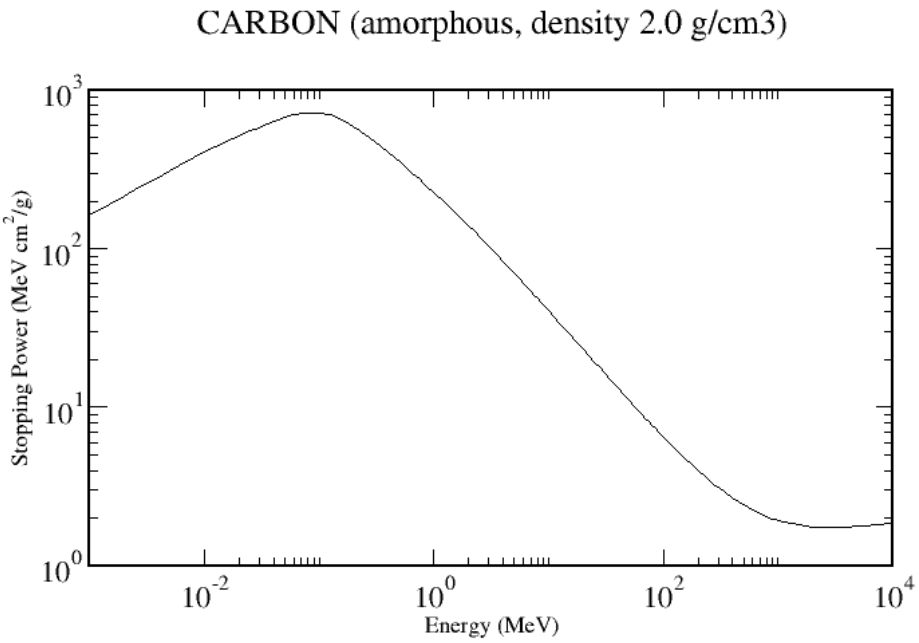

(a)

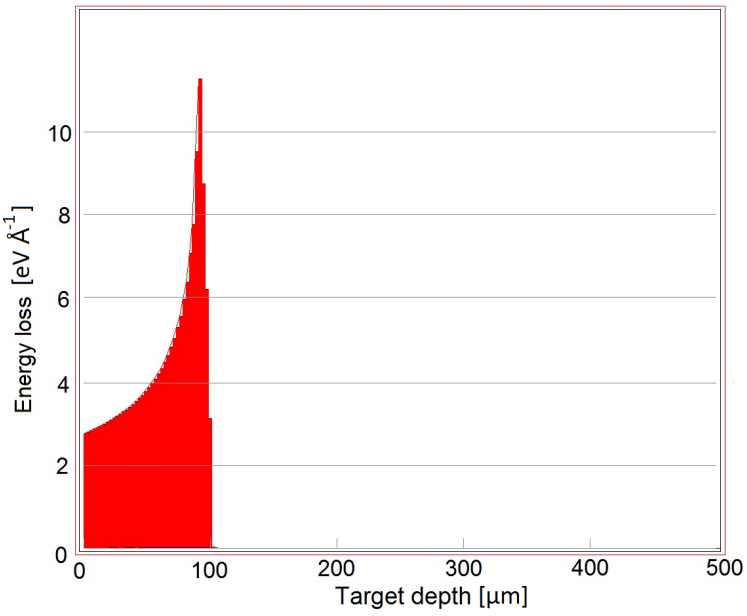

(b)

Figure 2.3: (a) The stopping power of protons in carbon as a function of energy. Note that the stopping power here is density-independent. (b) The energy loss of 4.5 MeV protons in diamond, of thickness 500 μm, as a function of depth. The integral of this curve would return the energy of the incident proton, which is generally true provided the range of protons at a given energy (in this case, 100 μm) is less than the target thickness. Figure (a) is taken from reference [27]. Figure (b) was created using software obtained from reference [28].

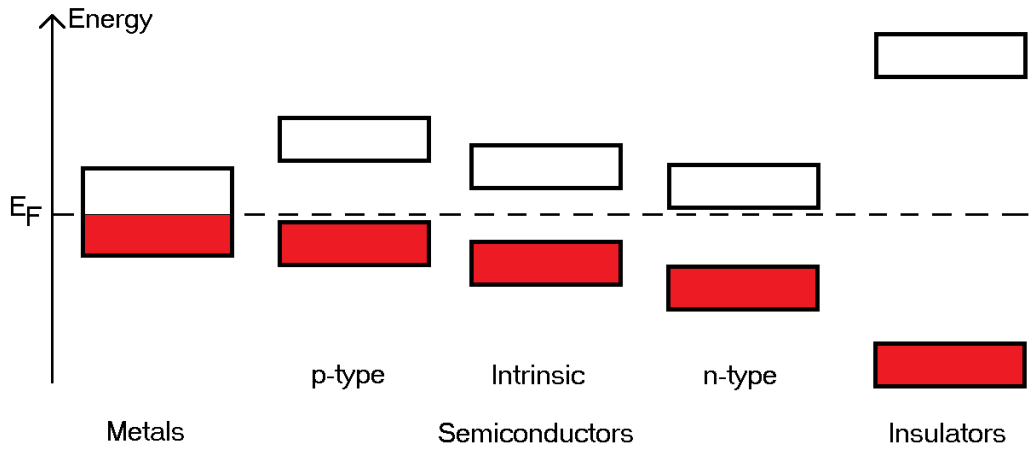

Figure 2.4: Structure of bands at 0 K for metals, semiconductors, and insulators, where E_F is the Fermi energy corresponding to the Fermi level, μ. Red indicates filled bands, and white indicates unfilled bands. The three different variations of semiconductors are due to doping.

overlap, thus electrons are free to move and hence metals are highly conductive. In insulators electrons need to have an energy greater than the band gap to be excited into the conduction band from the valence band, making insulators highly resistive.

The band gap in semiconductors is such that free electron movement (like in metals) is not possible but the probability of exciting an electron into the conduction band is higher due to a lower band gap versus insulators. The probability that electrons are thermally excited from the valence band is approximated by $\exp(-E_G/kT)$, where E_G is the band gap energy. This results in more thermal excitations with increasing temperature, which would correspond to a false signal (or noise) in a detector[4].

Semiconductors exist in one of three forms: intrinsic, n-type, and p-type. An intrinsic semiconductor is pure material without any dopants present, and typically consist of one chemical element (e.g. silicon) or two elements as a compound (e.g. gallium arsenide). On the other hand, n-type and p-type semiconductors are materials that are doped, that is, impurities are deliberately introduced to the semiconductor material to adjust the position of the bands relative to the Fermi level (as shown in Figure 2.4). For example, silicon doped with nitrogen will cause an excess of electrons and introduces a new energy state within the conduction band, effectively moving the valence band closer to the Fermi level and forming an n-type semiconductor. Conversely, a similar effect is seen when doping silicon with boron to result in an excess

[4]This is why the band structure in Figure 2.4 is true only at 0 K, since at higher temperatures there is the possibility of electrons occupying states in the conduction band.

of holes, which would result in a p-type semiconductor. The amount of doping of a semiconductor is expressed using a + or − symbol to denote either very high or low doping e.g. n^+-type and p^--type imply a high amount of electron doping and a low amount of hole doping respectively[5]. By bringing both n-type and p-type semiconductors together, one can form a diode which forms the basis of a semiconductor detector.

2.4 Principles of Semiconductor Detectors

The schematic of a semiconductor detector is similar to the basic detector configuration of electrodes on either side of the bulk material (shown previously in Figure 2.1), except the detector is a diode with the electrodes comprising of n-type and p-type material and weakly doped n-type material for the bulk as shown in Figure 2.5. The combination of these materials at equilibrium (i.e. with no applied bias voltage) forms a depletion layer within the detector where electrons from the n-type region diffuse into the p-type region and holes from the p-type region diffuse into the n-type region. This results in the recombination of diffused electrons with holes in the p-type region and the recombination of diffused holes with electrons in the n-type region. This diffusion near the interface of the p-type and n-type regions forms an intermediate region of these charged ions, and hence a net electric charge. The width of the depletion layer increases as the diffusion of charge carriers occurs due to further creation of charge ions. However, the depletion layer has an electric field due to these ions, resulting in charge carrier drift in the direction of the electric field. This prevents further diffusion of the charge carriers[6]. These processes reach an equilibrium state where the size of the depletion layer (under zero applied bias voltage) remains static and no more diffusion occurs.

The bias voltage of the electrodes is applicable in either the forward or reverse configuration. The forward bias case is shown in Figure 2.5, and this forces electrons

[5]Note that even for high levels of doping the relative amount of dopant to intrinsic atoms is low i.e. $O(\leq 10^{-4})$ for the case of silicon.

[6]Charge carrier drift occurs in the presence of an (applied) electric field, whereas charge carrier diffusion can occur independently of an applied electric field. As such, the charge carrier drift current and diffusion current are in opposite directions.

Figure 2.5: Schematic of a semiconductor detector, highlighting the electrode doping. A positive and negative bias are applied to the p-type and n-type electrodes (a forward bias).

from the n-type region to interact with (thus neutralise) the positive ions in the depletion layer and forces holes from the p-type region to interact with the negative ions. This causes the width of the depletion layer to decrease. With a sufficiently high bias voltage the depletion layer becomes sufficiently thin that its electric field no longer repels the diffusing charge carriers and thus increases conductivity in the device. Despite the applied bias voltage (hence the applied electric field) dictating the diffusion of charge carriers across the device to the electrodes, the charge carriers will preferentially combine i.e. electrons and holes have a diffusion length such that they will travel only a short distance into the p-type and n-type regions, respectively, before recombining. It is a necessity that the sum of the electron and hole currents is zero due to Kirchhoff's current law but the opposing directions of motion of the charge carriers and their opposing charges result in the same overall direction of current.

In reverse bias (where the applied bias is opposite to that shown in Figure 2.5) the opposite case occurs; charge carriers are forced away from the depletion layer, resulting in the generation of more ions and thus increasing the width of the depletion layer and its electric field. This increases the resistivity of the device and prevents current flow. With a sufficiently high applied bias voltage a breakdown effect occurs which allows the device to conduct. The breakdown effect occurs either as the Zener effect or as an avalanche breakdown (also known as impact ionisation). In the case of the Zener effect the electric field is high enough such that electrons may quantum tunnel

across the depletion layer, causing a rapid increase in free charge carriers and thus current. In the case of avalanche breakdown the electric field in the depletion layer accelerates charge carriers to such a degree that bound electrons in the semiconductor material are knocked free. This creates further free charge carriers and thus rapidly increases the current in the device. This effect may repeat with the now free charge carriers if they are liberated with sufficiently high energy. Despite the risk of these breakdown effects, reverse biased semiconductor detectors are preferable since they operate at low current versus forward biased semiconductors. This means that any signal induced current will be larger than the electron current in the diode.

For a semiconductor detector operating with some applied bias, it is unlikely that the charge carriers would be collected by the electrodes due to their preference to recombine with opposite sign charge carriers. This would mean the charge received by the electrode would be small. Instead, it is the motion of charge in the applied electric field that induces an electric current in the electrode as defined by the Shockley-Ramo theorem [29, 30] in Equation 2.3, where the instantaneous current, i is induced on a particular electrode by the motion of the charge carrier with instantaneous velocity v, and E_w is the component of the weighting field in the direction of v at the charge carrier's position. This assumes that the electrode in question is at unit potential and other electrodes are grounded. Hence, charge carriers far from the electrode in question will induce a much lower current (they are in a low field area) than charge carriers near the electrode.

$$i = q\, v\, E_v \tag{2.3}$$

The drift velocity of the charge carriers is given $v = \mu\, E$, where μ is the charge carrier mobility and dictates the collection of charge in a material. In low field regions the carrier mobility is constant (called μ_0, or the low field carrier mobility), but in high field regions there is a limitation on the drift velocity due to the detector material (and hence the doping in the detector). This is because at higher drift velocities there are more interactions occurring between the accelerated charge carrier and the detector material, resulting in phonon emission. The carrier mobility thus varies with the electric field such that the drift velocity is then described by Equation 2.4, where v_s is the saturation velocity [31].

$$v = \frac{\mu_0 E}{1 + \frac{\mu_0 E}{v_s}} \tag{2.4}$$

2.4.1 Radiation damage

The biggest problem with detectors used in environments with a high integrated flux is the interactions with the detectors on the microscopic level. The presence of radiation, from either α, β, γ-rays or from particles such as protons and neutrons, can induce defects in the crystal lattice. This accumulated radiation damage will unfavourably modify the macroscopic properties of the detector, such as the band gap energy (which may introduce more noise) or the detector efficiency. This would require either corrections to the analysis of the collected signal or even a replacement of the detector itself. The types of defects that may be induced are as follows:[7]

- Vacancies and interstitials. These are point defects that occur in the crystal lattice where vacancies refers to the non-existence of atoms in the lattice structure and interstitials refers to atoms occupying space between the lattice structure, both of which are shown in Figure 2.6. These are the simplest cases of radiation damage and are induced when the energy of the incident radiation is greater than the displacement energy of the detector material, E_d. These defects arise from particles such as electrons and may be thought of as a form of inelastic scattering. Vacancies and interstitials are often induced in pairs (known as Frenkel pairs) and are thus intrinsic defects[8].

- Cluster defects. These are vacancies and interstitials that occur en masse due to a high energy particle. If the incident energy is much larger than E_d, then a particle can induce pairs of vacancies and interstitials at multiple locations within the lattice. Atoms affected by this are known as primary knock-on atoms (PKAs) and can cause displacement cascades if each interaction imparts a significant amount of energy to the lattice atom i.e. PKAs may induce vacancies and

[7] It should be noted that this list is not exhaustive as the focus of the work in this thesis is not on radiation damage and the subsequent detector response. More information on radiation damage can be found in references [32–34].

[8] They may be induced individually and thus would be extrinsic defects. These defects would arise from impurities in the detector material (e.g. carbon atoms in a silicon substrate or from doping the material) and may substitute for lattice atoms or occur as an interstitial.

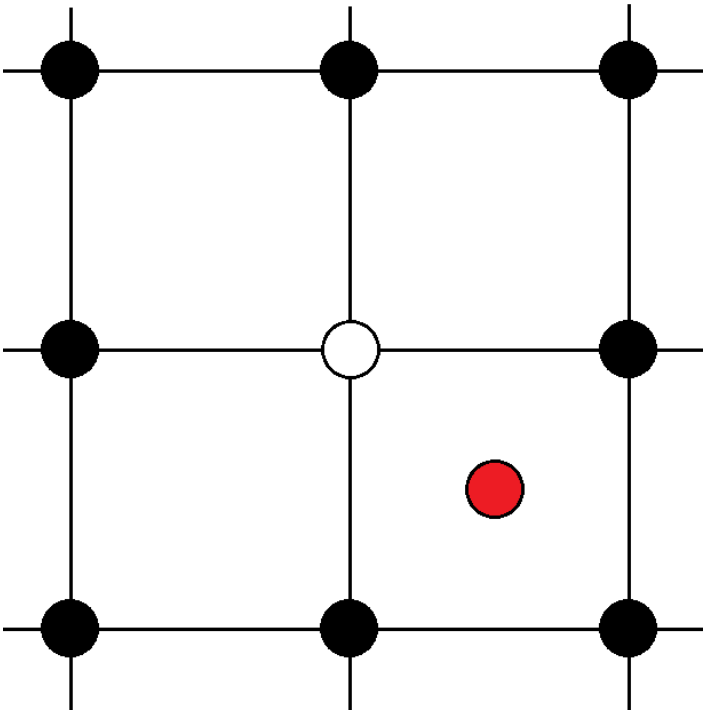

Figure 2.6: Illustration of the presence of vacancies (white circle) and interstitials (red circle) in the crystal lattice. In this example the vacancy and interstitial are Frenkel pairs.

interstitials of their own, which are called secondary knock-on atoms. Hence, cluster defects may occur in the form of large regions of vacancies (depleted zones) that would affect the positions of the energy levels within the material.

The most important issue in detector physics which arises from these two defects is trapping, which occurs when a charge carrier moving towards an electrode is not collected (due to defects within the material) and results in a loss of signal. Areas where the charge carriers are "lost" are known as traps, and the reduction of collected charge versus a non-damaged detector implies a reduction of the detection efficiency. The creation of these traps within a solid state detector is unavoidable (particularly in harsh radiation environments) so mitigating the effects of traps is imperative. One way is to greatly increase the electric field to ensure the charge is fully collected and (by definition) reduces the trapping probability. This is not ideal since the operation of these detectors requires bias voltages of $\mathrm{O}(10^2\,\mathrm{V})$, which is close to the breakdown field for the detector material (explained in Section 2.6) and would damage the detector. This issue is greatly rectified by changing the electrode configuration.

2.5 Detector architecture

There are two common detector architectures, known as planar and 3D detectors[9]. Planar detectors have been discussed in this section up to this point, where the electrodes lie on the top and bottom surfaces of the detector substrate (see Figure 2.7). This detector type is common due to its ease of manufacture, yet this has a few known issues. For example, it is known that high particle fluences induce defects in the detector substrate (as outlined in Section 2.4.1), and the creation of traps due to radiation damage implies that a wide separation between the electrodes increases the probability that charge carriers become trapped. This reduces the signal one expects to see from incident charge, limiting the viability of detectors in high radiation environments over a long time period. This is somewhat rectified by using a thinner substrate though it is difficult to make a very thin, homogeneous material and would result in fewer charge carriers due to a smaller active region. These problems are resolved using the 3D architecture.

3D detectors are a relatively new concept (proposed in the 1990s by Parker et al. [6]) where the electrodes penetrate through the bulk of the detector substrate (shown in Figure 2.7). The greatest advantage of this detector type is the distance between the electrodes, or rather, the decoupling of the electrode separation and the substrate thickness, which allows for more radiation hard detectors [7]. This decoupling also allows for 3D detectors with a large thickness (to maximise the number of charge carriers induced by an incident particle) but with a small electrode spacing. This results in faster collection times of the charge carriers versus planar detectors (for the same electric field strength and substrate thickness), and a closer electrode proximity also reduces the trapping probability to mitigate signal losses. Although this "3D" arrangement of the electrodes results in a more complicated electric field pattern, it also results in a much stronger electric field such that the applied bias voltage may be significantly reduced for 3D detectors. For example, typical bias voltages for planar detectors would be $\mathrm{O}(100\,\mathrm{V})$ for full charge collection, whereas the bias voltage for full charge collection for 3D detectors may be as low as $\mathrm{O}(20\,\mathrm{V})$ [36].

[9]There are other architectures such as silicon drift detectors [35], but this discussion is devoted to the most common architectures used in this field.

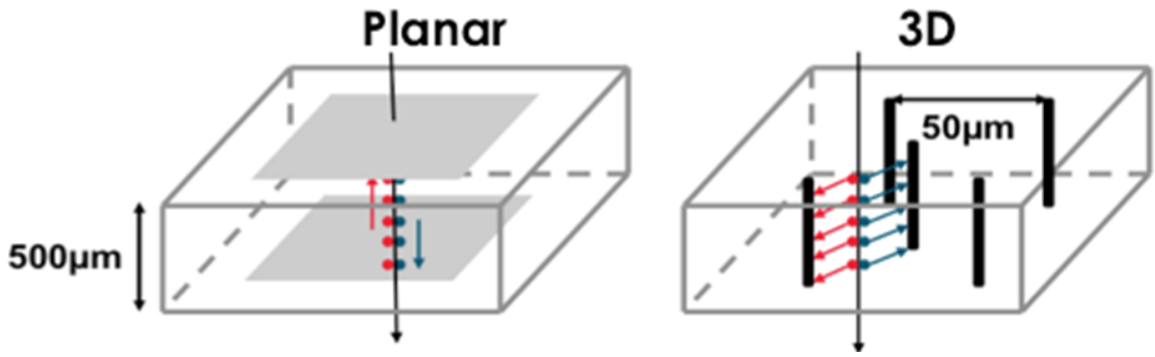

Figure 2.7: Schematics of detectors with planar (left) and 3D (right) architecture. In the planar case the electrodes are implanted within the top and bottom surfaces of the material. In the 3D case the electrodes penetrate perpendicular to the top and bottom surfaces through the bulk material. Figure taken from reference [37].

The greatest challenge with 3D detectors is the readout electronics, which is shown in Figure 2.8. To read out the central electrodes (blue) for each unit cell there are two options. One is to connect all of the readout electrodes together and read out strips (Figure 2.8, left) via wire bonding. This is a simple configuration that requires one readout channel per strip, and for the research and development of 3D detectors this is preferred. For a full scale tracking detector this would be insufficient since the capacitance of such a detector would be high[10]. The other option for the readout electronics is to read out each cell individually (Figure 2.8, right), which must be done in the case of tracking detectors in the LHC. The challenge then lies with the number of cells to read out simultaneously, where the number of readout connections required scales with the number of rows and columns[11]. Rather than using wire bonds to connect to each readout electrode bump bonding is used instead, where these electrodes are connected to intermediate pads (green). The detector is then sandwiched onto a readout chip that matches the arrangement of the bump bonds. While this is a necessity for tracking detectors, this work is focused on the development of 3D diamond detectors and thus it is preferable to investigate and analyse the response of a few readout strips rather than several cells, and so the former readout scheme is utilised throughout this thesis.

[10] Additionally, if charge were incident to one of the cells in the strip, information regarding exactly where along the strip the charge was detected would be lost, as is the nature of strip detectors versus reading out individual cells.

[11] As a demonstrative example, one can think of the number of readout connections required as $O(n^2)$ versus that of simply reading out strips ($O(n)$). Hence a detector with ten rows and columns of cells requires ten times more readout connections if one were to read out each cell versus each strip.

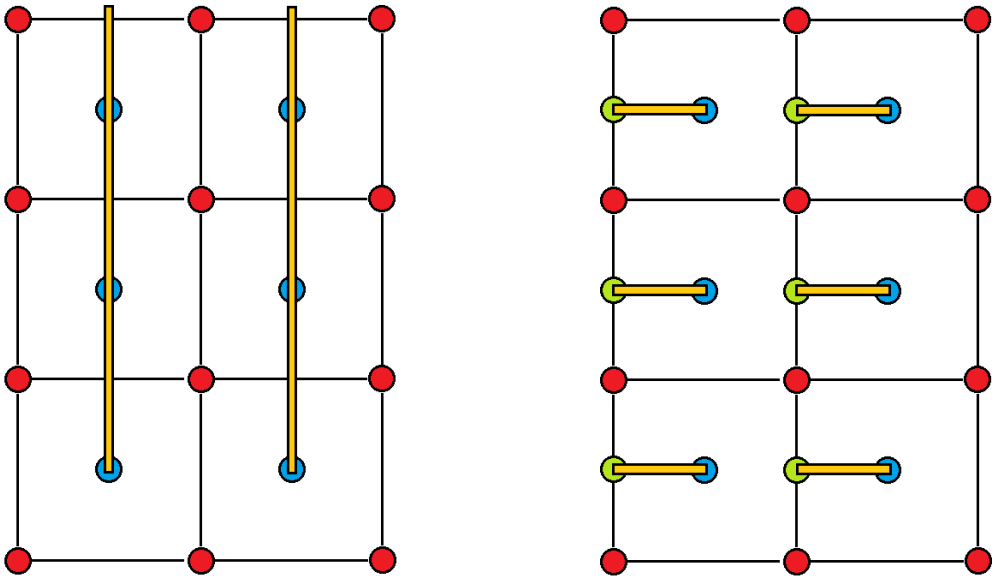

Figure 2.8: Two different methods to read out 3D detectors. Red and blue circles denote the bias and readout electrodes, respectively, and the gold areas denote metal contacts which connect readout electrode in either a strip formation (left) or to pads for bump bond readout (right).

One important detector characteristic is the concept of charge sharing, where charge induced by an incident particle may be collected by two or more strips (or cells). If there is high charge sharing (Figure 2.9a) then several cells could collect the induced charge so it may become difficult to spatially resolve the path incident particles take through the detector, resulting in low spatial resolution. Conversely if there is low or zero charge sharing (Figure 2.9b) then it may be difficult to determine the exact path of the incident particle. The level of charge sharing then dictates the viability of a detector for a specific purpose. For example, it is preferable to have some degree of charge sharing for tracking detectors (Figure 2.9c), since it can veto some possible paths taken by the incident charge. However, very little charge sharing is desired for dosimetry applications where it is vital that in the area that the radiation is delivered, the delivered and detected radiation match as best as possible, particularly when the target is living tissue (e.g. a patient)[12]. These detectors will also require submillimetre resolution such as those in reference [38].

[12] An example of when a discrepancy between the delivered and detected dose could occur is if the detector has a high level of charge sharing. In this case several adjacent cells may also collect some charge, hence there is a possibility of lower charge being collected in the region of interest. This may appear that the incident radiation spreads out more than in reality, so a level of radiation higher than is recommended may then be delivered to ensure the target tissue is "correctly" irradiated.

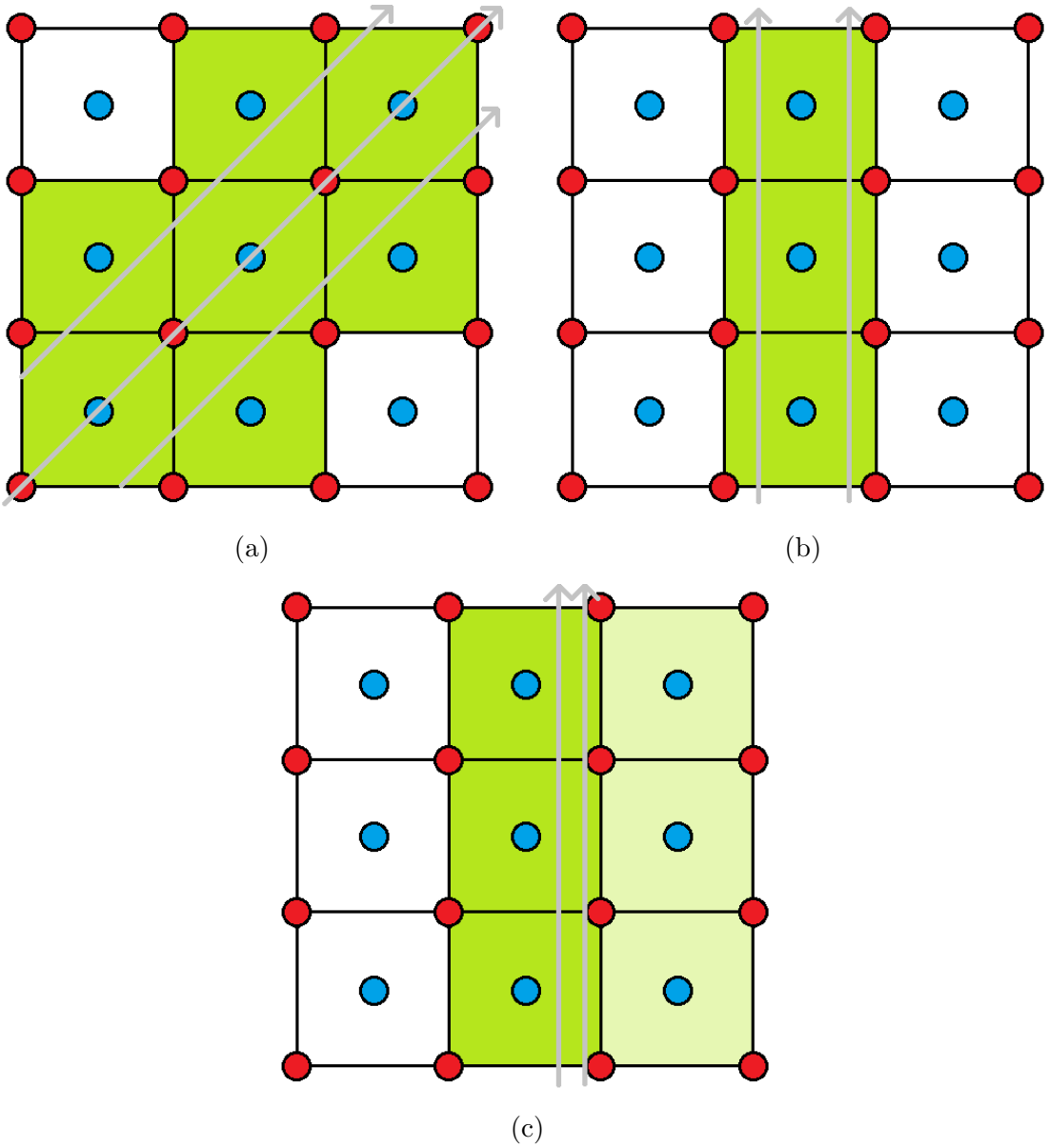

Figure 2.9: Examples of charge sharing in a pixel detector, as viewed top-down. Red and blue correspond to the bias and readout electrodes, green indicates the cells in which charge is collected, and grey indicates potential paths taken by some incident particle which induces charge in the detector. (a) High level of charge sharing. (b) Low (or zero) level of charge sharing. (c) An intermediate level of charge sharing. In this case the cells in the right hand column collect a smaller fraction (denoted in a lighter green) of the charge than the central cells. Note that in all of these cases not all of the potential paths have been drawn, and some have been included only to demonstrate some possibilities in each case.

Material Property	Diamond	Silicon	Germanium
Displacement Energy [eV]	43	$\leq$20	15
Thermal Conductivity [$Wm^{-1}K^{-1}$]	$\leq$2000	150	58
Dielectric Constant [a.u.]	5.6	11.7	16.2
Band Gap Energy [eV]	5.5	1.1	0.66
Electron-Hole Pair Energy [eV]	13	3.6	2.9
Low-field Electron Mobility [$cm^2V^{-1}s^{-1}$]	2200	1400	3900
Low-field Hole Mobility [$cm^2V^{-1}s^{-1}$]	1800	450	1900
Breakdown Field [Vm^{-1}]	10^6 - 10^7	3×10^5	10^5

Table 2.1: Properties of solid state detector materials [39, 40].

2.6 Detector materials

There are several materials used for solid state detectors, of which three are considered here: diamond, silicon, and germanium. The properties of these materials are summarised in Table 2.1. These properties may be advantageous for the material's use as a detector substrate, and these are discussed below.

The displacement energy of a material is the energy at which defects may be introduced (as discussed in Section 2.4.1). Radiation damage is already an issue with silicon detectors at the Large Hadron Collider. Despite improvements in radiation hardness through the 3D architecture future luminosity upgrades to the Large Hadron Collider will still present a problem for silicon and even more so for germanium, yet diamond should survive such a high particle environment based on this property alone and is expected to increase further using the 3D architecture.

The thermal conductivity of a material is a measure of the rate at which heat is conducted. It is crucial in detectors when dealing with thermal noise as sources of heat induced in a detector affect its performance, and must be corrected for through methods such as heat sinks and constant cooling of the detectors. The heat is conducted away via lattice vibrations, so diamond is therefore a great material since its compact atomic structure results in fast conduction of heat when compared to silicon and germanium. A corollary of this (and diamond's high band gap energy) is that the diamond substrate itself does not require constant cooling, and so can be operated at room temperature. However, it should be noted that the main heat source in the detector environment is the electronics used, which is the same regardless of the chosen substrate.

The dielectric constant (or relative permittivity) of a material denotes the ability to resist an electric field, that is, a higher dielectric constant implies a material will retain induced charge for a longer period of time. This is correlated with the polarisability of a material and indicates some probability of a remnant field even after a bias voltage is no longer applied to the detector, so extra care must be taken to remove this effect where possible. Hence, a low dielectric constant is correlated with a low capacitance. It is this quantity that is preferred for detectors, since this affects the amount of noise in the amplifier chain when such detectors are read out, making diamond the material of choice.

The band gap energy has been shown to be important when considering detector materials (see Section 2.3) and is summarised as follows: the band gap energy denotes the material's ability to promote electrons from the valence band into the conduction band and thus its susceptibility to noise through thermal excitations (see explanation for thermal conductivity). This implies a compromise between the performance of a detector and the need to suppress such noise. This implies less cooling is required for diamond versus silicon and germanium (for which thermal excitations are more likely) and that diamond exhibits a lower leakage current (thus does not require a p-n junction), so diamond is preferable in environments where the incident particles have high energy.

The electron-hole pair energy is a measure of the signal strength in a material such that a lower energy implies more electron-hole pairs are produced per interaction. This results in a larger charge signal, which is useful for increasing the signal to noise ratio of the detector. This is one of the biggest advantages of silicon versus diamond and one of the reasons for silicon's longevity in the Large Hadron Collider, since diamond has the largest electron-hole pair energy of the three materials and thus a lower signal is observed.

The charge carrier mobilities are a measure of the movement of charge in a material while experiencing an electric field, where a higher mobility implies faster collection of charge by the electrodes. Detectors made from materials with high mobilities (diamond and germanium) may be operated in a lower electric field versus detectors with low mobilities (silicon) while retaining fast charge collection. This may be preferable if the collection of the charge is limited by the electronics, so applying a high bias voltage

is both unnecessary and increases the probability of long term damage of the detector (see explanation for the breakdown field). Although it does not have the highest carrier mobilities diamond has similar carrier mobilities for both carrier types so all of the charge is collected on timescales of O(ns), whereas the charge carriers in silicon and germanium will have significantly different collection times.

The final characteristic is the breakdown field, where an applied field greater than this value results in a material becoming completely electrically conductive[13], thus limiting the voltage difference applied between two electrodes. Surpassing the breakdown field (particularly for a long time period) may damage a detector, so a higher breakdown field is preferable to mitigate any damage. This also allows for the operation of detectors at a higher bias voltage, which results in faster collection of charge (subject to the saturation velocities of the charge carriers and limitations on readout electronics). As such diamond is therefore the material of choice.

Aside from these characteristics, sources of noise vary between the different substrates. The total effect of all sources of noise are added in quadrature and can be summarised in Equation 2.5, where ENC is an abbreviation for the equivalent noise charge, i denotes the noise current sources, V denotes the noise voltage sources, and A denotes the amplifier noise, e is the electronic charge, I_d is the sensor bias current, k is the Boltzmann constant, T is the temperature, R_b is the bias resistor, i_{na} is the current source noise of the amplifier, τ is the differentiation and integration time constant (assumed to be equal), R_s is the series resistor, e_{na} is the voltage source noise of the amplifier, C_d is the detector capacitance, and A_f is the noise coefficient of the amplifier [41]. Note that Equation 2.5 assumes a circuit consisting of a detector and front-end amplifier. In all cases, the factor $e^2/8$ is used as a normalisation factor. The current sources consist of the sensor bias current, the shunt resistance, and the amplifier noise. The voltage sources consist of the series resistance and the amplifier noise[14].

The noise from current sources is partially dependent on the resistance of the substrate material. Diamond is an insulator (unlike the semiconductors silicon and germanium), so its higher resistance results in lower current noise. The noise from

[13]The breakdown field is related to the band gap energy of the material, so materials with a high band gap (e.g. diamond) are expected to have a larger breakdown field.

[14]These noise sources are discussed in greater detail in reference [41].

voltage sources is dependent on the detector capacitance. Given that diamond has a lower dielectric constant (and hence capacitance) than the other materials, the contribution from this noise source will be the lowest. Finally, the amplifier noise is also dependent on the detector capacitance, resulting in a low contribution for diamond detectors.

$$\begin{aligned} ENC_i^2 &= \frac{e^2}{8}\left(2eI_d + \frac{4kT}{R_b} + i_{na}^2\right)\tau \\ ENC_V^2 &= \frac{e^2}{8}\left(4kTR_s + e_{na}^2\right)\frac{C_d^2}{\tau} \\ ENC_A^2 &= 4A_f C_d^2 \end{aligned} \tag{2.5}$$

From these properties it is clear each of these materials is suited for a different purpose. For example, germanium detectors cannot withstand high particle fluence environments and require constant cooling to operate with low leakage current. However, its carrier mobilities are attractive properties in a detector so it is well suited to gamma ray spectroscopy, wherein it provides high resolution measurements when compared with the other materials. Silicon has been shown to be viable in reasonably harsh radiation environments (specifically those at the Large Hadron Collider), and while silicon detectors are still planned for high luminosity experiments (described in Chapter 1), diamond is the most likely material to succeed silicon in this area and further withstand such harsh radiation environments. Diamond has some downsides not previously mentioned, particularly that silicon has been used extensively in applications not limited to tracking detectors. This makes silicon a well understood and cheap material versus diamond.

Diamond has already been used in the LHC as part of the Diamond Beam Monitor (DBM), an upgrade to the Beam Conditions Monitor (BCM) [42, 43]. In these detectors, the radiation hardness of diamond is exploited to increase the longevity of the detectors as the beam luminosity is increased over the lifetime of the LHC and the HL-LHC (discussed in Chapter 1). Despite diamond's success in this area [44], these detectors lie further from the interaction vertex than the inner pixel detector [43]. It is the pixel detectors which is part of the motivation for this thesis. Optimisation of the manufacturing processes is hence required for diamond to be competitive with silicon as the desired pixel detector substrate, which includes both the fabrication of the diamond material with a high charge collection distance and the fabrication of 3D detectors (both discussed in Chapter 3).

Chapter 3

Manufacture of Diamond Detectors

The manufacture of diamond detectors consists of three stages: the growth of the diamond samples, the fabrication of the electrodes, and producing the metal contacts for the electrodes to apply a bias voltage and to read out the detector. The growth stage is performed by companies such as Element Six [45] and IIa [46], whereas the other two stages are performed in Manchester. The focus of this PhD thesis is on the formation of the graphitic electrodes in diamond, so more attention is given to this stage of the detector manufacture, whereas the metallisation of the graphitic electrodes is covered in greater detail by G. Forcolin [47].

3.1 Diamond Sample Growth

Naturally occurring diamonds are impractical for use in detectors; sourcing such diamonds would be expensive and cutting them to the required dimensions would be wasteful. Synthetic diamond films are used instead due to the inherently greater control over the growth and dimensions of such diamonds, with the most common growth method being chemical vapour deposition (CVD). There are many variations of CVD that affect the growth of different substances[1], such as the use of a plasma to allow for deposition at lower temperatures, so only the simplest set-up and processes for CVD is described.

Diamond films are commonly grown using a ratio of 1:99 of hydrogen gas and a

[1]For example, silicon films may also be synthesised using CVD, which along with diamond may include dopants in its growth in order to "fine tune" bulk properties such as the band gap energy.

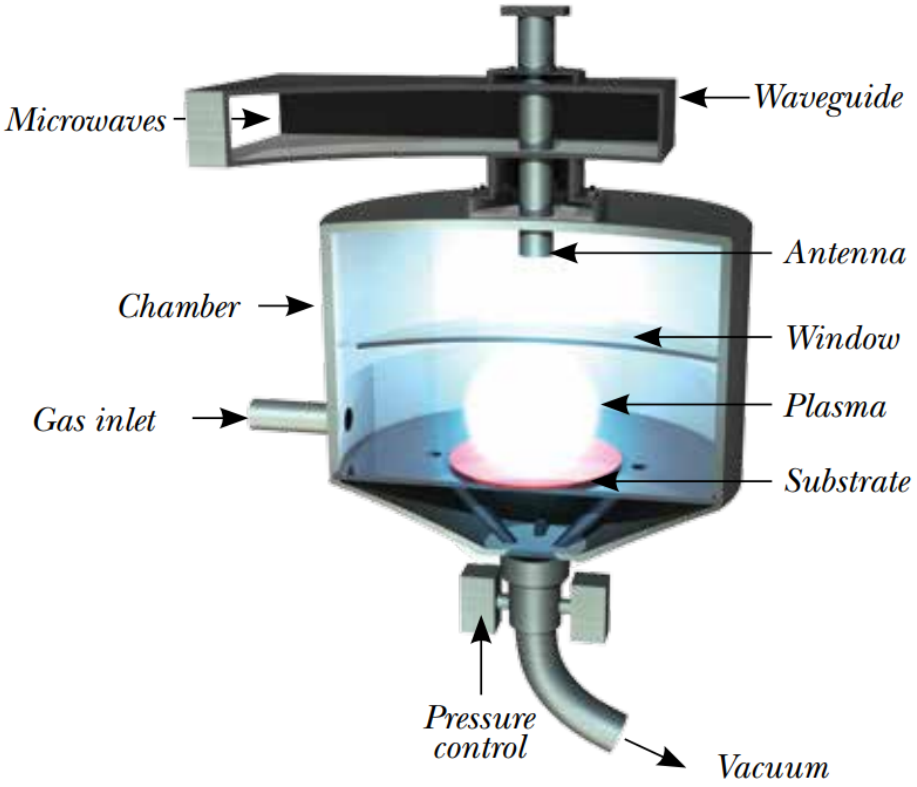

Figure 3.1: Summary of the chemical vapour deposition process. In this example, microwaves are used to assist the process (also called MPCVD) by igniting the carbon source. Figure taken from reference [45].

"carbon source" such as methane gas, due to its abundance and cost, that are fed into a chamber (Figure 3.1) operating at temperatures of $O(\geq 600\,^{\circ}\mathrm{C})$ and low pressure of $O(< 27\,\mathrm{kPa})$. The input gases are ionised, allowing the hydrogen gas to break the bonds of the carbon source to form an ion plasma, which are the precursors for the desired reaction. The carbon atoms are then deposited onto the chosen substrate on a rotary stage. The use of a low pressure environment and a rotary stage ensure uniform growth of the film, and the conditions are chosen such that the stable carbon configuration is diamond rather than graphite.

The chosen substrate affects the outcome of the growth of the diamond film. To grow single crystal diamond films, a diamond crystal (the "seed" for growth) is used for the substrate for the deposition of the carbon atoms, resulting in homoepitaxial growth, i.e. where one layer, which is the same material type as the substrate, is grown at a time on the existing diamond lattice. Alternatively, polycrystalline diamond films are grown using a non-diamond substrate which has been prepared in a way to aid the formation of diamond films. For example, silicon prepared with diamond powder

is often used where the powder acts as a seed in this case. This forms multiple crystals which during growth eventually form a layer of compacted diamond crystals called "grains". Polycrystalline diamond films are typically larger than that of single crystal diamond films, though the grain boundaries may induce local defects similar to those mentioned in Chapter 2. The growth rate of CVD diamond films is typically $10\,\mu\mathrm{m\,hr}^{-1}$, though this depends on the desired film quality and size.

An important quality of CVD diamonds for use in tracker detectors is the charge collection distance (CCD), which is the average distance an electron-hole pair travels in diamond before becoming trapped. This distance is the mean free path, δ, of both electrons and holes in diamond, and is given by Equation 3.1, where μ is the charge carrier mobility, τ is the charge carrier lifetime, and E is the electric field strength [48]. A high charge collection distance is desirable to ensure all of the induced charge is collected. This is achieved by either applying a high bias voltage to achieve a high electric field (which could cause electrical breakdown, as discussed in Chapter 2) or by increasing the lifetimes of the charge carriers. This is possible only by mitigating the number of traps in the diamond substrate, which is achieved through the manufacture of high quality CVD diamonds. A slow growth rate typically results in higher purity diamond [49]. Single crystal diamond films have been shown [50] to have a higher CCD ($\mathrm{O}(500\,\mu\mathrm{m})$ versus polycrystalline diamonds ($\mathrm{O}(200\,\mu\mathrm{m})$) [45].

$$\delta = (\mu_e \tau_e + \mu_h \tau_h)\, E \tag{3.1}$$

3.2 Laser-induced Graphitisation of Diamond

The formation of electrodes in 3D tracking detectors is usually performed via etching the bulk material and then implanting ions to form p-type and n-type electrodes[2]. This technique can be used for different bulk materials, including silicon and diamond. However, it is difficult to achieve high levels of precision with the etching process and the whole electrode formation process may be both time-consuming and expensive. Diamond is unique in that the electrodes can be manufactured using a laser-induced graphitisation process. The process uses a fast pulse length ($\leq$O((ns))) to induce

[2]There are several methods for etching and for the implantation/diffusion of electrodes, which are not relevant to this thesis though are explained further in reference [51].

a phase change in the bulk material at the focal point, that is, the bonds on the carbon atoms are altered from an sp^3 (diamond-like structure) to an sp^2 (graphite-like structure) configuration[3]. This process does not require the use of chemicals (unlike most etching processes) and allows for the formation of arbitrary 3D electrodes within the diamond bulk.

At the focal point of the laser, the electrons in occupied energy states are excited to unoccupied energy states at a rate determined by the laser intensity. The excitation process is fast enough such that a nonequilibrium distribution of electrons forms, resulting in electron-electron collisions and an equilibrium occupation of energy levels [52]. This is known as the nonthermal graphitisation process. During this process thermal graphitisation may also occur, whereby "hot" electrons, those which have sufficient energy to be elevated from the valence band to the conduction band, may move from the region excited due to nonthermal graphitisation to other nearby unexcited regions. Both of these process will cause local microstructuring of the diamond lattice to a graphite-like structure. The laser is initially focused on the bottom surface (the "seed side") of the diamond, as shown in Figure 3.2, and the focal spot is gradually moved towards the top surface (the "exit side") of the diamond to prevent light absorption by the newly-formed graphite. It should be noted that the speed at which the focal spot is moved within the diamond substrate is hereafter referred to as the "translation speed".

As the focal point is moved the graphitisation process is continually repeated for every layer of carbon atoms. The direction of movement of the focal spot, along with induced strain between the diamond and graphite structures that causes a pressure difference, results in the preferential formation of graphite in this direction and disfavoured formation in perpendicular directions. However, thermal graphitisation may, and generally does, occur perpendicularly to the processing direction and causes the formation of graphite structure larger than the effective spot size in diamond, as well as inducing more stress on the diamond lattice. This growth mechanism means the expected structure (observed via Scanning Electron Microscopy) is a large crater on

[3]The terminology refers to the type of bonds on the carbon atoms. For example, sp^3 implies each carbon atom is connected to four neighbouring atoms (four single bonds), whereas sp^2 implies each carbon atoms is connected to three neighbouring atoms (one double bond and two single bonds). The sp^2 configuration alters the shape of the "s" and "p" orbitals, causing less repulsion and greater overlap versus the sp^3 configuration.

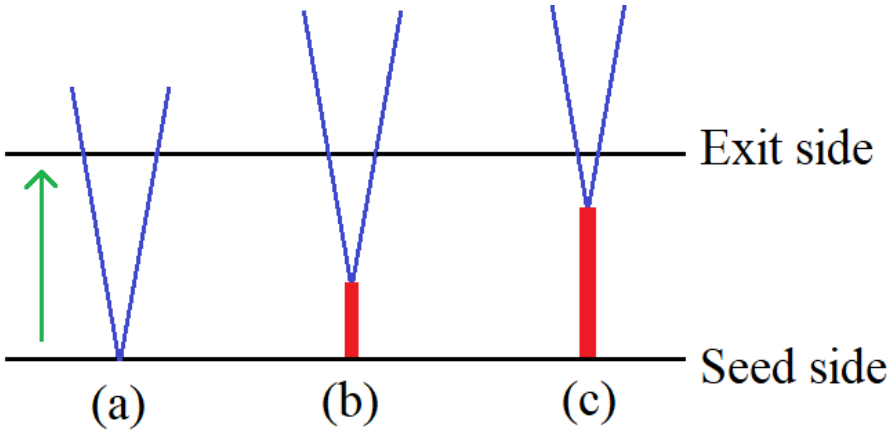

Figure 3.2: A summary of laser-induced graphitisation in diamond. Stage (a) shows the start of the graphitisation process, where the laser (blue) is focused onto the seed side of the diamond. The focal spot is moved towards the exit side, resulting in the gradual formation of graphitic structure (red), shown in stages (b) and (c). The growth direction is denoted by the green arrow.

the exit side of the diamond (resulting from a huge pressure build up that removes the top layers of the diamond), and a slight excess of material on the seed side of the diamond (with the possibility of a crater forming depending on the pressure build up, which is likely a function of the incident beam energy).

It has been shown that the graphitisation process is feasible for beams with nanosecond and picosecond pulse lengths [53]. For nanosecond pulse lengths, a significant amount of energy is absorbed by the surrounding bulk material, meaning it will induce a mix of thermal and nonthermal processes. The time scale of the thermal process is $\leq \mathrm{O}(ps)$, so a sufficiently fast pulse length will freeze out this process and the graphitisation is dominated by the nonthermal process. This reduces the fringe structure of the graphitic electrodes as demonstrated by Kononeko et al. [53].

The laser setup consists of three components: a seed laser, a pump laser, and an amplifier. The Ti:Sapphire seed laser, the Coherent Vitesse [54], and the pump laser, the Coherent Verdi, are used together such that the seed laser acts as the beam source injected into the pump laser. The pump laser elevates the Ti:Sapphire ions to higher energy states such that there is a higher occupancy of higher energy states than lower energy states and results in population inversion. This means the ions can then transition to a lower energy state via stimulated emission, resulting in the origin of the laser beam. The output of this is a low power, short pulse laser beam with a wavelength of 800 nm while operating in TEM_{00} mode, whereby the electric and magnetic fields

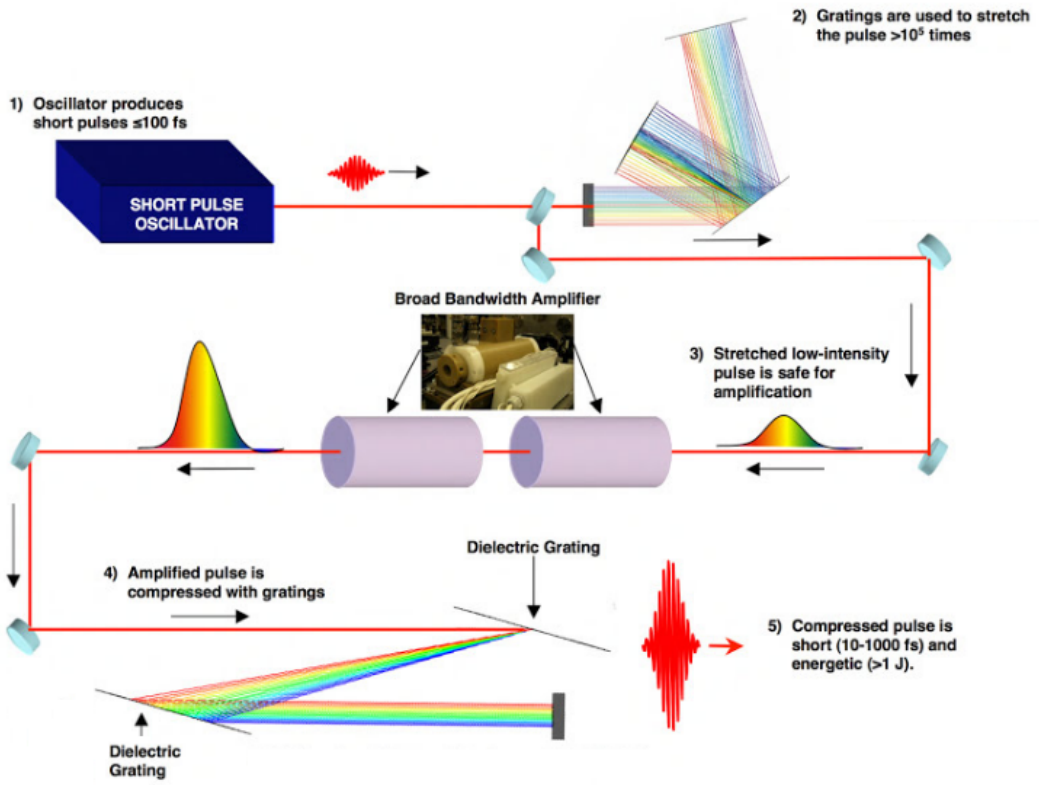

Figure 3.3: Schematic of the process of chirped pulse amplification to achieve a high power, short pulse length laser beam. Figure adapted from reference [59].

are transverse to the direction of propagation and the radial and angular mode orders are zero, resulting in a Gaussian beam [55]. The beam is then amplified using the chirped pulse amplification method [56] (Figure 3.3), where the beam is directed into a stretcher (diffraction gratings designed to cause dispersion of the beam) to increase the pulse length, making it safe for amplification [56]. The beam passes through the Coherent Synchronization and Delay Generator (or SDG) [57], which acts as an input to an amplifier and allows for tuning of the wave packets of the beam within the amplifier. The amplifier produces a high power (1 W) pulse by further pumping from the Coherent Evolution pump laser [58], which sets the repetition rate of the beam to 1 kHz. Finally, a compressor acts in the opposite way to the stretcher such that the pulse length is reduced, producing a high power, short pulse length (120 fs) beam.

There are some issues with this setup. It is possible that structural defects such as breaks in the electrodes may occur during this process. These breaks may arise as either: a few µm break along the electrode whereby the diamond has not undergone the graphitisation process, in which case the electrode may still function but with a much larger resistance than an ordinary electrode; or as a partially formed electrode,

whereby fabrication only occurs for a significant fraction (but not all) of the diamond and the electrode will likely not work as intended. It is also known that the size of the focal spot differs in medium in which the focusing objective is immersed (air) versus diamond due to the difference in refractive index ($\approx$ 1 for air and $\approx$ 2.4 for diamond [60]). This is a depth-dependent aberration which enlarges the focal spot and results in electrodes that are larger than the theoretical size dictated by the optics used in the setup. Issues such as these result in the lack of fine control of the graphitisation process, which is rectified through the use of a spatial light modulator (SLM).

An SLM is designed to dynamically alter the wavefront of the incident light in a specific way. For the formation of graphitic electrodes, it does this by altering the phase of the light to account for the aberration of the beam at a specific depth in the diamond, resulting in a more spherical focal spot. Hence, it must use a different phase correction at each position within the diamond to fully correct for the refractive index mismatch. The most common variation of SLMs are the electrically addressed SLMs (ESLMs), which are designed to modulate electronic signals and are hence preferable for coherent light, such as from a laser source. There are also variations of ESLM, such as liquid crystal SLMs, where the liquid crystal is the medium by which the phase of light is altered, and multiple quantum well SLMs, where the quantum-confined stark effect (QCSE)[4] is utilised to achieve extremely fast optical switching [62]. The cost, research and development, and availability of liquid crystal technology makes it the best option. Although the switching time can be quite slow e.g. around 20 ms for an analogue change to the phase using a nematic liquid crystal[5], this is acceptable for processing graphitic electrodes in diamond, though the switching time does put an limit on the minimum processing time.

The liquid crystal SLM used for electrode fabrication is a Liquid-Chip-On-Silicon (LCOS) SLM, shown in Figure 3.4. There are pixel electrodes on the silicon substrate, covering an effective area of approximately $16 \times 12\,\mathrm{mm}^2$ with a pixel pitch of $20\,\mu$m [63], where the electric potential may be independently changed. The pixel potential alters

[4]QCSE is an effect where the application of an electric field to a quantum well shifts the holes to higher energy states and the electrons to lower energy states such that incident light will cause less excitation through absorption. Exploiting this allows for a binary change to the phase of incident light on an SLM [61].

[5]A crystal where there is at least one preferred axis to which the molecules align in the presence of an electric field.

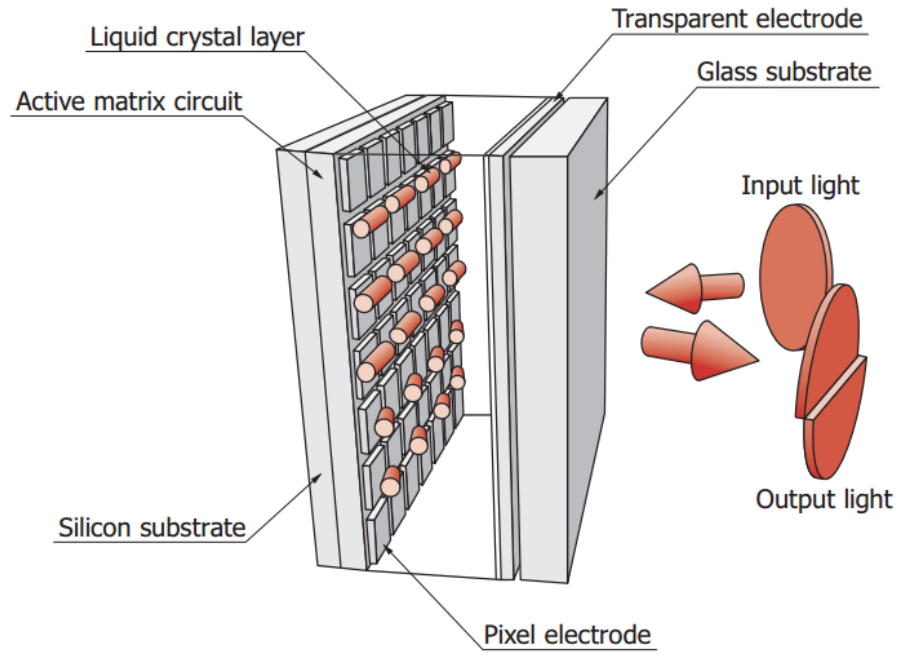

Figure 3.4: Schematic of a Liquid-Chip-On-Silicon (LCOS) SLM. Figure taken from reference [63].

the electric field along the central liquid crystal layer, which causes partial alignment of the liquid crystal. The angle of alignment of the liquid crystal molecules causes a slightly different refractive index, causing a change in the optical path length of the incident light and inducing a phase difference. The light is reflected off the silicon substrate layer, which results in phase modulated light. A "phase correction map" is sent from a PC to the SLM to display on the pixel electrodes which determines the applied pixel potential and allows for arbitrary changes to the phase of the incident light. The use of a pixelated device may cause issues with diffraction if there are insufficient pixels on such a device and thus requires accurate phase correction maps to be produced to accurately modulate the phase of the incident light.

One inherent advantage of using an SLM is the formation of graphitic electrodes whereby more of the diamond material is converted to graphite. This is possible by applying corrections to the beam to reduce the focal spot size considerably. This increases the energy density at the focal plane to aid the graphitisation process and allows for smaller electrodes, thus maximising the active area of the detector. The SLM also easily allows for fabrication of electrodes in arbitrary 3D paths [64], though the ideal electrode shape within the diamond bulk is a further area of research.

The optical setup is shown in Figure 3.5. The setup may be used either with or

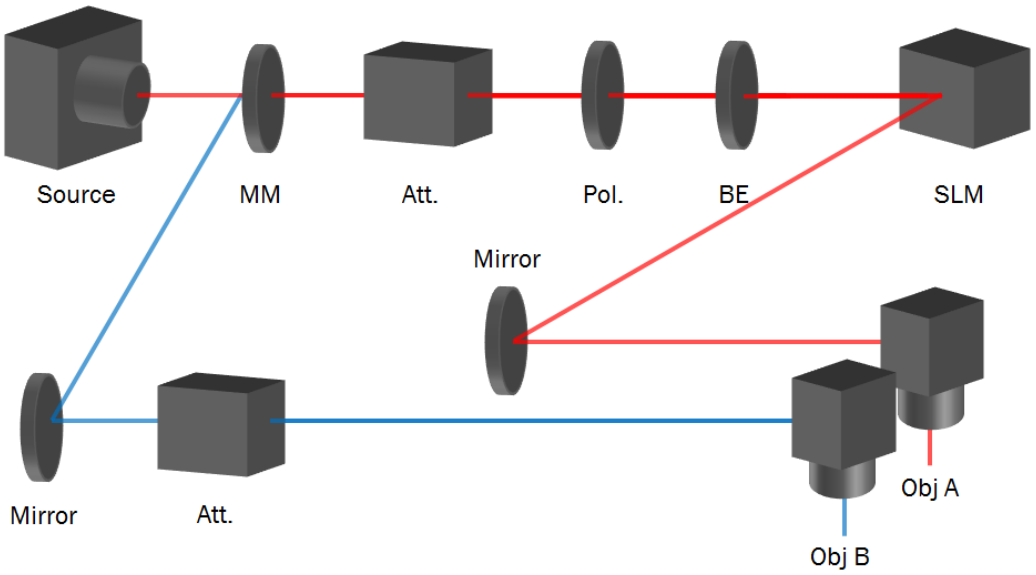

Figure 3.5: Schematic of the laser setup for producing graphitic electrodes. The following short-hand notation is used. MM: movable mirror. Att.: attenuator. Pol.: polariser. BE: beam expander. Obj: Objective. Not pictured is the 4f system, which is the set of lenses that lies in the red beam path between the SLM and Obj A.

without an SLM (red and blue paths, respectively) and only the SLM path is described here. The beam power is attenuated through two different methods, the first of which utilises neutral density filters (Att.). These reduce the total intensity of all light passing through it such that the fractional transmittance is given by 10^{-d}, where d is the optical density of the filter. This then provides a reduction in the beam power from 1 W to more typical beam powers required for graphitisation of O(mW). The second method uses a linear polariser (Pol.), where the polarising angle is adjusted to modulate the power of the linearly polarised laser light and hence provides a degree of freedom not available through using neutral density filters alone. After attenuation the beam then undergoes expansion (BE) such that all lenses (particularly the SLM display and the microscope objective used to focus the beam) are maximally filled, which allows for finer adjustments of the beam and for the beam focal point to be known. The beam is then incident on the SLM display. The pattern displayed on the SLM then adjusts the phase of the light to produce the required shape and is reflected onto the 4f system, which are a set of lenses designed to reduce beam aberration arising mostly from mechanical effects (the necessity of a 4f system in a laser setup using an SLM is explained in reference [65]). The beam is then incident on a high numerical

aperture lens (Obj A)[6] mounted onto a computer-controlled vertical stage to adjust the position of the focal point within the target.

It should be noted that in this setup, the beam power is measured using a Swamp Optics FROG beam profiler [66] at the focal spot of the laser prior to electrode fabrication. This is due to the difficulty in measuring the beam power at the focal spot inside the diamond substrate. In doing this, a 2D measurement is made, that is, the depth-dependent aberration is not taken into account here. The use of the beam profile also determines the focal spot size of the beam, allowing the beam fluence and the beam energy (given the repetition rate is constant) to be determined.

3.3 Electrode Metallisation

To apply a bias voltage and read out information from the detector, metal contacts are applied to the graphitic contacts. However, there are likely to be several contaminants on the diamond surface, ranging from carbon-like dust, arising from the graphitisation process, to atmospheric dust, arising from the transport of the sample and its handling in a non-clean room environment. Hence, the first stage of metallisation is rigorously cleaning the diamond sample in the following steps[7]:

1. Boil the sample in a 3:1 ratio of hydrochloric and nitric acid for approximately 5 minutes.
2. Boil the sample in a 3:2 ratio of sulphuric and nitric acid for approximately 5 minutes.
3. Boil the sample in a 1:1 ratio of hydrogen peroxide and sulphuric acid for approximately 5 minutes.
4. Rinse the sample with de-ionised water.
5. Repeat these steps additional (1-2) times as necessary.

The second stage is the design of a mask used in the metallisation process. The masks are designed using kLayout [67], a Computer Aided Design (CAD) program,

[6]The numerical aperture, or NA, of a lens is related to the minimum spot size, w_0 by $\mathrm{NA} \approx w_0^{-1}$, so a high NA implies a small spot size and hence focuses the beam more than a low NA lens.

[7]Only a typical sequence of steps is reported here, and further information and explanations for each step is shown in reference [47].

with an example shown in Figure 3.6a. Separate masks for the application of the bias voltage and for reading out the detector are usually made. This is because the bias voltage is applied to the opposite surface of the diamond to the readout electronics to minimise the risk of short-circuiting the device. The design criteria for any mask are as follows:

- Alignment marks. Each mask must be correctly aligned with the diamond sample, yet the field of view in the microscope objective for the alignment is very small. For example, a setup used in Manchester has a resolution of $> 5\,\mu$m, so distinct alignment marks help correct for this issue. Additionally, the use of alignment marks in the corner of a diamond sample may provide a sense of orientation of the mask.
- Circular contacts on the electrodes (see Figure 3.6b). These contacts also aid the alignment of the mask to the diamond sample, and also provide a point of contact for measuring the resistivity of the graphitic electrodes via a probe station.
- Rounded edges. Sharp edges cause large electric field gradients that results in a large charge density. Rounded edges mitigate this to some degree and are shown in more detail in Figure 3.6b.
- Width of metallisation. The metal strips used to connect readout electrodes and for the application of a bias voltage must be narrow enough such that the readout cells are not dominated by signal pickup by the metallisation. The strips must however be wide enough such that it minimises the probability of broken strips. The optimum width is between $5 - 10\,\mu$m, which is slightly dependent on the resolution of the microscope used during alignment.
- Guard ring. Applying a guard ring around the entire detector minimises the surface current and ensures the signal collected is only that from the detector itself.

The final stage is the deposition of metal in a three part process shown in Figure 3.7, the first of which is photolithography. In this process, a photoresist, a light-sensitive chemical, is applied to the entire substrate (step (a)). A mask with the desired metallisation pattern then overlays the photoresist (step (b)), which is exposed to light

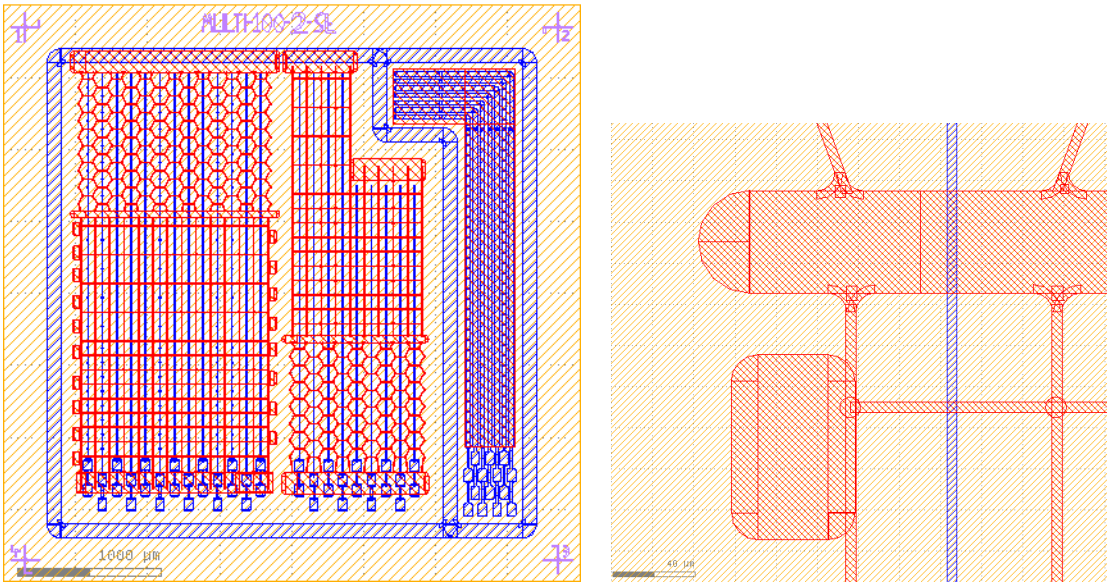

(a) (b)

Figure 3.6: Mask design used for the metallisation of a diamond detector, with the view such that the bias mask is on the top surface (out of the plane) of the diamond, and the readout mask is on the bottom surface. Yellow: diamond sample. Blue: readout mask. Red: bias mask. (a) overview of a mask design. The alignment marks (purple) can be seen in the corners of the mask. (b) zoom view of the rounded edges and circular contacts of the metallisation. The size of the strip patterns is also visible.

only in areas where there is no coating on the mask. The incident light causes the photoresist to become soluble such that it is easily removed from the substrate, resulting in a pattern completely opposite to the desired structured metallisation (step (c)).

The second stage of metallisation is sputtering (step (d)), which is a physical vapour deposition (PVD) process that shares some similarities with the manufacture of CVD diamond (Section 3.1). An input gas, typically Ar^+, will eject atoms from some source material via momentum transfer[8], which are directed onto a target comprising of the diamond sample with the metallisation mask aligned. Before deposition the diamond sample undergoes a plasma treatment for a few minutes to remove surface contaminants and thus help the metal adhere to the diamond. A bilayer of chromium[9] and gold is typically used to coat the entire diamond sample. The chromium layer, thickness of O(50 nm), adheres better to diamond than gold so acts as a interface layer

[8]The input gas thus depends on the atomic weight of material to be sputtered i.e. heavier inert gases such as krypton are preferred to sputter heavier elements.

[9]Chromium is typically used, though other metals such as titanium are also commonly used.

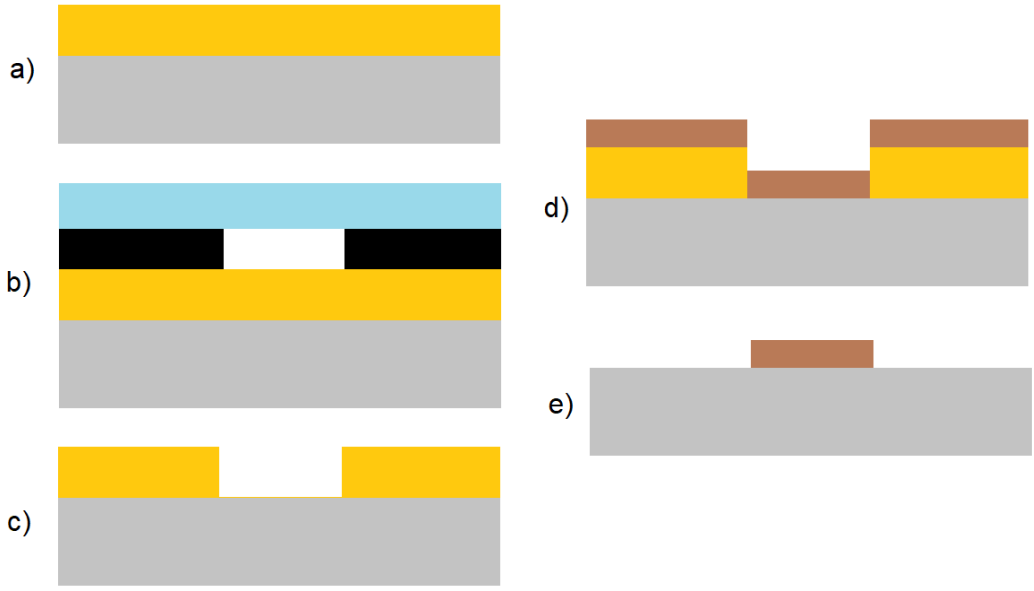

Figure 3.7: Summary of the stages of metallisation using the following colour scheme. Grey: substrate. Orange: photoresist. Blue: mask. Black: coated areas of the mask, which absorb incident light. Brown: bilayer metallisation. (a) Application of photoresist onto the substrate. (b) Overlay of the mask onto the photoresist. (c) Removal of photoresist in areas directly exposed to incident light. (d) The sputtering of the bilayer metallisation. (e) The lift-off process to remove excess photoresist.

between the diamond and gold, whereas the gold layer, thickness of O(70 nm), is used for its good electrical conductivity[10]. Once the sample is metallised on both the bias and readout side, it is then annealed for 4 minutes at 400 °C, designed to reduce the stress and brittleness of the bilayer metallisation such that the metal contacts are not easily broken.

The final stage of metallisation is the lift-off process (step (e)). In the sputtering process, the bilayer of metals coats the entire substrate, both areas intended for the metal coating, that is, the photoresist areas removed from the initial exposure to light, as well as areas containing excess photoresist. This excess is exposed to light and is thus removed. This results in the sample with a structured metallisation.

[10]More details on the bi-layer metallisation process can be found in reference [60].

Chapter 4

Characterisation of 3D Diamond Detectors

Once graphitic electrodes are formed within the diamond sample, it is important to assess their quality. Although the process is performed with known parameters such as the translation speed of the stage, there is some uncertainty in parameters such as the beam power. The power required to form graphite within diamond is very low, so any fluctuations could disrupt the process. Identifying areas where electrodes may be partially formed, or even checking the quality of the diamond itself is vital information for probing the sample with particle beams since these checks may explain unusual detector behaviour.

There are three key techniques used to probe the graphitic electrodes, and the diamond itself, which are discussed in this chapter:

- crossed polarisers, which are used to qualitatively identify areas of high stress in the diamond due to the presence of the graphitic electrodes and impurities.

- Raman spectroscopy, which is used to investigate the material content of the graphitic electrodes and hence serve as a diagnostic for the success of the graphitisation process.

- Scanning electron microscopy (SEM), which is used to image the graphitic electrodes to observe their structure, as well as to potentially identify areas where the metallisation has not adhered to the diamond.

These techniques are usually performed before the sample is metallised, as optical transparency is required for these measurements, and the presence of metallisation may also add a background contribution to signal obtained from Raman spectroscopy[1]. Of these techniques, the use of crossed polarisers (specifically the subsequent analysis of the crossed polariser images) is a new technique developed during this PhD, while the use of Raman spectroscopy and SEM imaging are standard techniques.

4.1 Crossed Polarisers

Crossed polarisers refers to two polarisers where the angular difference between their transmission directions equals 90°. The transmission of light through a polariser is given by Malus' law (Equation 4.1), where I is the intensity of light after the polariser, I_0 is the incident intensity, and θ is the angular difference in polarisation between the incident light and the polariser axis. For light which passes through one polariser, then the intensity of light that passes through a second, crossed polariser is zero by Malus' law.

$$I = I_0 \cos^2 \theta \tag{4.1}$$

Birefringence is a property of a material whereby the refractive index is dependent on the polarisation state of incident light. This property causes the incident light to be refracted in two different directions, as dictated by the "fast axis", where the refracted ray is due to the lower "effective" refractive index seen by the incident light and thus has a higher phase velocity, and the "slow axis". If a birefringent object were placed between two crossed polarisers, some light would pass through the final polariser and interference colours would be observed. If a hypothetical diamond with 100% purity were placed between two crossed polarisers, no light would be observed since diamond is not naturally birefringent. However, birefringence may be induced in a material and the most common source in the case of diamond is via stress.

The fabrication of diamond through chemical vapour deposition is not perfect and some defects are always present within the diamond, albeit at low concentrations. The

[1]SEM images can be taken post-metallisation to investigate its quality at the cost of potentially losing information on the structure of the graphitic electrodes.

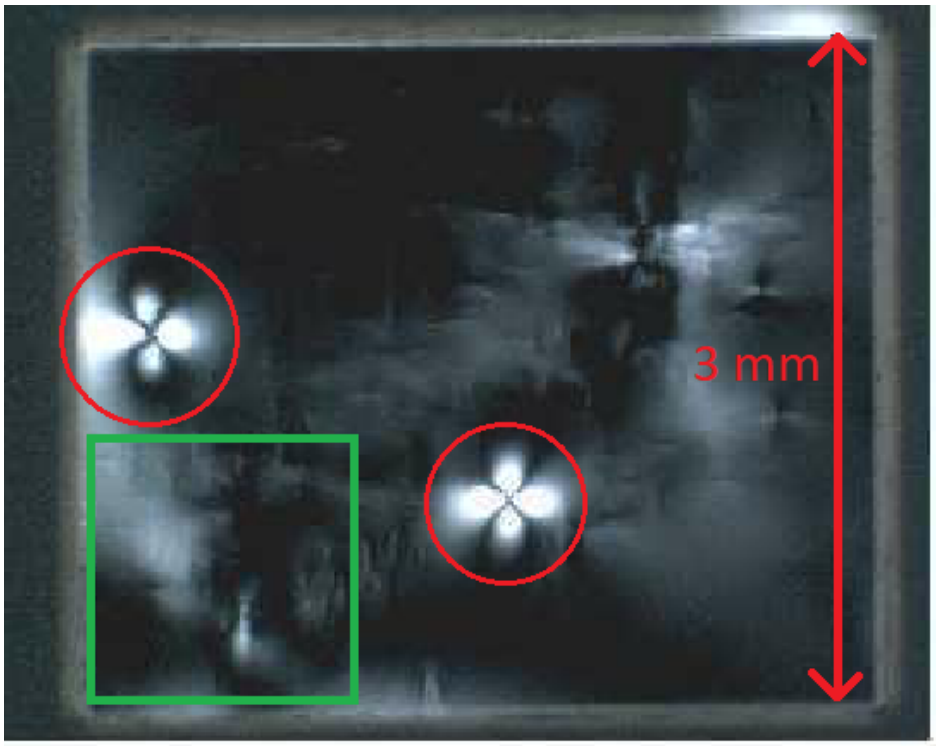

Figure 4.1: Birefringence observed in CVD single-crystalline diamond arising due to the presence of large scale defects (red) induced during its fabrication. Other defects such as the sample quality (one example highlighted in green) are also present. No graphitic electrodes were fabricated in this sample. Figure taken from reference [68].

presence of these defects induces stress in the diamond, and this resulting anisotropy in the diamond causes local birefringence at these defects (see Figure 4.1). For polycrystalline diamond, the presence of grain boundaries also induces stress in the diamond, though on a much larger scale. In this case, one may expect to see much larger regions where light is transmitted and so theoretically the grain boundaries are observable under crossed polarisers.

The use of crossed polarisers allows for the qualitative measurement of two important aspects of a 3D diamond detector: determining the amount of stress induced on the diamond by the presence of graphitic electrodes, and the inherent stress induced in diamond by its manufacture. The former is useful as feedback for the electrode processing stage of the manufacture because it can identify the electrode yield from the graphitisation, particularly whether the electrode diameter is apt so as to minimise breaks in the electrodes. Crossed polarisers may also assess if the electrode separation is sufficient so as to prevent high stress areas throughout the detector. Both sources of stress are also useful information for test beams, given that any unexpected defects

may slightly modify the characteristics of the detector and it is possible (though not proven) that these areas of high stress may also result in unexpected behaviour of the detector.

Images taken using crossed polarisers may be semi-quantitatively analysed using a program to measure the luminance in the image. Levels of high stress areas will appear bright in the resulting image, so counting the number of pixels above a luminance threshold gives a metric by which diamond detectors may be compared. The red, green, and blue (RGB) values of each pixel is determined using an image reading program [69], and these values are converted into a luminance value, I, given by Equation 4.2[2]. This results in a histogram of luminance values for all pixels in the image (Figure 4.2), at which point one can count the number of entries above a "luminance threshold", taken to be 200 in Figure 4.2[3], and is then used to find the relative stress between similar images. Although this does not give an exact measure of induced stress, it is useful nonetheless to decide what the best parameters are for graphitisation, and is useful when comparing different laser systems such as those which utilise a spatial light modulator, as explained in Section 3.2.

$$I = 0.21 \times R + 0.72 \times G + 0.07 \times B \tag{4.2}$$

4.2 Raman Spectroscopy

Raman spectroscopy is a method by which the observation of vibrational states in a system allows for the determination of its material content. The process involves the scattering of an incident photon, and this process is shown at the fundamental level in Figure 4.3. Rayleigh scattering occurs when the incident photon is elastically scattered, that is, there is no change in frequency between the initial and final states. Raman scattering occurs when the incident photon is inelastically scattered, and this is subdivided into Stokes Raman scattering, where the final state frequency is less than

[2]This formula is the photometric/digital ITU BT.709 conversion, a standard used to determine the perceived brightness of monitors [70], which closely matches the human eye's perception of brightness. The formula used for these calculations is somewhat arbitrary, provided the exact same image dimensions and light conditions were used across all analysed images.

[3]This number is also arbitrary, since is a compromise between ensuring the high luminance region is fully selected and minimising the additional counts from the lower stress regions.

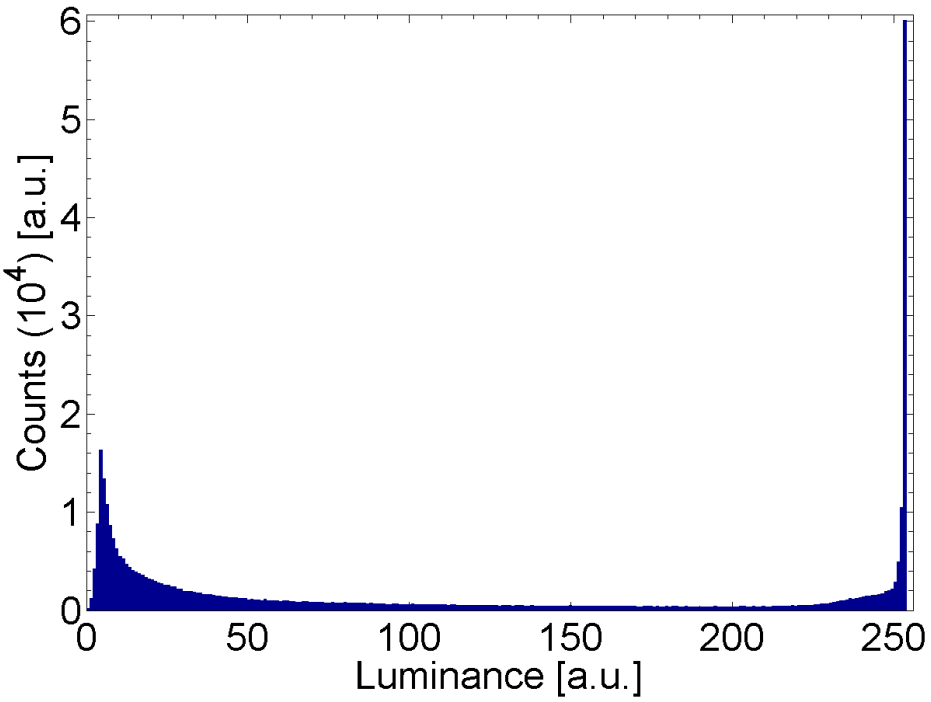

Figure 4.2: Example of a luminance histogram for an array of electrodes in a diamond detector. Low stress areas are represented by low luminance, whereas high stress areas are represented by high luminance.

the initial state, and anti-Stokes Raman scattering. In all of these cases, the scattering process produces an oscillating polarisation that excites molecules to virtual energy states, so the incident photon is re-emitted. In the case of fluorescence, this is an absorption process such that the photon is completely absorbed and an excitation to a real energy state occurs. Raman spectroscopy thus results in a difference in the frequency of the outgoing photon relative to the incident photon.

The difference in frequency, and thus energy, of the scattered photon is quantified though the Raman shift, Δw, shown in Equation 4.3, where λ_0 is the initial wavelength of the photon, and λ_1 is the scattered wavelength of the photon. The wavelength of the incident photon is known through the use of a laser source, so measuring the Raman shift and comparing with the allowed transitions for each chemical element results in the deduction of the sample's material content. For the formation of graphitic electrodes in diamond, spectroscopic studies are crucial as these indicate how much graphite has formed, which is then related to the conductivity of the electrodes, and the corollary of how much diamond was not converted to graphite. If the graphite content is low, that is, if only a small fraction of diamond was converted, this serves as a diagnostic for the laser graphitisation process and also indicates potential issues

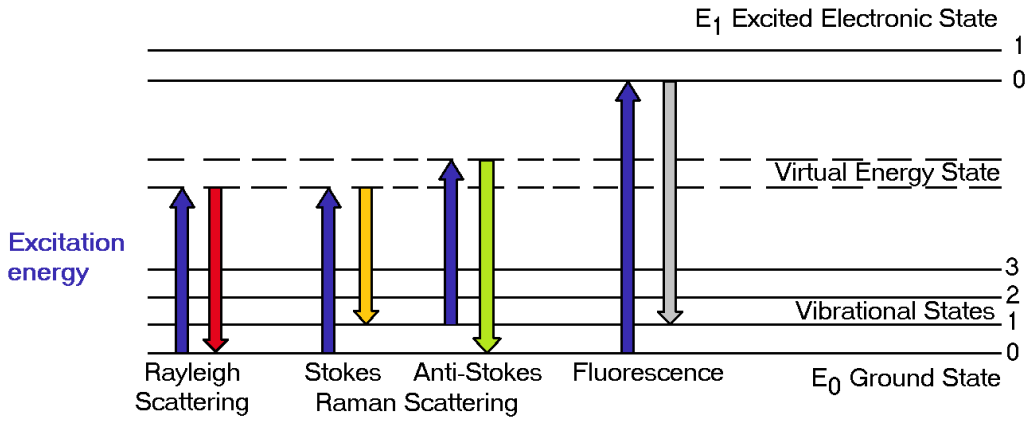

Figure 4.3: Energy-level diagram showing possible processes for an incident photon (blue), including (though not limited to): Rayleigh scattering (red), Stokes Raman scattering (yellow), Anti-Stokes Raman scattering (green), and fluorescence (grey).

with the diamond sample for use as a detector, such as potentially identifying "dead areas" within the detector.

$$\Delta w = \left(\frac{1}{\lambda_0} - \frac{1}{\lambda_1} \right) \tag{4.3}$$

The setup for Raman spectroscopy is shown in Figure 4.4. A continuous wave (CW) laser is used as the excitation source (red in Figure 4.4) and is focussed via an objective onto the sample. The scattered light (blue) is collected using a combination of collecting and focusing lenses, and is then directed onto the spectrograph (Spec) consisting of three components: an initial monochromator (Mc 1), crucial for separating out the Raman scattering from the Rayleigh scattering, which is much more common and dominates the signal; a second monochromator (Mc 2), used to isolate individual Raman peaks by increasing the dispersion further; and a light detector such a charge-coupled device (CCD), where the photons at each Raman shift are counted and a spectrum (example in Figure 4.5) is formed on the output computer (CPU). Attenuators are used in the spectrograph itself to prevent the saturation of signal onto the light detection system. For quantifying the material content of an electrode after graphitisation, the ratio of the diamond to graphite G peaks is reported. This is because diamond has a sharp, narrow peak at $1332\,\mathrm{cm}^{-1}$, which may dominate the graphite D peak at approximately $1350\,\mathrm{cm}^{-1}$ [71]. The theoretical origin and physical meaning of these graphite peaks is discussed further in work performed by Reich et al. [72].

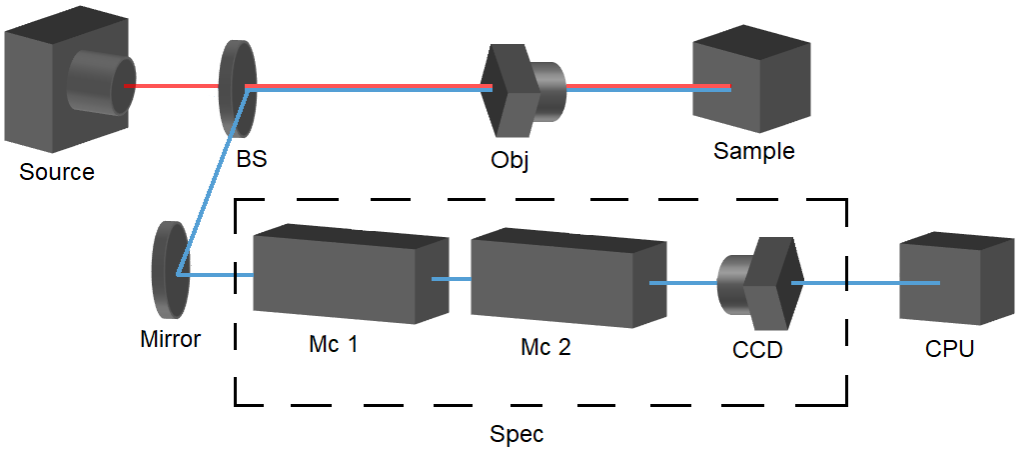

Figure 4.4: A basic schematic diagram of the system to perform Raman spectroscopy. The source light is in red, and the collected light is in blue. Note that not all of the lenses are shown. The following shorthand notations are used. BS: Beam Splitter. Obj: Objective. Spec: Spectrograph. Mc: Monochromator. CCD: Charge-Coupled Device. CPU: Computer.

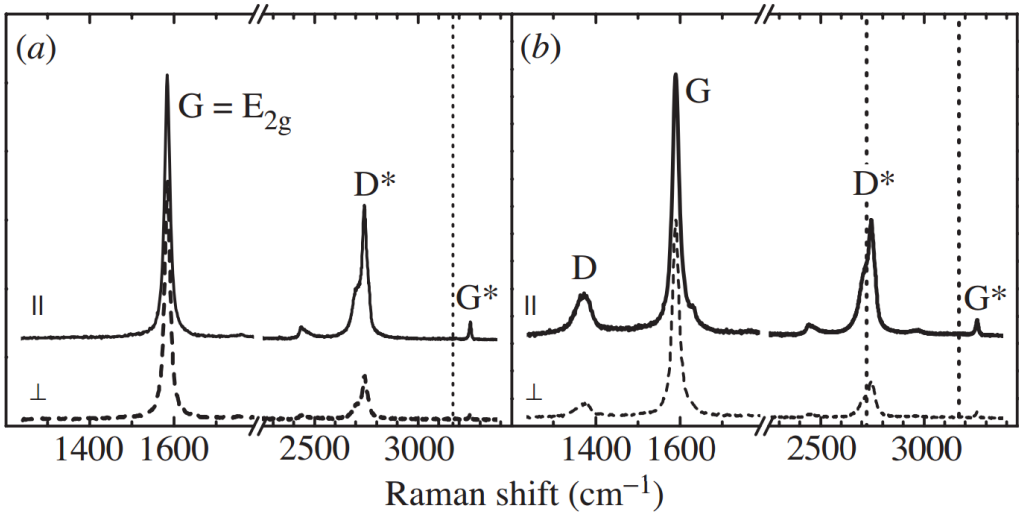

Figure 4.5: Raman spectrum of graphite. The D and G peaks are colloquially the "disordered" and "ordered" graphite peak, so for graphite with no disordered structure, the D peak would not be observed, as in (a). The * peaks are overtones of the D and G peaks. The full and dashed lines indicate the polarisation of the incident and final photons being parallel and crossed respectively. Figure taken from reference [72].

4.3 Scanning Electron Microscopy (SEM)

Scanning Electron Microscopy (SEM) is used to image graphitic structure in diamond after laser processing and it is useful for identifying substructure within the top surfaces of the graphitic columns. It is also useful for identifying areas with defects, such as artefacts and residue induced from cleaning the sample, and to highlight areas where the metallisation has not adhered to the diamond, resulting in breaks that may affect the detector's performance. While optical microscopy is useful to image the entire diamond, the resolution is diffraction-limited, given by angle θ in Equation 4.4, whereby the minimum size of structure, d, that may be resolved is dependent on the wavelength ,λ, of the source used to image it[4]. Due to wave-particle duality, electrons have a de Broglie wavelength given by $\lambda = h/p$, where h is Planck's constant and p is the electron's momentum, and for an electron with kinetic energy of 1 eV it can be shown that the electron wavelength is O(nm), whereas a 1 eV photon has a wavelength of O(μm). This demonstrates the resolution of SEM versus optical microscopy.

$$\sin\theta = 1.22\,\frac{\lambda}{d} \tag{4.4}$$

The operating principles of SEM is shown in Figure 4.6. Electrons (red) are emitted from a source and are directed and focussed towards the sample through a set of magnetic lenses (ML). The sample is imaged by adjusting the focus of the electron beam in a raster pattern, performed by scanning coils (SCo) situated above the sample. The electrons are accelerated towards the sample and penetrate the sample to a depth corresponding to the accelerating voltage and hence their incident energy, typically $\leq$ O(μm). These primary electrons (PE) will mainly interact with the sample via inelastic scattering at a depth of O(nm), causing the emission of secondary electrons (SE) that are detected and amplified using a system comprising of scintillators (Sci) and photomultipliers (PM). The number of SEs detected is dependent on the morphology of the sample, so scanning the beam and identifying the change in the number of SEs allows for a topographical image to be constructed on a computer (CPU). The chamber housing the sample and the electron source is evacuated such that attenuation of the beam is minimised.

[4] As a practical example, assuming a diffraction minimum of 90^o, then for visible light at 700 nm, the maximum resolvable structure size would be $\leq O(1\,\mu\text{m})$.

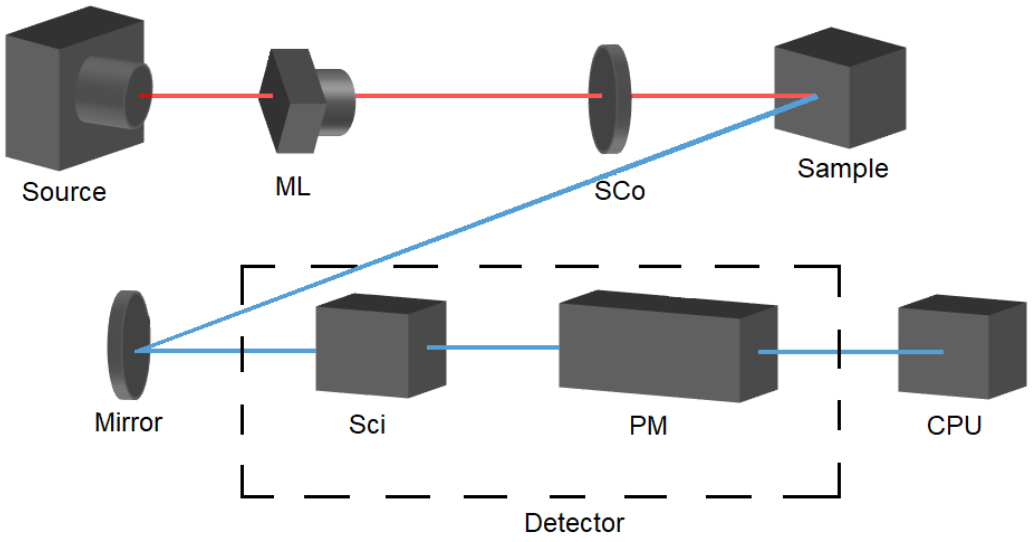

Figure 4.6: A schematic of the SEM setup. The source electrons are in red and the detected electrons are in blue. The following shorthand notation is used. ML: Magnetic Lens. SCo: Scanning Coil. Sci: Scintillator. PM: Photomultiplier. CPU: Computer.

The PEs may produce other particles such as back scattered electrons (BSE) and X-rays may be emitted if the incident energy is high enough to ionise the atoms of the sample, though it is not cost effective to include detectors to identify all such particles. BSEs are formed from elastic collisions between the PEs and the sample, and are typically formed at greater depths ($O(10\,\text{nm} - 1\,\mu\text{m})$) than SEs. This implies images formed using BSEs are of lower resolutions than those formed using SEs. However, the intensity of BSEs is proportional to the atomic number of the sample due to a scattering effect, so detecting and imaging these particles is useful in identifying local structural differences in the sample. Similarly, the detection of X-rays is useful in SEM studies where the material content of the sample is unknown.

One issue with SEM is a "charging" effect of non-conductive samples, whereby negative charge accumulates as the PEs interact with the sample, if it is not properly grounded. This charging effect will deflect further incident PEs at the scanned position which may result in an artefact on the SEM image. This is circumvented through coating the sample with a conductive layer, such as gold. The removal of such layers post-imaging is difficult and involves harsh chemicals, not unlike those explained in the cleaning process in Section 3.3. This may not be ideal if the sample is already metallised for use as a detector. Instead, environmental SEM (ESEM) is preferable, where the fundamental operation is the same as SEM but after evacuating the sample

chamber, a high pressure gas and water vapour are pumped through the chamber. The gas is itself electrically conductive through ionisation from PEs, which prevents the accumulation of charge in the sample.

Chapter 5

Results from Characterisation Methods

For each set of graphitic electrodes fabricated it is imperative to characterise them using the methods outlined in Chapter 4. This is because electrode parameters, such as their size and material content, may change with different sets of processing parameters and such methods are crucial to the optimisation of such parameters. Additionally, verifying the success of the process also influences the optimisation of the processing parameters, and electrodes that are significantly different may result in unusual behaviour when exposed to particle beams. The important parameters are outlined in the following paragraphs.

The size of the graphitic electrodes, and hence the laser fluence, is expected to manifest in different methods of characterisation, discussed in Chapter 4. In crossed polariser studies, one should expect that large diameter graphitic electrodes will induce more stress in diamond than small diameter electrodes. Therefore, arrays of electrodes with different electrode diameters can be used to quantify the relative levels of induced stress. The crossed polariser studies also contribute to a graphitic electrode yield, where electrodes with lower surrounding stress (versus the other electrodes within the diamond substrate) can be identified as partially formed electrodes[1]. One would also naively expect that there exists an optimum photon density, and thus focal spot

[1]This is reliable only if the electrodes are fabricated with the same electrode diameter. If the electrode diameter varies within an array of graphitic electrodes (e.g. if the beam energy is changed, demonstrated later in this chapter), then it becomes harder to identify partially formed electrodes. However, in all applications of these devices, consistent electrode size is required to maintain similar resistances for each electrode.

size, which optimises the probability of graphite formation and the induced stress in diamond (and thus the probability of cracked electrodes). Studies involving an SEM will directly image the difference in electrode size to a higher resolution than is possible from optical microscopy. They also provide an insight into the processes which occur at the seed and exit side of an electrode's fabrication, which aids data taken through Raman spectroscopy.

In Raman spectroscopy studies, the electrode material content is probed. Electrodes with the highest probability of graphite formation would, by definition, have the lowest ratio of diamond to graphite content. A comparison of Raman spectra between arrays of different electrode diameters would provide an insight into the optimum size, and therefore beam fluence, for electrode formation. Additionally the electrode content at the seed and exit sides can be studied, which may identify differences in graphite formation at these two points.

Finally, measurements of the current-voltage (I-V) curves will probe the electrical characteristics of the electrodes. These measurements are correlated to the Raman spectroscopy studies, that is, if the diamond to graphite ratio is small then more conductive materials exists inside the electrode. This would naturally result in a larger electrical conductivity. One advantage of these measurements over Raman spectroscopy is that the Raman spectra only probe the top surface of the electrode, and so assumptions are made about the electrode composition in the diamond bulk. I-V curves are reliably obtained only if the electrode is fully formed, implying these measurements not only give insight into the electrode characteristics in the diamond bulk[2] but also provide another measure of the electrode yield.

This chapter is structured into four main sections, with each section focussed on the results for one particular diamond sensor. The first section details in depth results from characterisation for detector Man-001 and provides a basis of results to which results in later sections are compared. The second section investigates the effect of the processing parameters on the graphitic electrodes (sample Goe-001). The third section shows the effects from using an SLM for electrode fabrication (detector Ox-001), with

[2]Second order effects such as variations in the electrode structure with depth are smeared out. Investigations into such effects would require the manufacture of graphitic electrodes on the edge of a diamond sample, something which is difficult to achieve due to the imperfect cut edges of diamond samples and the level of precision in the position of the electrodes required.

its results compared to Man-001 and Goe-001. Finally, an investigation into the effect of the processing parameters on the graphitic electrodes both with and without the use of an SLM is demonstrated (sample Ox-002), including an outlook towards the future of 3D diamond detector characterisation. Throughout this chapter "sample" refers to devices characterised with these methods only, and "detector" refers to devices which were in addition characterised using particle beams, as presented in Chapter 6.

5.1 Detector Man-001

5.1.1 Motivation

One reason for the manufacture of Man-001 was to investigate the effect of the laser fluence on graphite formation in diamond. Consider the shape of the laser pulse at the focal point, which is assumed to be a 2D Gaussian profile and neglecting the effects of astigmatism. There is an energy threshold at which point diamond is restructured to form graphite. Hence, graphite is expected to form for all positions where the beam energy is greater than the threshold (Figure 5.1, black). If one were to increase the pulse energy, and thus the laser fluence, a greater fraction of the beam is above the energy threshold for graphite formation. This results in a larger graphite region (Figure 5.1, red). The implication is that the size of the electrodes can be fine-tuned, provided the pulse energy is above the threshold for electrode formation. The other reason for the manufacture of Man-001 is to investigate the response of a diamond detector to particle beams, which is discussed in Chapter 6.

5.1.2 Detector Overview

The electrodes were fabricated without the use of the spatial light modulator, with a constant translation speed of $20\,\mu\text{ms}^{-1}$. Laser fluences in the range of $2 - 4.8\,\text{Jcm}^{-2}$ were used to fabricated four arrays on a single crystal electronic-grade diamond (Figure 5.2a) obtained from Element Six [45] with dimensions $4.7\times4.7\times0.5\,\text{mm}^3$. Although the translation speed is also an important processing parameter to be varied, which affects the formation of graphitic electrodes, this was kept constant due to limited

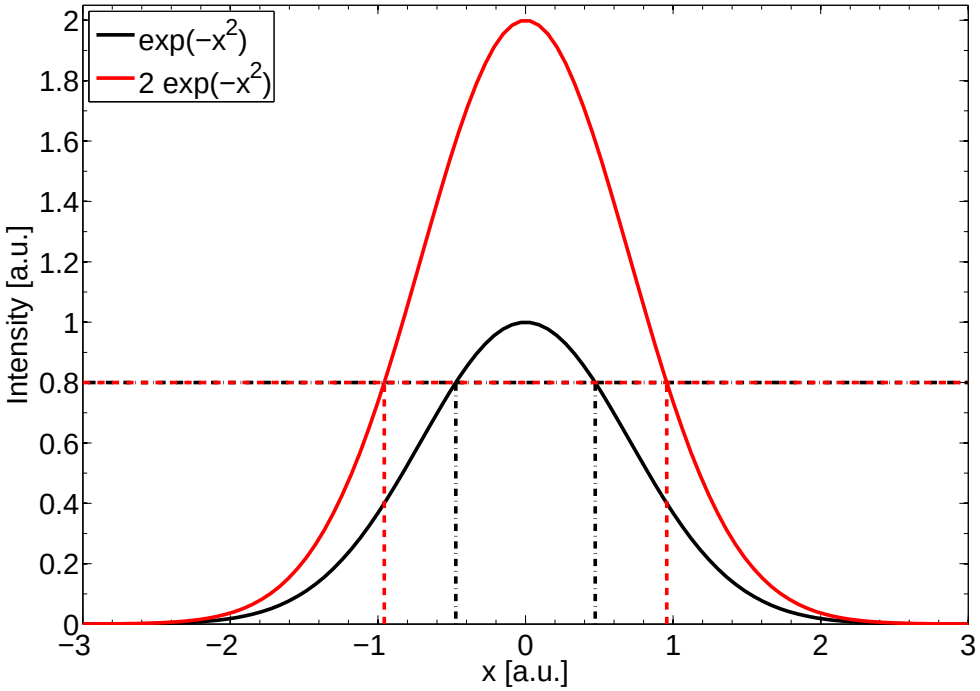

Figure 5.1: Examples of Gaussian profiles in 1D with amplitudes of 1 (black) and 2 (red). If one were to assume that the threshold for graphitisation is 0.8 (in arbitrary units), then the graphite region is defined by the width of the Gaussian where its energy is higher than the threshold. The higher intensity Gaussian, therefore, has a wider graphite region.

space on the diamond substrate and the primary focus was on the response of a diamond detector to particle beams[3]. The variation in the laser fluence corresponds to a electrode diameter range of $8 - 18\,\mu$m. The size of each array of electrodes is $600 \times 600\,\mu\text{m}^2$ (Figure 5.2b), and the electrodes were arranged in a square geometry with an electrode separation of $120\,\mu$m (Figure 5.2b, red).

The electrodes were then metallised with a strip pattern on one side of the diamond and small pads on the reverse side, seen in Figures 5.2a and 5.2b, respectively. This was achieved through photolithography, sputtering, and lift off process (explained in Chapter 3), which then allows for the electrical properties to be characterised through I-V measurements. The sample was annealed in a nitrogen atmosphere at 250 °C for 5 minutes to improve the adhesion of the metallisation. The low quality of metal adhesion is characterised by the metallisation breaking and "flaking off", and it is likely to occur when the sample is probed in any way, such as during I-V measurements, and can be observed in Figure 5.2b. A combination of titanium and gold with thicknesses of

[3]Note that this parameter was later varied on a different diamond sample as part of a larger study into the effects of the processing parameters on graphite formation, discussed in Section 5.2.

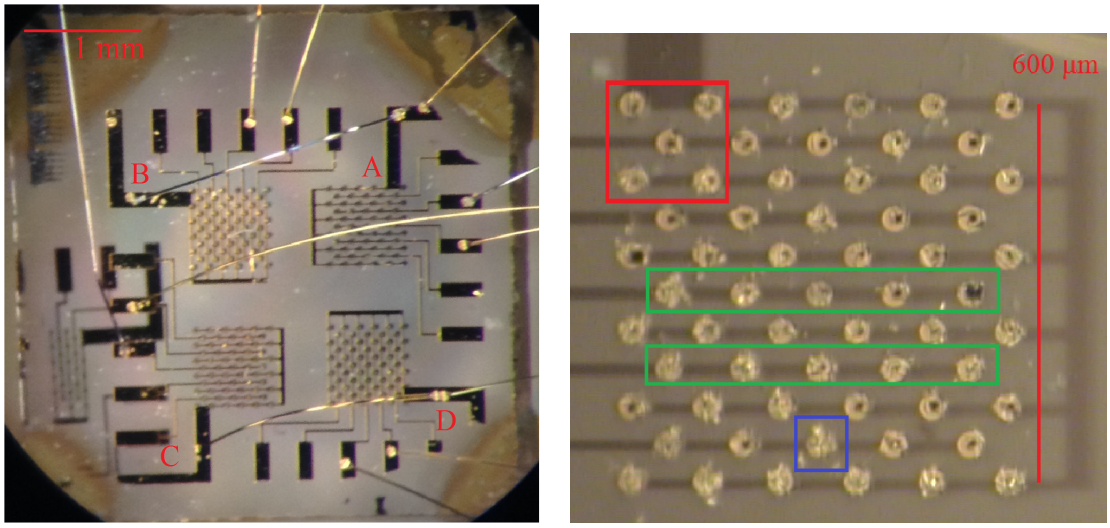

(a) (b)

Figure 5.2: (a) Optical image of the detector after the metallisation process. The four arrays are referred to as A, B, C, and D, from top right anti-clockwise. The bias and readout metallisation are applied on the same side. (b) Array A on the detector, viewed on the opposite side to that shown in Figure (a). The readout of two neighbouring strips as described in the text are outlined in green, and a basic cell is outlined in red. An example of the metallisation "flaking off" is outlined in blue. Both figures adapted from reference [73].

35 nm and 60 − 70 nm were used. It is from this point that the sample was characterised using the methods outlined in this section and in Chapter 4.

5.1.3 Crossed Polarised Image Characterisation

Images were taken through a pair of crossed polarisers for each array of electrodes. An example of one array is shown in Figure 5.3a, which reveals some electrodes with lower surrounding stress (highlighted in red and green). These areas were subsequently viewed under optical microscopy and partially formed electrodes were observed (Figures 5.3b and 5.3c), implying that images taken under crossed polarisers may provide a metric for the electrode yield. The reason for these partially formed electrodes is likely due to the laser setup itself. For example, if the beam power drops below the threshold for graphitisation, which is not unreasonable since fluctuations in the beam power are possible, then the process stops and thus ceases electrode growth.

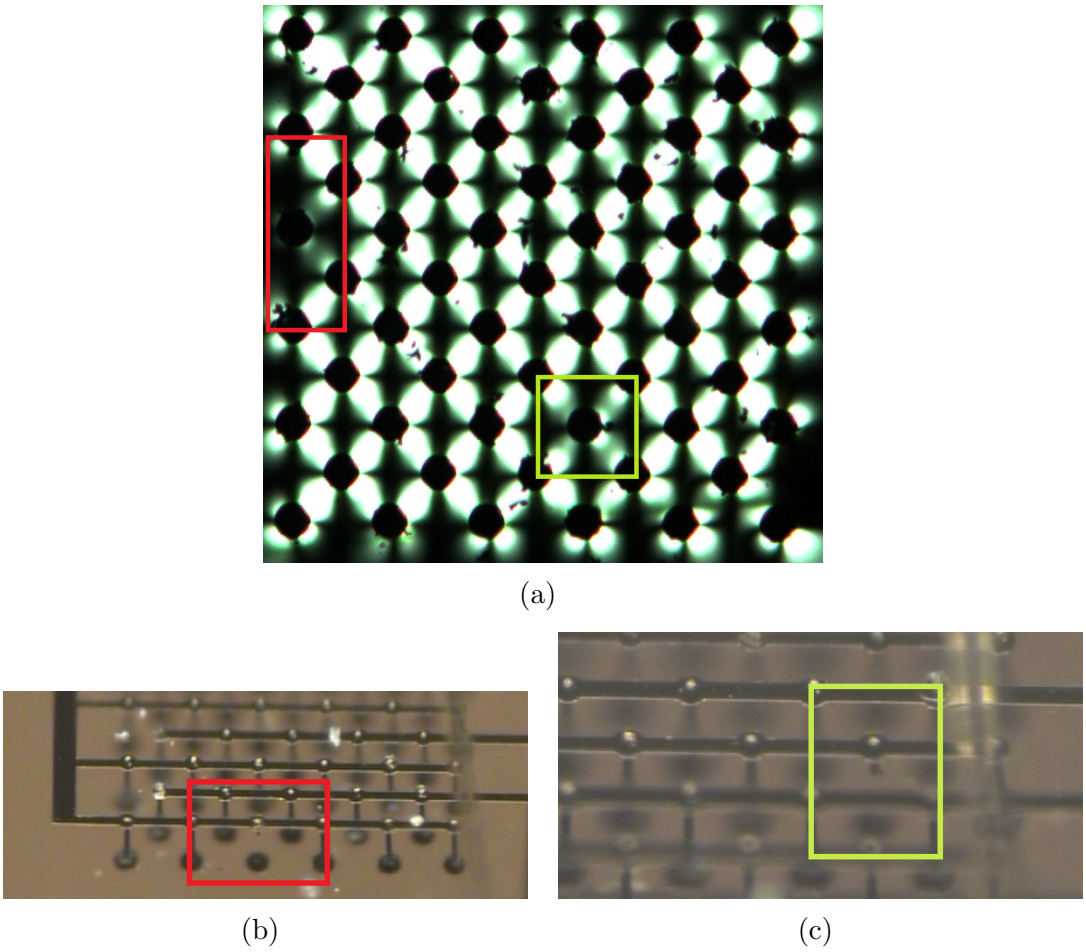

(a)

(b) (c)

Figure 5.3: (a) Image of array B taken under crossed polarisers. High brightness areas show high levels of stress within the array induced by the presence of the graphitic electrodes. Partially formed electrodes are highlighted in red and green. (b) and (c) Malformed electrodes are identified under optical microscopy from Figure 5.3a. All figures taken from reference [73].

Each of these images taken under crossed polarisers used a constant backlight intensity. This is important for calculating the stress induced in diamond, given that a luminance threshold is used and variations in the backlight intensity would alter the calculated value. The images taken were of a fixed size[4] and were used as input to the image reading software, described previously in Section 4.1. A threshold at a luminance of 200 was used for each array, and absolute values of stress measurements were made relative to array A due to the difficulty in quoting the induced stress for each array. These relative measurements are shown in Figure 5.4, alongside the electrode diameters (measured optically by viewing the side profile of the electrodes)

[4]Note that some electrodes were identified as partially formed electrodes, as demonstrated in Figure 5.3a. These partially formed electrodes were not corrected for in this analysis.

and the fluence used to form the electrodes (measured by placing a beam profiler at the focal spot of the laser prior to electrode fabrication). This figure illustrates that not only is the electrode diameter approximately linear with the laser fluence, but also confirms the stress induced by the electrodes on the diamond lattice increases with laser fluence, and thus electrode diameter. These results, therefore, indicate smaller electrode diameters are recommended to induce lower stress in the diamond lattice surrounding the electrodes, which would increase the active area of a detector, and minimise the risk of local defects arising from induced stress, versus one with larger electrode diameters.

Comparing the measured electrode diameters against the beam fluence in Figure 5.4 reveals a linear ($\chi^2 = 0.719$) relation between them, which when compared to Figure 5.1 is not intuitive. A linear relationship between the beam fluence[5] and the electrode diameter should be expected only in the case where the threshold for graphitisation is quite high relative to the beam fluence. This threshold can be estimated from these data by making a few assumptions[6]: the beam fluence is known to an accuracy of 5%; the beam profile at the focal point is Gaussian; and the beam width is known to an accuracy of 10%. Hence, one can draw a Gaussian profile of the form $A\exp(-(x/a)^2)$ for each of the arrays, where A is the beam fluence and a is related to the beam width, with upper and lower bounds dictated by the uncertainties in beam fluence and width. Marking the measured electrode diameters on the plot allows for a "by eye" fit to determine the graphitisation threshold region, which is set by the two uncertainties and the electrode radii. This fit is shown in Figure 5.5 and yields a threshold region of $1.67 - 1.78\,\mathrm{Jcm}^{-2}$. Although this relies on a few assumptions, it does mean that a better estimate of the graphitisation threshold is known other than through trial and error[7], and this value is rarely quoted in literature. For example,

[5]The beam fluence, pulse energy, and beam power are all measured using a beam profiler at the focal spot of the laser prior to electrode fabrication. For a fixed focal spot size and repetition rate, all three of these parameters are related. While these terms are different, it is the general effects of these quantities that is investigated in this thesis. It should be noted that these quantities differ in the diamond bulk, due to the translation speed of the focal spot and due to effects discussed in Section 5.3.

[6]This is a novel estimate that is particularly useful when the graphitisation threshold is not known, such as when commissioning a new setup for electrode fabrication. As such, this analysis is not repeated for later diamond sensors since the fabrication parameters were constant for all electrodes and also due to greater understanding of the graphitisation threshold.

[7]Typically through varying the beam power and attempting to form graphite in the diamond lattice, which is subsequently confirmed through optical microscopy.

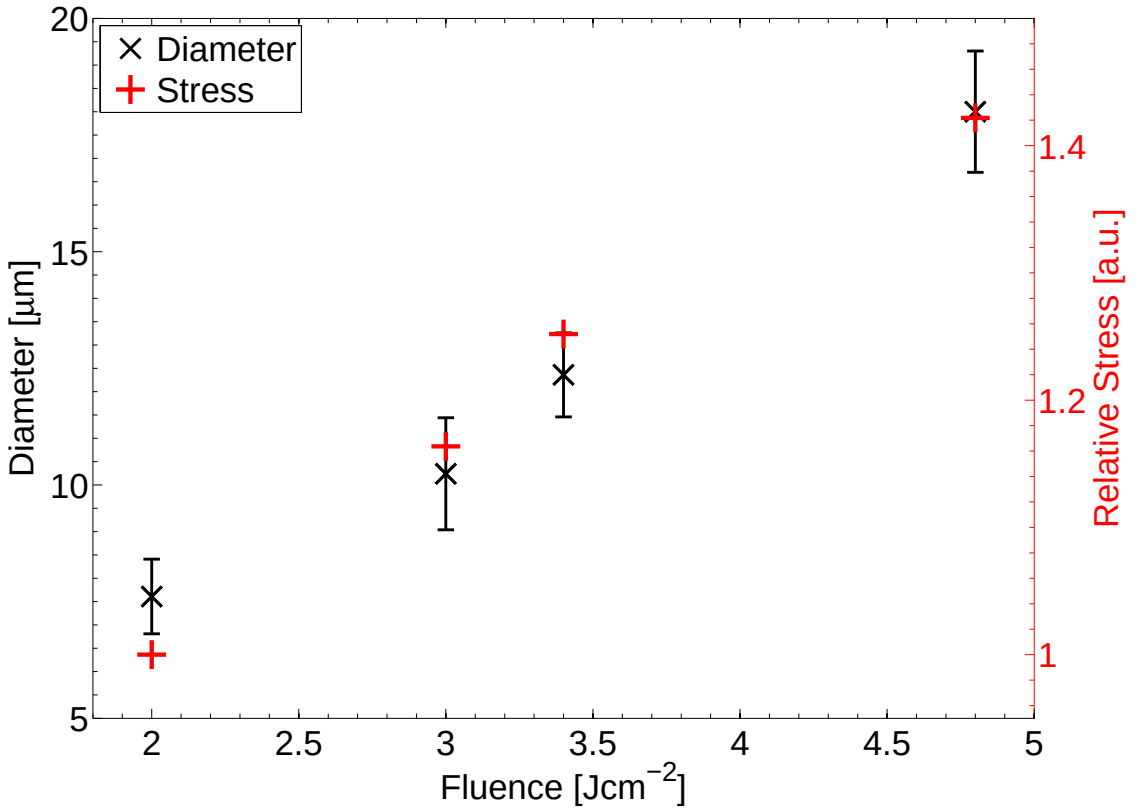

Figure 5.4: Beam fluence used to fabricate electrodes in each array versus the electrode diameter measured by optical microscopy (black) and the relative stress induced on the diamond lattice (red). Figure adapted from reference [73].

the graphitisation threshold has been shown to be a function of photon energy (as presented by J. Gaudin et al. [74]), but are for photon energies higher (by O(10-100)) than that used in this thesis.

Following the confirmation of partially formed electrodes in Figures 5.3b and 5.3c, further images of the detector were taken using an optical microscope. Although Figure 5.3a identified some partially formed electrodes on one array, with no other partially formed electrodes identified in any other array using this method, it is necessary to confirm the reliability of this method. An overview of the detector is shown in Figure 5.6a, which demonstrates that the electrodes are seemingly uniform and the metallisation has adhered well to the surface. A higher resolution image of array A is shown in Figure 5.6b, left, further confirming the uniformity of the electrodes. However, Figure 5.6b, right, shows the presence of secondary electrodes in array C, which is likely due to an astigmatism in the beam at the time of fabrication. The lack of secondary electrodes in arrays fabricated at lower beam fluences indicates that the intensity of the secondary focal spot due to the astigmatism is below the graphitisation

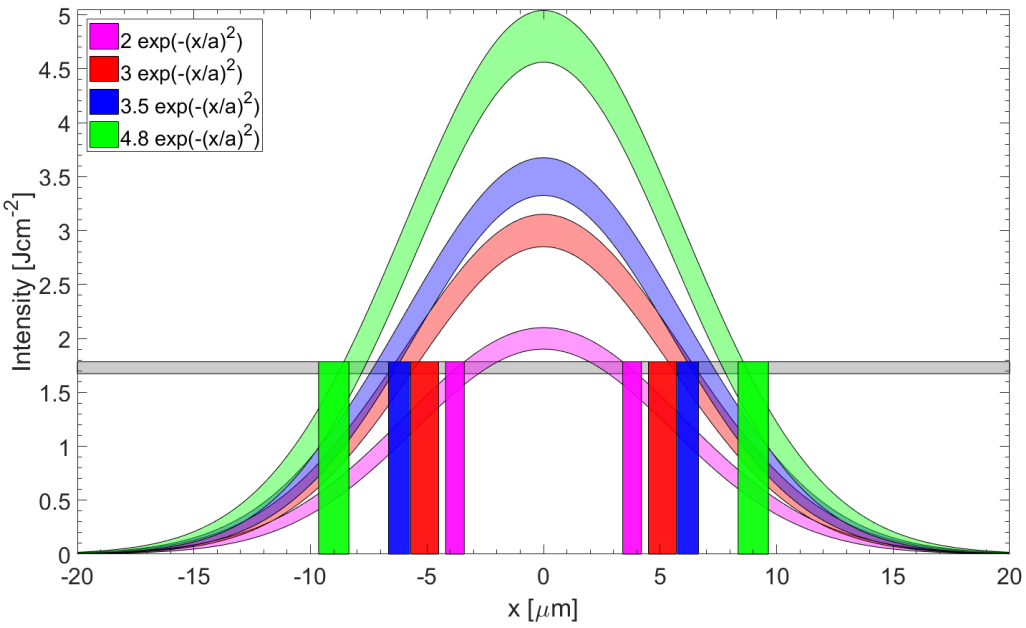

Figure 5.5: Gaussian fits for each beam fluence used to fabricate each array of electrodes (transparent colour), with the measured electrode radii (solid colour) shown. The graphitisation threshold (black transparent region) is then dictated by the allowable region set by the uncertainty in the beam fluence, the uncertainty in the beam width, and the measured electrode radii. The value of a has a lower bound of $6.5 \times \sqrt{\ln(2)}\,\mu$m and an upper bound of $7.0 \times \sqrt{\ln(2)}\,\mu$m.

threshold. However, these secondary electrodes should be expected at higher beam fluence, that is, array D. This discrepancy is explained in Section 5.1.4.

5.1.4 SEM Characterisation

After the identification of unusual structure in one array of electrodes, it was prudent to take SEM images of the electrodes to investigate their morphology. Images were taken on both the seed and exit sides since the growth of the electrode is likely to result in different structure on these sides, as explained in Chapter 3. This is shown in Figure 5.7a, where the higher density diamond surrounding the electrode dictates the growth direction through a build-up of pressure. On the exit side a few microns of the diamond surface is ejected, revealing the electrode and forming a crater. On the seed side a similar effect as observed on the exit side is also seen, albeit less diamond material is ejected, alongside an excess of graphite.

The presence of secondary electrodes has also been confirmed on array C through SEM, as shown in Figure 5.7b. Combining this information with the optical images

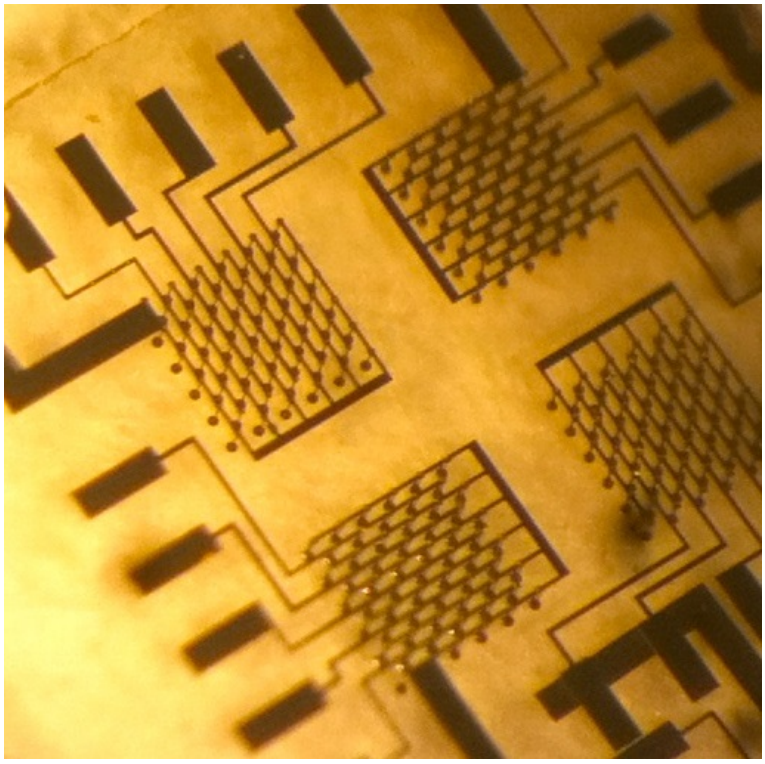

(a)

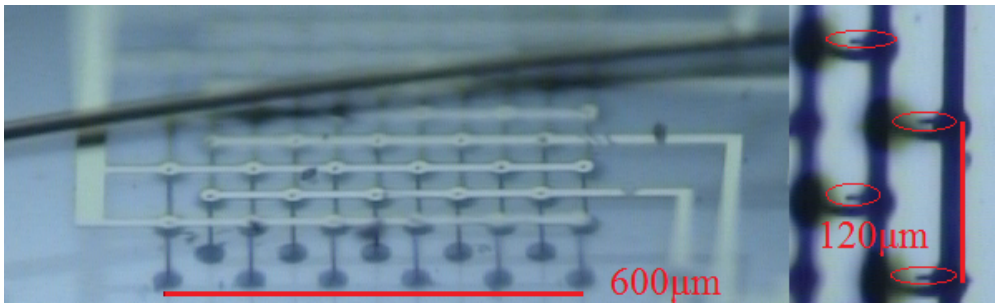

(b)

Figure 5.6: (a) Side-on optical image of the detector after the metallisation process. The electrode uniformity within each array is observed. (b) Side-on optical image of an array, showing a higher resolution view of the electrodes. On the left is array A, which has been used at two different test beams [73]. On the right is array C where secondary electrodes are present, highlighted in red. Figure (b) taken from reference [73].

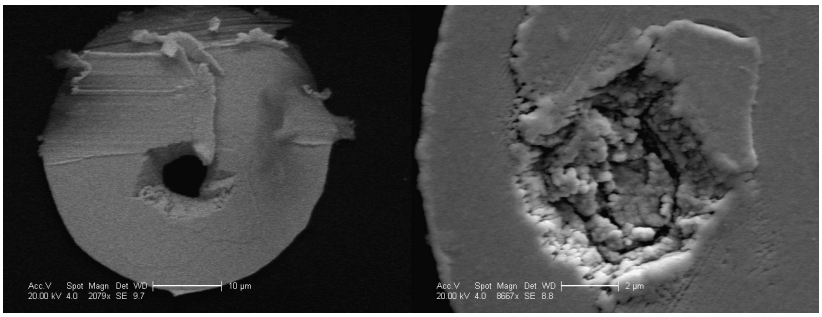

(a)

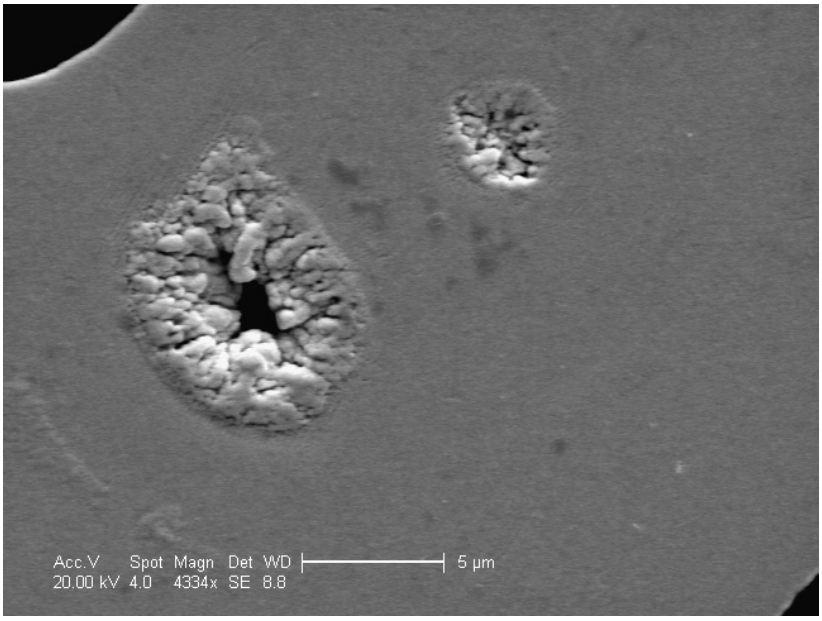

(b)

Figure 5.7: (a) SEM image of an electrode from array B. On the left is the exit side, and on the right is the seed side. (b) SEM image of an electrode from array C on the seed side, highlighting the presence of a secondary electrode initially confirmed by optical microscopy. Figure (a) is taken from reference [73].

implies that the secondary electrodes are likely to form from the seed surface, as opposed to just beneath the surface or within the diamond bulk, and have a constant separation of approximately 5 μm.

The use of SEM also reveals two other interesting aspects to the graphitisation process. The first pertains to array D, whose electrodes formed at the highest fluence. It has been shown that array C exhibits secondary electrodes, whereas array D did not (through the use of an optical microscope and through the use of crossed polariser images). SEM images of array D reveal that these electrodes may well exhibit secondary electrodes, as shown in Figure 5.8a. The electrode structure on the exit side, in this case, is atypical when compared to Figure 5.7a and the shape on the exit side appears

to be two closely spaced electrodes. The proof for this is the separation of the centres of these two electrodes is of the same order as the separation observed in Figure 5.7b. Given that the fluence used for array C resulted in only a partially formed secondary electrode, one should expect, with one such example highlighted in Figure 5.4, that a higher fluence will result in a larger electrode size and a larger ejection of the diamond material on the exit side. Due to the size of the electrode in the diamond bulk and given the difficulty in viewing electrodes in the diamond bulk, which slightly blurs the focal point due to the refraction of light, it is reasonable to suggest that either the electrodes do intertwine (as seen on the exit side in Figure 5.8a), or there is a small ($< 5\,\mu$m) separation between these electrodes in the diamond bulk which cannot be resolved.

The main source of astigmatism (hypothesised in Section 5.1.3) in the beam is likely to be mishandling the lenses at any point in the beam path, which then corresponds to two possibilities: unclean lenses, due to the presence of dust or finger marks on the lenses; and a misalignment of the lenses. In light of the results from arrays C and D, it is therefore likely that the astigmatism in the beam is due to a lens misalignment, since the presence of contaminants on lenses would most likely scatter the light rather than consistently focus it in one particular spot. Secondary electrodes, therefore, were not observed in arrays A and B since the beam fluence in the secondary focal spot was less than the threshold for graphitisation.

The second interesting observation from these SEM images pertains to array A, whose electrodes were formed at the lowest fluence. By comparing Figure 5.8b with Figure 5.8a, it is clear that the characteristic ejection of the uppermost diamond layers is much less pronounced in array A versus array D. This in itself is not surprising since the level of stress induced in the diamond lattice scales with beam fluence (Figure 5.4), hence the pressure build-up, which drives the formation of the graphitic electrodes, would also be reduced at lower beam fluences. However, the electrodes in Figure 5.8b indicate the effect is lessened to such an extent that the presence of the electrodes on the exit side surface is questionable, given that only a handful of electrodes are clearly visible. There are two possible explanations for this. One is the electrodes do completely penetrate the diamond bulk and reach the exit side surface, but the beam fluence is low enough such that the ejection effect is simply weaker. The other reason

is that the lack of emergence on the exit side surface is due to insufficient translation of the stage in the direction of electrode formation. In the case of the latter, one would expect that resistance of the electrodes would be much higher, since some portion (O(1μm)) of the electrode would consist of diamond in lieu of graphite. This is later confirmed with I-V measurements.

Additionally, there are groove marks on/damage to the metallisation on the exit side, which is also shown in Figure 5.7a, left. This is likely due to excessive probing with a probe needle used to take I-V measurements of the electrodes, the results of which are in Section 5.1.6, and indicates that the adhesion of the metallisation to the diamond is not optimal.

The resolution of the exit side of the electrode in Figure 5.7a and Figure 5.8 is lower than the seed side due to a charging effect[8] observed while taking the images, discussed in Chapter 4. This is unavoidable without the use of a conducting medium. The sample was later imaged using an ESEM, which used water vapour as its conducting medium. Higher resolution images of an electrode on the exit and seed sides are shown in Figures 5.9a and 5.9b, where submicron feature sizes are observed. For example, small fringes are apparent in Figure 5.9a, with the crater-like structure observed previously, while in Figure 5.9b these fringes are not as apparent, though the excess material build-up is seen. The ejection of the uppermost diamond layers is also observed in the area surrounding the electrode, also seen in the right of Figure 5.7a, where these layers have been "pushed off" but not fully ejected.

5.1.5 Raman Spectroscopy Characterisation

The graphitisation process and the SEM images have highlighted key differences between the seed and exit sides of the electrode in the diamond bulk. For example, it is evident there is a build-up of material on the seed side, while there is a large ejection of material on the exit side. However, it is not necessarily the case that the excess material on the seed side is graphite. Even though a similar, albeit weaker, ejection process is observed on the seed side, it is entirely possible that there is still some diamond material remaining. It is also possible that there are still traces of diamond

[8]The seed side was imaged first, and it is presumed that the diamond substrate retained some charge accumulation prior to the imaging of the exit side.

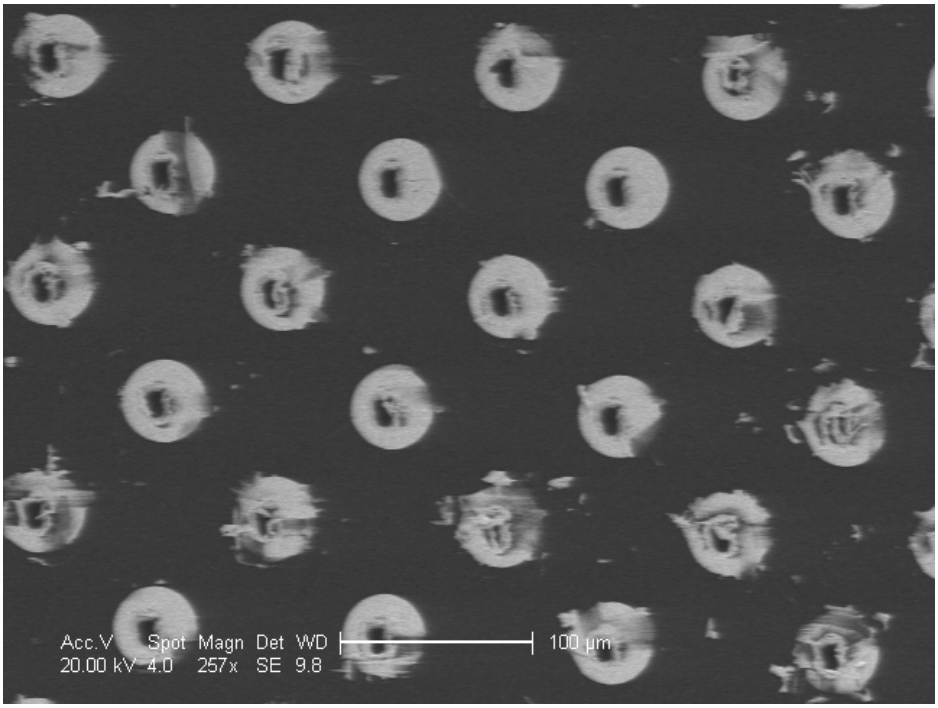

(a)

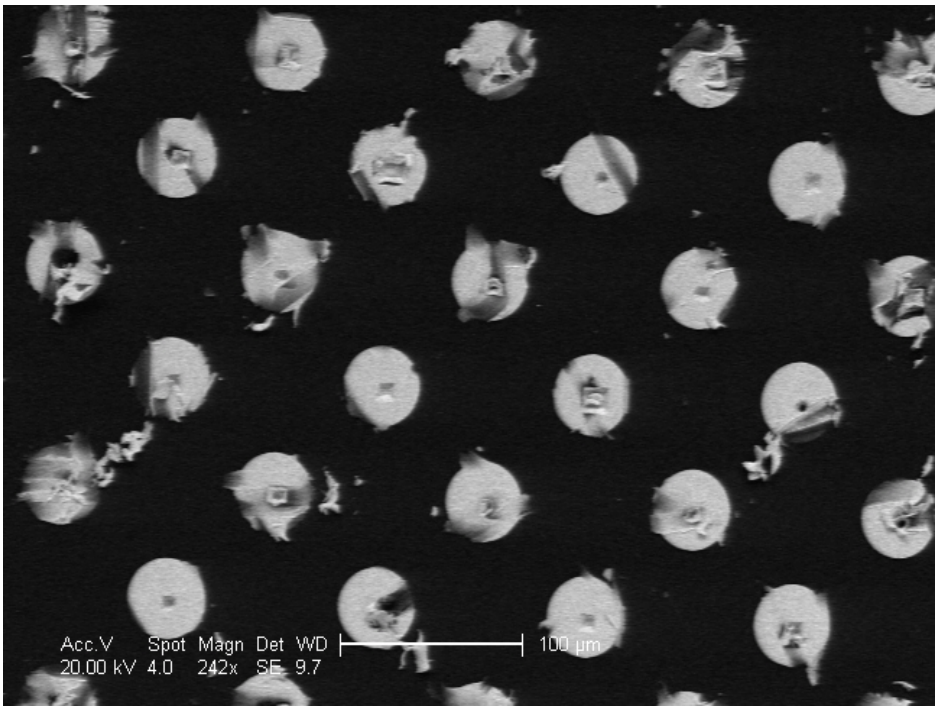

(b)

Figure 5.8: (a) SEM image of an electrode from array D on the exit side. The structure is common to all electrodes, which seem to exhibit features of a secondary electrode. The exit side of the electrode is denoted by the deep black region and is seen clearly in all electrodes. (b) SEM image of an electrode from array A on the exit side. Unlike Figure 5.8a, the exit side of the electrodes is not as clearly seen.

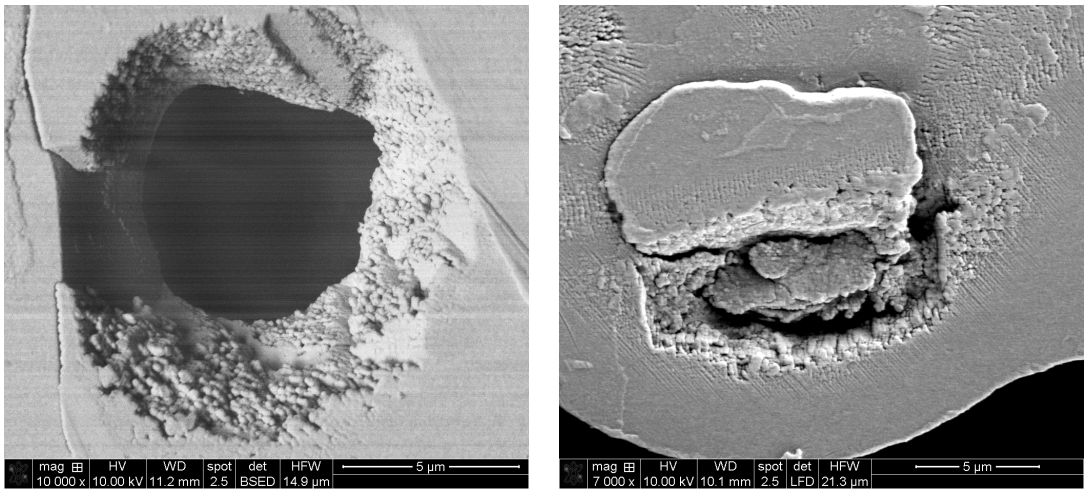

(a) (b)

Figure 5.9: High resolution SEM images of Man-001, which reveal greater detail in the electrode structure and in the surrounding area. Images were taken for an electrode from array B on (a) the exit side, and (b) the seed side of the diamond. Note that these images were not taken on the same electrode as that pictured in Figure 5.7a.

material on the exit side, and the ejection process could remove a significant fraction of the graphitic material. These issues are addressed through Raman spectroscopy.

Spectra for the electrodes in each array were taken using a HORIBA LabRAM HR Evolution Raman Spectrometer [75] with a helium-neon laser source of wavelength 633 nm[9] and a focal spot size of 5 μm. The recorded data were then fitted using the Curve Fitting toolbox in MATLAB [76, 77] by three Gaussians of the form $A\exp(-((x-B)/C)^2)$, that is, one narrow diamond peak at 1332 cm^{-1}, and two broader graphite peaks corresponding to the graphite D and G peaks at 1350 cm^{-1} and 1583 cm^{-1}, respectively [72]. Raman spectra were recorded on both the seed and exit sides of the diamond.

The result of Raman spectra taken on the exit and seed side are shown in Figures 5.10a and 5.10b, respectively. A comparison of these two figures shows the ratio of the diamond peak between the seed and exit sides is $<< 1$, while the shape of the data, in red, is otherwise similar. A comparison of the height of the graphite peaks between the two sides reveals similar graphite content on both sides, with slightly more graphite content on the seed side than the exit side. Both of these facts together

[9]Other wavelengths for the Raman setup exist, such as 325 nm and 488 nm wavelength sources. For the purposes of these studies the wavelength will not impact the results, provided the same wavelength source is used in all measurements. The effect of a different wavelength source is likely to shift the position of the peaks in the Raman spectra by O(cm^{-1}).

imply that the ratio of diamond to graphite is significantly higher on the exit side of the diamond[10]. The reason for this is the mechanism by which the electrode forms, that is, as the focal point is moved towards the exit side of the diamond, the pressure build-up is sufficiently large that the top layers of the diamond are ejected, exposing more of the diamond material on the exit side. This effect is weaker on the seed side, where an excess of material forms and thus more graphite is observed in these Raman spectra. Therefore, these findings corroborate well with the SEM images shown in the previous section.

These results also motivate further study into the parameter space for graphitic electrode processing, which could reveal optimal conditions for the formation of graphite. Since the pressure build-up is linked to the morphology (shown in SEM and Raman data) of the electrode, particularly on the exit side, it is possible that the beam fluence is linked to the induced pressure, which could form electrodes with a higher graphite content. Additionally, the Raman spectra were taken after Man-001 was metallised. It is possible that this may affect the spectra via the suppression or exaggeration of the material content, though this is stated without proof, since these are surface measurements. Such a study which probes these ideas is presented later in this chapter in Section 5.2.

5.1.6 I-V Curve Characterisation

After observing the morphology of the electrodes, the final method of characterisation of Man-001 is using I-V curves, which were taken for each electrode in the arrays through the use of a Keithley 2410 SourceMeter [78] using two probe needles. One needle was attached to the metal strip pattern on the seed side of the diamond, and the other needle then probed each individual electrode on the exit side. An ohmic response was observed up to $\pm 200\,\mathrm{V}$, at which point an exponential increase in the current occurred. This ohmic response is seen in Figure 5.11a, and these electrodes are classed as "ohmic electrodes". Although the side view images of the electrodes, Figures 5.6a and 5.6b, show fully formed electrodes in the diamond bulk, it is possible

[10] "Graphite" here refers to the graphite G peak. A study into the variation of this ratio is presented in Section 5.2.

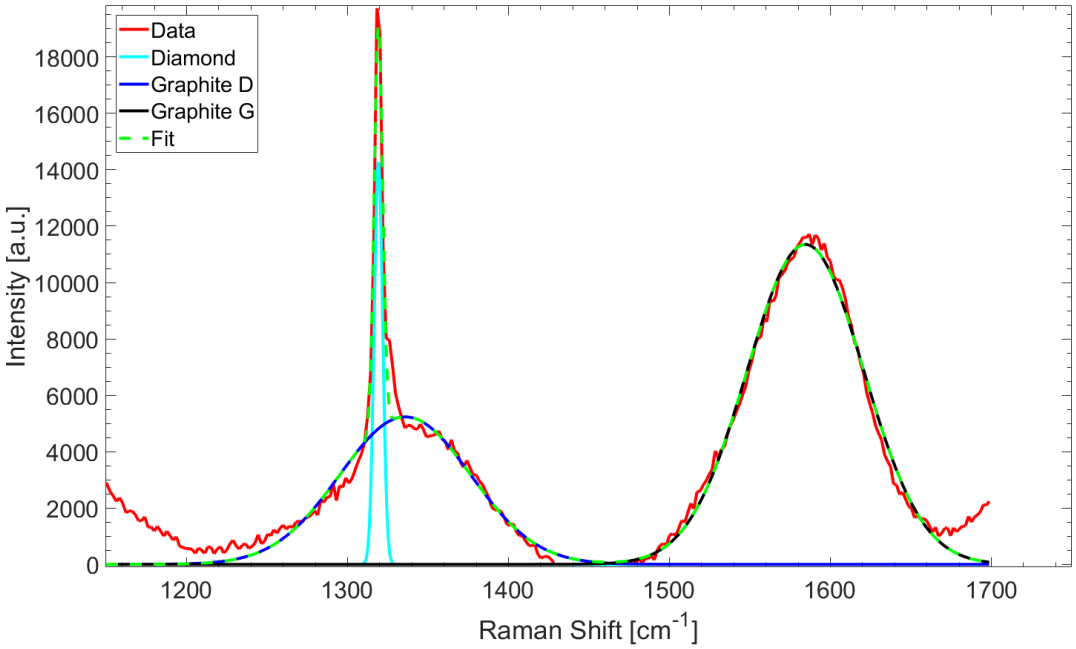

(a)

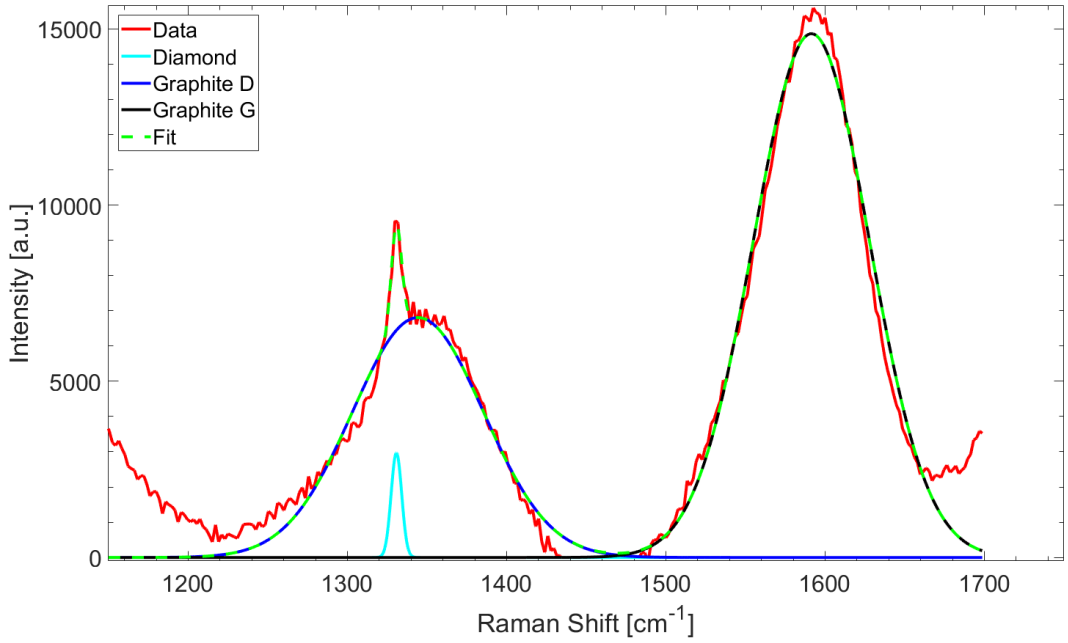

(b)

Figure 5.10: Raman spectra of one electrode on Man-001 taken on (a) the exit side, and (b) the seed side of the diamond. Fits to these data use three Gaussian peaks; one for the diamond peak and two for the graphite peaks, with a fit reconstructed from these Gaussians shown in green. There are artefacts at around 1200 cm^{-1} and 1700 cm^{-1} due to background subtraction used to isolate the peaks.

that the electrodes do not fully penetrate the diamond bulk. In that case, the electrodes would cease forming several microns from the exit surface of the diamond, or the electrodes would begin forming within the diamond bulk rather than at the seed surface of the diamond[11]. All but one electrodes in array A showed this behaviour, whereas only six, one, and zero electrodes in arrays B, C, and D respectively exhibited this phenomenon and thus are characterised as "non-ohmic electrodes". A combination of this behaviour and a high measured resistance implies that there is likely a discontinuity in the electrode formation.

The typical resistance of the ohmic electrodes, as measured by the inverse gradient of the I-V curves, is $\mathrm{O}(100\,\mathrm{k}\Omega)$, compared with the typical resistance of the non-ohmic electrodes of $\mathrm{O}(200\,\mathrm{G}\Omega)$. I-V curves were taken between two unconnected electrodes on the detector on each array to probe the resistance of the diamond bulk, yielding resistances in the range $158 - 216\,\mathrm{G}\Omega$. A comparison of these resistances with that of the non-ohmic electrodes confirms that most electrodes do not completely penetrate the diamond bulk in array A.

In some cases the exponential increase in current occurred at lower voltages, resulting in a non-ohmic response, such as that observed in Figure 5.11b. Only measurements exhibiting an ohmic response were used when calculating the resistance of the electrodes, so these curves were omitted. The average resistivity is shown in Table 5.1, which is calculated using the measured electrode diameter. The yield for array A is low due to only one measured electrode having an ohmic response, which also gives a significantly lower resistivity than the other arrays. Although it has already been confirmed that the beam fluence has a significant effect on the electrode diameter, no significant trend is observed in the resistivity measurements since they are consistent with each other, provided array A is neglected. This implies that the electrodes are of the same conductive material, but a comparison of these values to the resistivity of graphite, $\mathrm{O}(10^{-4} - 10^{-3}\,\Omega\mathrm{cm})$ [79, 80], indicates the measured resistivity is at least three orders of magnitude higher, which is likely due to a significant fraction of the diamond bulk not being converted to graphite.

[11] Imaging the top and bottom surfaces to show the electrode is fully formed is particularly difficult, especially due to the presence of metallisation.

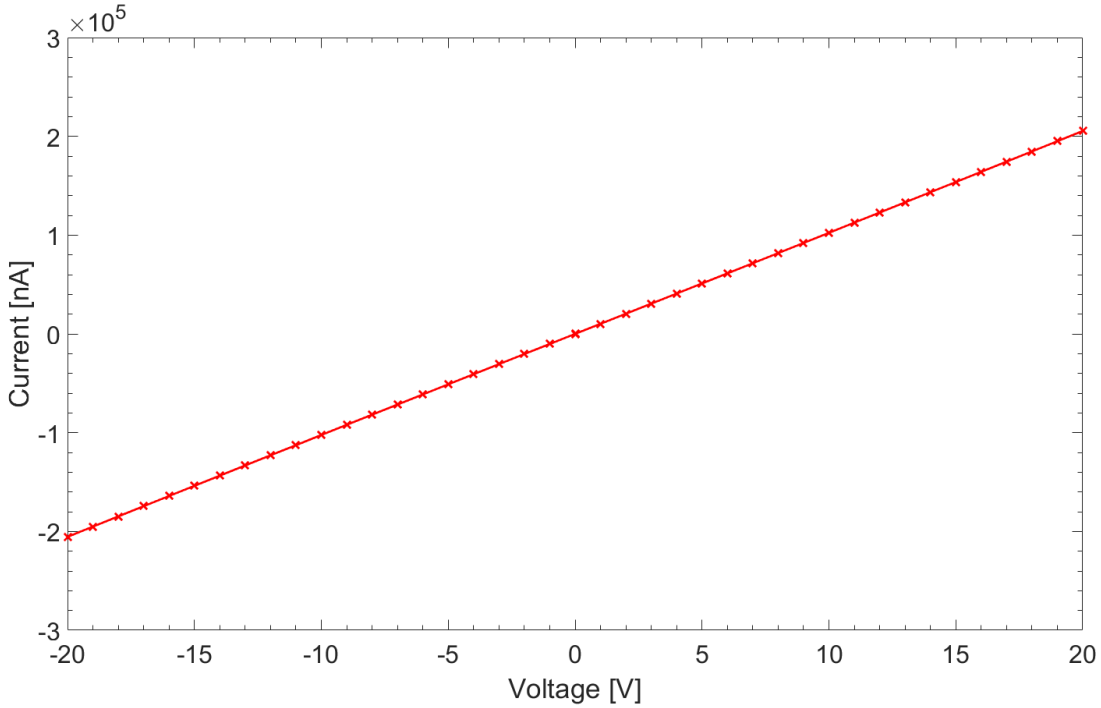

(a)

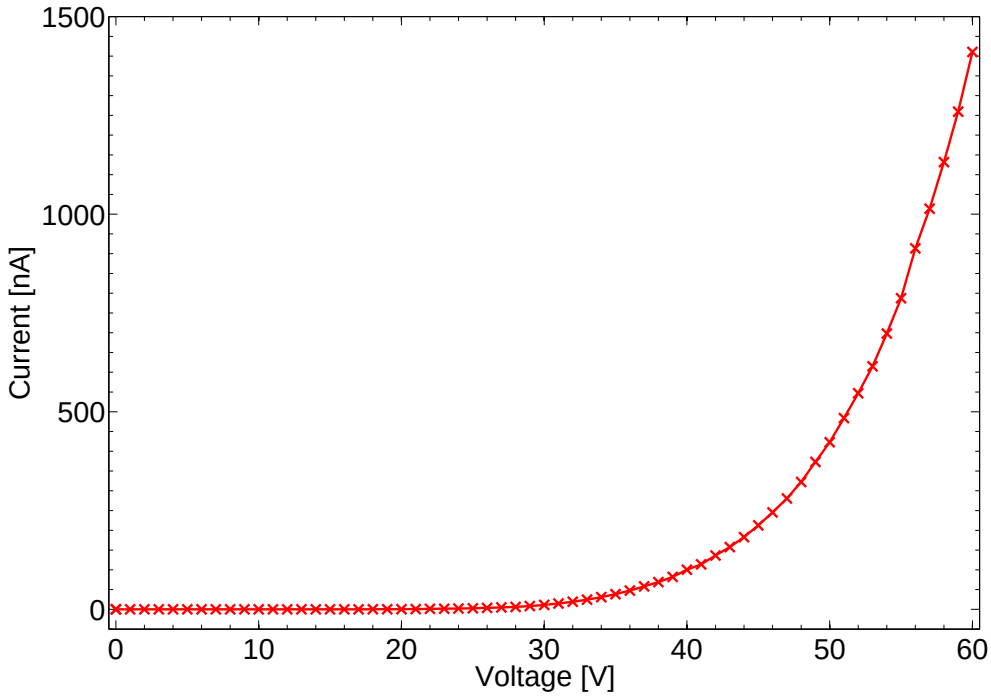

(b)

Figure 5.11: (a) Typical "ohmic electrode" I-V curve taken on array C, showing an ohmic response. (b) Exponential increase in current occurring at a much lower voltage for an electrode taken on array A. In cases such as this, there is no definitive ohmic region, and are one type of "non-ohmic electrode" observed in array A.

Array	Fluence Jcm^{-2}	Diameter μm	Resistivity Ωcm	Yield %
A	2.0	7.6 ± 0.8	0.75	3
B	3.0	10.2 ± 1.2	2.47 ± 0.86	83
C	3.5	12.4 ± 0.9	2.58 ± 0.89	97
D	4.8	18.0 ± 1.3	2.63 ± 0.71	100

Table 5.1: Average electrode diameter and resistivity for each array on Man-001, along with the yield. The yield is the number of electrodes with an ohmic response and are identified as fully formed electrodes through optical microscopy and images taken through two crossed polarisers.

5.1.7 Detector Summary

In summary, Man-001 reveals that there is a trend between the beam fluence used to fabricate the graphitic electrodes and the resulting electrode diameter, along with the level of stress induced in the diamond lattice by the presence of these electrodes. While it is unfortunate there is some irregularity in the morphology of the graphitic electrodes, the identification of this, resulting from an astigmatism in the beam path, does allow for these effects to be rectified before future electrode fabrication. Data recorded using SEM also reveals some structure in the formation of these graphitic electrodes and reinforces the understanding into how the graphitic electrodes form in diamond, particularly the processes that govern the start and end of the electrode fabrication. The analysis of the Raman spectra indicate different electrode structure on the seed and exit sides of the diamond, supporting the current understanding of the formation of graphite through this laser-induced process. Finally, I-V measurements have confirmed that the electrode resistivity between the fabricated arrays does not vary with beam fluence and, in conjunction with SEM images, the measurements highlight some issues with the formation of the graphitic electrodes likely due to insufficient translation of the movable stage in the direction of electrode processing. Further issues such as an incompatibility of the measured resistivity values versus known values were identified, indicating that the electrodes are not purely graphitic and likely contain some fraction of diamond unconverted from the laser-induced process.

5.2 Sample Goe-001

5.2.1 Motivation

The characterisation of Man-001 improved our understanding of the growth mechanism of graphitic electrodes in diamond, and a study into their properties has identified a potential difference between the seed and exit sides of the electrodes. However, the metallisation on the electrodes has made the results hard to interpret. Characterisation through Raman spectroscopy must be performed on electrodes without surface metallisation in order to further probe the seed and exit side characteristics. Additionally, only the beam fluence was varied in the fabrication of Man-001, and probing the full parameter space, that is, the beam fluence and the translation speed of the movable stage, would be ideal. Goe-001 was fabricated for these reasons. The sample was fabricated by L. Graber at the University of Göttingen, whose work [81] involved the characterisation of graphitic electrodes in 3D diamond detectors via Raman spectroscopy. It should be noted that the results presented here are from Raman spectroscopy performed at the University of Manchester and serve as comparison to that performed by L. Graber.

5.2.2 Sample Overview

The diamond substrate used for these studies is an electronic grade polycrystalline diamond, with dimensions of $10 \times 10 \times 0.5\text{mm}^3$. The laser setup at the University of Göttingen is functionally the same as that used at the University of Manchester to fabricate Man-001, with the exception that the repetition rate of the laser is a thousand times greater, that is, 1 MHz[12]. The implication of this is the higher number of laser pulses incident on the diamond would benefit from faster translation speeds to be compatible with similar fabrication results at the University of Manchester. This is a highly desirable characteristic, given that the fabrication time per electrode drastically decreases from O(100s), subject to translation speed and the diamond thickness, to O($\leq$ 1 s) with the higher repetition rate, resulting in fast fabrication of large scale detectors.

[12]A full description of the laser setup is described in reference [81].

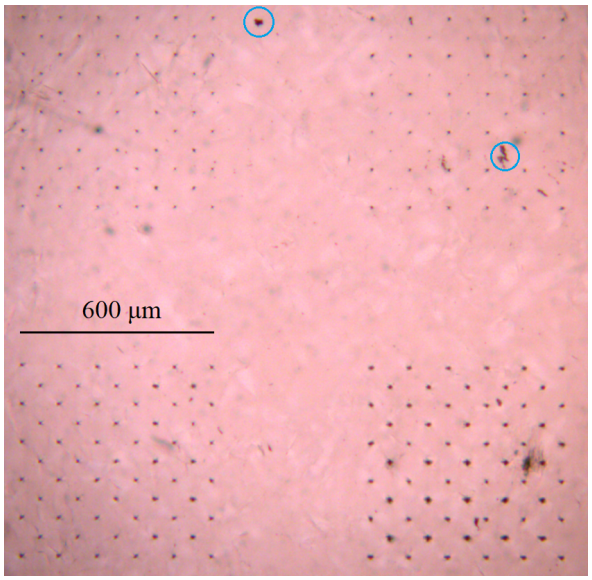

(a)

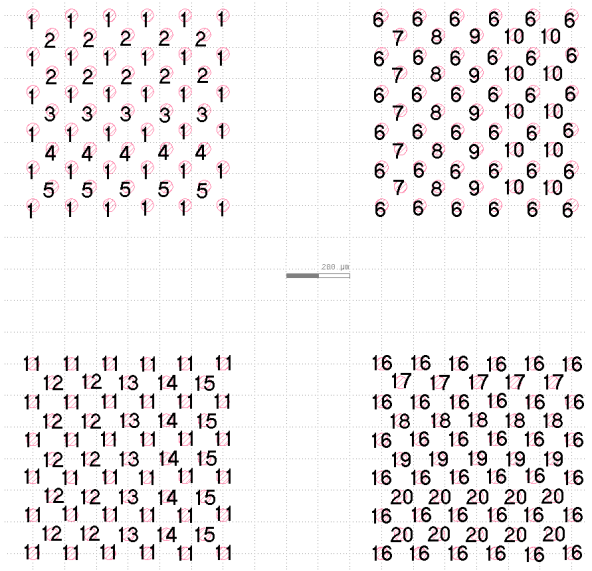

(b)

Figure 5.12: (a) The exit side of Goe-001. The outer electrodes in any given array, in the 6×6 formation, are fabricated with the same processing parameters, while the inner electrodes, in the 5×5 formation, are fabricated with varying processing parameters, indicated in Figure 5.12b. Some surface contaminants are highlighted in blue. (b) Layout of the electrodes in Goe-001. The beam powers and translation speeds for the electrodes are summarised in the table below.

Speed [μms^{-1}] / Power [mW]	10	25	60	150
50	7	2	12	17
200	8	1 & 3	11 & 13	18
2000	9	4 & 6	14 & 16	19
10000	10	5	15	20

The electrodes were fabricated with translation speeds in the range of $50-10000\,\mu\text{ms}^{-1}$ and beam powers in the range of $10-150\,\text{mW}$. The exit side of the electrodes is shown in Figure 5.12a, with a supporting figure outlining the parameters used to fabricate each electrode shown in Figure 5.12b. The electrode separation is $120\,\mu\text{m}$ and uses a pattern identical to that of Man-001. The optical image of the exit side highlights that surface contaminants are an issue, with examples highlighted in blue in Figure 5.12a, and may obscure the visibility of electrodes at the surface. However, both this figure and Figure 5.12b also shows the visibility of the electrodes on the exit side improves with beam power, particularly when comparing electrode parameters 7-10 (fabricated at 10 mW) with electrode parameters 17-20 (fabricated at 150 mW). This increase in visibility, and thus electrode size at the surface, was noted on Man-001 so it is likely that the electrode diameter will again increase with beam power. The figure also shows that, optically, the variation in translation speed for electrode processing is not as easily observed unless the beam power is quite high, such as those fabricated with electrode parameters 17-20.

5.2.3 Crossed Polarised Image Characterisation

The sample was imaged under a pair of crossed polarisers to confirm and compare to the results presented in Section 5.1, with examples shown in Figures 5.13b and 5.13d. It is clear from these figures that there is greater inherent stress in the diamond itself due to the presence of impurities, as opposed to the stress induced by the electrodes on the diamond lattice. One issue with this is it becomes difficult to use this characterisation to identify partially formed electrodes in the same manner as for Man-001. This is particularly a problem for electrodes fabricated with low power, such as 10 mW, as it has been noted that the presence of such electrodes is hard to identify optically. However, Figure 5.13b can still be used to identify some partially formed electrodes, highlighted in red, without being obscured by stress arising from impurities. Work performed by L. Graber [81] indicates that not all of the electrodes identified in Figure 5.13b are partially formed, confirming the difficulty in using this method on diamond samples with high inherent stress.

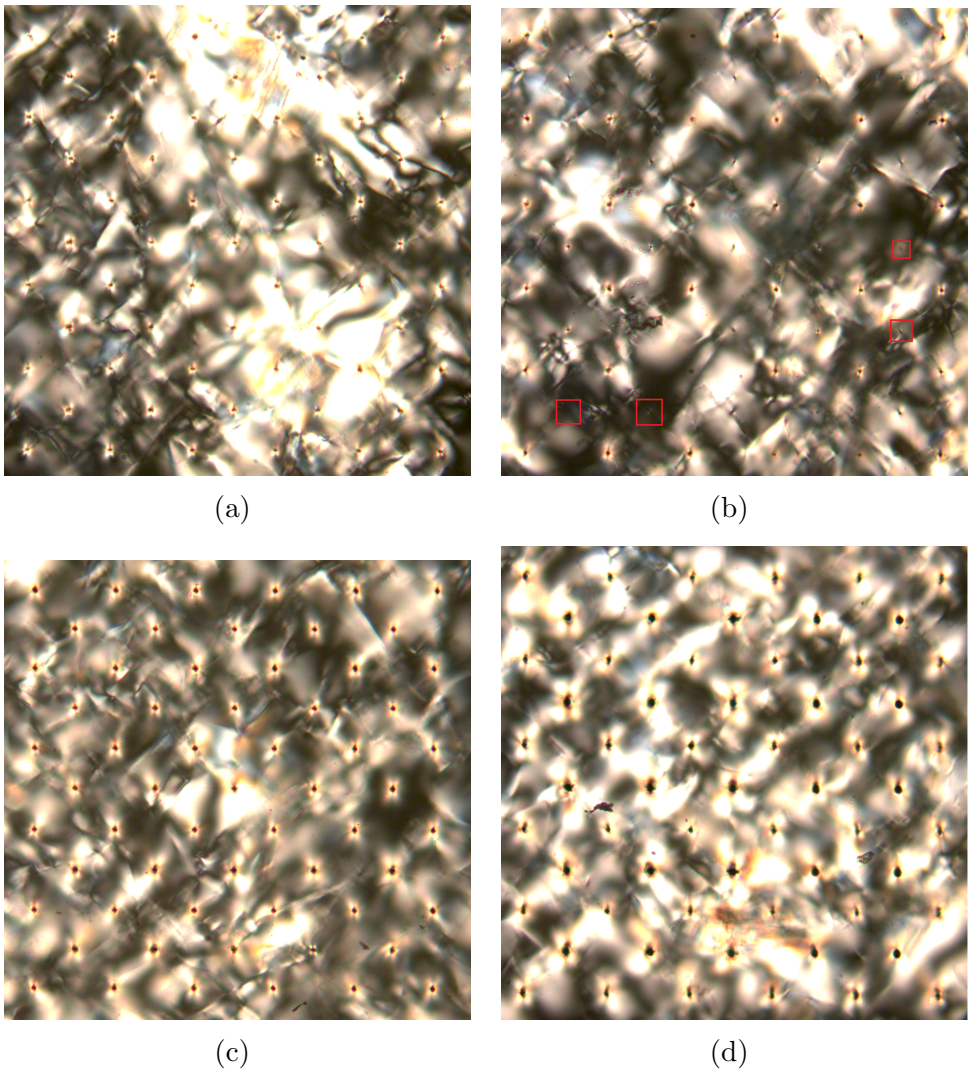

(a) (b)

(c) (d)

Figure 5.13: Crossed polariser images taken on Goe-001 for four different arrays for beam powers of (a) 25 mW, (b) 10 mW, (c) 60 mW, and (d) 150 mW. These images correspond to the arrays as depicted in Figures 5.12a and 5.12b. Examples of electrodes which are partially formed are highlighted in red. High levels of inherent stress in the diamond lattice due to the presence of impurities can be seen in all the arrays, with the highest levels observed in (a).

The other issue with the level of inherent stress is that it makes a comparison into the level of stress as a function of beam power difficult. As a result, any comparisons between the stress in each array should only be taken lightly. Nevertheless, measurements of the stress performed in a method identical to that in Section 5.1 confirms once again that the stress induced by the electrodes on the diamond lattice seems to increase with beam power, which is shown in Table 5.2. The presence of the inherent stress does skew the results slightly, since the stress induced by the electrodes fabricated with a beam power of 25 mW is in fact higher than those fabricated at 60 mW,

corresponding to the top left and bottom left arrays, respectively, in Figure 5.12a[13]. This is known to be unlikely given results already presented in Section 5.1.

Array	Beam power mW	Stress relative to top right array a.u.
Top left	25	1.56
Top right	10	1
Bottom left	60	1.52
Bottom right	150	2.20

Table 5.2: Relative stress measurements for Goe-001. The location of the arrays is identical to that in Figure 5.12a, and the stress is relative to the top right array. The beam power shown is for the inner 25 electrodes of the arrays in the 5×5 formation.

One advantage of this sample versus Man-001 is the ability to probe the stress induced by each parameter set. In this case, extracts of the original images taken under crossed polarisers are used. While it is impossible to avoid the effect of the inherent stress in the diamond lattice, as was already demonstrated, and such sources of stress may drastically skew the measured stress, performing this measurement allows the effect of the translation speed on the stress induced by the electrodes to be probed. For each image extracted for these measurements, the same image size was used in order to minimise the effect of the inherent stress as much as possible and to provide a fair comparison between the results. These measurements are shown in Figure 5.14.

Although Figure 5.14 further demonstrates that the stress induced by the electrodes increases with beam power, it is not clear that the induced stress also increases with translation speed due to the inherent stress. For example, if one were to ignore the results for electrodes fabricated at 60 mW then trend becomes clearer, though there is no reason to suggest an issue with these measurements, judging from the image taken under crossed polarisers (Figure 5.13c). As such, the effect of translation speed on the stress induced on the diamond lattice is inconclusive.

[13]Note that this observation is made using the output of the analysis. In reality, one can see by eye that the stress induced by the electrodes fabricated at a beam power of 60 mW is higher than those fabricated at 25 mW, but the presence of the inherent stress in this diamond sample obscures this when taking all of the electrodes into account. This is one obvious downside of using this technique.

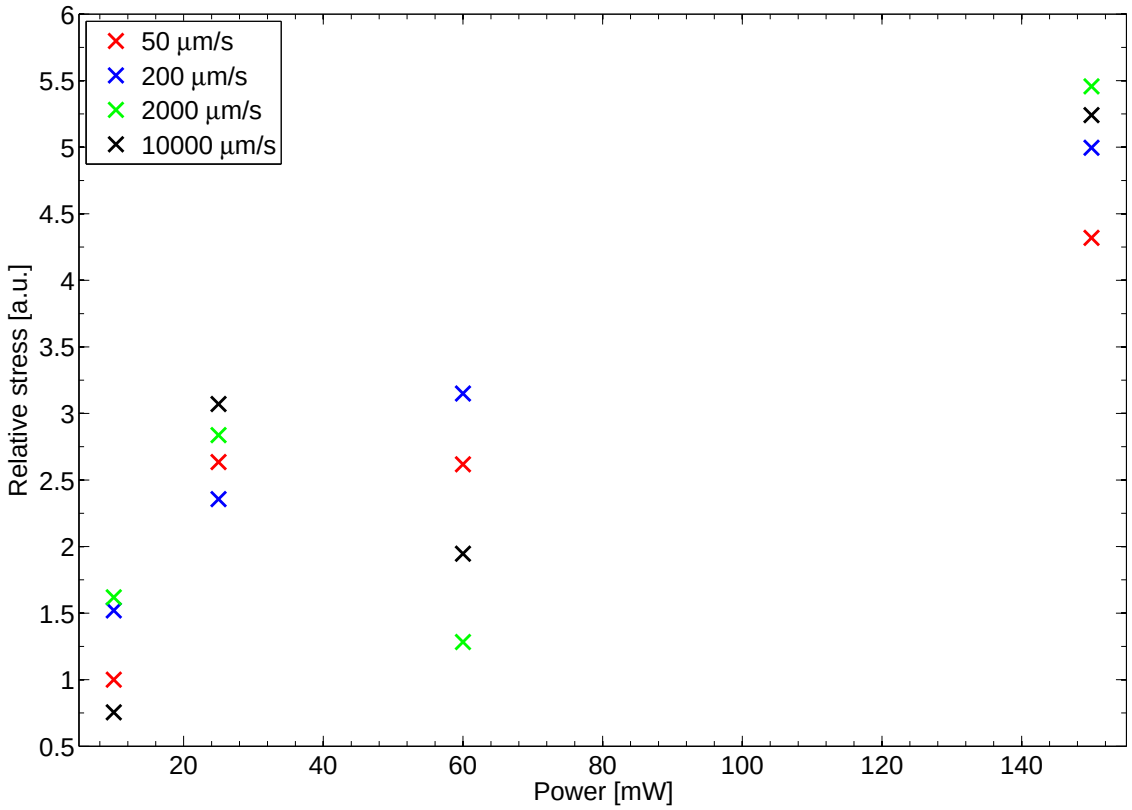

Figure 5.14: Relative stress measurements as a function of beam power and translation speed for electrodes fabricated on Goe-001. The stress measurements are calculated relative to electrodes fabricated with a beam power of 10 mW and a translation speed of 50 μms^{-1}. No error bars are shown as it is not possible to provide meaningful errors without the subtraction of the stress due to impurities within the diamond.

5.2.4 Raman Spectroscopy Characterisation

Raman spectra were taken for the sample using the same method outlined in Section 5.1.5. In this work the helium-neon source with a wavelength of 633 nm was used, contrasting with the spectra recorded by L. Graber at 488 nm using an argon ion laser source [81]. This difference in wavelength will result in a slight shift in the location of the peaks recorded in the Raman spectra, likely of O(1 cm^{-1}). Although the Raman setups are different in this work and that performed by L. Graber, any trends should remain the same.

Examples of Raman spectra for two different parameter sets on the seed side are shown in Figures 5.15a and 5.15b. There are some differences between these spectra versus those for Man-001, which is likely due to the exploration of a much wider parameter space in these measurements. For example, the beam fluence, and thus beam energy since the spot size of the laser in diamond is expected to remain constant,

for Man-001 had a variation of a factor 2, whereas these measurements have a variation of up to a factor 15. Results presented in Section 5.2.3 have demonstrated a vast difference between the electrodes at the extrema of the parameter space probed, so such a different response in the Raman spectra is unsurprising. It should also be noted that these measurements were performed with no surface metallisation, which may have some slight effect on the peak amplitudes versus those of Man-001, though this is hard to quantify. In these spectra the amplitude of the graphite D and G peaks is noticeably greater at a higher beam power and translation speed, with a slight reduction in the amplitude of the diamond peak.

As was the case in the Man-001 data, the Raman spectra for Goe-001 also show notable differences between the seed and exit side spectra, the former of which are shown in Figures 5.16a and 5.16b. Although no SEM data were taken for Goe-001, these results do support the explanation offered for the formation of graphite, also outlined previously in Chapter 3. The benefit of these data is the appearance of a trend dependent on the processing parameters. That is, in these spectra the amplitude of the graphite peaks is higher at higher beam power and translation speed, as was the case on the exit side. This shows higher power and faster speeds are preferable, though the effect of either is not clear from these plots alone. This can be explained through an analysis of the peaks for each parameter space.

The amplitude of the diamond and graphite G peaks were measured from fits to the data, for each spectrum taken, to calculate the ratio of diamond to graphite on the seed and exit sides of the electrode. It should be noted that once again it is difficult to fit the data in cases where the diamond peak is dominant, such as in Figure 5.15a. The calculation of the diamond:graphite ratio is modified such that if the fit fails, judged by the location of each peak with respect to their experimentally known locations, then a simple measurement of the amplitude at the known peak locations is made instead. This is expected to skew the ratio such that it is higher for electrodes fabricated at a lower beam power. It is possible to improve the accuracy of these fits by using two Gaussian peaks for each of the graphite D and G peaks, as presented in the work by L. Graber [81]. This was avoided in this analysis as these extra peaks, while potentially improving the fit quality, are non-physical.

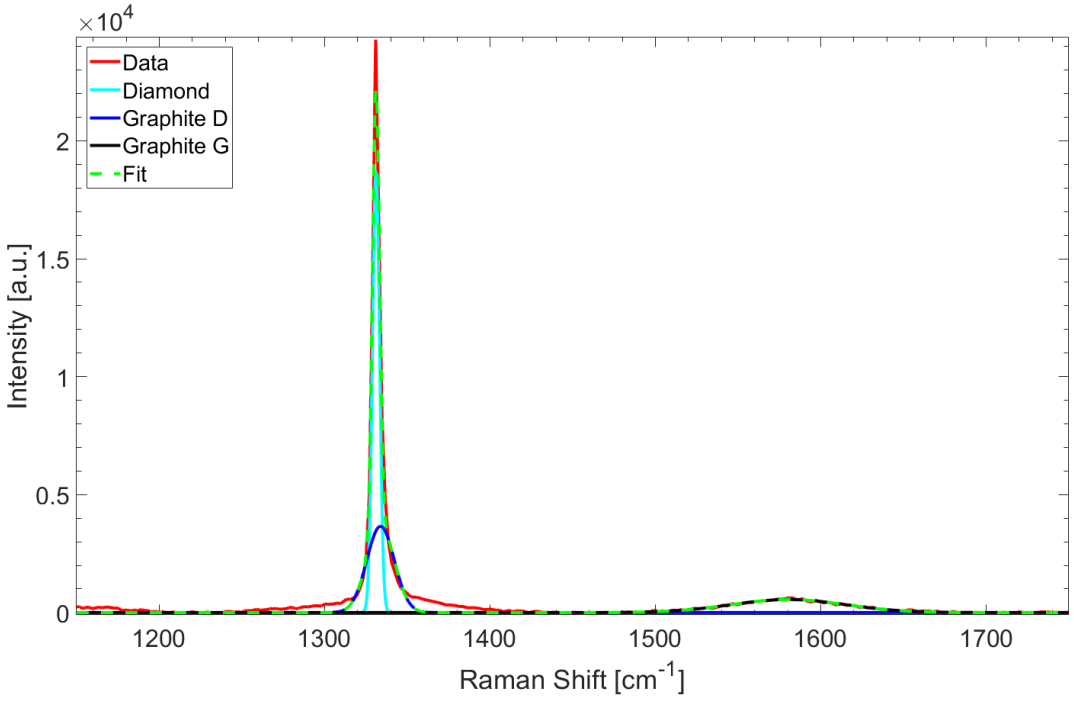

(a)

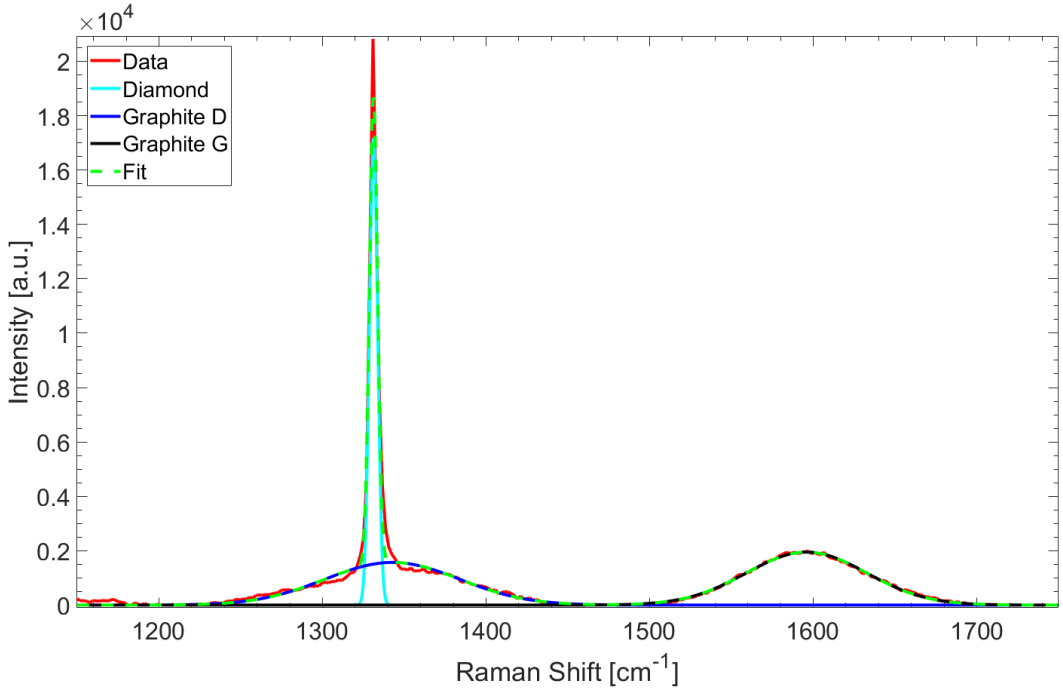

(b)

Figure 5.15: Raman spectra of Goe-001 taken on the exit side for electrodes fabricated with (a) a beam power of 60 mW and translation speed 200 μms^{-1}, and (b) a beam power 150 mW and translation speed 10000 μms^{-1}. The graphite D peak is completely dominated by the diamond peak in (a), which explains the unusual fit.

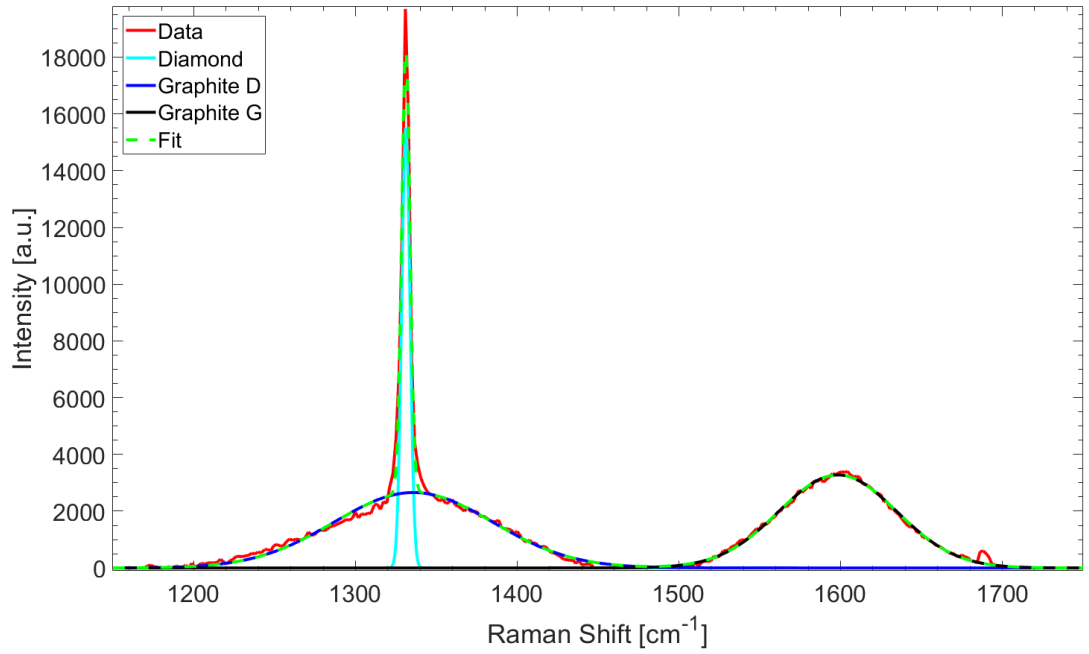

(a)

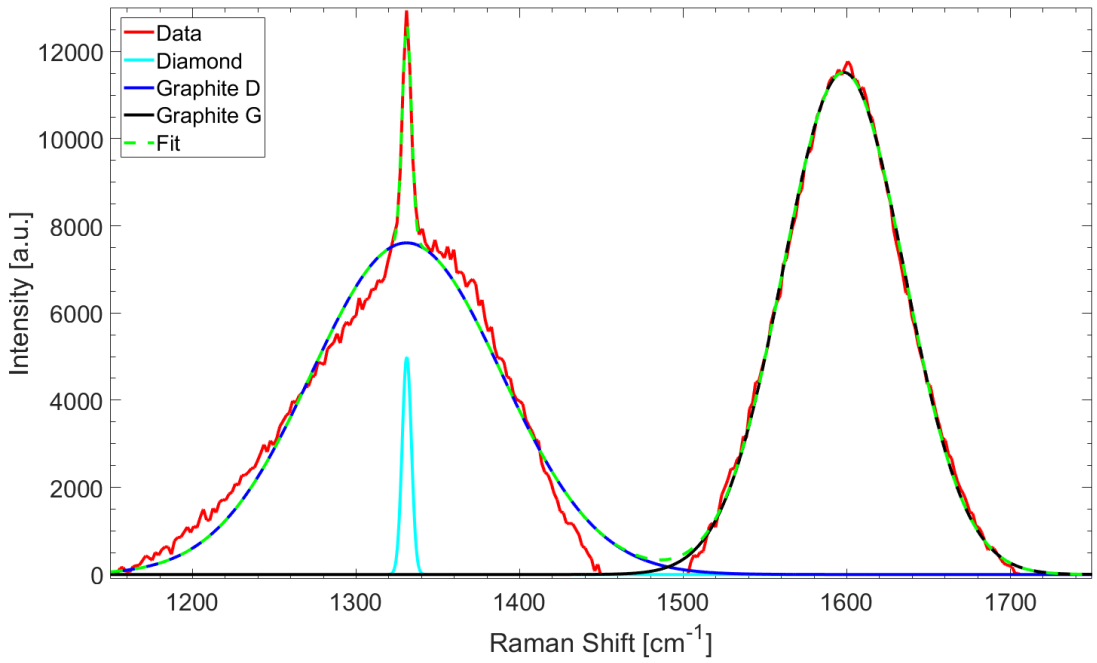

(b)

Figure 5.16: Raman spectra of Goe-001 taken on the seed side for electrodes fabricated with (a) a beam power of 60 mW and translation speed 200 μms^{-1}, and (b) a beam power 150 mW and translation speed 10000 μms^{-1}. Figures (a) and (b) correspond to the seed side of the same electrodes presented in Figures 5.15a and 5.15b, respectively.

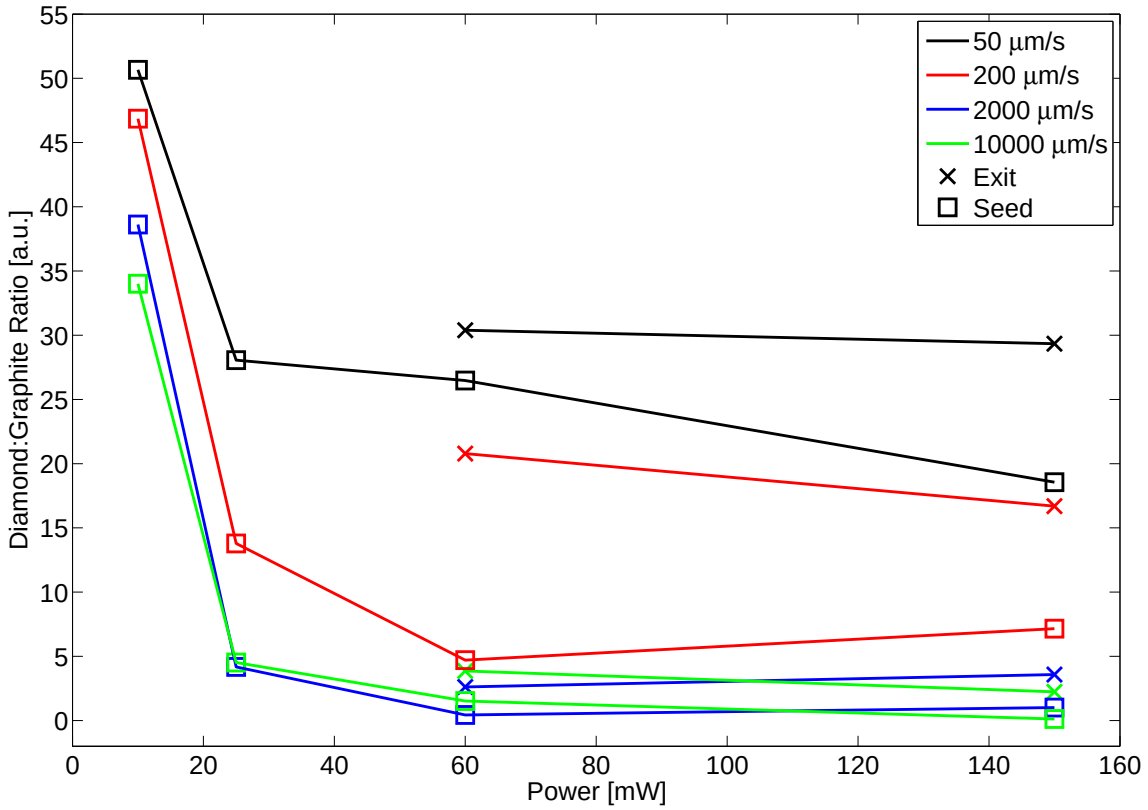

Figure 5.17: Measured diamond to graphite ratios on Goe-001 as a function of beam power. The line and marker colours show the different translation speeds used in the fabrication of the electrodes, while the marker type denotes the seed and exit side measurements.

The measured diamond:graphite ratios are presented in Figure 5.17 and show several key results. The first outcome is that a low beam power results in a much higher diamond to graphite ratio on both the seed and exit side. This is naively expected, since it has been shown previously that a lower beam power implies a lower fraction of incident beam is above the threshold for graphitisation, resulting in less diamond converted to graphite. While a lower beam power would also result in a smaller electrode diameter, both this result and the I-V measurements presented in Section 5.1.6 indicate a low beam power is not recommended to achieve conductive graphitic electrodes. It should be noted that measurements of the exit side for electrodes fabricated at beam powers of 10 & 25 mW were completely dominated by the diamond peak, so reliable measurements of the diamond to graphite ratio were unfeasible.

The other outcome is that a higher translation speed results in a lower diamond to graphite ratio. This is explained through the growth mechanism of the electrodes. For example, at the seed side there is preference for electrode formation in the direction of

the moving focal spot of the beam, governed by a pressure build-up and the repetition rate of the laser pulses. As the electrode grows this pressure also increases, and thus so does the stress induced by the electrode, until the focal spot (and electrode) reaches the exit side. At this point, the pressure lifts off the top few layers of the diamond at the seed side. The graphitisation process occurs on a time scale of O(ps), so the longer the focal spot dwells at a particular position, or rather the more laser pulses incident at a given position, the more energy is deposited and likely increases the electrode size and, consequently, the pressure. On the exit side this implies more of the electrode is lifted off, meaning that the size of the probed area, that is, the electrode itself, is smaller than for faster translation speeds. It is not clear why this ratio is lower on the seed side for faster translation speeds, though one may speculate this is related to the pressure build-up and warrants further theoretical investigation. A comparison of the translation speeds used in the fabrication of Man-001 and Goe-001 highlights that an increase in the repetition rate necessitates a proportional increase in the translation speed. This implies that diamond detectors can be fabricated en masse using a laser setup with a higher repetition rate.

The final outcome, shown previously in this chapter, is more graphite is observed on the seed side of the electrode versus the exit side across the entire parameter space. This proves there are fundamental differences in the formation of the graphitic electrode as it is fabricated. Therefore, there is some indication that how diamond samples are metallised and read out for detector applications is crucial. For example, consider the exit side of the electrodes whereby the upper layers of the diamond lattice, and the electrode, are blasted off due to the mechanism of electrode formation. If there is in fact a higher diamond to graphite ratio on this surface, then this implies two things. The first is that the adherence of the metallisation to the electrode could be worsened, which would then make the metal contacts easy to damage and "flake off". Such a systematic study into the metal adherence on the graphitic electrodes (and diamond) has not been performed but would be invaluable to the future of diamond-based detectors.

The second implication of a higher diamond to graphite ratio on the exit side is if there is more diamond on the exit side, then this could cause issues with reading out such a detector if the readout metallisation were applied to the exit side due to

the higher resistance in the electrode. While this particular observation could dictate exactly where the bias and readout metallisation are applied, both of these implications point to one simple solution, which is the use of surface contacts. Such contacts could affect studies into the stress induced by the electrodes on the diamond lattice, as well as further Raman spectroscopy studies. However, the surface contacts would not affect the quality of the electrodes inside the diamond bulk, nor their detection properties[14], and would offer a larger area to which the metal may adhere. In the best case scenario, this would improve the adherence of the metallisation, but at the very least this would aid in the accuracy of the metallisation onto a diamond sample, which requires the alignment of a metallisation mask to the electrodes and to other alignment marks.

5.2.5 Sample Summary

Goe-001 has established the effect of the beam power and translation speed on the morphology of the electrodes, from Raman spectroscopy, and in terms of the stress induced by the electrodes on the diamond lattice, from crossed polariser images. This work has highlighted that using cross polarised images for the identification of partially formed electrodes should always be supported by optical images, and for a true understanding into the induced stress from the electrodes it is necessary to image the sample under crossed polarisers prior to electrode fabrication. The result of Raman spectroscopy into this parameter space has shown that higher beam powers and faster translation speeds are recommended for the fabrication of electrodes with a low diamond to graphite ratio, which should result in lower resistance electrodes. By comparing to Man-001, the results of the characterisation methods also show that an increase in the repetition rate of the laser results in a proportional increase in the translation speed used for electrode fabrication, and has also opened up a potential area of research into the quality of the metallisation on diamond detectors.

[14]The exceptions to this would be in the event of any surface current in such a detector, which could be more easily collected, and the presence of these contacts would reduce the active area of the detector. However, both of these effects would be negligible, provided these contacts are small.

5.3 Detector Ox-001

5.3.1 Motivation

Despite some success of Man-001, both in terms of its fabrication and its performance in particle beams (discussed later in Chapter 6), there were some issues with the detector. The laser setup in Manchester was limited to producing electrode diameters no smaller than O($8\,\mu$m), with a resistivity of O($2\,\Omega$cm). This poses an issue for future detectors with a high cell density, that is, those with a small electrode separation, whereby there is less active material for particle detection. Therefore, reducing the size of the electrodes without resulting in partially formed electrodes would be ideal. The resistivity is also an issue, since it has been established the material produced from this process, based on the resistivity measurements, is graphite-like but not truly graphite. Reducing the resistivity, or rather the resistance of the electrodes, would allow for faster charge collection, required for environments with a high number of incident particles such as the LHC, which is likely possible only through improvements to the laser setup. One such improvement is the incorporation of a spatial light modulator (SLM).

The use of an SLM for the fabrication of electrodes in diamond was demonstrated by B. Sun et al. [64], and its benefits have been explained in Chapter 3. In short, the use of an SLM reduces any aberration of the focal spot in diamond through correction of the refractive index mismatch between the diamond and medium of the lens. This results in more sharply focussed focal spot, which is shown in Figure 5.18, thereby increasing the energy density of the focal spot. This allows for the fabrication of electrodes with not only a lower beam power than without the use of an SLM but also allows for smaller electrode diameters to be fabricated. The result of the incorporation of an SLM has been shown to reduce the resistivity by up to O(100) versus electrodes fabricated without an SLM, both in Manchester and in other setups [64]. The electrodes could also be fabricated with sub-micron sizes [64], indicating the benefits of an SLM for the use in 3D diamond detector fabrication.

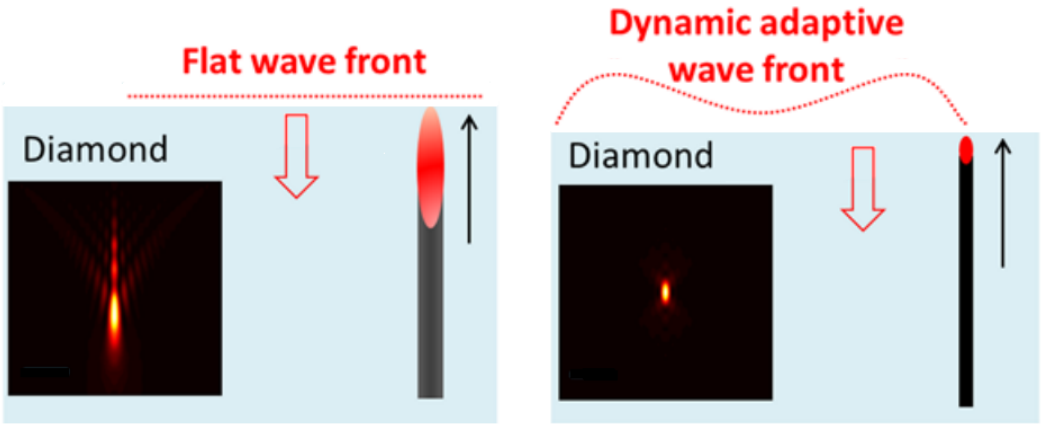

Figure 5.18: A simulation of the focal spot in diamond without, left, and with, right, the use of an SLM. A flat wave front implies the focal spot experiences significant elongation in the processing direction, marked by the direction of the black arrow, with some distortion in the lateral directions, which will influence the electrode diameter. A dynamic adaptive wave front, that is, a correction of any aberrations with depth, drastically reduces any elongation of the focal spot, resulting in a larger energy density. Figure taken from reference [64].

5.3.2 Detector Overview

The diamond substrate used for these studies was an electronic grade single crystal diamond, with dimensions $4 \times 4 \times 0.4\,\mathrm{mm}^3$ from IIa technologies [46]. The laser setup for the fabrication of the electrodes using an SLM is described in Chapter 3, with a complete description detailed in reference [64]. The objective lens in the Oxford setup for the focussing of the beam onto the diamond used oil as its immersion medium rather than air, as was used for the fabrication of Man-001. The reason for this is the refractive index of oil, 1.52, is closer to that of diamond, 2.4, versus air, ≈ 1, implying that the aberration effects are weaker and the corrections are thus less severe. However, the setup may be utilised with air as the immersion medium, and the electrodes were fabricated with the lens in air to compare more directly the use of an SLM in a laser setup to one without.

The focal spot of the laser in the Oxford laser setup is of sub-micron size, so electrodes were fabricated by scanning laterally in the diamond and "building up" layers of the electrodes in the processing direction[15]. The electrode diameter was set

[15]In the laser setups used for the fabrication of Man-001 and Goe-001, the focal point was simply moved in one direction (the growth direction) at a constant speed (see Figure 3.2 in Chapter 3). However, the focal spot of the laser in the setup used in the fabrication of Ox-001 is so small that it requires movement in directions perpendicular to the growth direction in order to fabricate electrodes with a diameter larger than $\mathrm{O}(1\,\mu\mathrm{m})$.

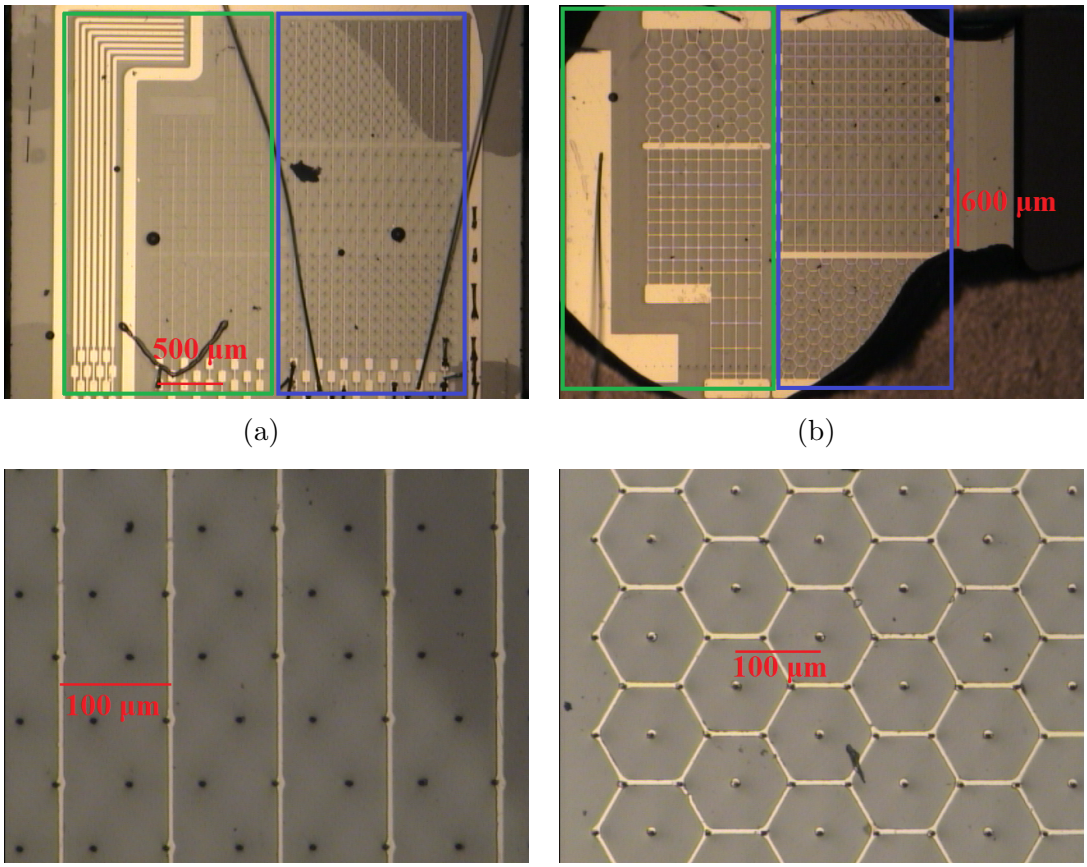

(a) (b)

(c) (d)

Figure 5.19: Optical images of Ox-001 as seen on (a) & (c) the readout side, and (b) & (d) the bias side. On the readout side bond wires are observed crossing the arrays, along with circular areas likely to be epoxy resin as a result of cleaning the diamond substrate. The strips used on the readout side are also seen. On the bias side the viewpoint is obscured by the PCB to which the detector is fixed, though the mesh structure connecting the bias electrodes is visible. (a) and (b) show a complete overview of the detector, while (c) and (d) show the hexagonal cell structure. In Figures (a) and (b), areas containing the 3D structure are highlighted in blue, while areas without graphitic electrodes, consisting of the "phantom area" and the planar detector area, are highlighted in green. Figures (a) and (c) are adapted from reference [82].

at O(4 μm) so that the results may be compared to those presented in Sections 5.1 and 5.2, and so that it is possible to resolve electrode features when imaged at an angle. The translation speed was set to 10 μms^{-1}, with a pulse energy of 140 nJ.

Three arrays of electrodes were fabricated with these parameters, with a readout electrode separation of 100 μm: an array of square cells; and array of rectangular cells with size 100 $\times$ 200 μm^2; and an array of hexagonal cells with a side length of approximately 67 μm. Cells from each array were arranged such that data was read out via strips, in a similar manner as Man-001 and is visible in Figures 5.19a

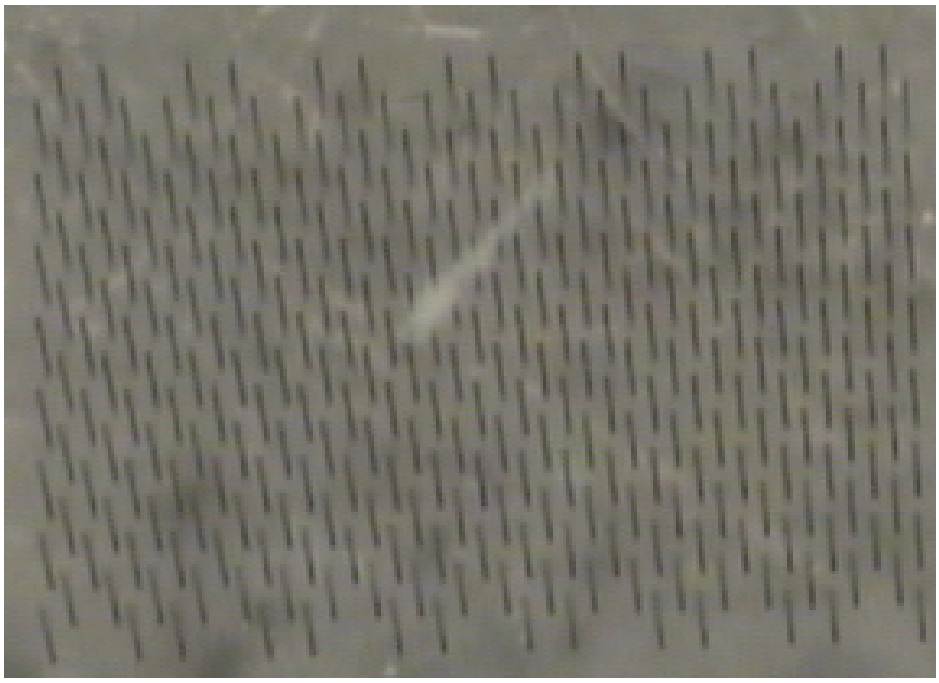

Figure 5.20: Side view of electrodes in the hex array in Ox-001. All the electrodes appear to fully penetrate the diamond bulk.

and 5.19c, while the bias electrodes were all connected in a mesh formation, as shown in Figures 5.19b and 5.19d. The metallisation was a combination of chromium and gold with thicknesses of O(50 nm) and O(75 nm) to cover not just the electrodes but also an area devoid of electrodes. This area, the "phantom area", contains a planar metallisation structure and a mesh structure similar to that used for the electrodes, but without the graphitic electrodes, in order to probe the effects of the metallisation, and is shown in Figures 5.19a and 5.19b.

One issue with the metallisation is the alignment of the mask to the electrodes. Figure 5.19c shows an offset of the metallisation of O(5 μm) from the electrodes where the metal just contacts the electrodes. The reason for this is a combination of two effects: the resolution of the microscope used for the alignment of the metallisation mas, O(10 μm), and the size of the graphitic electrodes at the surface, O(5 μm). It was therefore difficult to correctly align the metallisation mask onto the sample, although results presented later in Chapter 6 demonstrate this is not an issue.

A side view image of the electrodes is presented in Figure 5.20, which highlights the reproducibility of using an SLM, and that the electrode yield appears to be 100%

through optical inspection. Results from crossed polariser images, presented in Section 5.3.3, and I-V measurements also confirm this. For example, all electrodes measured via I-V characterisation were ohmic up to $\pm 40\,\mathrm{V}$, and exhibit exponential behaviour beyond that in a manner demonstrated in Man-001. The electrode resistivity is $0.7 \pm 0.1\,\Omega\mathrm{cm}$, which already demonstrates the benefits of an SLM in electrode processing versus without an SLM, as was the case for Man-001, and shows the resistivity is of a similar magnitude as electrodes produced in Oxford with a lens immersed in oil [64].

5.3.3 Crossed Polariser Image Characterisation

Cross polarised images of Ox-001 were taken via methods described previously in Section 5.1. Unlike the previous cases the laser parameters were kept constant on this detector, so little can be inferred about the level of stress induced by the graphitic electrodes based on their processing parameters. Instead, these images highlight how much inherent stress is in the diamond sample, as a measure of its purity, and how the stress is distributed based on the cell geometry. For example, electrodes in the rectangular cells should be separated enough such that they induce stress only in the area surrounding the electrodes, $\mathrm{O}(10\,\mu\mathrm{m})$. On the other hand, the electrode separation is so low, thus the electrode density so high, that more stress should be induced in the hexagonal cells.

Figure 5.21 shows the cross polarised image for the full detector and highlights the three different cell geometries. Three outcomes are observed from this, the first of which is practically zero inherent stress in the diamond is seen. This is a high quality single crystal diamond, which implies there are very few impurities in the diamond, and there are no grain boundaries, unlike Goe-001. The presence of these defects is likely to cause some slight changes to the detector properties of the diamond, outlined in Chapter 2, and while such effects have not been properly quantified the quashing of such sources is preferable for diamond detectors.

The second outcome, a corollary of the first, is significantly less stress is observed in this detector versus Man-001. This is a consequence of a greater control on the graphitic electrode formation using an SLM, whereby the focal spot is much smaller and reduces the effect of “fringes” observed, presented in work by T. V. Kononenko

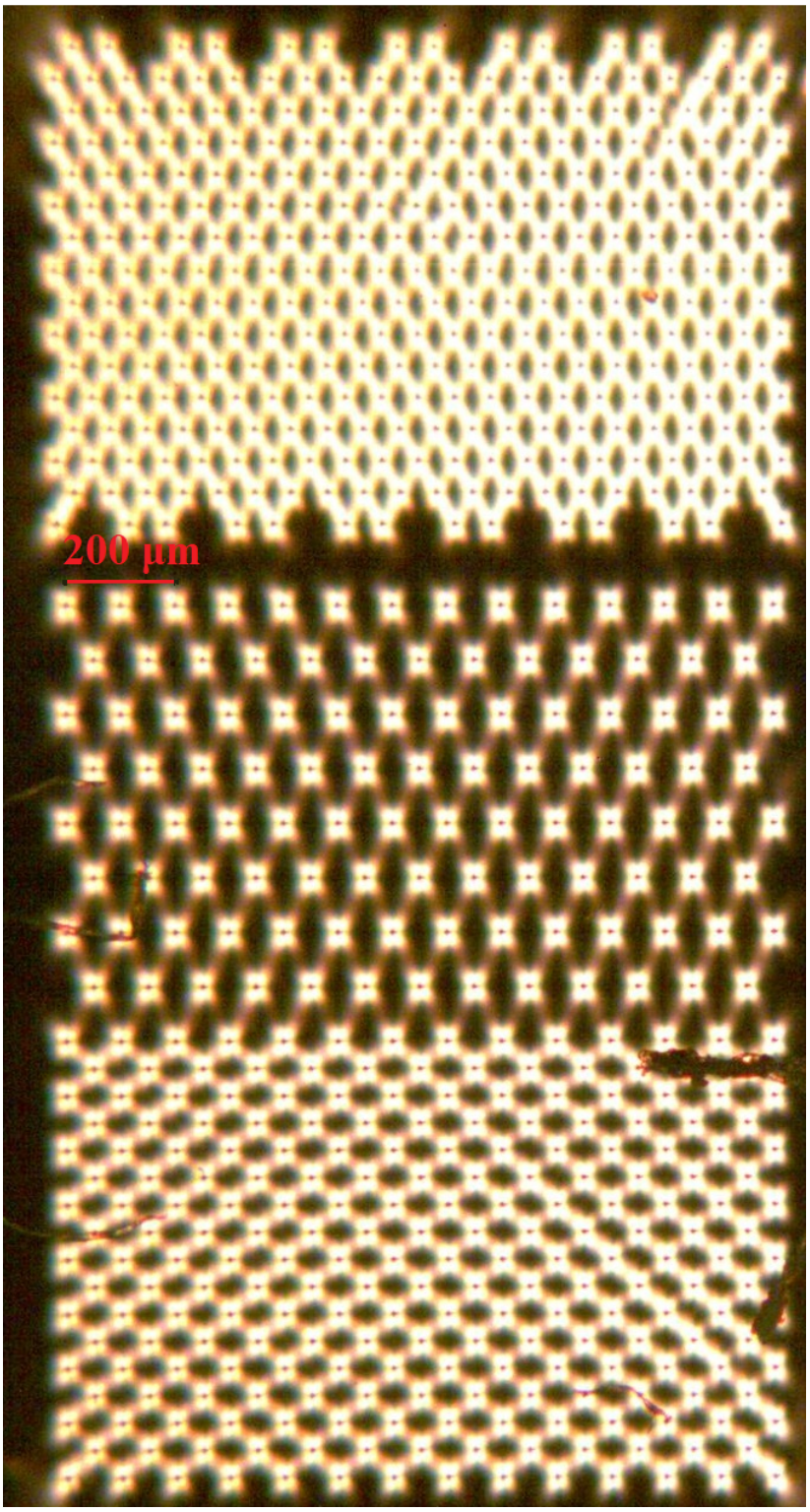

Figure 5.21: Crossed polariser images of Ox-001. The three arrays are from top to bottom: hexagonal cells, rectangular cells, and square cells. The lowest level of induced stress due to the graphitic electrodes is seen in the rectangular cells, while the highest level is observed in the hexagonal cells due to their different electrode separation. Some artefacts are apparent that obscure part of the image, particular in the square cell array.

et al. [53], which contributes to the induced stress. Inducing less stress is, once again, beneficial for diamond detectors, which demonstrates the need for electrode fabrication with an SLM.

The third outcome is the pattern of the induced stress in each of the three arrays. Figure 5.21 shows that there is some pattern in the induced stress for the rectangular cells, where induced stress from electrodes at the corner of a cell "connects" to the stress induced from the central electrode in a cell. While this level of stress is certainly low versus that induced by the electrodes, its presence and manifestation is not clear. One would naively assume that the pattern in induced stress would be due to the presence of the nearest neighbour electrodes, that is, between corner electrodes along one edge of a cell or between central electrodes. However, this is not the case in any of the three cell geometries[16], despite the fact that the minimum separation between two corner, and two central, electrodes in the rectangular geometry is 100 μm, versus 119 μm separation between a corner and a central electrode.

On the other hand, the pattern in the stress induced in the square arrays is identical to that seen previously, so the induced stress pattern is not linked to the use of an SLM. It is not likely that the resulting pattern arises from the crystal growth direction (thus crystal orientation), given that this pattern is observable in both single crystal (Detectors Man-001 and Ox-001) and polycrystalline diamond (Sample Goe-001). To rule out the crystal type and to determine the origin of this stress pattern, a finite element analysis is recommended, though this would require extensive work and is an area of future research.

5.3.4 SEM Characterisation

Although some benefit was observed in using an SLM in the crossed polariser image versus Man-001, it did not show anything unique to using an SLM. That is, greater control in the electrode formation is preferable, but using an SLM to fabricate electrodes at this size appears to be an inexpensive solution versus investment in higher quality optics, judging from the crossed polariser image. The effect of using an SLM

[16]Such effects can be observed in Man-001 and Goe-001, though this conclusion could not have been made at that time since the geometries were the same. Under the naive assumption, one could have argued stress due to nearest neighbours on the cell edge etc. were suppressed by the proximity of the central and corner electrodes.

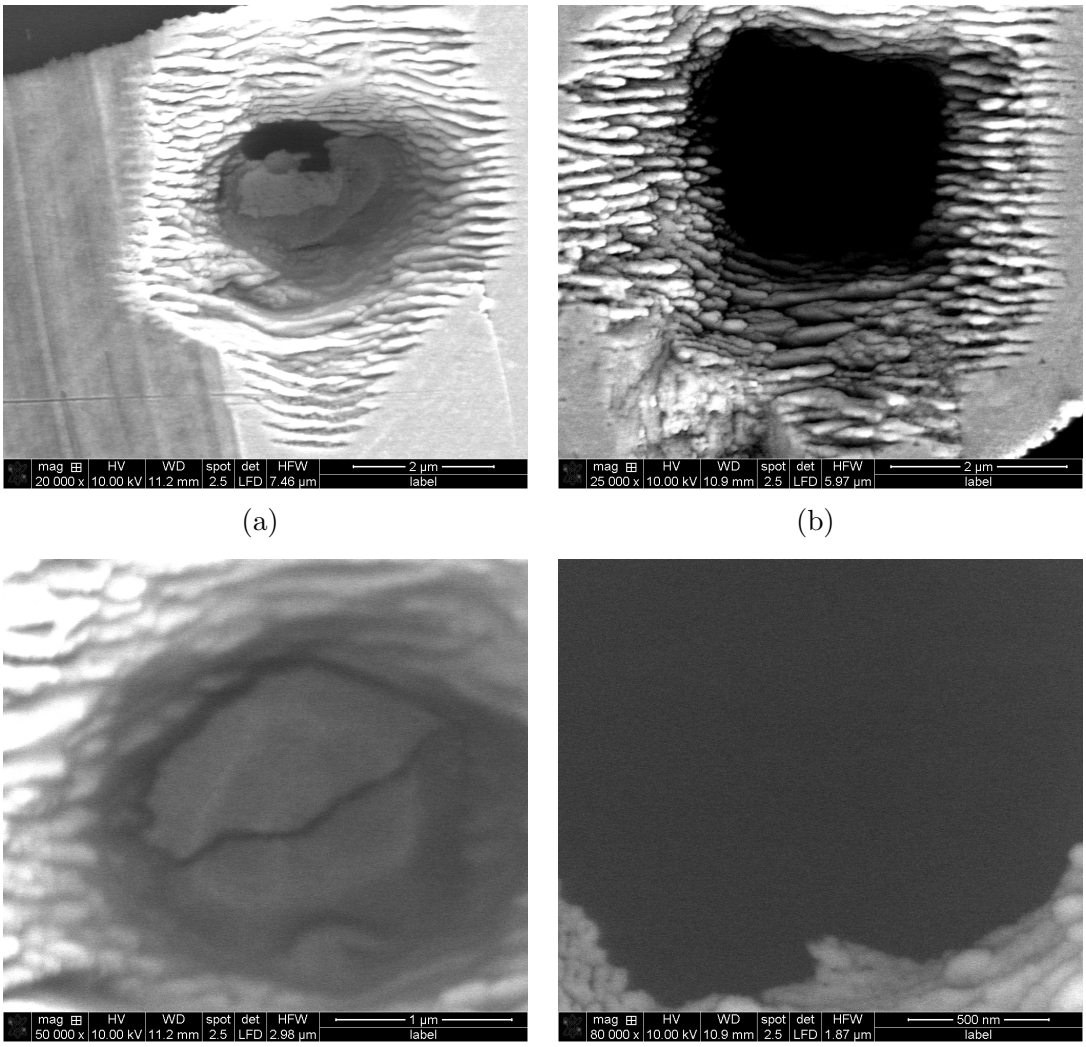

Figure 5.22: SEM images of Ox-001 as seen on (a) & (c) the seed side, and (b) & (d) the exit side. A fringe structure is observed on both sides. Structure is also observed on the seed side electrode itself, whereas there is no structure on the exit side electrode. Figures (c) and (d) show higher resolution images of (a) and (b) to image this structure (or lack thereof) further. Note that the electrode imaged in (a) and (b) is not the same as in (c) and (d).

should be observed in different characterisation methods, perhaps in particular from SEM images.

As was the case for the crossed polariser image, no variation in the fabrication parameters implies only a general comparison can be made between the morphology of the electrodes on this detector versus Man-001. Figures 5.22a and 5.22b show the seed and exit sides of an electrode on Ox-001, which highlight two crucial differences from the use of an SLM in electrode fabrication. The first difference is the structure of the electrode itself, where on the seed side, Figure 5.22a, the electrode morphology is

quite different. Man-001 revealed that slight removal of the surface layers was observed on the seed side, with only some observable structure, likely due to a low beam fluence used for the electrode fabrication, whereas Ox-001 does show observable structure, with significantly more material removal. This structure appears to be a combination of the upper surface of the electrode and the metallisation, and demonstrates that the use of an SLM allows finer control over the electrode formation, which might not be possible from improved optics alone. On the exit side, Figure 5.22b, there appears to be a significant amount of material removed from the upper layers of the diamond surface. This effect has been noted previously on Man-001.

The second, and arguably the most notable, difference is the presence of fringes on both the seed and exit sides of the electrode. Such fringes were not observed with Man-001, which implies this may only be observed through high quality optics or from the use of an SLM[17]. It is known that the beam diameter of the Oxford laser setup is of submicron precision. This is hard to achieve through optics alone, especially since the fringe width is $\mathrm{O}(129 \pm 10\,\mathrm{nm})$ thick, with a fringe spacing of $\mathrm{O}(178 \pm 10\,\mathrm{nm})$. The reason for the appearance of these fringes is presented later in this chapter in Section 5.4.

5.3.5 Raman Spectroscopy Characterisation

Examples of Raman spectra for Ox-001 are shown in Figures 5.23a and 5.23b, and these results highlight findings already presented for both Man-001 and Goe-001. For example, the diamond peak is more dominant on the exit side versus the seed side, and thus the diamond:graphite ratio is higher on the exit side. The average ratio is 16.3 ± 7.6 and 2.8 ± 1.3 on the exit and seed sides, respectively. These results are no better than the results from Goe-001[18], indicating no immediate improvement in using the SLM in terms of characterisation via Raman spectroscopy. The reason for this lack of improvement is uncertain. One possible explanation is that the reduced size of the focal spot, via the removal of aberrations, allows for finer control on the size

[17] One could argue slight fringe structure is observed in Man-001, but this is extremely hard to resolve when compared to the clarity on Ox-001.

[18] Figure 5.17 can be converted into pulse energy by dividing the pulse power by the repetition rate, 1 MHz, so the pulse energies effectively range from $0 - 150\,\mathrm{nJ}$. The translation speed is assumed to scale with repetition rate, so the speeds are 1000 times faster than speeds typical in Oxford, though this has not been definitively proven.

of the electrodes. This finer control also affects the processes that occur on the seed and exit side of the diamond. For example, there is less diamond material removed such that the diamond:graphite ratio is higher at this pulse energy and translation speed versus Goe-001. This is observed through the smaller structures seen in the SEM images. However, this can only be verified through a systematic study of the parameter space for electrode fabrication on the same diamond substrate and directly comparing electrodes fabricated with and without the use of an SLM.

It should also be noted that the optics used in the two setups are very different, implying an immediate "like for like" comparison for the same parameters is not trivial, and further prompts the need for further investigation. Nevertheless, the results for Ox-001 more closely resemble that of Goe-001 than Man-001. It is possible, therefore, that this is because the Raman measurements were taken prior to metallisation for both Goe-001 and Ox-001, while these measurements were taken after metallisation for Man-001. However, the effect of metallisation, and even the cleaning procedure outlined in Chapter 3, on the Raman spectra is not fully understand and warrants further research.

5.3.6 Detector Summary

In summary the use of an SLM has established an improvement in the resistivity of the electrodes versus previous laser setups, motivating the requirement for an SLM in the fabrication process. The electrode yield is also O(100%), which results from the improved focal spot. Crossed polariser images highlight that the level of induced stress is reduced as a direct result of smaller electrode sizes, and stress appears to be more easily induced in the diamond depending on the diamond's growth direction and crystal orientation, prompting further research. The SEM images have revealed visible structure on the seed and exit sides of the electrode, both in the electrode itself, in the case of the seed side, and surrounding the electrode. This visible structure appears to be from a process previously not seen/considered during electrode fabrication, and investigations into this structure are recommended. Finally Raman spectroscopy has shown no improvement in the diamond:graphite ratio of the electrodes, though this also prompts a larger study into the effect of the SLM on the characterisation of electrodes.

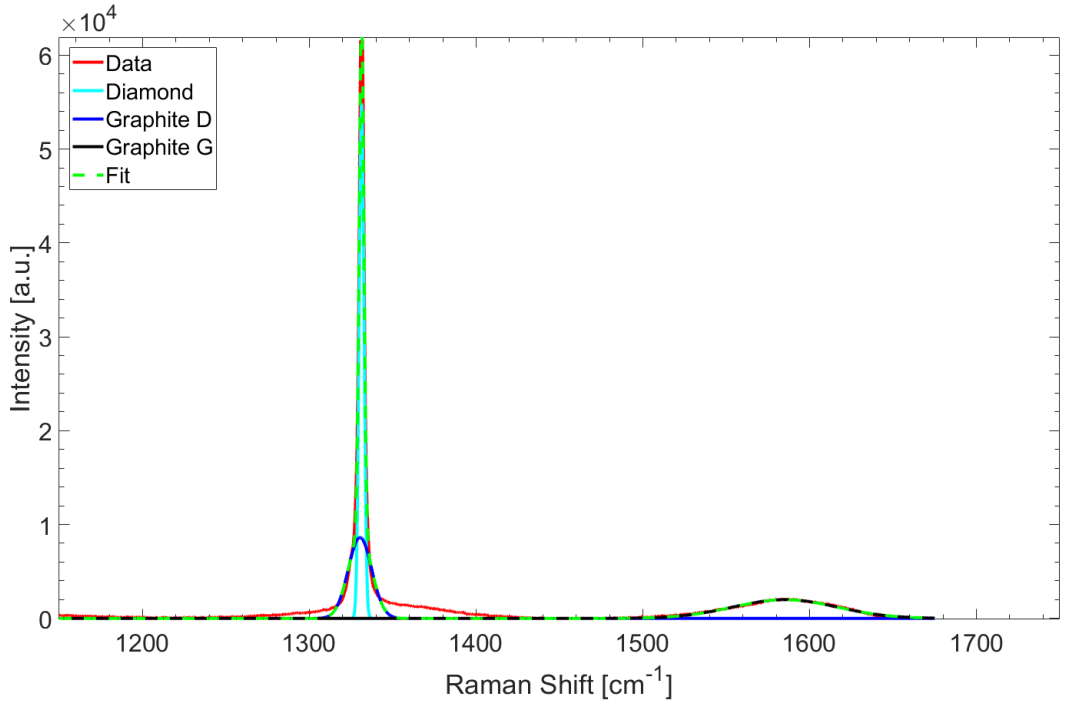

(a)

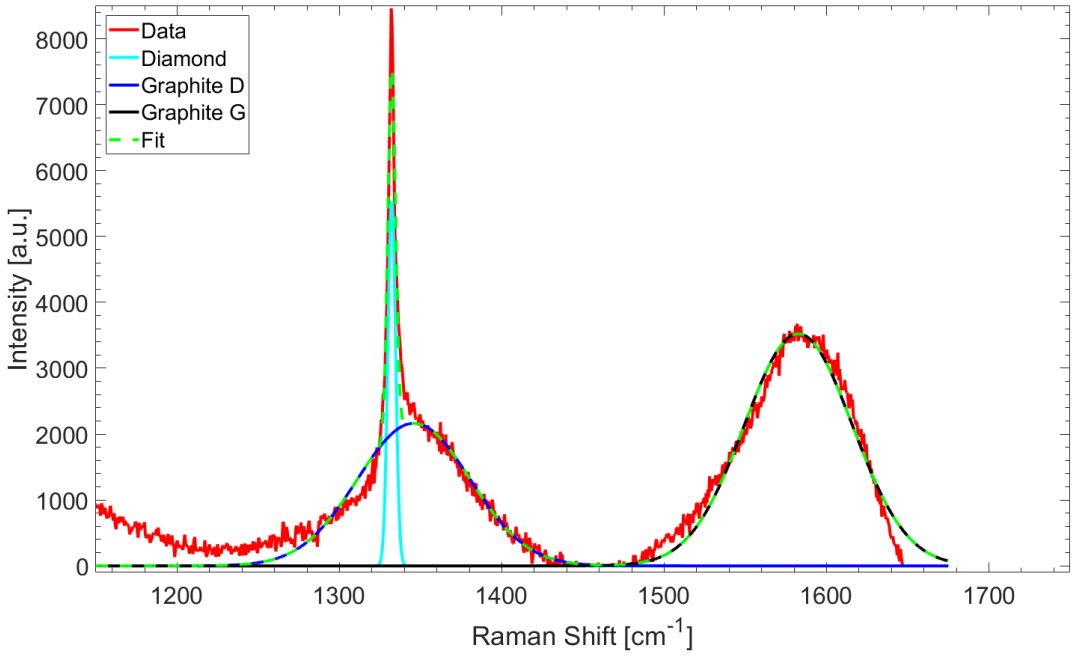

(b)

Figure 5.23: Raman spectra of Ox-001 taken on (a) the exit side, and (b) the seed side of the electrode. The graphite D peak is completely dominated by the diamond peak on the exit side, which explains the unusual fit.

5.4 Sample Ox-002

5.4.1 Motivation

Data taken on Man-001 and Ox-001 detectors have already shown some differences between fabricating graphitic electrodes with and without an SLM. However, the electrodes were fabricated with different optical setups, meaning it is difficult to disentangle the benefits of high quality optics versus the use of an SLM. This issue was apparent in the SEM characterisation of Ox-001. The parameter space used for electrode fabrication also differed between the two techniques, making it hard to observe the effect of the SLM, particularly in comparisons of Raman spectra between Ox-001 and Goe-001. Therefore, a study into the processing parameters for both fabrication techniques, with the same optical setup, is recommended to prove the usefulness of an SLM.

The aim of Ox-002 is to address these issues. Fabricating electrodes at the same processing parameters for both fabrication techniques provides insight into the effect of the SLM on electrode formation, which will demonstrate the need, or lack thereof, for an SLM for the future of 3D diamond detectors.

5.4.2 Sample Overview

Two diamond substrates (Ox-002a and Ox-002b) were used for these studies, both of which are optical grade single crystal diamonds, with dimensions $4 \times 4 \times 0.4\,\mathrm{mm}^3$ from IIa technologies [46]. The reason for this is to perform I-V and crossed polariser image characterisation on Ox-002a using the existing Man-001 mask design, while the other characterisation methods are performed on Ox-002b. While it is likely the two samples will differ, it is not expected to affect any of the characterisation except the cross polarised image characterisation[19].

It is expected that there will be significant impurities in these sample since it is not the highest quality diamond, which will affect the cross polarised image characterisation, as was observed in Goe-001. The objective used for these studies is a 0.75

[19]Due to the nature of the impurities it is impossible to obtain two diamond samples with the same level of impurities, and even more unlikely for both samples to have the same distribution in these impurities.

NA air lens, so it is expected that difference between the fabrication techniques may be great in parts due to the refractive index mismatch between the objective and the diamond. The setup otherwise remains unchanged from that described for Ox-001. A small range of beam energies, $100-600\,\text{nJ}$, and translation speeds, $10-30\,\mu\text{ms}^{-1}$, were used to minimise fabrication time, with several electrodes (≥ 5 and 3 for Ox-002a and Ox-002b, respectively) fabricated per parameter set. This is shown in Figures 5.24a and 5.24b, with all electrodes identified as fully penetrating the diamond bulk, as shown in Figure 5.24c. While the parameters probed are the same across the two samples, their configuration differs and so data from Ox-002a (the I-V and cross polarised image characterisation) is presented in Sections 5.4.3 and 5.4.4, while data from Ox-002b (the SEM and Raman spectroscopy characterisation) is presented in Sections 5.4.5 and 5.4.6.

5.4.3 I-V Curve Characterisation

The electrodes in the sample used for these measurements are arranged in the same form as Man-001 to save time and cost designing and purchasing a new mask for the structured metallisation. In this case four arrays were fabricated, where two arrays were devoted to the two fabrication techniques. Prior to the metallisation, images of the side profile of the electrode were taken for two different beam energies, shown in Figure 5.25. From this it is clear that a higher beam energy results in more graphitisation, or rather a more visible electrode, which is expected from previous measurements such as those taken for Goe-001. The most important observation is that this structure is not continuous. Instead, the electrode features a "tree-like" structure, which is also observed to some extent in reference [53], arising due to areas that undergo less graphitisation than others. This is likely due to a combination of thermal and nonthermal graphitisation processes, outlined in Chapter 3, in conjunction with the translation speed of the focal spot, the repetition rate of the laser pulses, and the beam energy. For example, this structure is expected to be more prevalent for a lower repetition rate since fewer pulses would imply less continuous structure, but the incident energy might still be enough to cause the thermal graphitisation process and exacerbate the tree structure. It has already been shown, for data taken with the Goe-001 sample,

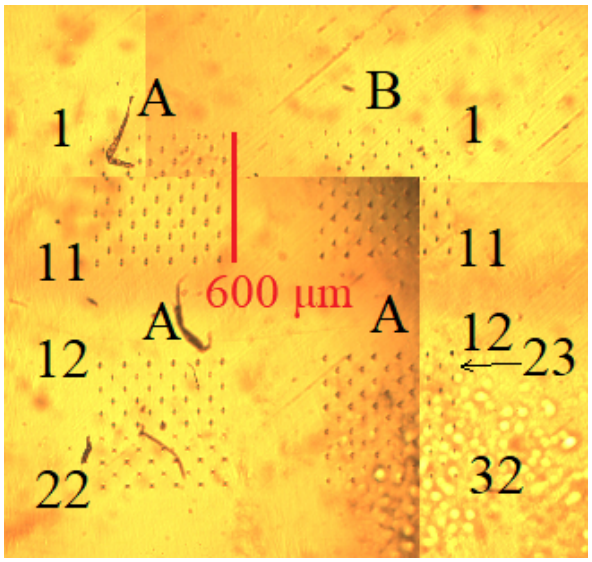

(a)

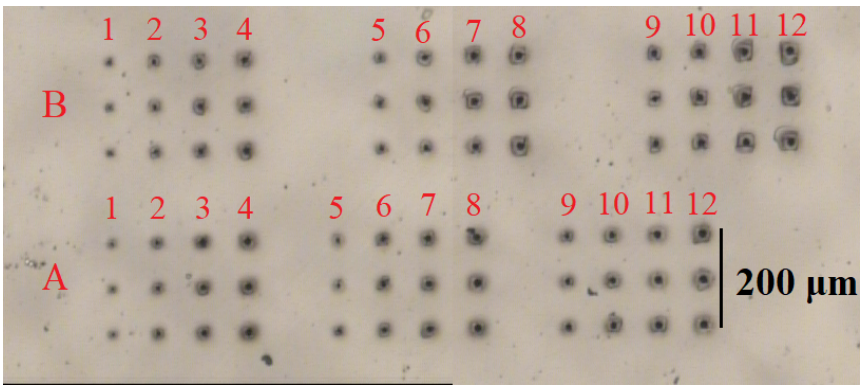

(b)

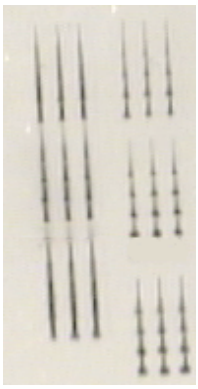

(c)

Figure 5.24: Optical images of (a) Ox-002a, as viewed from the exit side. (b) Ox-002b, as viewed from the exit side. (b) Ox-002b, as seen on exit side while titlted. All of the electrodes seem to penetrate the diamond bulk fully, as evidenced in (c). Arrays labelled "A" are those fabricated with an SLM, whereas arrays labelled "B" were fabricated without an SLM. The parameters are numbered to denote the parameters used in their fabrication. (1) 10 μms^{-1}, 100 nJ, (2) 10 μms^{-1}, 200 nJ, (3) 10 μms^{-1}, 300 nJ, (4) 10 μms^{-1}, 400 nJ, (5) 20 μms^{-1}, 200 nJ, (6) 20 μms^{-1}, 300 nJ, (7) 20 μms^{-1}, 400 nJ, (8) 20 μms^{-1}, 500 nJ, (9) 30 μms^{-1}, 300 nJ, (10) 30 μms^{-1}, 400 nJ, (11) 30 μms^{-1}, 500 nJ, (12) 30 μms^{-1}, 600 nJ, (13) 0.8 NA oil lens, 15 μms^{-1}, 60 nJ, (14) 0.8 NA oil lens, 15 μms^{-1}, 100 nJ, (15) 0.8 NA oil lens, 15 μms^{-1}, 20 nJ, (16) 0.8 NA oil lens, 30 μms^{-1}, 100 nJ, (17) 0.8 NA oil lens, 30 μms^{-1}, 200 nJ, (18) 0.5 NA air lens, 10 μms^{-1}, 60 nJ, (19) 0.5 NA air lens, 10 μms^{-1}, 100 nJ, (19) 0.5 NA air lens, 10 μms^{-1}, 200 nJ, (21) 0.5 NA air lens, 30 μms^{-1}, 100 nJ, (22) 0.5 NA air lens, 30 μms^{-1}, 200 nJ, (23) 2 passes of the focal spot, 10 μms^{-1}, 200 nJ, (24) 3 passes of the focal spot, 10 μms^{-1}, 200 nJ, (25) 2 passes of the focal spot, 30 μms^{-1}, 400 nJ, (26) 3 passes of the focal spot, 10 μms^{-1}, 200 nJ, (27) 5 μms^{-1}, 100 nJ, (28) 5 μms^{-1}, 200 nJ, (29) Area graphitised, sampled flipped and a second pass of the focal spot, 10 μms^{-1}, 100 nJ, (30) Area graphitised, sampled flipped and a second pass of the focal spot, 10 μms^{-1}, 200 nJ, (31) Circularly polarised beam, 10 μms^{-1}, 100 nJ, (32) Circularly polarised beam, 10 μms^{-1}, 200 nJ.

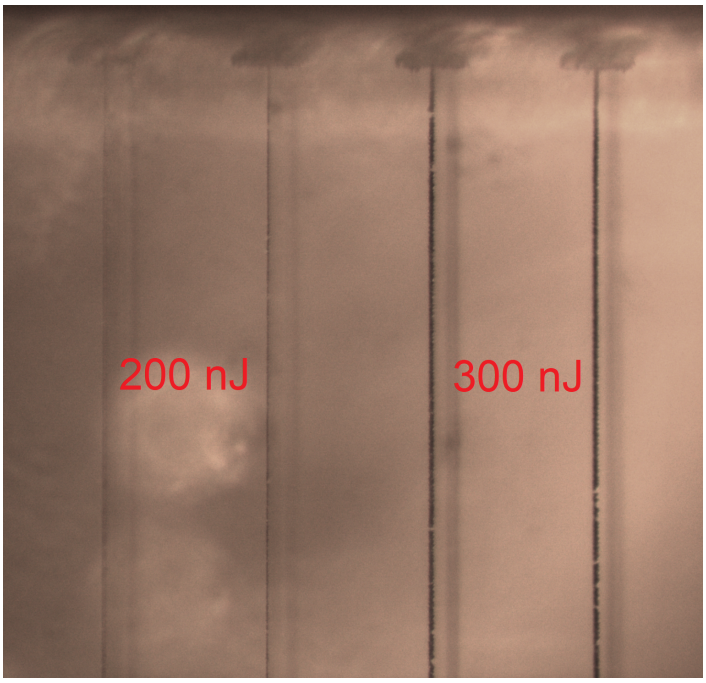

Figure 5.25: Side view of electrode formation for Ox-002a, highlighting discontinuous structure in the electrode. The two left electrodes were fabricated with a beam power of 200 nJ, while the two right electrodes were fabricated at 300 nJ.

that the repetition rate and translation speed scale with each other, so a similar argument is made for the translation speed. In this case, it is suspected (stated without proof here, though discussed later in this chapter) that the slower translation speed works against the pressure build-up from the formation of graphite, which could result in less continuous structure, arising from the nonthermal graphitisation process, but also exacerbates the thermal graphitisation process. The effect of the beam energy has been shown to form more graphite, and for the same translation speed and repetition rate it is likely to increase the structure size arising from thermal graphitisation.

Measurements of the I-V curves for the graphitic electrodes were taken using a Keithley 2410 SourceMeter [78], in the same process as outlined for Man-001. While some of the electrodes exhibited an ohmic response, with an example shown in Figure 5.26a, the majority exhibited a non-ohmic response, with an example shown in Figure 5.26b, whereby some "barrier potential" must be applied in order for a response to be observed. The reason for this is likely related to the formation of graphite in the bulk. For example, electrodes showing a completely continuous region of graphite are expected to be completely conductive, and thus show an ohmic response, whereas electrodes that exhibit the tree-like structure have more non-conductive (diamond)

material and so the response is non-trivial. Exactly how these two electrode types respond to particle beams is an area of future research.

A new method for determining the barrier potential and resistance of both electrode types was devised, given the large percentage of electrodes showing a non-ohmic response. In both types the non-linearity intercept, U_ϕ, which is related to the barrier potential, is defined as the point where the linear (ohmic) region intercepts with the zero current line (i.e. the line current = 0.0 mA), as shown in Figure 5.27a. For these calculations this is performed for both ohmic regions, that is, the positive and negative bias polarities, and an average is taken. This non-linearity intercept is zero by definition for ohmic electrodes, and for non-ohmic electrodes that do not exhibit an ohmic region at any bias voltage, the barrier potential is set to be beyond the measurement range, that is, 999 V. The resistance is defined in the usual way, except for non-ohmic electrodes the resistance is the average of the result from each slope, as demonstrated in Figure 5.27b. If no conductive region is observed, then the resistance is set to be beyond the measurement range, that is, 999 MΩ.

The measurements of the non-linearity intercept and resistance versus beam energy using the SLM are shown in Figures 5.28a and 5.28b, respectively. In each of the plots, the lowest beam energy in each parameter set was omitted (i.e. 100 nJ at 10 μms^{-1}, 200 nJ at 20 μms^{-1}, 300 nJ at 30 μms^{-1}), since both the barrier potential and resistance were beyond the measurement range. This indicates that low beam energies are not preferential, and in fact as the translation speed increases the beam energy must also increase. This is because there are fewer beam pulses at a given position inside the diamond substrate at higher translation speeds versus lower translation speeds, resulting in lower energy deposition at that position. This would cause lower levels of graphite formation, necessitating higher beam energy at higher translation speeds.

There are two important ramifications from the measurements of the non-linearity intercept, as shown in Figure 5.28a. The first is that for a given beam energy, this intercept is proportional to the translation speed, which is somewhat intuitive. For example, if the translation speed is too fast then less graphite forms, since the speed is too fast to form at least a continuous region of graphite and potentially too fast to form the fringes of the tree-like structure, meaning a larger bias voltage must be applied before the region becomes completely conductive. This is why this intercept

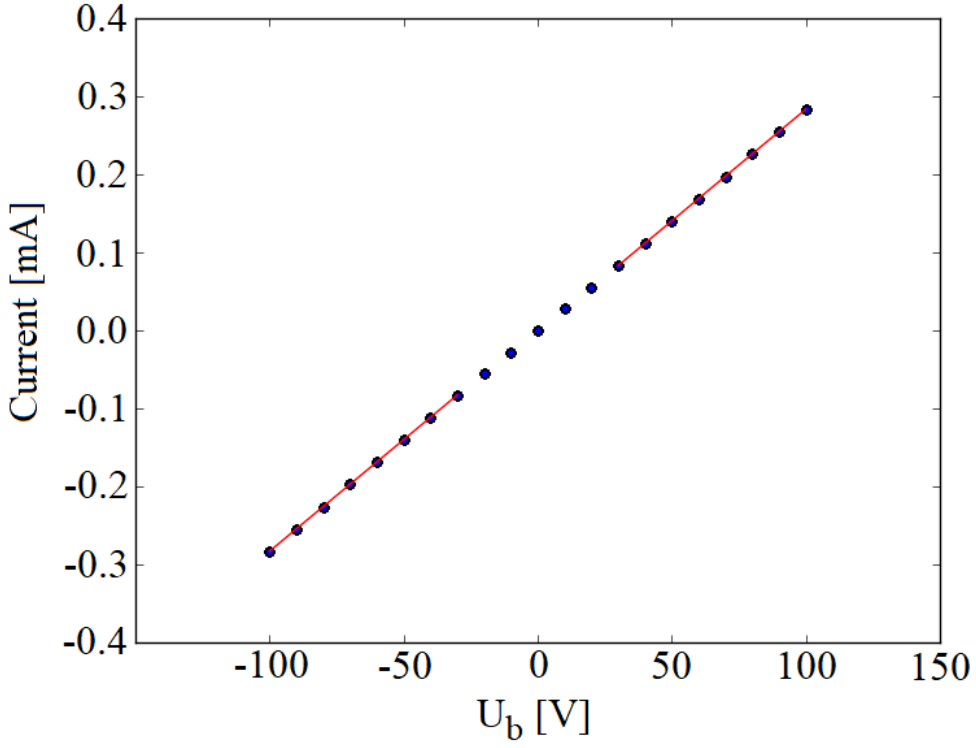

(a)

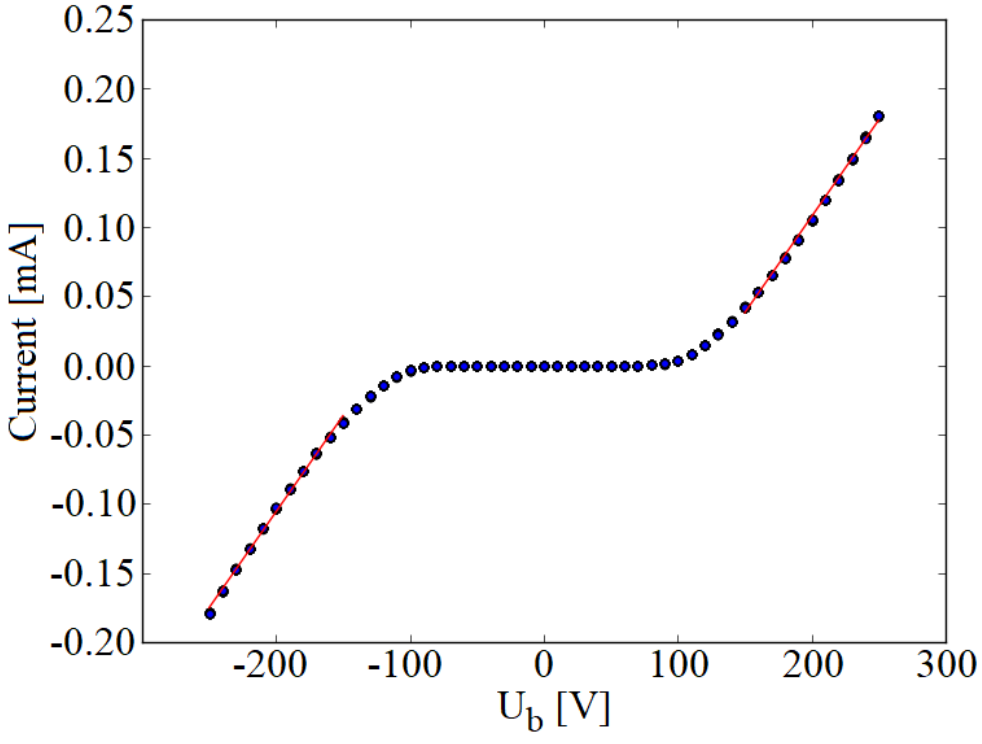

(b)

Figure 5.26: Examples of I-V curves for Ox-002a showing (a) an ohmic and (b) a non-ohmic response. The red lines are examples of how the resistance of the electrodes is measured in each case, which is explained in the main text. Figures (a) and (b) are both preliminary and are taken from reference [83].

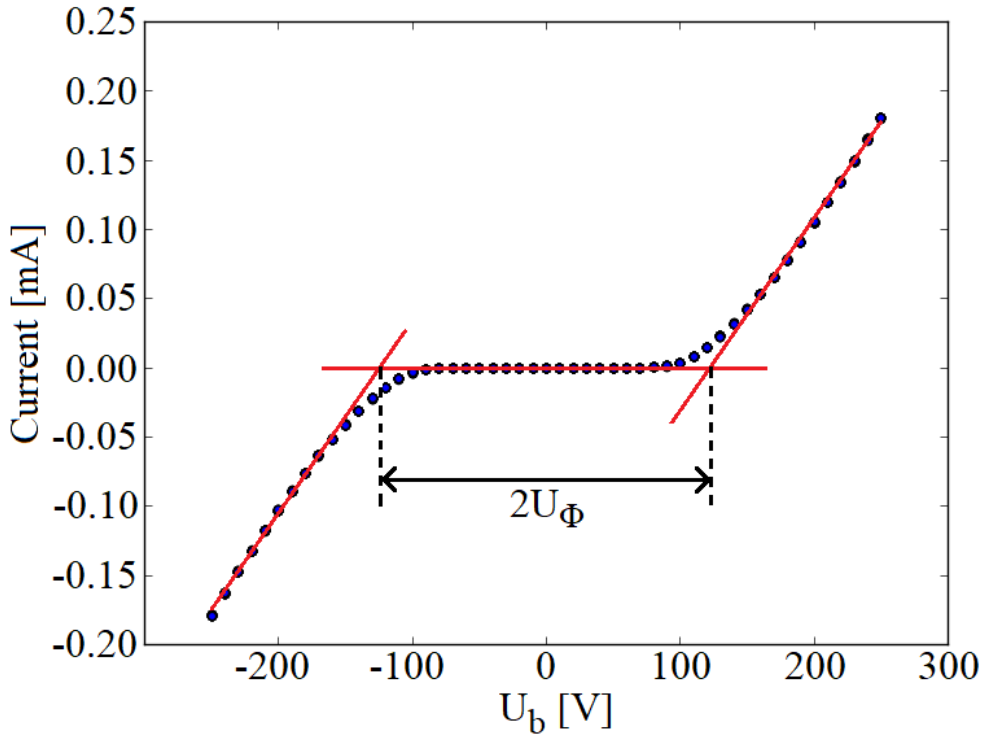

(a)

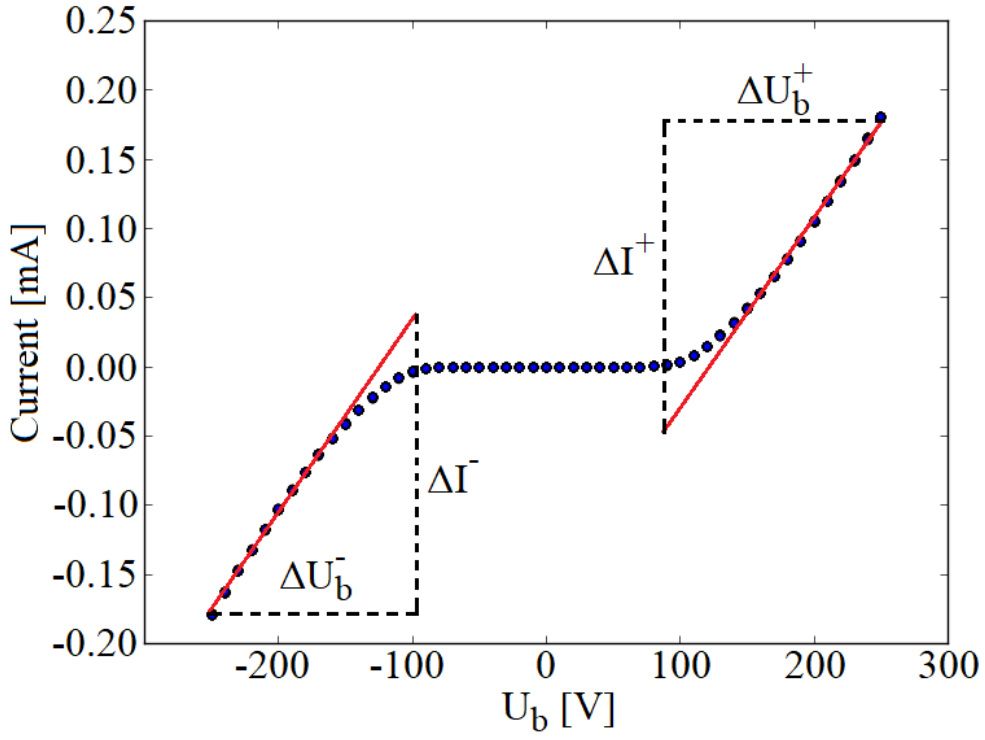

(b)

Figure 5.27: Demonstrations of the calculation of (a) the non-linearity intercept, and (b) the resistance for Ox-002a. Figures (a) and (b) are both preliminary and are taken from reference [83].

is likely related to some barrier potential for the electrodes.

The second ramification is that for a translation speeds less than $30\,\mu\text{ms}^{-1}$, there appears to exist a beam energy at which the electrodes are likely to be ohmic, whereby the non-linearity intercept approaches or equals zero. Although one could potentially fabricate ohmic electrodes at lower translation speeds, thus reducing their size and increasing the active detector area, this effect is counteracted by the fact that the fabrication process is expensive. As such, it is preferable to fabricate devices quickly with good electrical properties, at the cost of a slight increase to electrode size, which is feasible from Figure 5.28a. This fact, combined with the corollary that a higher translation speed requires a higher beam energy to lower the intercept, re-iterates observations seen for Goe-001, where high beam energy and high translation speeds are recommended for electrode formation[20].

The measurements of the resistance, presented in Figure 5.28b, shows a similar result to the non-linearity intercept, whereby the resistance is lowered as the beam energy increases. Although the results for the translation speeds are consistent at $10\,\mu\text{ms}^{-1}$ and $20\,\mu\text{ms}^{-1}$, these results also show that higher beam energies and translation speeds are recommended for electrode fabrication, and that slower speeds appear to hinder the formation of conductive material (an explanation of this is offered later in the chapter). It is not known exactly why measurements of the resistance and non-linearity intercept do not tend towards zero at $30\,\mu\text{ms}^{-1}$, though it is possible that this is an upper limit on the translation speed for electrode fabrication with a 1 kHz repetition rate. Extending this systematic further is the only way to identify whether such a limit exists.

A comparison of these two measurements for electrodes fabricated with and without an SLM are shown in Figure 5.29. This result readily shows that not only does a higher beam energy result in a lower non-linearity intercept and resistance for a given translation speed, as demonstrated previously, but the use of an SLM significantly reduces these measurements more than is possible by simply increasing the processing parameters. This is the first clear evidence that the use of an SLM is valuable for electrode fabrication in diamond.

[20]There is an upper limit on the beam energy, at which point the diamond is likely ablated, and the translation speed, at which point there is not enough energy deposition for graphitisation to occur. The exact limits on these parameters remains a future area of research.

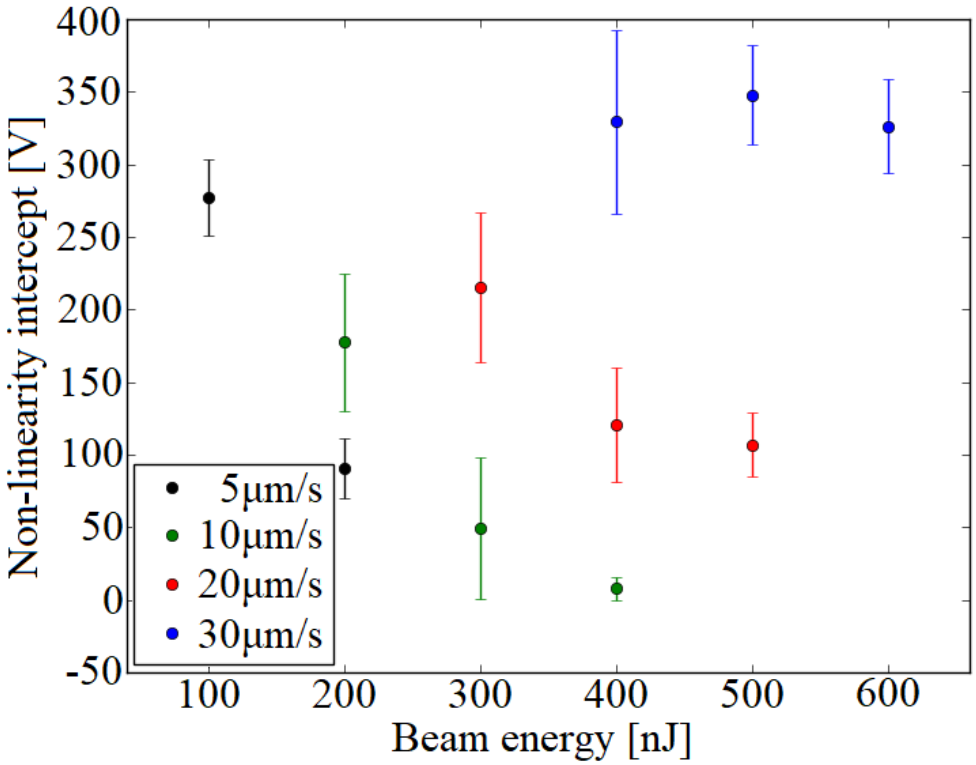

(a)

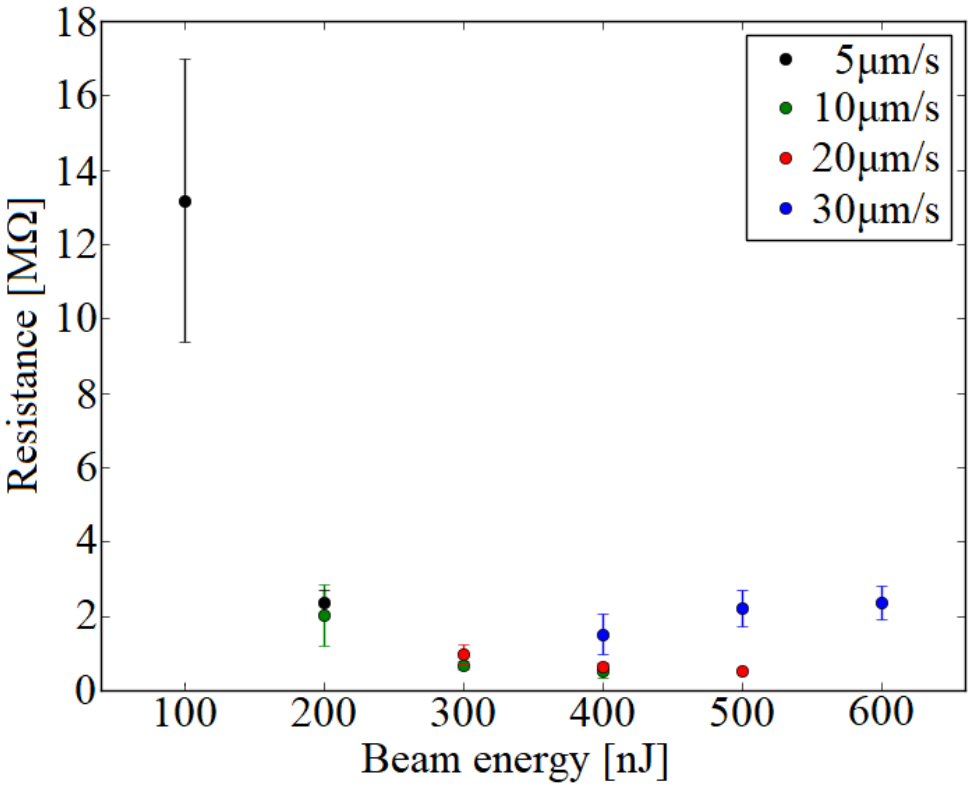

(b)

Figure 5.28: Results for (a) the barrier potential, and (b) the resistance for SLM-fabricated electrodes for Ox-002a. Figures (a) and (b) are both preliminary and are taken from reference [83].

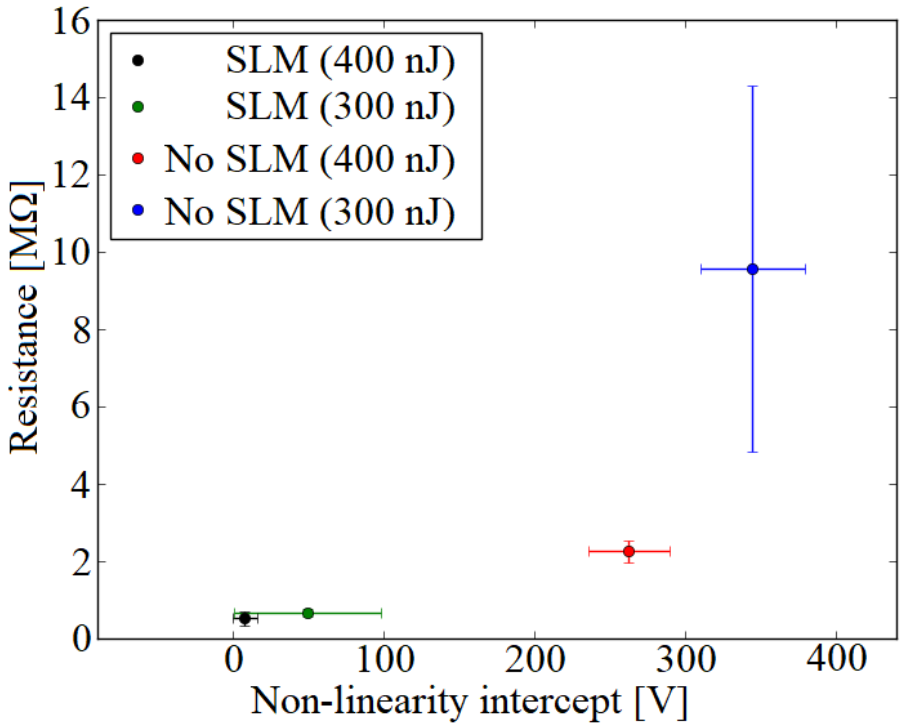

Figure 5.29: A comparison of the measured resistance and barrier potential for both SLM and non-SLM fabricated electrodes. The translation speed of the electrodes is $10\,\mu\text{ms}^{-1}$. This figure is preliminary and is taken from reference [83].

5.4.4 Crossed Polariser Image Characterisation

Crossed polariser images were taken on Ox-002a before (Figure 5.30a) and after (Figure 5.30b) electrode formation. The immediate outcome of these images is the level of inherent stress in the diamond sample due to impurities. This is unsurprising, given that the diamond is optical grade rather than electronic grade. This outcome was also seen in previous diamond samples (particularly Goe-001), and the level of impurities in these samples dominates the stress induced by the presence of the graphitic electrodes[21]. Collecting images before and after processing allows for a qualitative discussion of the effect of the electrodes on the induced stress, though even this is somewhat limited if the light intensity in the two images is not the same. In such cases, the effects of the impurities and the electrodes, at a qualitative level, cannot be disentangled. However, it is possible to isolate the effect of the electrodes to some extent via a series of steps, which are outlined below.

[21] Only Ox-002a definitively demonstrates this, given that no crossed polariser images were taken for Goe-001.

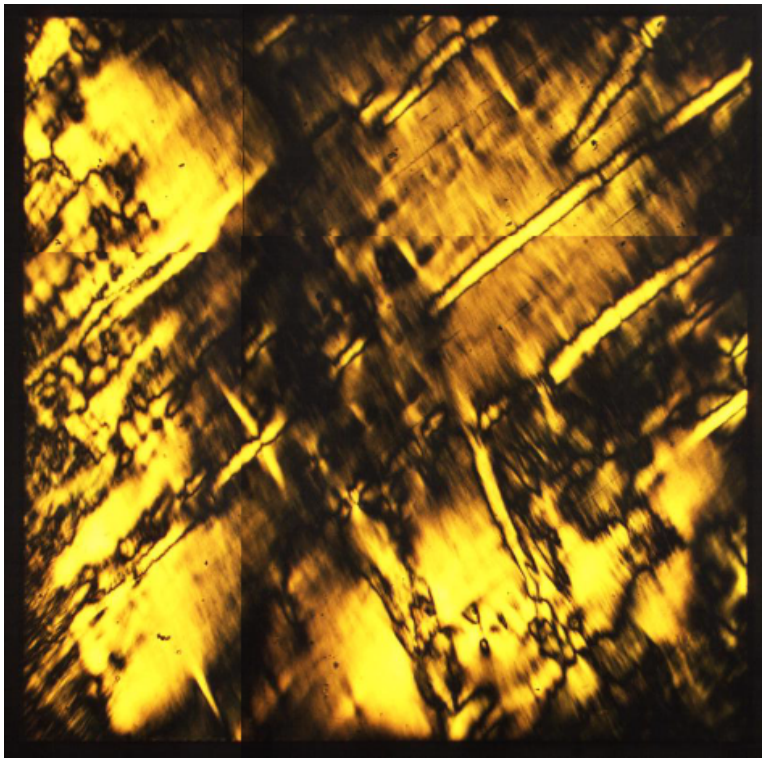

(a)

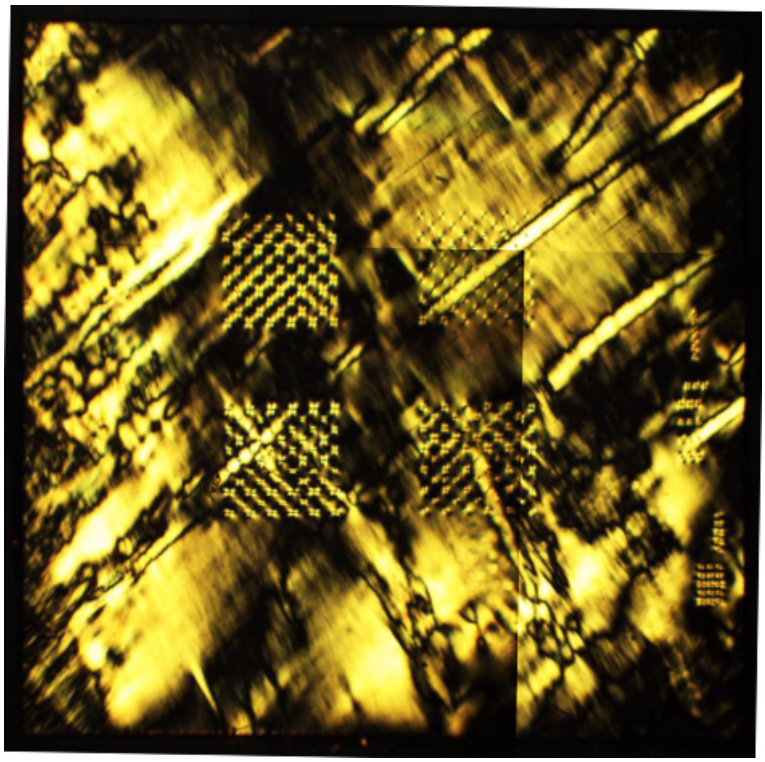

(b)

Figure 5.30: Crossed polariser images of Ox-002a taken (a) before and (b) after electrode formation. The structure on the right hand side in (b) are graphitisation trials.

The ultimate aim of these series of steps is to subtract the image prior to electrode formation (the "before" image) from the image after electrode formation (the "after" image), resulting in a "difference" image, whereby the first step is to correct for the difference in the alignment of the images. For an accurate difference image, the locations of the same pixels in the before and after images must match. This pixel-by-pixel alignment is done manually and requires a correction for the tilt between the two images, and subsequent translational alignment of the two images. For the angular alignment, similar segments are chosen (e.g. the corners of the images of the sample), the angles are calculated, and the after image is then rotated to match the before image. Similarly, the translational alignment involves a comparison of similar locations and manipulating the after image such that the pixel locations match exactly. This process is repeated for each of the four images taken for the sample (visible in Figures 5.30a and 5.30b). The accuracy of these steps is approximately a few pixels, so for an image size of O(1000) pixels, an error of 1% is assigned to this step[22].

The second step is a correction for the light intensity difference between the two images. Choosing the exact same light intensity for the images, while this would be ideal, is not practical. Instead, the histograms of the red, blue, and green ("RGB") colours in the before image are mapped to the after image. This is performed by reading the two images into MATLAB [76], and the RGB histograms of the before image are mapped to the after image via the "imhistmatch" function. The result of this operation is shown in Figure 5.31, where the output (Figure 5.31b) closely resembles the after image (Figure 5.31c). It should be noted that while this method gives an overall contrast and brightness adjustment of the images, it cannot completely account for the light intensity. That is, some of the structure observed under crossed polarisers may only be visible under high light intensities. The success of this step for image subtraction is, therefore, dependent on how different the light intensities are in the two images. However, this method will never give an exact match between the two images, given that the presence of electrodes in the after image will slightly distort the RGB histograms. Due to this, the accuracy of this step is estimated to be O(1%)[23].

[22]That is, when comparing the location of structure between the two images, it is unlikely that the structures will be more than 10 pixels apart as this would be recognised by eye.

[23]In a similar manner for the alignment correction, a larger uncertainty of the histograms would result in visibly distinct images. This uncertainty is an order of magnitude estimate.

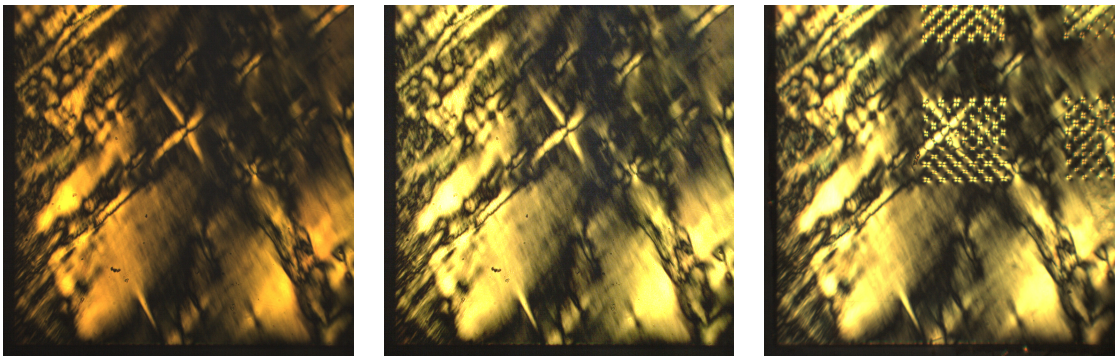

(a) (b) (c)

Figure 5.31: Crossed polariser images of one corner of Ox-002a taken (a) before electrode formation and before intensity mapping, (b) before electrode formation and after intensity mapping, and (c) after electrode formation.

The final step is then the subtraction of the intensity-mapped image from the after image. Once again, this is performed using MATLAB [76] using the "imabsdiff" function, with the final difference image of the entire sample shown in Figure 5.32. Qualitatively, the subtraction exhibits very few artefacts, especially in the top left array. However, the subtraction is not perfect due to the presence in the electrode (mentioned previously), which results in dark but not black areas[24]. The most prominent artefact, however, are the dark blue regions that result from an imperfect subtraction of the inherent stress in the sample. Such regions may impact on the quantitative analysis (discussed later in this chapter).

Qualitatively comparing the parameters provides an insight into the effect of the parameters, specifically the effect of the SLM. For example, comparing the top two arrays in Figure 5.32 shows that the stress induced by electrodes in the left array (using the SLM) is higher than that in the right array (without an SLM), which seems counter-intuitive (and an undesirable outcome). However, these electrodes were fabricated with the same beam energy and translation speed, which means the energy density for the SLM-fabricated electrode is significantly higher (as explained previously in Section 5.3). This, in conjunction with the I-V measurements taken in the previous section, implies more graphite forms using the SLM.

One other visible effect from the parameters from the top two arrays is that stress

[24]Completely black areas (i.e. with an RGB value of (0,0,0)) would be expected for two pixels with the exact same RGB content.

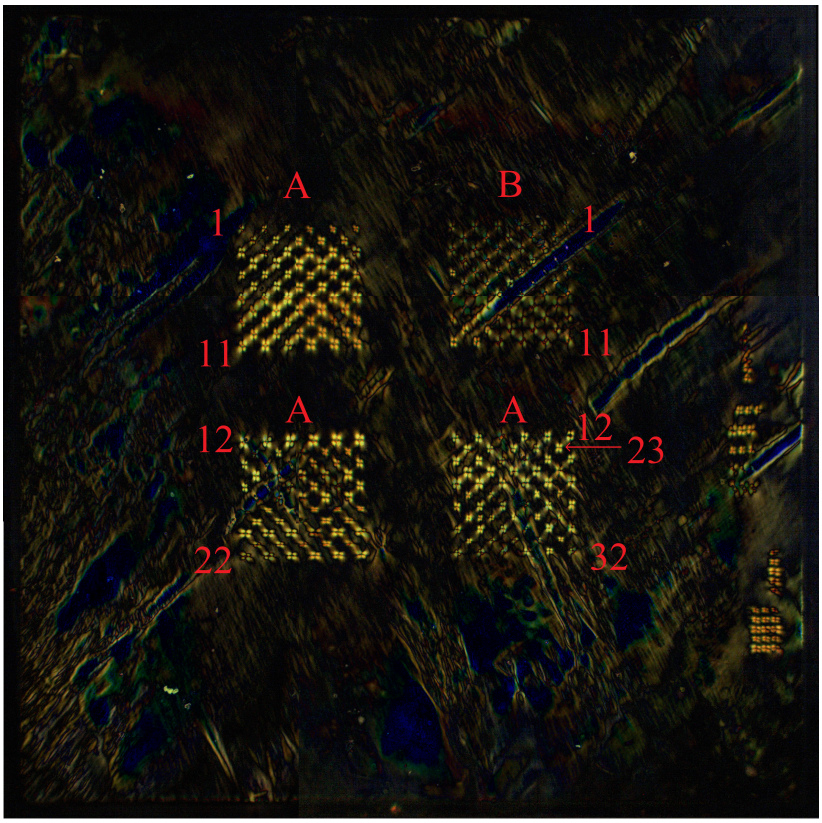

Figure 5.32: Difference image from crossed polariser images for Ox-002a. The same electrode labelling is used here as for Figure 5.24.

increases with increasing beam energy. Given there is a threshold for electrode formation (discussed in more detail in Section 5.1), this implies more graphite forms as the beam energy increases, since a greater fraction of the beam width is above the threshold. However, it is unclear (qualitatively) exactly how the translation speed affects the induced stress, though the effect from the translation speed appears to be dominated by the beam energy. These effects will be disentangled via quantitative measurements of the stress later in the chapter.

Although electrodes fabricated with different NA lenses and beam polarisation states are not present on Ox-002b, they are discussed in reference [83] and offer insight into the optimisation of the electrode fabrication process, so these effects are also discussed. Comparing the bottom two arrays in Figure 5.32 also shows the effect of other parameters. For example, the bottom five rows of electrodes in the bottom left array were made with a lower NA lens (0.5) versus all the other electrodes (0.8). A lower NA lens results in a wider field of view and subsequently a less focused focal spot. This results in a larger area of graphite, though only in cases where the energy

density is significantly higher than the graphitisation threshold. However, the fact the stress appears to only widen is not clear.

The final observation to be made from these images is the effect of a circularly polarised beam on the stress induced by the electrodes (the bottom two rows on the bottom right array). Comparing these with other electrodes, specifically the top two rows of the top left array, shows that the stress induced appears to be less, despite resulting in more conductive material (evidenced in results presented in reference [83]). This is a crucial outcome for the formation of graphitic electrodes in diamond, which would require confirmation by some form of quantitative analysis, which is presented in the next section.

Quantitative Analysis of Crossed Polariser Images

The analysis of the images is performed in a similar manner as that demonstrated in Section 5.2.3, whereby regions of electrodes with the same beam energy and translation speed are selected. The number of electrodes per parameter set varies (either 5 or 6 electrodes), so a continuous region of 5 electrodes is selected in all cases to prevent any introduction of bias to the measurements. Similarly, a fixed region is used for each parameter set. For these measurements, the same luminosity formula presented in Section 5.2.3 is used, and histograms of the pixel luminance are drawn. However, the threshold is set to 100 as the basis of comparison since the luminance of the non-SLM fabricated electrodes is very low such that the previous threshold (200) yields zero counts for the electrodes fabricated at $10\,\mu\text{ms}^{-1}$.

The effect of the SLM on the relative stress is shown in Figure 5.33, which confirms the qualitative observations stated in the previous section, and that the SLM induces more stress due to more graphite formation. It is apparent that induced stress greatly increases with beam energy for the SLM-fabricated electrodes versus the non-SLM fabricated electrodes. This is because the energy density is higher than the graphitisation threshold for the SLM electrodes, whereas the energy density is close to this threshold for the non-SLM electrodes. This, in combination with the translation speed, implies the formation of electrodes without the use of an SLM is somewhat disfavoured (an explanation of this is offered both later in this section and in Section 5.3), and so the effects of the processing parameters are lessened. It should also be noted that there is a

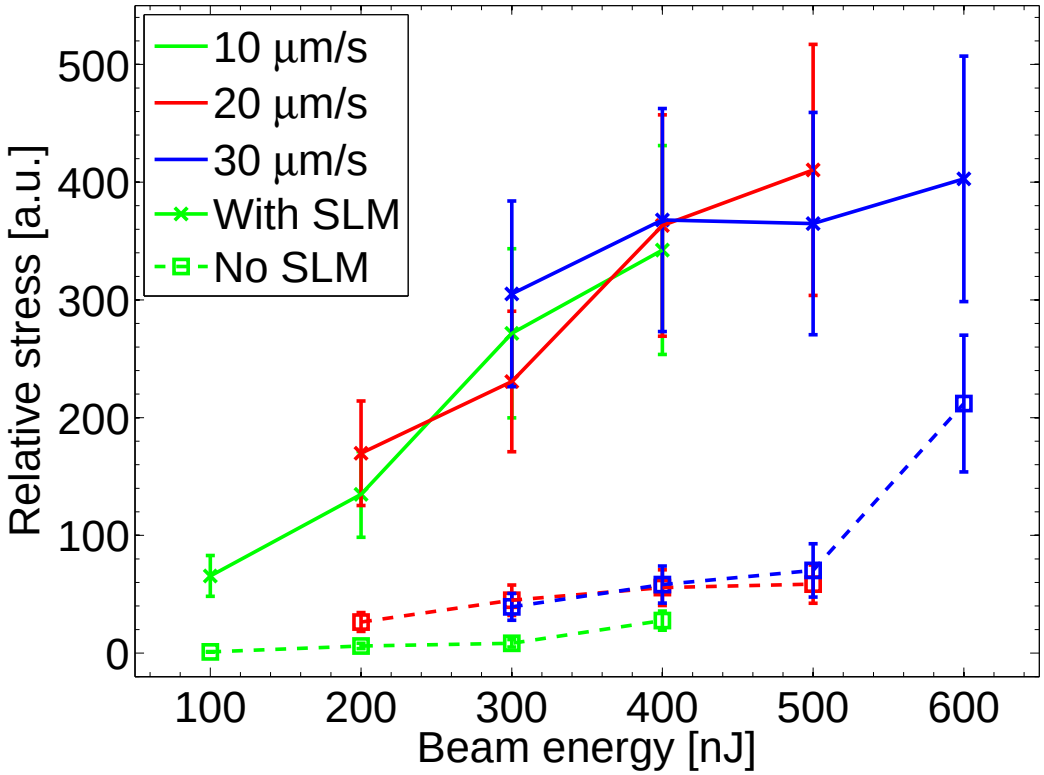

Figure 5.33: The effect of using an SLM on the stress induced in diamond. The stress is relative to the stress induced by the non-SLM fabricated electrodes with a beam energy of 100 nJ and a translation speed of 10 μms^{-1}.

significantly lower effect on the relative stress due to the translation speed, given that the values are largely consistent, versus the effect due to the beam energy. As such, this shows the translation speed is a secondary effect on the relative stress, and thus electrode formation, and for the range of speeds probed in this study, faster speeds are preferable to decrease the fabrication time.

The errors on the relative values were deduced from the standard deviation in the counts above threshold for each electrode in a given parameter set. This value, therefore, accounts for the repeatability of the electrode formation, as well as the effect of an imperfect subtraction of the before and after images. The effect of the rotational and translational alignment of the before and after images has not been included in the error analysis due to the complexity of calculating these values, and any estimation of these errors is somewhat arbitrary.

The effect due to different NA lenses on the induced stress is shown in Figure 5.34. These results also agree with the qualitative discussion in the previous section, and demonstrate a higher NA lens is recommended for electrode fabrication to minimise

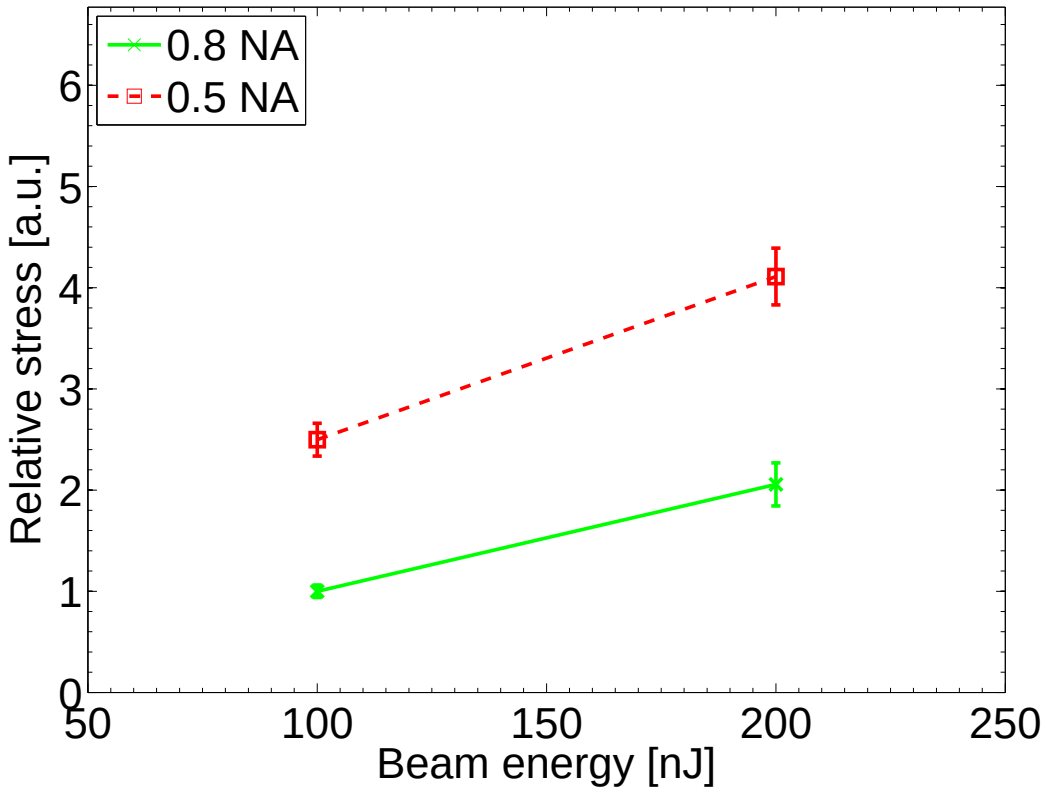

Figure 5.34: The effect of using a 0.5 NA lens (red) and 0.8 NA lens (green) on the stress induced in diamond. The electrodes were all fabricated using an SLM. The stress is relative to the stress induced by the SLM-fabricated electrodes with a beam energy of 100 nJ, a translation speed of 10 μms^{-1}, and a 0.8 NA lens.

the level of stress induced with diamond. One reason for the discrepancy is a slight corollary of the reason previously given; for a higher NA lens, the field of view is smaller and results in a highly focused focal spot, thus the energy density is higher than a lower NA lens. It has been shown previously that discontinuities exist within the graphitic electrodes, and it is likely that a higher energy density minimises this effect through a higher conversion percentage of diamond to graphite. This can be truly confirmed only through the use of modelling software, which is a project beyond the scope of this thesis.

Finally, the effect due to linearly and circularly polarised beams on the induced stress is shown in Figure 5.35. The reason why circular polarisation results in lower stress is not fully understood, given it results in higher conductivity electrodes [83]. It is possible that the interaction of the circularly polarised beam with diamond is significantly different than a linearly polarised beam, but how this manifests in terms

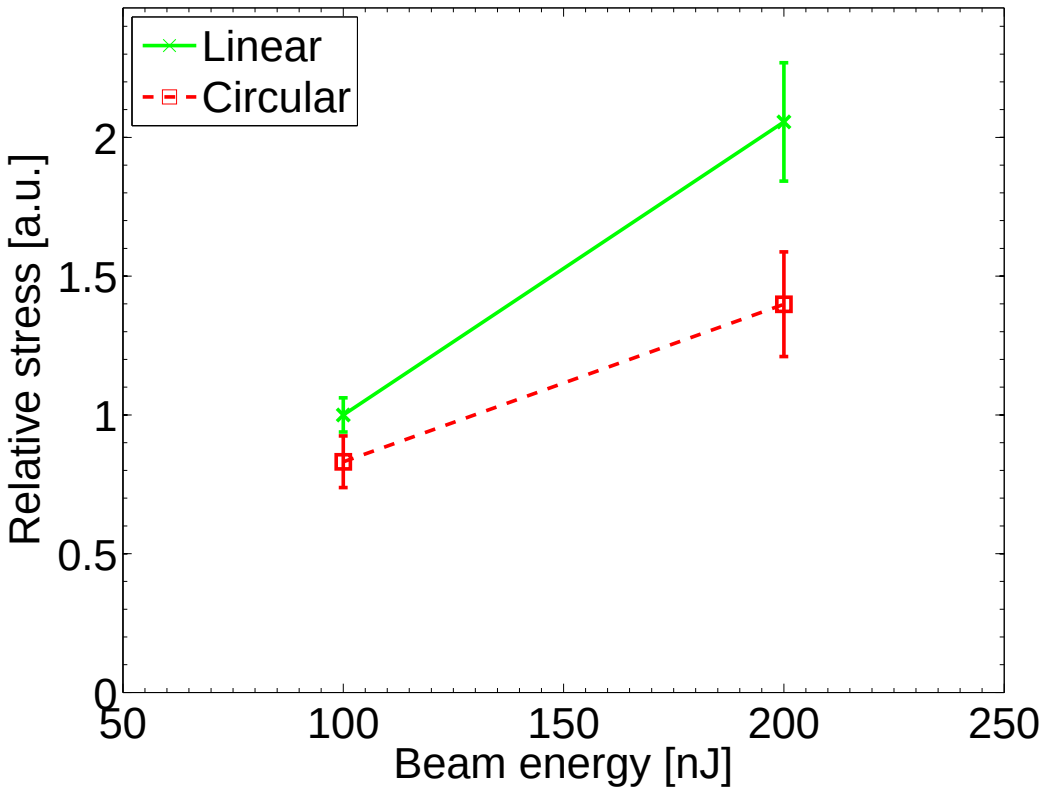

Figure 5.35: The effect of using linearly polarised (green) and circularly polarised (red) beams on the stress induced in diamond. The electrodes were all fabricated using an SLM. The stress is relative to the stress induced by the SLM-fabricated electrodes with a beam energy of 100 nJ, a translation speed of 10 μms^{-1}, and a linearly polarised beam.

of the resistivity and induced stress is not clear[25]. Nevertheless, this implies a step forward in terms of the optimisation of graphitic electrode formation.

It should be noted that while a general trend is observable in Figures 5.34 and 5.35, this study is not conclusive. For example, it is not obvious whether such trends hold for different beam energies, or for different translation speeds. As such, these results offer an insight into the effects of these fabrication parameters and hint at recommendations for future graphitic electrode formation, but further study into these effects (by including a larger parameter set of beam energies and translation speeds) is required.

[25]This sample demonstrates that surface plasmon polaritons, discussed later in this chapter, have a visible effect in terms of the morphology of the electrodes, as seen in the SEM images. References explaining this phenomenon are offered in Section 5.4.5, and also provide a brief insight into the effect of circularly polarised beams on the surface.

5.4.5 SEM Characterisation

Overview images were taken using an SEM for all the electrodes fabricated with and without an SLM, as seen in Figure 5.36. This shows there appears to be no difference in the size of the graphitic electrode at the surface of the diamond on the exit side for the two fabrication techniques. This is expected since the parameter space used for both techniques is the same, but also because of how the aberrations are corrected for in the diamond. That is, the corrections are a function of depth, meaning that stronger corrections are required as the focal point of the laser approaches the seed side of the diamond. By definition, this also implies the corrections weaken towards to the exit side such that to a first approximation the correction needed on the exit side of the diamond is zero.

Although the electrodes appear to be the same size on the exit side for both fabrication techniques, it should be expected that their size in the diamond bulk will differ due to the aberration corrections applied by the SLM, thus reducing the focal spot size. This is difficult to measure optically, due to the refractive index mismatch between air and the diamond itself, but it is also difficult to measure through SEM since the depth the electrons penetrate is O(μm). Measurements of the differences in electrode size could only be made if electrodes were fabricated on the edge of the diamond, but this is difficult to fabricate at the precision required to make such a measurement. The only way their sizes can be inferred is through qualitative measurements. For example, it can be seen in Figure 5.36 that the characteristic "pop off" effect on the exit side increases with beam energy. However, this effect is seen much more prominently for electrodes fabricated without the use of an SLM. If these electrodes are compared to those fabricated with an SLM, where aberration corrections are applied, it is clear that the SLM does reduce the focal spot size. This manifests as lower stress induced by the presence of the graphitic electrodes, which is the main proponent of this "pop off" effect.

Figures 5.37 and 5.38 show SEM images of the electrodes produced with a low beam energy and translation speed and with a high beam energy and translation speed, respectively. For the electrodes fabricated at low energy, there is a slight difference between the electrodes on the seed side for each fabrication method, observed in Figures 5.37a and 5.37b, whereas there is almost no difference between the electrodes

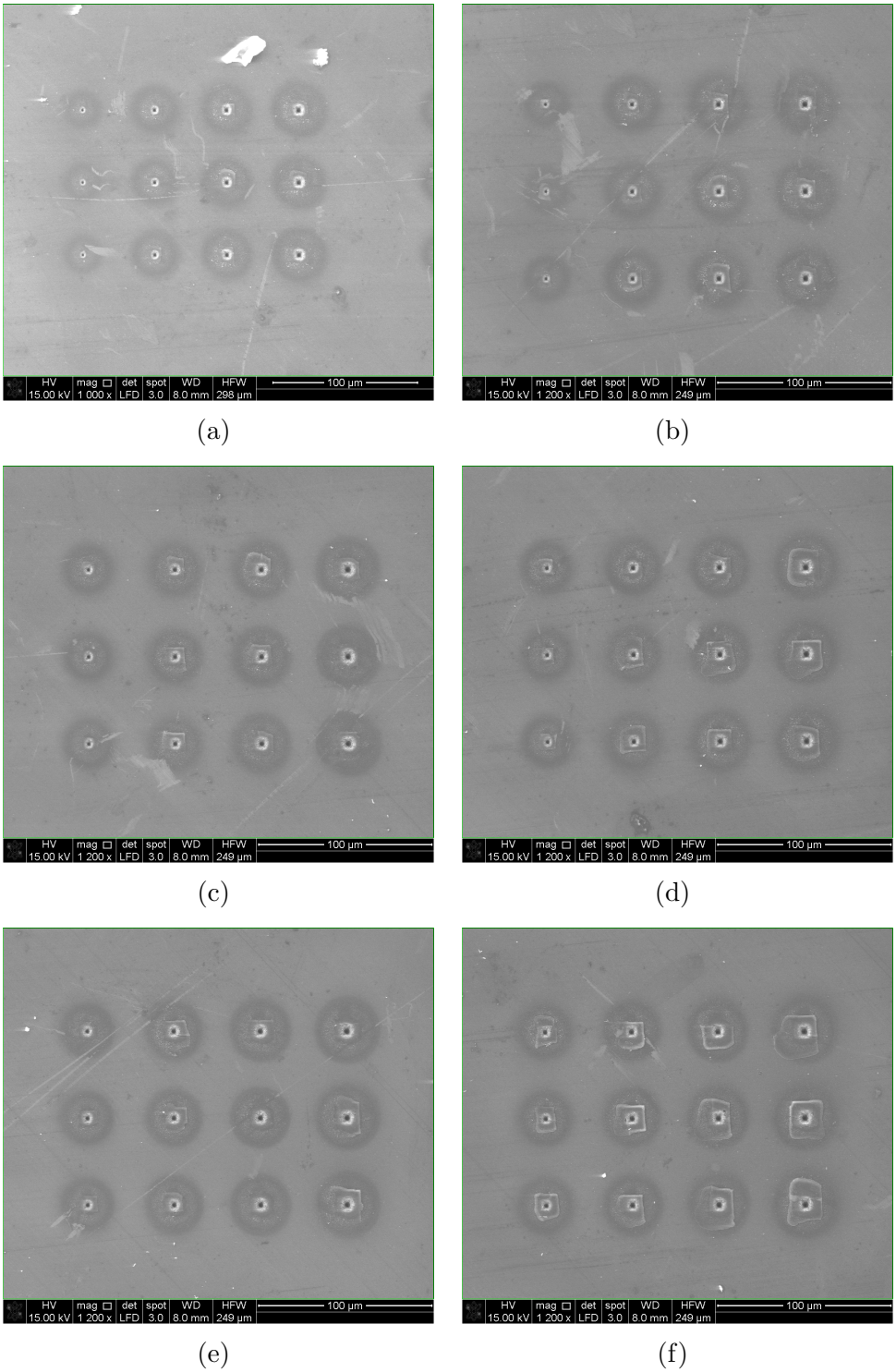

Figure 5.36: SEM overview images of Ox-002b as seen on exit side. (a), (c), and (e) are images of electrodes fabricated using an SLM, while (b), (d), and (f) are electrodes fabricated without an SLM. Columns of electrodes (from left to right in each image) were fabricated with the same parameters both with and without an SLM, as detailed in Figure 5.24. (a) With SLM, parameters 1, 2, 3, and 4. (b) Without SLM, parameters 1, 2, 3, and 4. (c) With SLM, parameters 5, 6, 7, and 8. (d) Without SLM, parameters 5, 6, 7, and 8. (e) With SLM, parameters 9, 10, 11, and 12. (f) Without SLM, parameters 9, 10, 11, and 12.

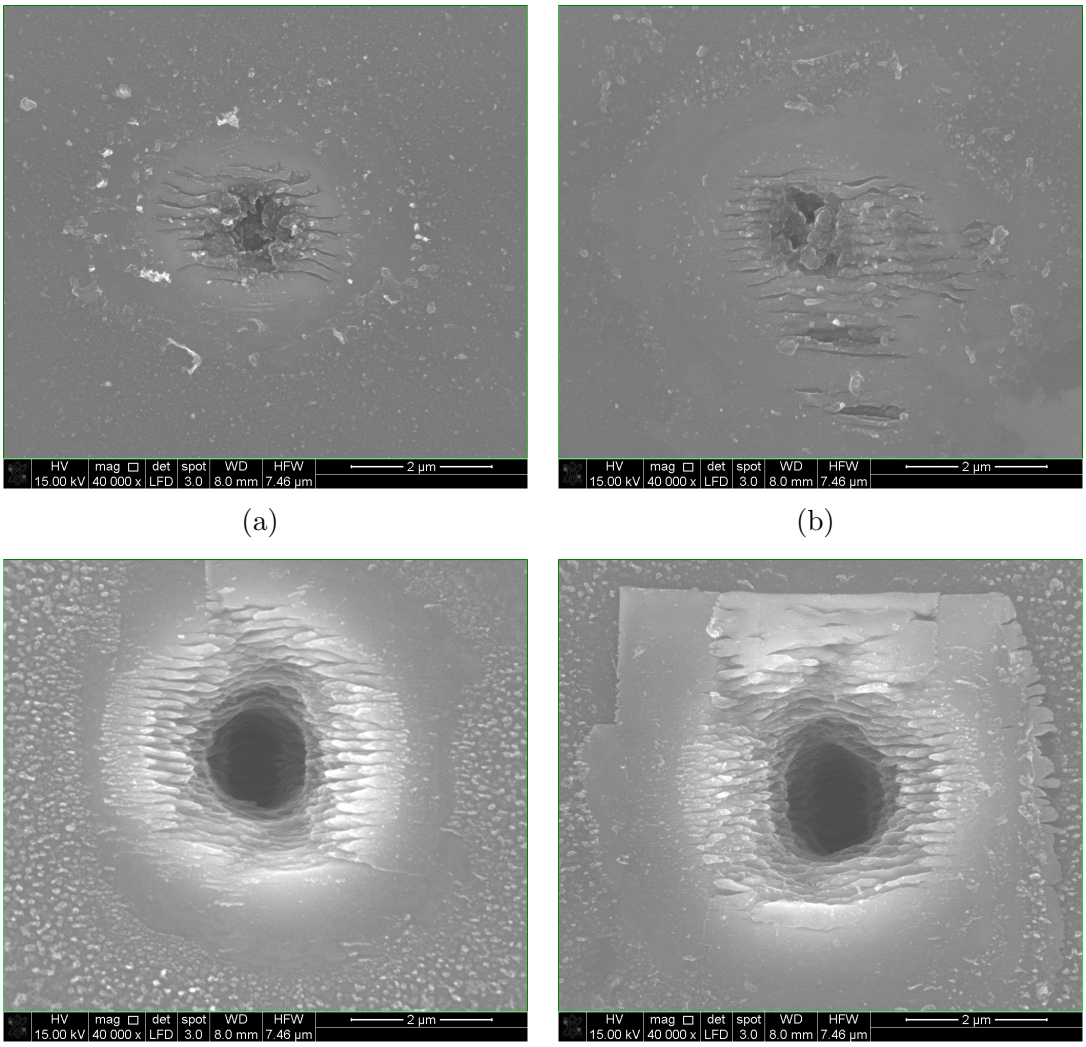

Figure 5.37: SEM images of Ox-002b for electrodes fabricated with a low beam energy, 100 nJ, and low translation speed, 10 μms^{-1}. The seed and exit sides of the electrodes are shown in the top, Figures (a) & (b), and bottom, Figures (c) & (d), respectively. Electrodes fabricated with and without an SLM are shown in the left, Figures (a) & (c), and right, Figures (b) & (d), respectively. The electrodes were fabricated with a beam energy of 100 nJ and translation speed of 10 μms^{-1}.

on the exit side, visible in Figures 5.37c and 5.37d. Both of these results are consistent with the explanation already offered in this section. The sizes remain the same on the exit side, with the "pop off" effect more visible for electrodes fabricated without an SLM, and some periodic "fringes" are observed on both the seed and exit sides. This effect was observed in the SEM images for Ox-001, which rules out the possibility that this arises purely from the use of an SLM. Instead these fringes are likely to result from the higher quality optics used in the Oxford laser setup.

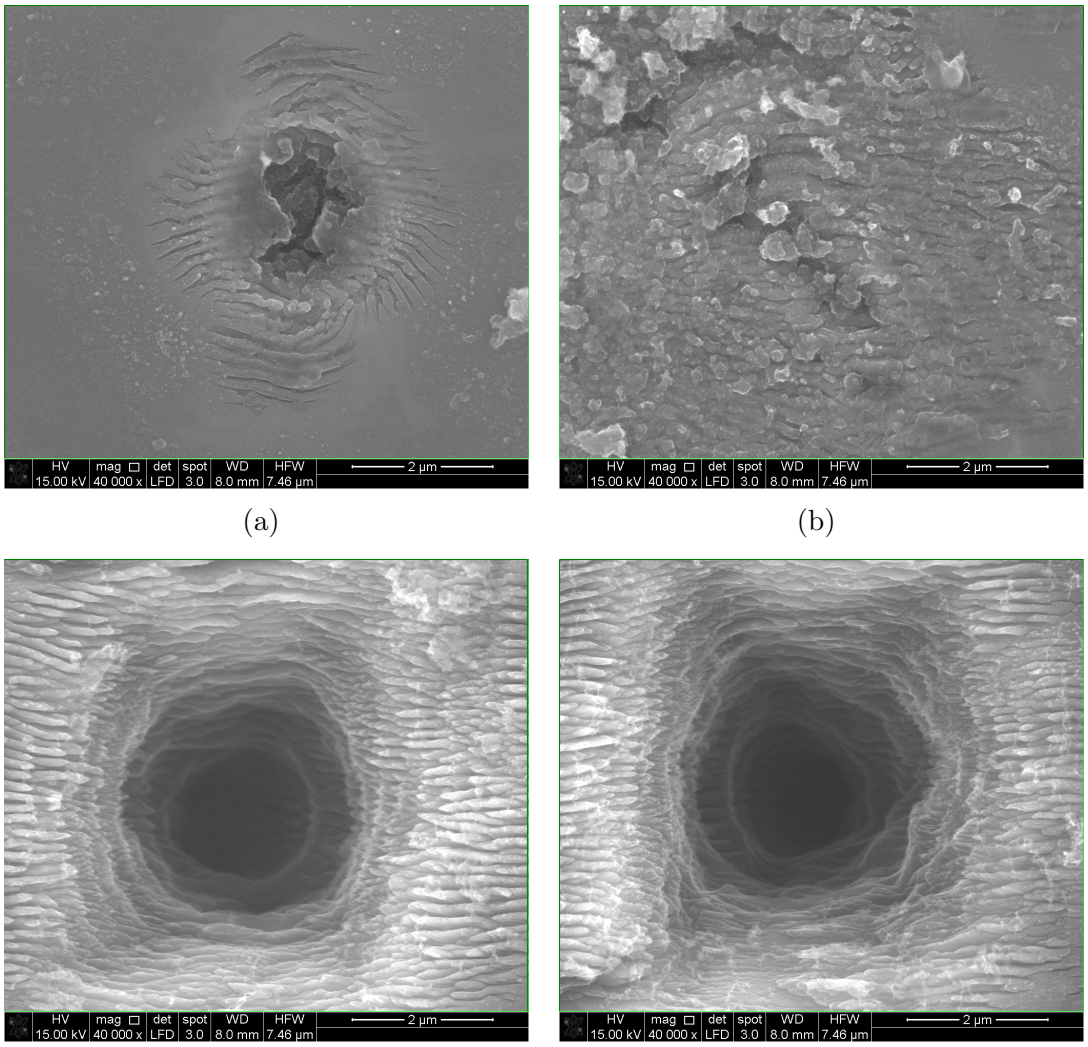

Figure 5.38: SEM images of Ox-002b for electrodes fabricated with a high beam energy, 600 nJ, and high translation speed, 30 μms^{-1}. The seed and exit sides of the electrodes are shown in the top, Figures (a) & (b), and bottom, Figures (c) & (d), respectively. Electrodes fabricated with and without an SLM are shown in the left, Figures (a) & (c), and right, Figures (b) & (d), respectively.

The appearance of such a periodicity of this fringe structure is likely linked to physics not observed in the electrode processing in Manchester and is, therefore, important in the formation of graphitic electrodes. Studies by P. Calvani et al. [84] highlight that a femtosecond laser is capable of inducing fringe periodicity of 170 nm, which is within the uncertainty of the periodicity measured from the SEM images (approximately 175 ± 15 nm). This periodicity is likely linked to the wavelength of the laser used for electrode fabrication. This is defined as $\lambda/2n$, where n is the refractive index of diamond, so the periodicity for the laser setup in Oxford is equal to 167 nm. This structure is induced by the presence of surface plasmon polaritons.

The work performed by T. Derrien et al. [85] explains this mechanism further. In short, surface plasmon polaritons are excited due to interactions between the laser pulse and the laser-induced plasma, which result in laser-induced periodic surface structures (LIPSS). It is stated that the periodicity observed in the SEM images is explained through the repetition rate of the laser, which decreases with increasing frequency [86]. The exact periodicity of these fringes, however, is affected by a number of parameters, including the laser wavelength, pulse duration, and the repetition rate, making it difficult to modulate the periodicity. While these conclusions were derived from a silicon substrate, it is expected that this is transferable to other semiconductor crystals, including diamond. As such, the effect of the periodicity, if any, on the electrode characteristics, including the resistivity and diamond to graphite ratio, are unknown.

It has also been noted in work by T. Derrien et al. [85] and J. Bonse et al. [86] that the orientation of these fringes are perpendicularly oriented to the polarisation direction of the laser. Therefore, it is possible that the creation of graphitic electrodes using a circularly polarised beam, rather than linear polarisation currently used, that these fringes would form in a circular pattern, or at the least a pattern that differs from a linearly polarised beam. It is not clear how or why the polarisation state, and thus this structure, would be beneficial to the formation or functionality of graphitic electrodes (which was shown to be true in the previous section, as well as in reference [83]). The polarisation state, along with the effect of surface plasmon polaritons in diamond, remains an area of further research in the field of 3D diamond detectors.

The biggest difference observed in these images are on the seed side of the electrodes. Although the general structure is the same, the structure is much more confined for the SLM fabricated electrode. Conversely, there is some additional structure observed in the electrode fabricated without the use of an SLM, located south of the electrode in Figure 5.37b. Similarly, the centre of the electrode shows more of a crater-like structure for fabrication with an SLM versus without an SLM. The corrections applied by the SLM reduce the focal spot size significantly, which in turn increases the energy density at the focus of the beam. This implies structure forms more readily at the same beam energy when an SLM is utilised, so less graphitic structure appears to be visible in the non-SLM fabricated electrode.

A comparison of these figures with those in Figure 5.38 reveal several differences. The different electrodes on the seed side highlight few changes for the SLM fabricated electrodes, but a noticeable change is readily observed in the non-SLM fabricated electrodes. It seems that less graphite is visible for high beam energy and fast translation speed for the non-SLM fabricated electrodes, whereas the opposite is true with the SLM fabricated electrodes. This is not intuitive, given the Raman results taken on Goe-001. The only explanation is that there is likely an upper limit on the fabrication speed for non-SLM produced electrodes, whereby if the speed is too fast then graphite formation, on the seed side, is hindered. Other explanations for this include a) the effect of the beam energy, and b) difficulty in locating the position of the focal spot with respect to the seed side. The latter option can be neglected, as this would have impaired the formation of graphite at all beam energies and translation speeds, and the former option is counter-intuitive, since a higher beam energy increases the energy density at the focal point which appears to aid in the formation of graphite. It is possible that there is also an upper limit on the beam energy. Such a limit would result in the ablation of the material rather than the formation of graphite, but this limit is likely to be significantly higher than the beam energies probed in this study. Since the study is limited systematically, due to the parameter space probed, and statistically, due to so few repetitions per parameter set, no further explanation can be given on this phenomenon.

Finally, a comparison of the exit side between these two parameters for both processing techniques reveals some differences. The size of the crater on the exit side is larger at high energies and fast translation speeds, which is a direct result of a higher energy density of the focal spot. This has been shown to be true for the previous diamond samples. The depth of the crater on the exit side, denoted by the darkness of the image, is much greater for high energies and fast translation speeds. This is because the higher energy density results in greater stress induced by the electrode on the diamond bulk, so as the focal point is moved towards the exit side this greater stress, and thus pressure build-up, will cause a more volatile ejection of the diamond. This manifests both as the material surrounding the electrode being ejected, the “pop off” effect, as well as more material ejected within the centre of the electrode itself. This effect is also supported by the appearance of greater substructure observed in the

crater, which likely indicates diamond material and not graphite.

5.4.6 Raman Spectroscopy Characterisation

Examples of Raman spectra on electrodes produced using both fabrication techniques are shown in Figures 5.39 and 5.40, for the seed and exit side, respectively. The spectra are vastly different on the seed side of the electrode, where the graphite peaks, relative to the diamond peak, are much larger for SLM fabricated electrodes. However, the spectra are largely the same on the exit side of the electrode. This effect supports the explanation offered for the SEM images. That is, the aberrations are a function of depth in the diamond, meaning a strong correction is applied on the seed side whereas minimal, or no, correction is applied on the exit side. This difference results from a change to the energy density of the focal spot, which is significantly higher when using an SLM versus without. As a result, it is likely that this energy density is high enough for graphite to reliably form on the seed side of the diamond at lower energies when using an SLM, whereas the energy density is quite close to the threshold required for graphite formation in the non-SLM case.

Raman spectra were taken for each combination of beam energy and translation speed probed, and the diamond to graphite G peak ratio was measured, as described for previous diamond samples. The results of this are shown for both with and without the use of an SLM in Figure 5.41. There is a clear trend that this ratio is lower on the seed side versus the exit side for SLM fabricated electrodes, shown in Figure 5.41a, which is in agreement with the results for Goe-001. It also shows that the ratio, to a first approximation, decreases on both sides as the beam energy and the translation speed increases. Such a result is crucial for future electrode fabrication, particularly the translation speed, since an issue with electrode fabrication is the time spent fabricating large scale devices. For example, if the translation speed can be increased beyond conventional speeds, that is, $\mathrm{O}(20\,\mu\mathrm{ms}^{-1})$, this would reduce the fabrication time, and thus the cost, of diamond detectors and improve their viability as tracking detectors.

However, this trend is not apparent for ratios measured on non-SLM fabricated electrodes, shown in Figure 5.41b. In fact, this trend appears to oppose the findings for the SLM fabricated electrodes. In this case, the ratio is lower on the exit side, which slightly decreases with translation speed and beam energy, versus the seed side, which

slightly increases with translation speed but the effect of the beam energy is unclear. It has been shown that the exit side ratio is comparable for both techniques, and SEM images hinted at low graphite formation for the non-SLM fabricated electrodes, which is confirmed in this figure. The effect of the translation speed is likely due to an upper limit on the translation speed for non-SLM fabricated electrodes, as stated previously, but this is inconclusive since the study is systematically and statistically limited. For a definitive conclusion, more electrodes should be fabricated at more combinations of beam energy and translation speed, though these data still suggests the use of an SLM greatly improves the formation of graphite, and hence the conductive material, of the electrodes.

A comparison of Figures 5.41a and 5.41b with the I-V measurements indicate they generally agree. This indicates that although it is non-trivial to determine the resistance of the electrode through the use of Raman spectroscopy, it is a useful method for characterising graphitic electrodes, especially since it minimises potential damage to the metallisation that is likely to occur during I-V measurements. Both characterisation methods show that the use of an SLM is highly recommended, though measurements of electrodes fabricated at $30\,\mu\text{ms}^{-1}$ seem to indicate a lack of agreement between the two characterisation methods. It was stated previously that the reason for the difference in the I-V measurements was uncertain, and so the reason for this disagreement is also uncertain. It is possible that there is a significant difference between the surface and bulk properties of the electrode, the regions probed by Raman spectroscopy and I-V measurements, respectively. This is difficult to reconcile and prompts either a significantly larger study, as required for Raman spectroscopy, or simply further research into this area.

5.4.7 Sample Summary

In summary, the effect of processing parameters on the formation of graphitic electrodes has been investigated for both fabrication techniques. The non-linearity intercept and resistance of the electrodes reduces with increasing beam energy, with a slight effect due to the translation speed. These results also indicate that an SLM reduces these parameters more than is possible through simply altering the processing parameters. Qualitative and quantitative measurements on the crossed polariser

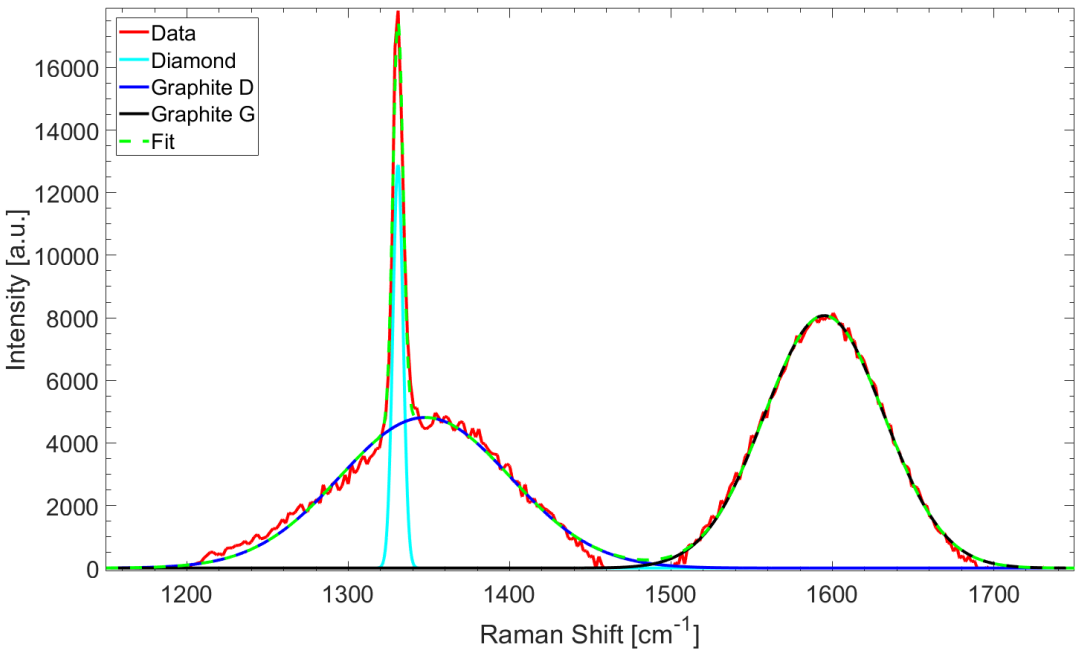

(a)

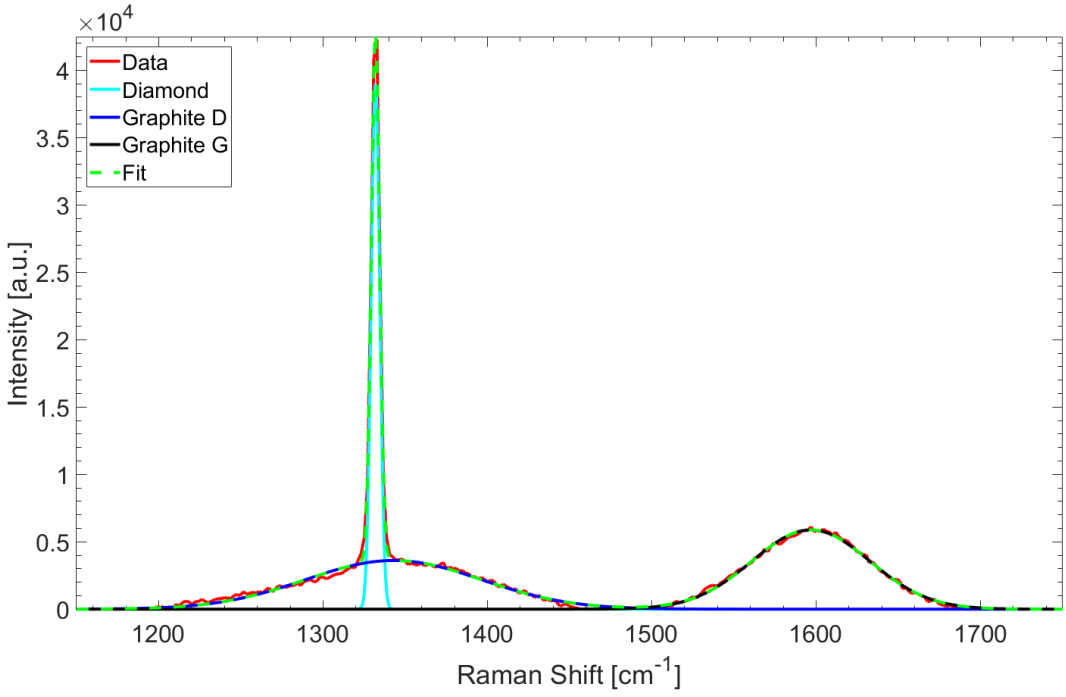

(b)

Figure 5.39: Raman spectra of Ox-002b taken on seed side of the electrode fabricated (a) with, and (b) without an SLM. The beam energy was 300 nJ and the translation speed was 10 μms^{-1}.

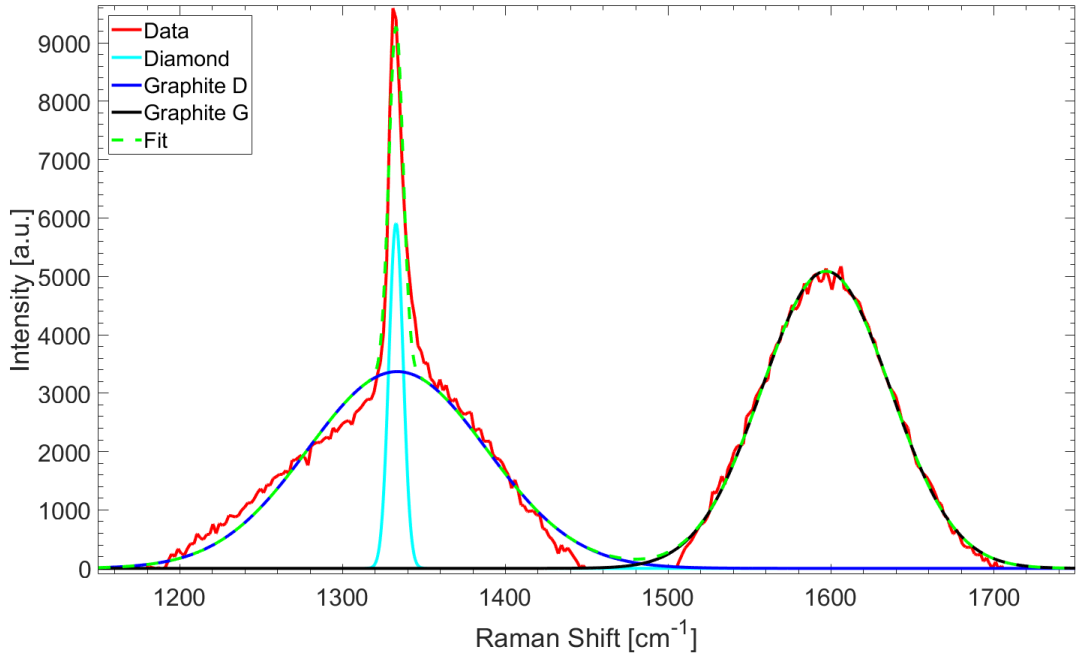

(a)

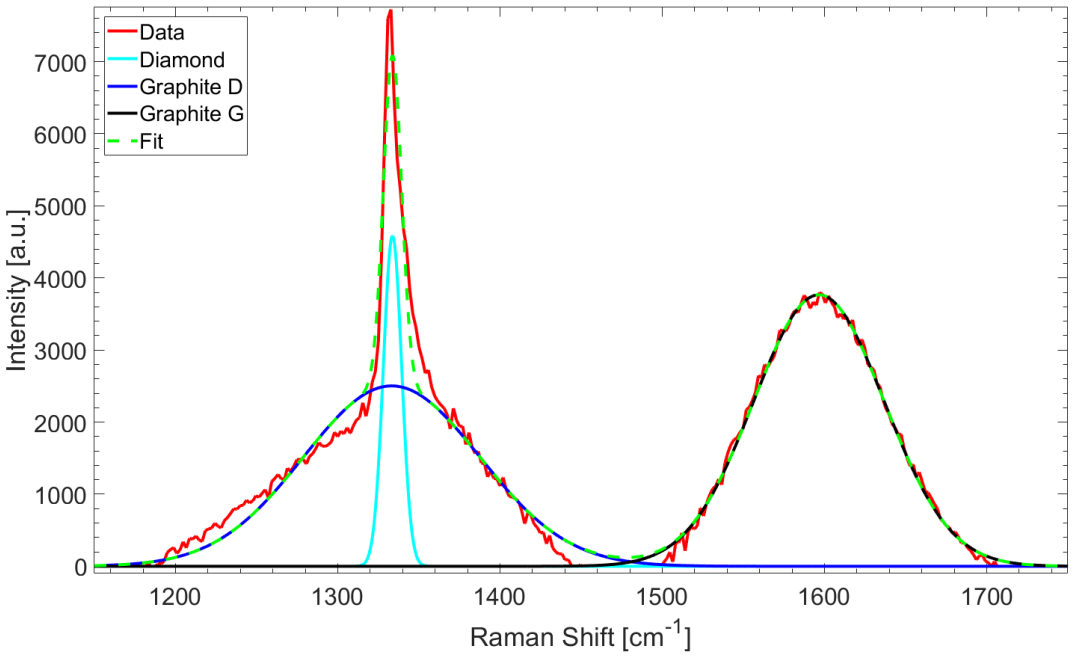

(b)

Figure 5.40: Raman spectra of Ox-002b taken on seed side of the electrode fabricated (a) with, and (b) without an SLM. The electrodes in these spectra are the same as those in Figure 5.39.

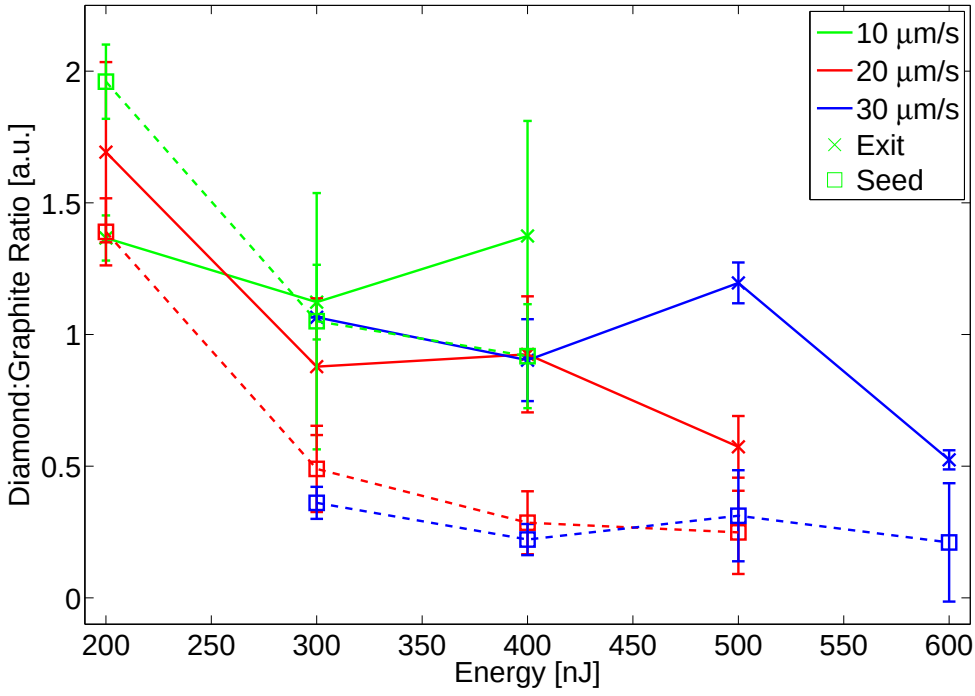

(a)

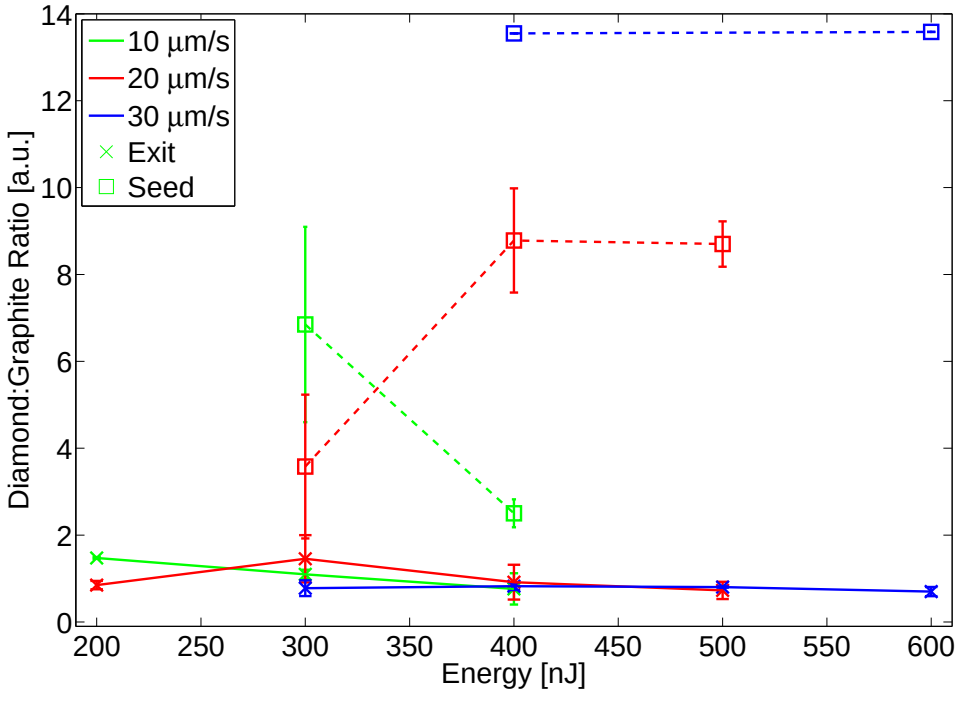

(b)

Figure 5.41: Ratio of diamond to graphite content for Ox-002b for electrodes fabricated (a) with, and (b) without an SLM. Some data points are missing from (b) since the study is systematically and statistically limited. Data published in reference [83].

images confirm, alongside the resistivity measurements, that more graphite is fabricated through the use of an SLM, and the level of induced stress generally increases with beam energy. Results for different NA lenses and beam polarisation states are also presented, showing that a high NA lens and circularly polarised beams are recommended to minimise stress while maximising the formation of graphitic electrodes, though both remain an area for further investigation. The presence of fringe structure on the electrodes in SEM images on both sides for each fabrication technique, also seen on Ox-001, appears to be due to high quality optics rather than the use of an SLM. The appearance of such fringes has been explained, and further investigation is recommended to observe any fluctuation in the fringe separation and orientation, particularly with varying processing parameters and beam polarisation. The SEM characterisation also reveals a strong difference between the graphite formation on the seed side between the two fabrication techniques, while little difference is observed on the exit side, and is likely due to the functionality of the SLM. Raman spectra also shows this effect, and indicates the use of an SLM is preferable for consistent electrode formation and for optimisation of the fabrication process. A much larger study into the variation of the processing parameters is also recommended for the Raman spectra to make a definitive conclusion on the benefits of using an SLM, as well as further investigating the limits of electrode formation.

The work performed on all four diamond samples using the characterisation techniques described in Chapter 4 shows how the processing parameters (specifically, the beam power and the translation speed) affect the desirable electrode properties (that is, a small electrode diameter and a low electrode resistance). The work presented also shows steps towards greater understanding and optimisation of the processes involved in the formation of graphitic electrodes in diamond. Man-001 demonstrates how the beam fluence affects the physical properties of the graphitic electrodes, in particular the electrode diameter. Goe-001 shows a comprehensive study in the effect of the processing parameters on the formation of graphitic electrodes, and highlights that a high beam power and fast translation speed are recommended for highly conductive electrodes. Goe-001 also shows that a laser with a high repetition rate (O(1 MHz)) could greatly decrease the fabrication time of the graphitic electrodes whilst also forming highly conductive electrodes. Ox-001 demonstrates the benefits of incorporating an

SLM into laser setups used for fabricating graphitic electrodes, such as smaller electrode diameters with a lower resistivity than was possible in Man-001 and Goe-001. Ox-002 shows a direct comparison of graphitic electrodes produced with and without an SLM, also illustrating that electrodes fabricated with an SLM exhibit lower resistance than those fabricated without an SLM. As was the case for Goe-001, Ox-002 reinforces the outcome that high beam energy and high translation speeds are required for highly conductive graphitic electrodes, with some results suggesting the use of a circularly polarised beam may further reduce the electrode diameter and resistance. Across all four diamond devices, there is a clear insight into the formation of the graphitic electrodes from the seed to the exit sides of the diamond through the use of Raman spectroscopy and SEM. Additionally, the novel technique of using crossed polarisers to highlight partially formed electrodes was demonstrated across all these devices. Using the previously outlined background subtraction process, images taken with crossed polarisers can be quantitatively analysed to provide further insight into the effects of the processing parameters.

Chapter 6

Results from Test Beam Data

This chapter is divided into two sections, the first of which describes the Ox-001 detector, a 3D diamond detector probed with a proton microbeam. This section also details the experimental setup for both of this test beam, as well as results for Ox-001. Following these results, the second section describes the Man-001 detector, which was the first 3D diamond detector to be tested with photon and proton microbeams [73]. The results of this detector are compared to Ox-001. A brief outlook for the future of 3D diamond detectors at test beams is also discussed.

6.1 Detector Ox-001

6.1.1 Motivation

The primary reason for the manufacture of detector Ox-001 is to investigate the response of a diamond detector to a proton microbeam. Work by S. I. Parker et al. [6] established the viability of the 3D architecture and work by T. V. Kononenko et al. [53] demonstrated the process by which electrodes in diamond may be easily manufactured. However, the first 3D diamond detector was manufactured in 2011 [92], so such detectors are in their infancy and require significant research into their response and viability. Chapter 5 details problems with the limited resistivity and electrode diameter for Man-001, both of which were significantly reduced using an SLM. It is due to these characteristics that the response of Man-001 to particle beams was satisfactory (briefly discussed later in Section 6.2), though the degree of uniformity in the readout

strip responses is generally poor. Hence, the manufacture of a detector using an SLM (Ox-001), known to improve these detector qualities, should increase the uniformity of the signal in the cells.

A second reason for its fabrication is to obtain higher quality TRIBIC data. It is expected that improvements in the resistivity will significantly affect the quality of the TRIBIC data, but using a PCB designed to filter out high frequency noise should eliminate the ringing in the waveforms. This is crucial for resolving any possible substructure in the TRIBIC data, such as the observation of peaks in the signal arising from different charge carriers, and, more importantly, simulations may be compared to the data once more in an attempt to extract information on the charge carriers. The effect of ringing on this TRIBIC data, taken on Man-001, is presented later in this chapter.

6.1.2 Proton test beam (IBIC)

The proton microbeam at Ruder Boskovic Institute (IRB) at Zagreb [87] was used to study the response of Ox-001 via IBIC. The setup itself is based on a Van-de-Graaff accelerator producing a beam of 4.5 MeV protons, with a FWHM of O($\leq$ 2 μm). The data were recorded at $U_b = \pm 2\,\mathrm{V}$, $U_b = \pm 5\,\mathrm{V}$, $U_b = \pm 10\,\mathrm{V}$, $U_b = \pm 20\,\mathrm{V}$, and $U_b = \pm 40\,\mathrm{V}$, with data taken for the square and hexagonal cell geometries (refer to Chapter 5 for further details on the geometries). One readout strip was wire bonded to a readout pad, referred to as the "inner channel", while its two adjacent strips were connected together to a second readout pad, referred to as the "outer channel".

The two readout strips on array A were connected via SMA connectors to the readout electronics, where the readout chain consisted of a charge integrating amplifier and a shaping amplifier with a shaping time of 2 μs. The DAQ system was self-triggered and recorded the charge with a trigger threshold of 20 ke.

The IBIC data was recorded via deposition of signals into an arbitrary channel number from 0 to 255 for each position axis, which corresponds to a physical size of O(700 μm). The signal was calibrated using a silicon detector as reference. Hits in this detector were recorded and a histogram was made to find the signal channel number at which the number of hits is maximum. It is assumed that there are no defects in the reference device, so this peak channel number is assumed to be the channel in which

there is 100% charge collection. Multiplying this value by the ratio of electron-hole pair energies of silicon to diamond would then give the channel number in diamond corresponding to 100% charge collection. A comparison of this expected value to the peak channel number observed from a histogram of hits in Ox-001 indicates a difference of O(1%). This provides a basis for the uncertainty on the measured signal in the IBIC data.

The response of adjacent readout strips to protons as a function of position is shown in Figures 6.1 and 6.2, for the square and hexagonal cell geometries, respectively. A comparison of Figures 6.1a and 6.1b demonstrates that a higher bias voltage results in a higher C.C.E. within the cell, and with a more uniform response. These effects are due to the applied bias voltage itself, that is, a higher bias voltage results in a much stronger electric field, so a larger fraction of the induced charge is collected compared to that at lower bias voltages. This is because the induced charge is more likely to be trapped by defects in the diamond substrate at lower bias voltages, and is not collected. The induced charge is, hence, less likely to be trapped if it is induced in a region where the electric field is the strongest. The increased uniformity across the cell is also observed in the negative polarity, shown in Figures 6.1c and 6.1d. The two bias polarities show a similar response, with the only difference being a slightly higher C.C.E. in the negative polarity plots[1]. Finally, a comparison of the square and hexagonal cells reveals no advantage in one particular geometry at this point, where both geometries show the same increased uniformity with bias voltage. However, one difference between the geometries is the appearance of high C.C.E. "diamonds" in the hexagonal cells. The reason for this is uncertain, but given the fluctuations are O(few %) this could be related to one (or more) of three effects: the reproducibility of the electrodes, that is, there are some small fluctuations in the electrodes which could cause some structure in the cell; a visual artefact introduced by the colour scheme; or from the geometry itself, whereby the hexagonal cells are not regular hexagons, as they are slightly "squashed" in the y direction. Given this effect is also observed in Figure 6.2f it would appear this effect most likely results from the cell geometry. It should be noted that the pickup due to the metallisation is negligible with Ox-001[2].

[1]The average C.C.E. as a function of bias voltage is quantified later in this section.

[2]This is not the case for Man-001 likely due to issues with the detector outlined in Section 6.2.

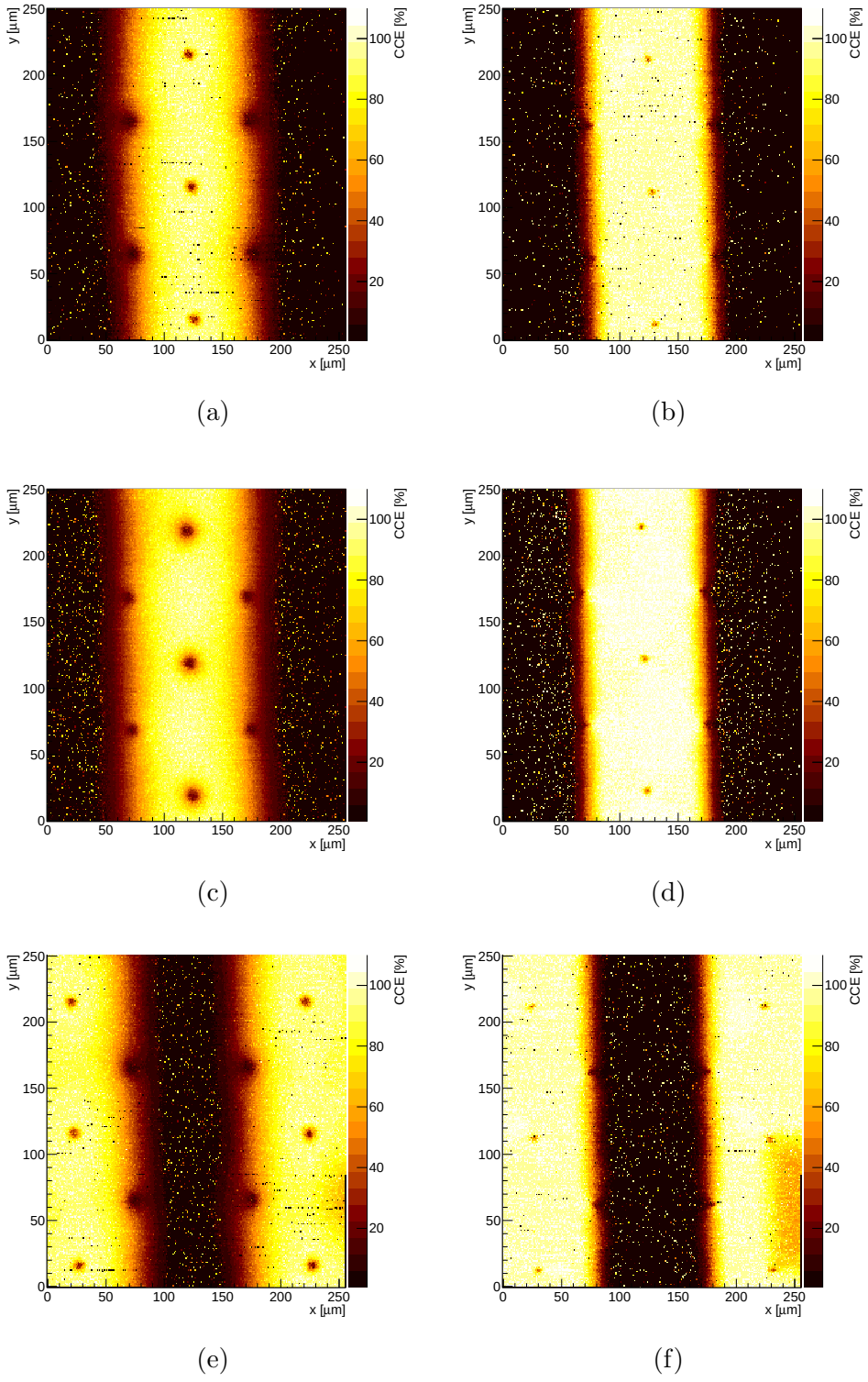

Figure 6.1: Response of square cells to a proton beam on Ox-001. The white areas beyond $\approx x < 50\,\mu$m and $\approx x > 200\,\mu$m denote signal recorded in the outer readout channel, shown in (e) and (f). No tilt correction has been applied to these images. (a) $U_b = +2\,\mathrm{V}$. (b) $U_b = +20\,\mathrm{V}$. (c) $U_b = -2\,\mathrm{V}$. (d) $U_b = -20\,\mathrm{V}$. (e) Signal recorded in the outer channel at $U_b = +2\,\mathrm{V}$. (f) Signal recorded in the outer channel at $U_b = +20\,\mathrm{V}$. Figures (c) and (d) are taken from reference [82].

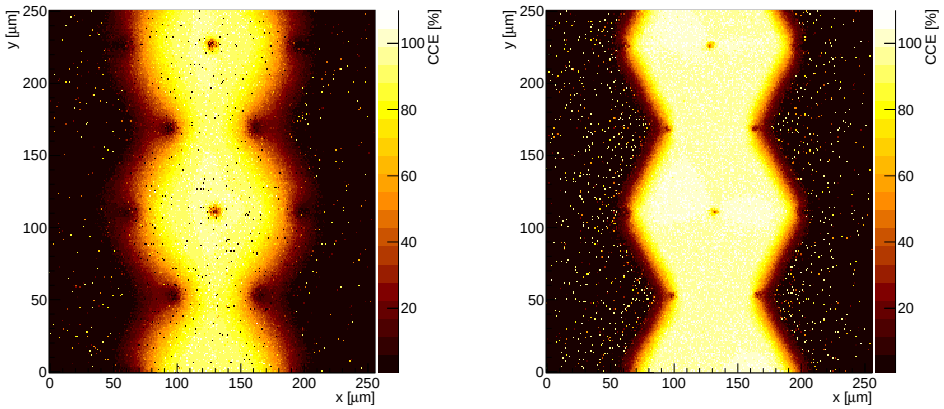

(a) (b)

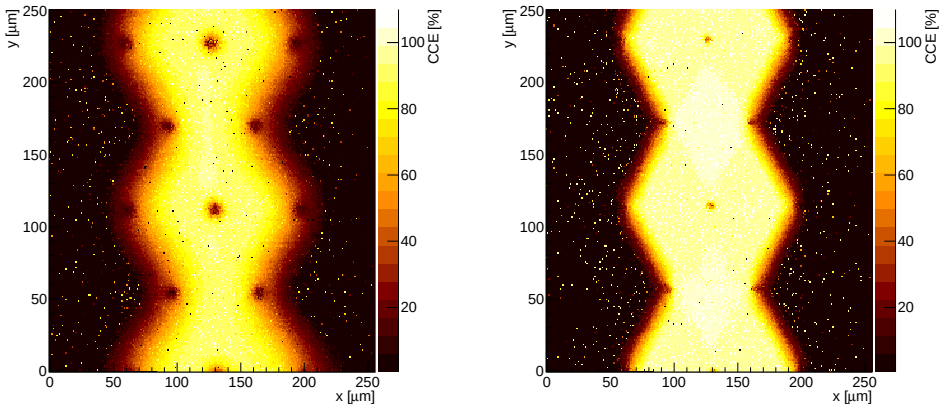

(c) (d)

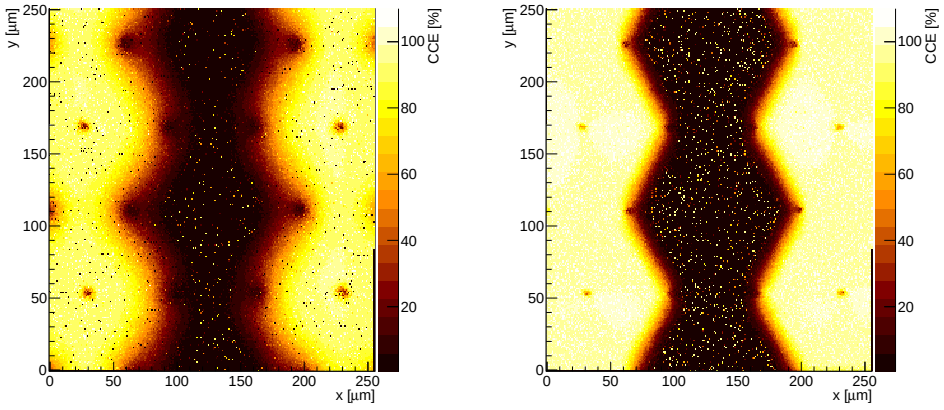

(e) (f)

Figure 6.2: Response of hex cells to a proton beam on Ox-001. No tilt correction has been applied to these images. (a) $U_b = +2\,\mathrm{V}$. (b) $U_b = +20\,\mathrm{V}$. (c) $U_b = -2\,\mathrm{V}$. (d) $U_b = -20\,\mathrm{V}$. (e) Signal recorded in the outer channel at $U_b = +2\,\mathrm{V}$. (f) Signal recorded in the outer channel at $U_b = +20\,\mathrm{V}$. Figures (c) and (d) are taken from reference [82].

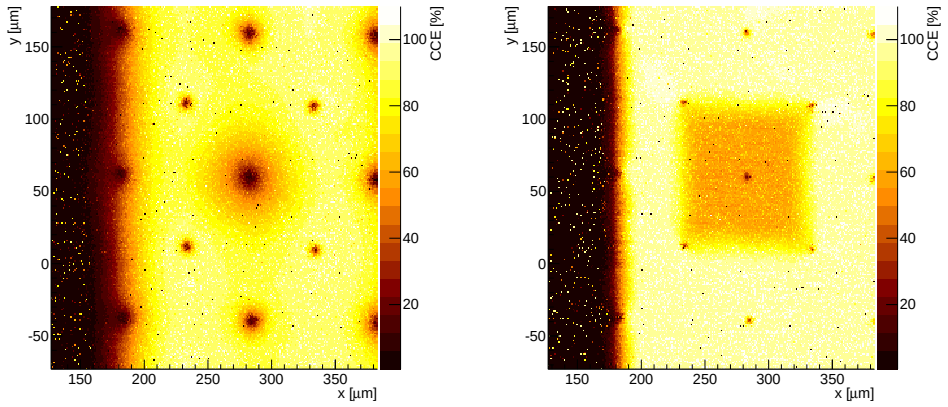

(a) (b)

Figure 6.3: Response of a square cell to a proton beam on Ox-001 with a partially formed central bias electrode. (a) $U_b = +2\,\mathrm{V}$. (b) $U_b = +20\,\mathrm{V}$.

Figures 6.1e and 6.1f also show a fraction of a cell, at $x > 230\,\mu\mathrm{m}$ and $y < 110\,\mu\mathrm{m}$, that has a significantly lower C.C.E. This indicates that the dead cell is related to a bias electrode, given the symmetry of the square cells and the location of bias electrodes at $y \approx 62\,\mu\mathrm{m}$. This cell is imaged more clearly in Figure 6.3. Optical and crossed polariser images of the sample did not highlight a partially formed electrode, so the exact cause for this dead cell is uncertain. Underperforming cells were observed in the data for Man-001 (Section 6.2), so one could make a similar conclusion, where it is likely the electrode did not fully penetrate the diamond bulk, resulting in cell behaviour that differs from its neighbours.

The average C.C.E. for each strip, shown in Figures 6.1 and 6.2, at each bias voltage was calculated by fitting a Gaussian curve to a histogram of all recorded signals, an example of which is presented in Figure 6.4a. The location of the Gaussian and its FWHM were taken as the C.C.E. and its uncertainty, respectively, with the results of these fits shown in Figure 6.4b. Comparing the two geometries reveals that their efficiencies are consistent at any given bias voltage, indicating no preference for either cell type. The lower efficiency for the square cells at $U_b = -2\,\mathrm{V}$ results from difficulty in the Gaussian fit to the signal histogram. Nevertheless, a comparison of this data with the C.C.E. measurements on Man-001 show the results are consistent, but the overall C.C.E. is slightly higher on Ox-001 at any given bias voltage, and the uncertainty on these measurements is more constrained. Both of these effects are due to the improved fabrication of the electrodes, including the lower resistivity of the electrodes, as well

as a greater understanding of the readout system.

One other similarity between both cell geometries is the width of the charge sharing region, which reduces with bias voltage. This is seen when comparing Figures 6.1a and 6.1e with Figures 6.1b and 6.1f, where the size of the collected charge region along the x axis decreases with bias voltage. The width of the region from low to high C.C.E., such as from $170\,\mu\text{m} \leq x \leq 200\,\mu\text{m}$ in Figure 6.1a, also decreases with bias voltage. Both of these effects are related to the increased uniformity of the cell at higher bias voltages, which has been demonstrated to be related to the increased electric field strength.

The effect of bias voltage on the width of the charge sharing region can be quantified by considering areas for which signals are recorded in both readout channels. This occurs when protons are incident near the boundaries of a cell, and so the induced charge is collected by both readout channels. The charge sharing, η, is then defined in Equation 6.1, where q_1 and q_2 are the signals recorded in the inner and outer readout channels, respectively. Figure 6.5 shows the charge sharing region for different bias voltages and cell geometries. It was observed previously that the width of the charge sharing region reduces with bias voltage, though a comparison of Figures 6.5a and 6.5b demonstrates this more clearly. It is also apparent from these figures that the boundary of the charge sharing region is more well defined at higher bias voltages, which is a result of less charge sharing between the two readout channels and thus the cell geometry is more accurately observed. These effects are reproduced in both cell geometries, with no differences visible between these cells. A qualitative measure of the size of this charge sharing region was determined through 1D cuts to these data taken every $10\,\mu\text{m}$ at multiple positions in y for the central cell in each geometry. The signal across these cuts was averaged, accounting for the tilt and the geometry of the hexagonal cells, with examples of these averaged cuts shown in Figures 6.5e and 6.5f. These figures further show the charge sharing region is smaller at higher bias voltages.

$$\eta = \frac{q_2}{q_1 + q_2} \tag{6.1}$$

A quantitative measure of the charge sharing region was defined from these 1D cuts, where the width was defined to be the region between $0.25 \leq \eta \leq 0.75$ and was averaged for both the left and right regions of the central cell. Figure 6.6 shows the

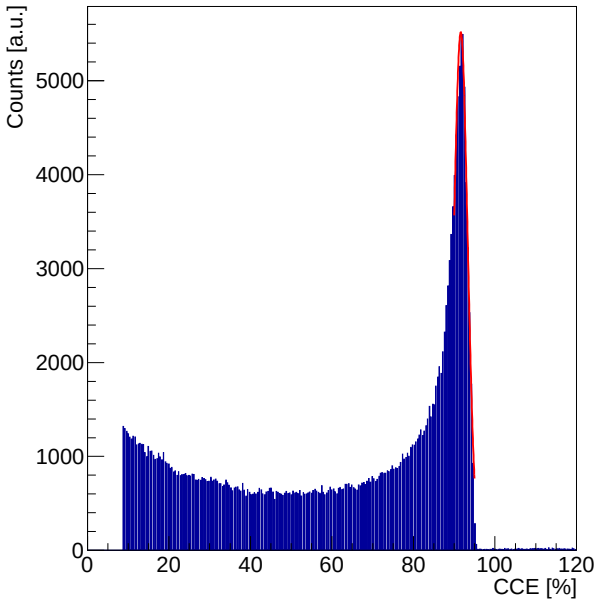

(a)

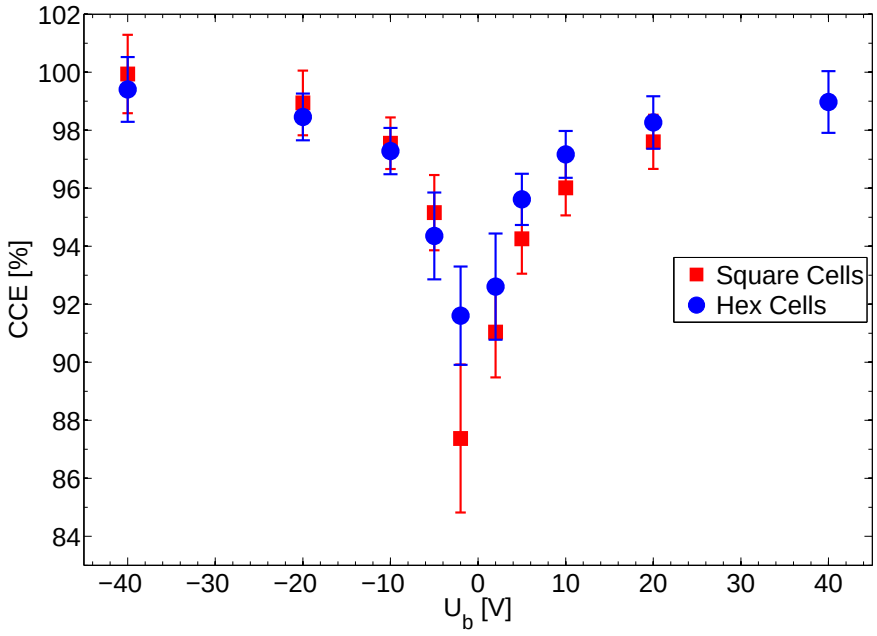

(b)

Figure 6.4: Determination of the charge collection efficiency of the inner readout strip and the results plotted against bias voltage. (a) Example of a histogram of signals for hexagonal cell geometry at $U_b = -2\,\mathrm{V}$ to which a Gaussian curve, red, was fitted at the peak C.C.E. The trigger threshold is observed as the sharp rise in the signal collected at low C.C.E. (b) Charge collection efficiency as a function of bias voltage for Ox-001 for square cells, red, and hexagonal cells, blue. No data was recorded for the square cells at $U_b = +40\,\mathrm{V}$ due to high leakage current. Figure (b) taken from reference [82].

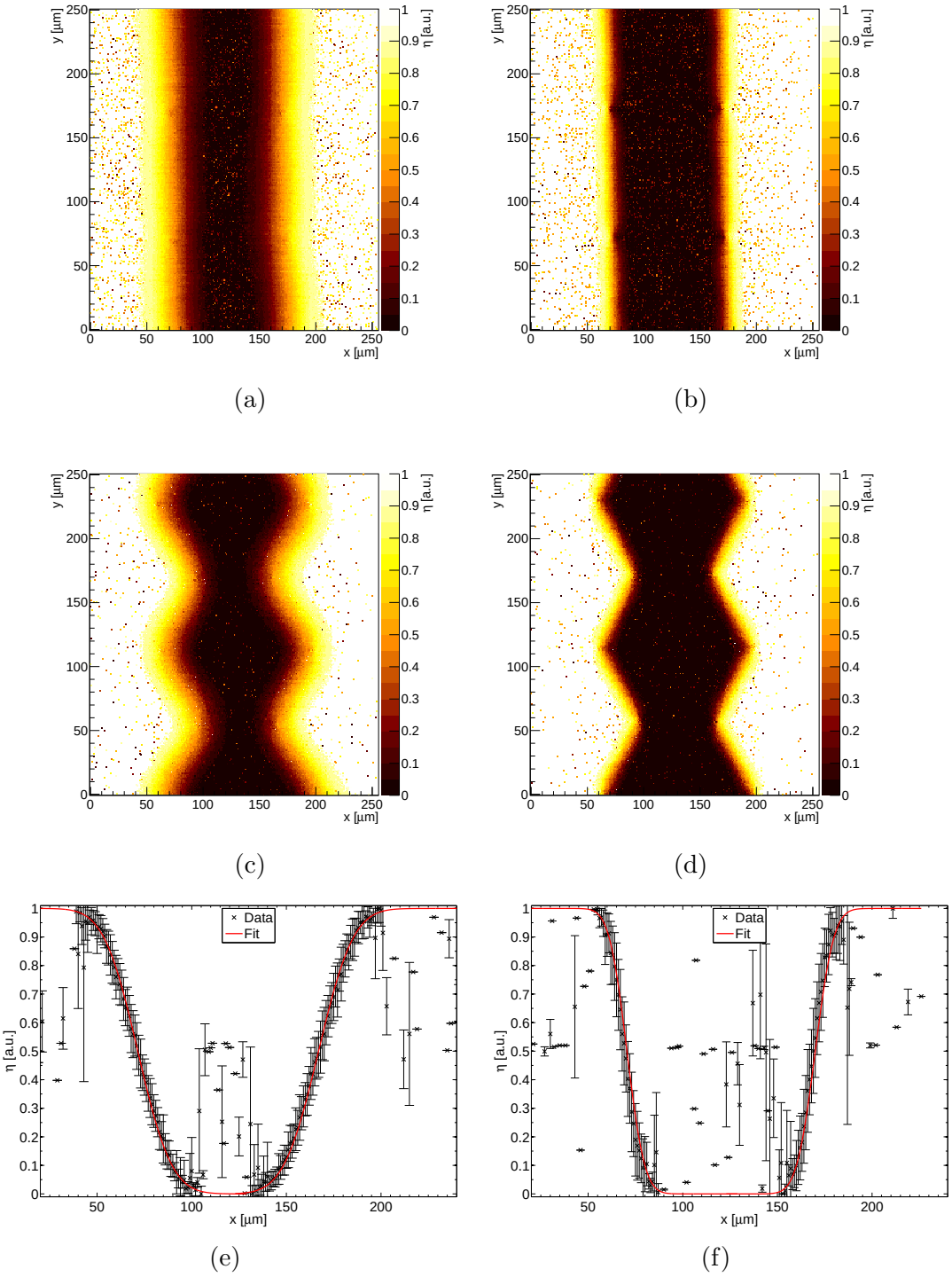

Figure 6.5: Plots of the charge sharing in square and hexagonal cells on Ox-001. Figures (a)-(d) show the charge sharing in 2D, while Figures (e)-(f) show cuts averaged in y and demonstrate the width of the charge sharing region. (a) 2D plot of charge sharing in square cells, $U_b = -2\,\mathrm{V}$. (b) 2D plot of charge sharing in square cells, $U_b = -20\,\mathrm{V}$. (c) 2D plot of charge sharing in hex cells, $U_b = -2\,\mathrm{V}$. (d) 2D plot of charge sharing in hex cells, $U_b = -20\,\mathrm{V}$. (e) 1D cut of charge sharing from Figure (a). (f) 1D cut of charge sharing from Figure (b). Figures (a)-(d) taken from reference [82].

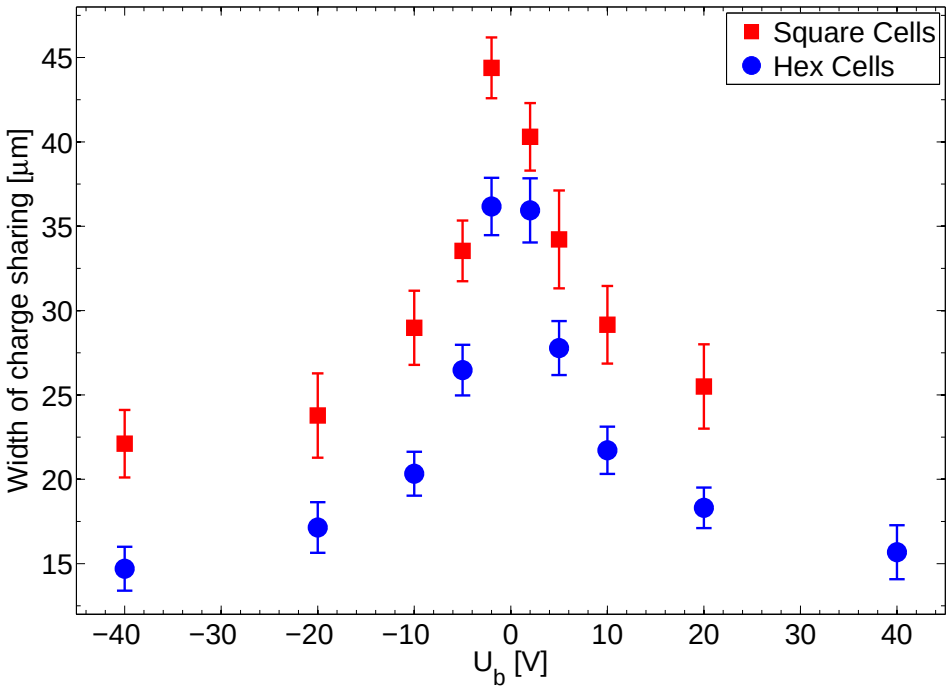

Figure 6.6: Variation of charge sharing with bias voltage on Ox-001 for square cells, red, and hexagonal cells, blue. The charge sharing width is consistently smaller in the hexagonal cells than the square cells by O(25%). Figure taken from reference [82].

variation of this charge sharing region with bias voltage for both cell geometries. This quantitatively illustrates the reduction of the charge sharing width with increased bias voltage, and the widths are consistent at different bias polarities. This also shows no clear indication of better performance with one bias polarity. However, a comparison of the square and hexagonal cells shows a higher charge sharing region for the square geometry, and these widths are also inconsistent for any given bias voltage. The data presented up to this point shows no anomalies that could result in this effect, which means this is entirely due to the cell geometry. These results indicate that the different cell geometries may be used for different purposes, such as the square geometry for use as a tracking detector and the hexagonal geometry for use as a dosimeter, as was previously highlighted in Section 2.5.

6.1.3 Time-resolved IBIC (TRIBIC)

Time-resolved ion beam induced current (TRIBIC) technique is a measure of the transient currents as a function of position within a detector and allows the determination of the electric field distribution. The electric field will not vary with the translational

position of the incident particle, in this case protons, for a planar detector. However, the electric field distribution is non-trivial for a 3D detector, and such measurements are crucial in determining and understanding the electric field within 3D detectors.

The TRIBIC data uses the existing setup for the IBIC data acquisition with some modifications. In these data, the signal generated by the incident protons is amplified using a Cividec C2 2 GHz broadband current amplifier [88] and then digitised using a WaveMaster-8500 5 GHz oscilloscope from Lecroy [89].

The TRIBIC waveforms were recorded at positions corresponding to a 50×50 grid, of arbitrary size, on the detector. Parameters such as the amplitude were extracted for each of these waveforms, with the results plotted in 2D. These plots were then used as a means of calibrating the arbitrary grid to a physical size by identifying structures within the 2D plots of the waveforms by eye, such as the electrode separation.

The signals recorded on the oscilloscope (in volts) are calibrated to a current via the known amplification factor, 40 dB equivalent to a gain of 100, and the amplifier resistance (50 Ω). The signal offset was calculated by measuring the average recorded signal in the first 5 ns of each waveform and then subtracted. The integral of each waveform is the charge collected at that position. The peak of the 1D integral plots were normalised to the IBIC data, given that approximately 100% charge collection was observed in the IBIC data. This calibration was applied to the 2D plots shown later in this section. The data were recorded at the highest achievable bias voltage of ±20 V for both square and hexagonal cells, with protons incident on the readout side of the detector. Ox-001 is mounted on a high-frequency carrier board to eliminate any ringing effects[3].

Examples of TRIBIC waveforms are shown in Figure 6.7, and a comparison with the data taken on Man-001 reveals there is no ringing component in these data. This proves the effectiveness of a better designed PCB to match the impedance of the graphitic electrodes with the readout electronics. This also demonstrates a necessary step towards understanding the charge carrier dynamics in the 3D detector and the extraction of important carrier properties, such as their lifetimes. A comparison of the two geometries reveals a similar shape observed in both the high field region,

[3]This ringing effect is demonstrated in Section 6.2 and is the primary reason for the low quality data observed in Man-001.

Figures 6.7a and 6.7c, and the low field regions, Figures 6.7b and 6.7d, of the detector, with comparable widths at these positions.

There are two differences between the two geometries, the first of which being the pulse height at these locations. The pulse height of the hexagonal cells is consistently higher than that of the square cells, which seems entirely due to the configuration of the electrodes and thus the shape of the electric field within each geometry. While their area of the hexagonal cells is 15% larger than square cells, the proximity of the central readout electrode with any bias electrode is lower than in the square cells. This further implies that the electric field strength is thus higher in the hexagonal geometry for the same given bias voltage, thus a faster collection time, or "rise" time, and a higher amplitude are to be expected. While the higher amplitude is observed in Figures 6.7a and 6.7d, the faster rise time is only observed in the low field plots, Figures 6.7b and 6.7d. This is likely due to limitations on the readout electronics. For example, the 2 GHz amplifier frequency implies periods significantly shorter than 0.5 ns cannot be accurately resolved, which is exactly the lower limit of the rise time in the high field region. Using an amplifier with a higher sampling frequency could potentially resolve the differences between the rise times in the different geometries.

The second difference between the geometries is the appearance of a two peak structure in the hexagonal cells in the low field regions. These two peaks are related to the charge carriers induced inside the diamond bulk. That is, charge injected near an electrode will induce a current on the nearby electrode, where the signal is induced by electrons on the nearby bias electrode, causing a sharp rise in the signal[4]. The other charge carrier, the holes, will drift to the opposite electrode, the readout electrode, which is recognisable by a second peak later in time than the first. The charge carriers will also drift to electrodes for charge injected near the midpoint between a bias and readout electrode, but the induced signal is larger with a longer rise. This is also because the mobilities of the electrons and holes are similar enough, and the electric field high enough, that the charge carriers cannot be easily resolved. This two peak structure can only be definitively explained through accurate simulations modelling the TRIBIC signal, presented later in this section.

[4]This explanation of two peak structure assumes positive bias polarity. If a negative bias polarity was applied, it would cause the holes to drift to the bias electrode, and electrons to the opposite electrode.

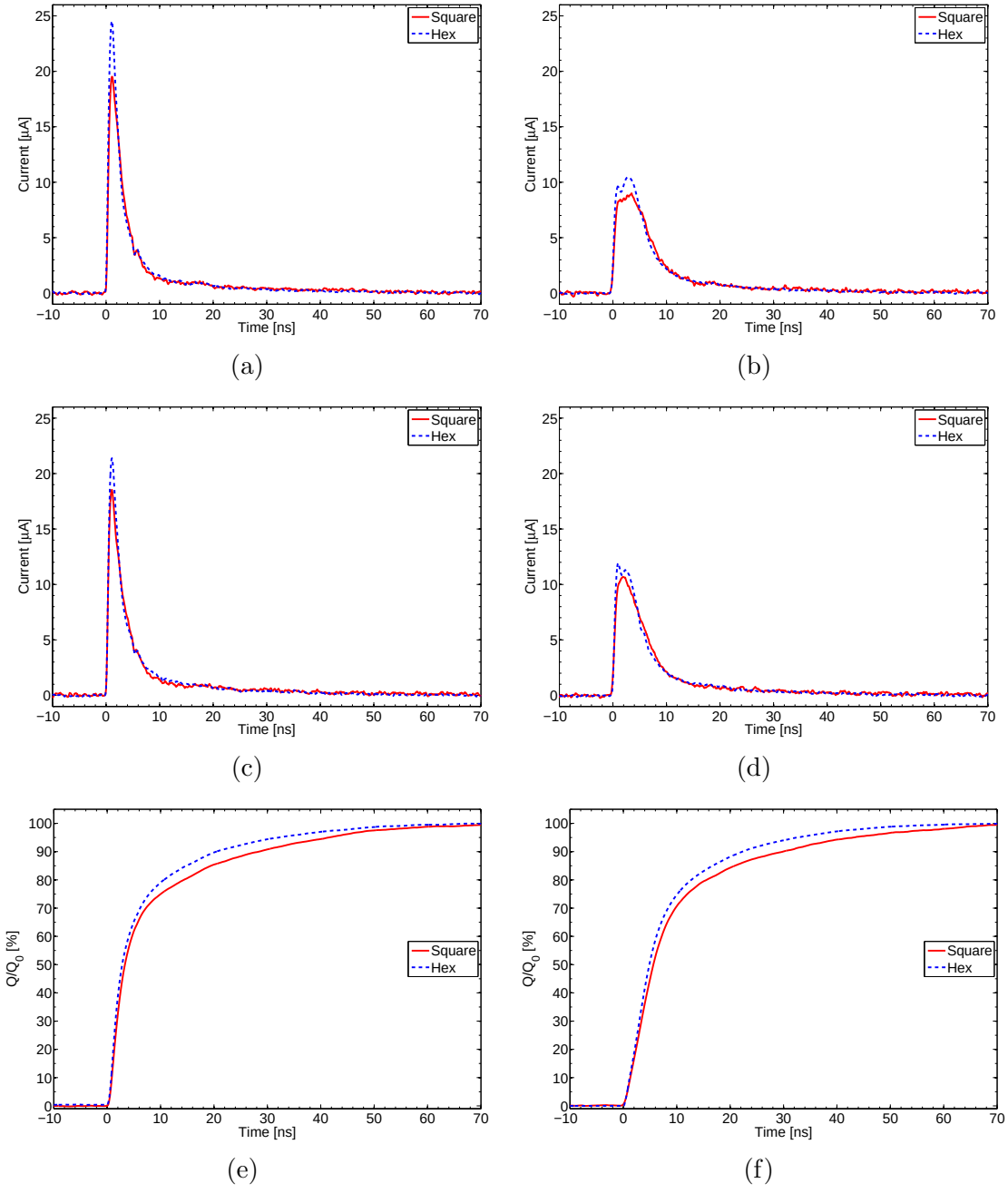

Figure 6.7: TRIBIC waveforms on Ox-001 for square cells, red, and hexagonal cells, blue. The traces were averaged at four positions indicated in Figures 6.8 and 6.9. (a) High field region, $U_b = +20\,\mathrm{V}$. (b) Low field region, $U_b = +20\,\mathrm{V}$. (c) High field region, $U_b = -20\,\mathrm{V}$. (d) Low field region, $U_b = -20\,\mathrm{V}$. (e) Cumulative integral of traces from Figure (a). (f) Cumulative integral of traces from Figure (b). Figures (c)-(f) taken from reference [82].

Figures 6.8 and 6.9 show the measured amplitude, FWHM, and integral for $U_b = \pm 20\,\mathrm{V}$ for the square and hexagonal cells. In the amplitude plots, Figures 6.8a and 6.8b, the amplitude is highest near the electrodes and lowest at the edges of the cell. This structure is also observed in the FWHM plots, Figures 6.8c and 6.8d, where a smaller FWHM is observed in the centre of the cell and a larger FWHM is seen at the cell edges. This effect is solely due to the magnitude of the electric field from the 3D geometry, as outlined previously. The use of an improved PCB and lower resistivity electrodes both result in significantly higher quality data versus Man-001. Hence, these qualities result in less variation in the integral of the TRIBIC waveforms, Figures 6.8e and 6.8f, which again shows that all the charge is collected at all positions in the cell.

A comparison of the same geometry at different bias polarities reveals few differences. All three measurements are comparable and show no preference in the collection of one particular charge carrier. This could be due to the significantly improved fabrication of the electrodes. For example, a lower resistivity implies a greater signal is induced on the electrodes for a given bias voltage. The lower resistivity could be significant enough that it is difficult to resolve the differences between the charge carriers unless either the bias voltage is lower, increasing the drift time and thus the trapping probability of the charge carriers, or by increasing the sampling frequency of the amplifier, which was already mentioned with regards to the TRIBIC waveforms.

A comparison of the two different geometries at the same bias polarity reveal differences already observed in the TRIBIC waveforms, that is, the hexagonal cells have a consistently higher amplitude and a consistently lower FWHM than the square cells. This information is presented in Table 6.1. This contrast is purely due to differences in the electric field, which arises from the different cell geometries. However, these measurements are consistent and do not indicate a preference for one cell geometry.

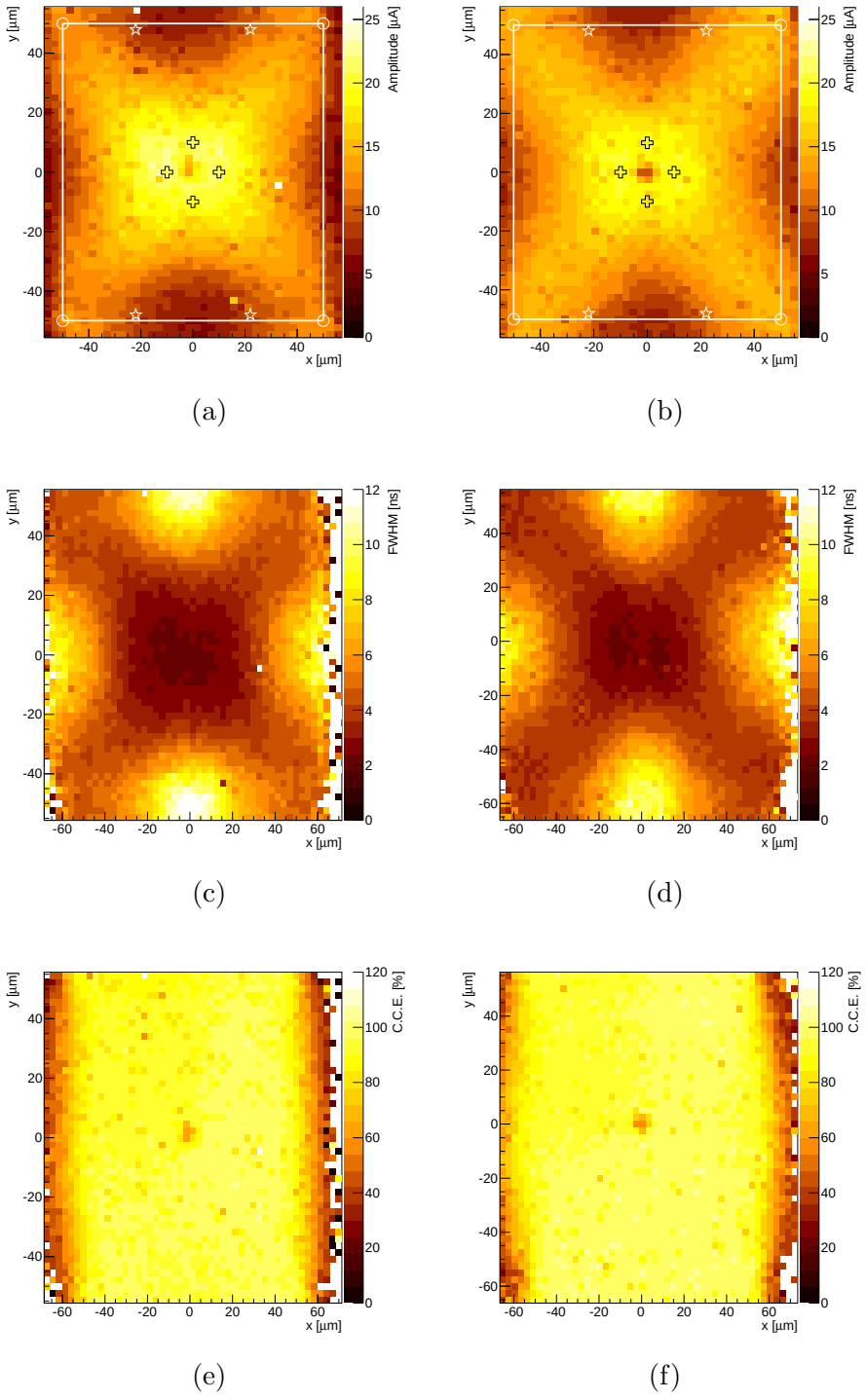

Figure 6.8: 2D TRIBIC plots for square cells on Ox-001 showing the amplitude, FWHM, and integral of the TRIBIC pulses at two different bias polarities. The outline of the square geometry is shown in Figures (a) and (b), with the locations of the bias electrodes shown as white circles. The black crosses and white stars refer to the high and low field regions used in Figure 6.7. (a) Amplitude plot, $U_b = +20\,\mathrm{V}$. (b) Amplitude plot, $U_b = -20\,\mathrm{V}$. (c) FWHM plot, $U_b = +20\,\mathrm{V}$. (d) FWHM plot, $U_b = -20\,\mathrm{V}$. (e) Integral plot, $U_b = +20\,\mathrm{V}$. (f) Integral plot, $U_b = -20\,\mathrm{V}$. The peak value in the integral plots is normalised to the IBIC data. Figures (a)-(d) taken from reference [82].

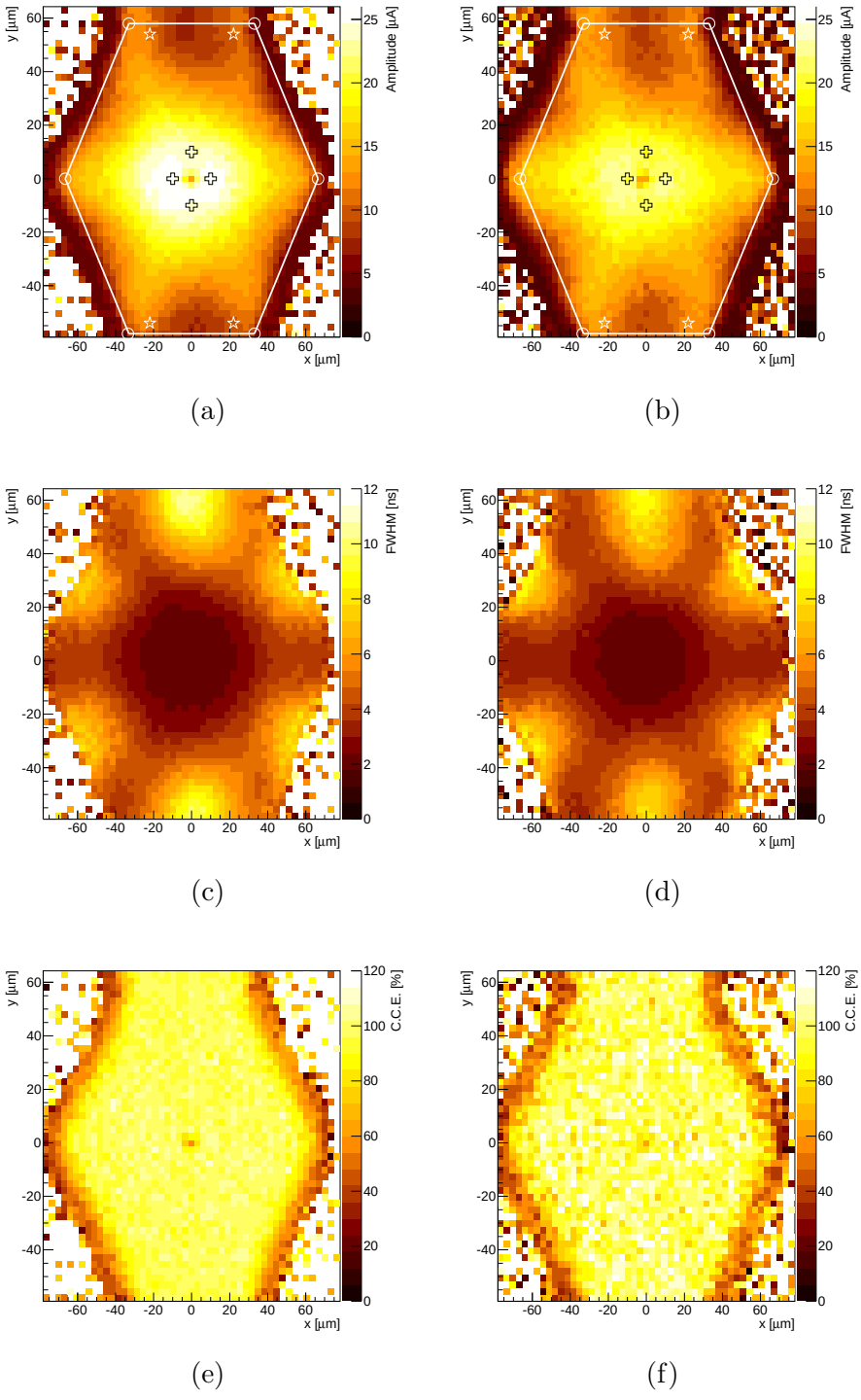

Figure 6.9: 2D TRIBIC plots for hexagonal cells on Ox-001 showing the amplitude, FWHM, and integral of the TRIBIC pulses at two different bias polarities. The outline of the hexagonal geometry is shown in Figures (a) and (b), with the locations of the bias electrodes shown as white circles. The black crosses and white stars refer to the high and low field regions used in Figure 6.7. (a) Amplitude plot, $U_b = +20\,\mathrm{V}$. (b) Amplitude plot, $U_b = -20\,\mathrm{V}$. (c) FWHM plot, $U_b = +20\,\mathrm{V}$. (d) FWHM plot, $U_b = -20\,\mathrm{V}$. (e) Integral plot, $U_b = +20\,\mathrm{V}$. (f) Integral plot, $U_b = -20\,\mathrm{V}$. The peak value in the integral plots is normalised to the IBIC data. Figures (a)-(d) taken from reference [82].

Field	U_b [V]	Cell geometry	Amplitude [μA]	FWHM [ns]
Low	+20	Hexagonal	10.9 ± 0.8	5.9 ± 0.4
Low	+20	Square	9.4 ± 0.9	6.8 ± 0.5
Low	-20	Hexagonal	12.3 ± 0.7	5.1 ± 0.4
Low	-20	Square	11.8 ± 0.9	5.3 ± 0.1
High	+20	Hexagonal	25.2 ± 1.4	2.0 ± 0.1
High	+20	Square	21.2 ± 0.5	2.3 ± 0.1
High	-20	Hexagonal	21.0 ± 1.2	2.1 ± 0.1
High	-20	Square	19.0 ± 0.8	2.5 ± 0.3

Table 6.1: Average amplitude and FWHM of TRIBIC waveforms on Ox-001 for square and hexagonal cells at $U_b = \pm 20\,\mathrm{V}$.

A study into protons incident on the bias side of the detector was carried out on Ox-001, with density plots of the incident protons for all waveforms on the readout and bias side shown in Figures 6.10a and 6.10b. There is significant variation in the waveforms on the readout side, characterised by the "blurring" between $0-10\,\mathrm{ns}$, which was evidenced in the amplitude and FWHM plots shown previously. There is a clear dominant pulse shape with little variation on the bias side, with an average FWHM of $\mathrm{O}(35\,\mathrm{ns})$. This effect is likely due to the difference in the resistance "observed" by the protons. That is, protons incident on the readout side would travel $\mathrm{O}(100\,\mu\mathrm{m})$ into the diamond bulk and so the charge nominally travels 25% of the detector thickness[5], whereas protons incident on the bias side travel the same distance into the diamond bulk but the charge nominally travels 75% of the detector thickness. The increased path length results in a significantly increased RC time constant. It is suspected that this high RC time constant dominates the signals, that is, larger than $\mathrm{O}(\geq 20\,\mathrm{ns})$ estimated from Figure 6.10b, and thus decouples the amplitude and FWHM from the position at which the proton was incident. This effect is observed in Figures 6.10c and 6.10d, where no structure is observed.

Simulations of the waveforms were performed using the Synopsys TCAD package [90]. These simulations were performed by G. Forcolin and are discussed in more depth in reference [47]. A combination of 2D and 3D simulations were utilised to minimise the computing power, where 2D simulations were used for predictions for

[5]The exact distance induced charge carriers travel along the readout electrode is entirely dependent on where the charge was induced in the diamond, though "nominally" refers to where the bulk of the charge is induced corresponding to the Bragg peak of the protons.

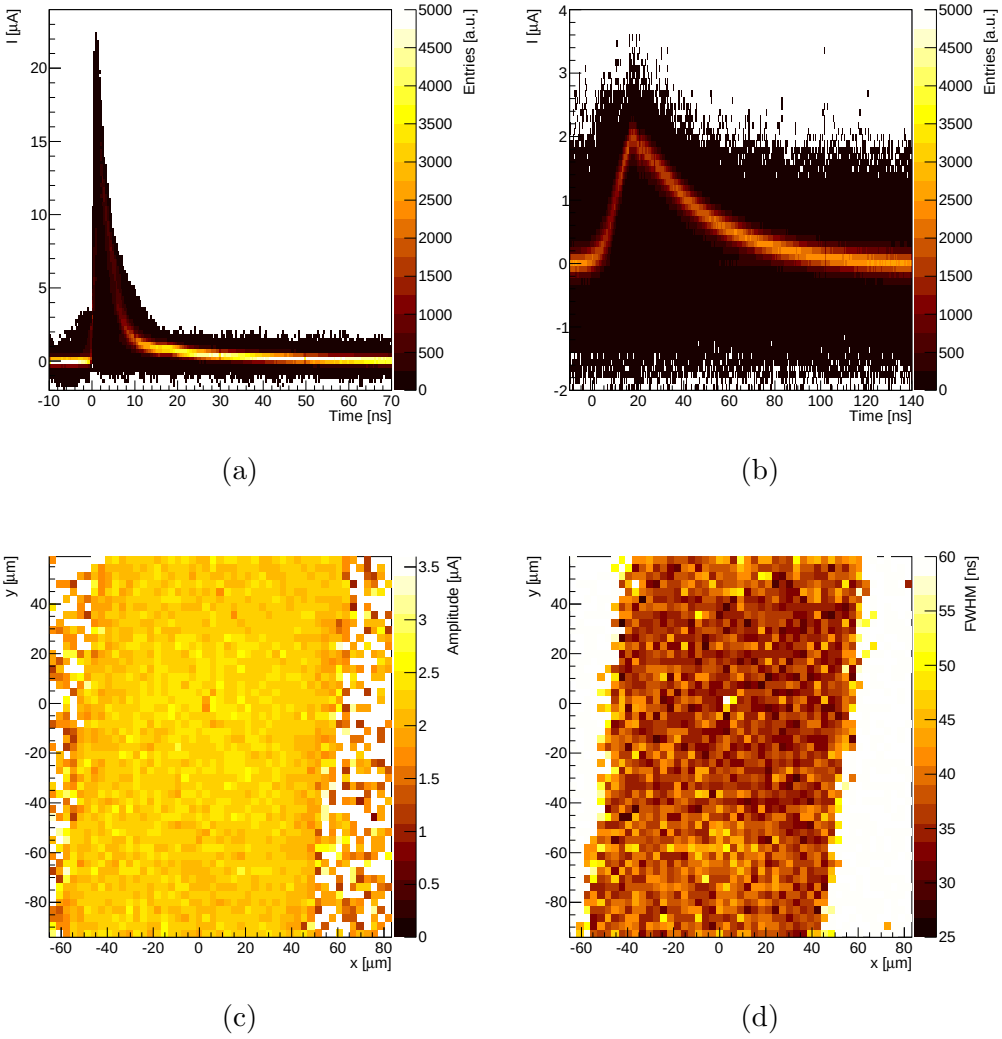

Figure 6.10: Results of protons incident on the bias side of Ox-001. Figures (a) and (b) show 2D density plots of protons incident on the readout and bias sides of the detector respectively, while Figures (c) and (d) show the amplitude and FWHM 2D plots for the bias side of the detector. The bias voltage for these measurements was $U_b = +20\,\mathrm{V}$. No tilt correction was applied to Figures (c) and (d). Figures (a)-(c) taken from reference [82], while Figure (d) was adapted from reference [82].

larger areas of the detector. These simulations used a mesh corresponding to a 2×2 cell area to simulate the effects of neighbouring cells. The downside to using 2D simulations is the inability to simulate a Bragg peak, hence the requirement to use some 3D simulations of a quarter cell to verify the 2D simulations. Further details of these simulations can be found in reference [47].

The first stage of the simulations is forming a grid of the detector, simulating both the graphitic electrodes, modelled with a radius of $2\,\mu$m, and the diamond bulk itself. No defects were introduced in the simulation, which assumes the diamond is intrinsically perfect, and the only other characteristics defined for the electrodes were the applied bias voltage and their resistances, due to the complexity of the simulations and the time taken to simulate each position within the diamond substrate. The bandgap energy and dielectric constant of the diamond substrate were taken as 5.5 eV and 5.7, respectively.

The 3D simulations model the incident 4.5 MeV protons as a Bragg peak, with a charge density of $5.88 \times 10^{-5}\,\mathrm{pC}\mu\mathrm{m}^{-1}$ at the diamond surface, that is, $0 - 80\,\mu$m. A higher charge density of $4.24 \times 10^{-3}\,\mathrm{pC}\mu\mathrm{m}^{-1}$ was used at the range of the protons, that is, between $75 - 85\,\mu$m. The propagation of the charge carriers and the signal they induce on the readout electrode is then simulated by applying boundary conditions, to model the electric potential, and solving Poisson's equation alongside the electron and hole continuity equations [91]. The parameters for the electron and hole saturation velocities were taken from simulations performed by H. Pernegger et al. [31] to calculate the field dependent mobilities.

An electrode resistance of 175 kΩ was also simulated. The 2D simulations used a simulated charge of 6.40×10^{-6} pC, while the electrode resistance was modified from the 3D simulations in an attempt to alter the RC constant. The signal frequency spectrum is limited to 2 GHz in these simulations, corresponding to the bandwidth of the current amplifier, to simulate the effect of the amplifier chain used in the TRIBIC data acquisition.

A comparison these simulations is shown in Figure 6.11 and show good qualitative agreement, despite the use of an effective resistance in the 2D simulations and an overly simplified amplifier model. A faster rise time is observed in the high field region in the TRIBIC data and the simulations for both geometries, likely as a result

of the higher electric field strength in that region. The simulations of the square geometry, Figure 6.11a, in the low field region reveal a two peak structure which is not immediately visible in the TRIBIC data. In the hexagonal geometry, Figure 6.11b, this two peak structure is more easily observed in both the simulation and the TRIBIC data. It has been established previously that a two peak structure in low field regions is expected, so it is likely that there is a two peak structure in the square geometry but it is smeared out somewhat due to slight variations between the averaged positions. The shape of the peak in the TRIBIC data reflects this, given it is an unusually wide plateau that isn't observed in the hexagonal geometry.

Despite the high quality TRIBIC data, the agreement between the data and simulations is ultimately still qualitative. Although the peak amplitude agrees well between both data sets in the high field region, the width of the pulses is not in perfect agreement, though the agreement is still good. The agreement between the data sets in the low field region arguably opposes the agreement in the high field region. For example, the width of the pulses agree very well, but the amplitudes do not. It should be noted that the location of the two peaks in both data sets does agree very well and validates the steps performed in the simulations, in particular with the use of 2D simulations. Nevertheless, the assumptions made in the simulations, that is, modelling in 2D and the amplifier model, require some improvement in order to extract the charge carrier properties, such as their lifetimes.

6.1.4 Summary of Ox-001

Ox-001 was probed with a proton microbeam, and the improvement in the fabrication of the graphitic electrodes through the use of an SLM (including a higher electrode yield), and thus lower electrical resistivity, has resulted in high quality data. The cell uniformity increases with applied bias voltage for both square and hexagonal cell geometries. The charge collection efficiency of each geometry was compared and showed no indication that one geometry was preferable, and both geometries were consistent, with full charge collection observed at $|U_b| = 40\,\mathrm{V}$. Measurements of the charge sharing between neighbouring readout strips revealed a lower level of charge sharing for hexagonal cells versus square cells, with the potential for unique applications for each

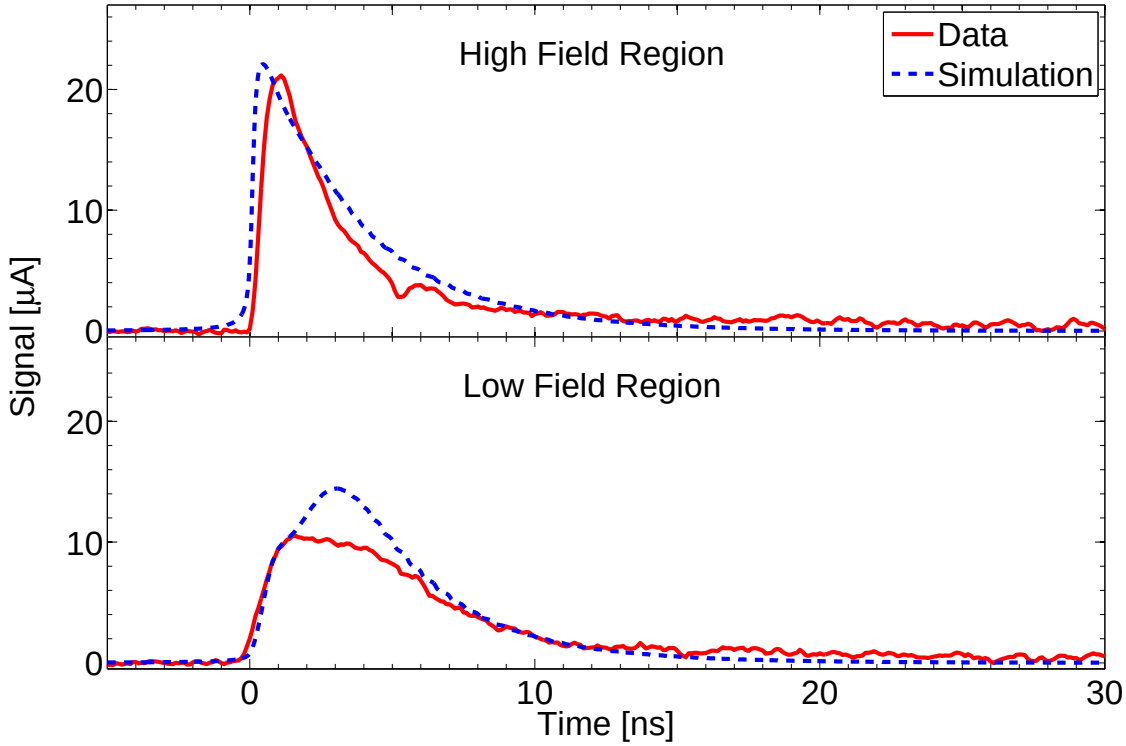

(a)

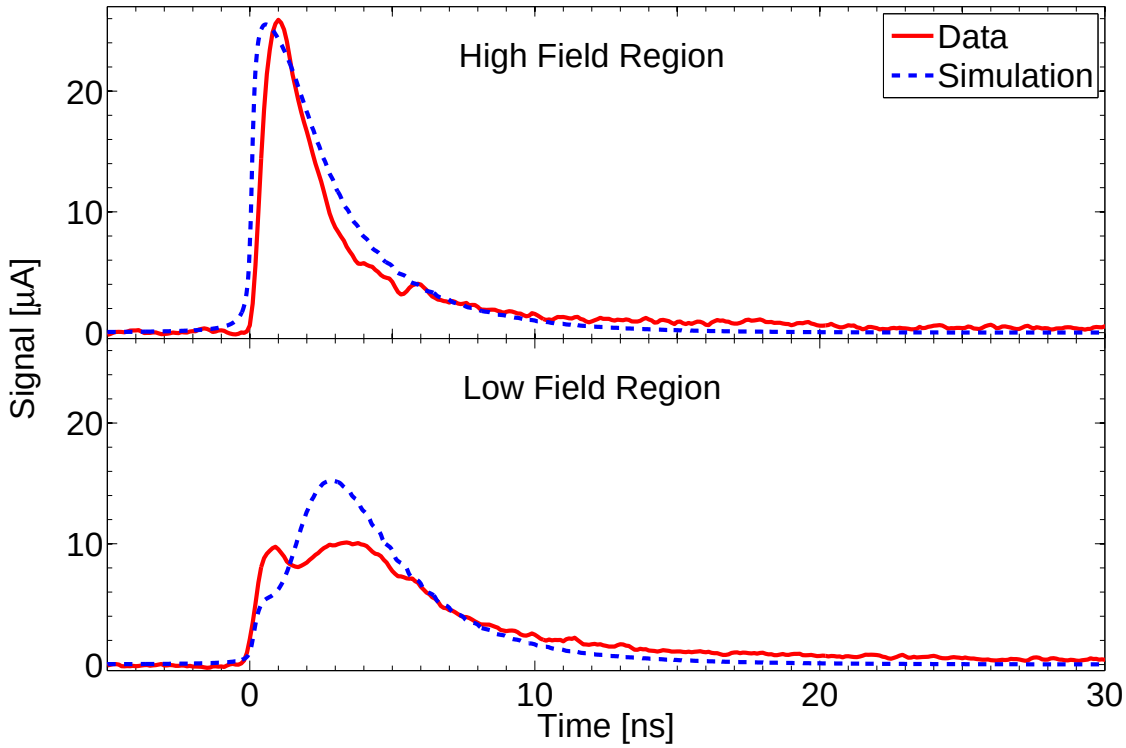

(b)

Figure 6.11: Comparison of TRIBIC and simulation data for (a) square cells, and (b) hexagonal cells. The protons were incident on the readout side of the detector in each case, with a bias voltage of $U_b = +20\,\mathrm{V}$. The simulation data were normalised to the TRIBIC data. All figures taken from reference [82].

cell geometry as a result. TRIBIC data were also acquired and is also of high quality, whereby no ringing component was observed due to the use of a high frequency carrier board. Comparisons of the two geometries reveal similar responses, with a higher amplitude and lower signal FWHM generally observed in the hexagonal cells due to a higher electric field strength from its geometry, though the measurements for each geometry are consistent. TRIBIC data were also recorded for protons incident on the bias side of the detector, where a higher RC time constant smeared the variation of the amplitude and FWHM of the waveforms, though this marks a step towards the ability to record the depth of induced charge in a 3D diamond detector. Finally, TRIBIC data was compared with simulations, showing good qualitative agreement. However, quantitative measurements for this detector are limited by the accuracy of the simulations, but such measurements are likely to be made in the future.

6.2 Detector Man-001

6.2.1 Motivation

The primary reason for the manufacture of detector Man-001 is to investigate the response of a diamond detector to particle beams. The response of 3D diamond detectors were investigated only for one beam type per detector prior to the fabrication of Man-001, so this device was the first 3D diamond detector to be probed with both photon and proton microbeams. The intention of this is to check if the response of the detector is similar for any incident particle, up to differences in collected charge resulting from different charge density profiles (explained later in this chapter).

A secondary reason for the manufacture of the detector is to characterise the detector in terms of its electrical resistivity, amongst other characterisation methods, which was discussed in Chapter 5.

It should be noted that the results presented in this chapter use array A (see Chapter 5 for details on this array). The choice of this array was made without prior information on the characteristics of the electrodes, specifically the electrode yield. As such, the results are of poorer quality versus those presented for the Ox-001 detector, so only key results for this detector are presented.

6.2.2 Photon test beam (XBIC)

The beam-line B16 [93] at Diamond Light Source, in Oxfordshire, was used to study the detector through X-ray beam induced current (XBIC). A monochromatic beam of photons was produced with an energy of 15 keV, with a full width half maximum (FWHM) of 5 μm. The beam flux was determined using an ionisation chamber, which was attenuated through the use of aluminium absorbers to O(10^6 photons per second). Further information about the beam-line can be found in reference [93].

Man-001 was mounted in a metal box and was shielded from light and electromagnetic noise [18] via an aluminium foil entrance window, with the photon beam incident perpendicular to the detector surface. Only arrays A and C were tested due to limitations in the beam time. In each array two adjacent readout strips were used, with applied bias voltages of ± 5 V, ± 40 V, and ± 60 V. Two Keithley 428 current amplifiers [94] measured the signals from two readout channels, while a data acquisition (DAQ) system recorded the beam current and position, the current of the ionisation chamber, and the ring current of the accelerator.

The fraction of particles which are transmitted through a substance is given by the Beer-Lambert law [95]. The signal response of the detector is calibrated by taking into account the fraction of photons that pass through the aluminium absorbers, T, and the fraction of photons which are absorbed by the diamond substrate, A, which by the law of total probability is given by $1 - T$. This is shown in Equation 6.2, where α is the attenuation coefficient of the material, and x is the material thickness. The attenuation coefficients for aluminium and diamond are $\alpha_{Al} = 21.48\,\mathrm{cm}^{-1}$ and $\alpha_C = 2.82\,\mathrm{cm}^{-1}$, respectively[6]. Taking $x_{Al} = 1.5$ mm and $x_C = 0.5$ mm, with an incident photon flux of 6.2×10^7 photons per second prior to the aluminium absorbers, gives the photon flux in the diamond of 3.3×10^5 photons per second.

$$F = T \times A = \exp\left(-\alpha_{Al} x_{Al}\right) \times \left[1 - \exp\left(-\alpha_C x_C\right)\right] \tag{6.2}$$

The expected current induced by incident 15 keV photons is the product of this photon flux in the diamond and the charge induced by a single photon, where the

[6]These values are calculated by taking the product of the known values of the mass attenuation coefficient, $\mu_{Al} = 7.96\,\mathrm{cm}^2\mathrm{g}^{-1}$ and $\mu_C = 0.81\,\mathrm{cm}^2\mathrm{g}^{-1}$ [96], and the density for each material, $\rho_{Al} = 2.70\,\mathrm{gcm}^{-3}$ and $\rho_C = 3.50\,\mathrm{gcm}^{-3}$ [97].

latter is the ratio of the photon energy to the electron-hole pair energy in diamond. Therefore, a current of 60 pA corresponds to 100% charge collection efficiency. The DAQ system was a triggerless DC readout, using an amplification factor of $10^9\,\mathrm{VA}^{-1}$.

The response of adjacent readout strips to photons as a function of position is shown in Figure 6.12, with the same readout line at $U_b = -5\,\mathrm{V}$ and $U_b = -40\,\mathrm{V}$, shown in Figures 6.12a and 6.12b, respectively. The response of the strips (that is, the charge collection efficiency) increases with bias voltage, as is observed (and explained) in data presented in Section 6.1. It is clear that the charge collected by each readout strip at $U_b = -40\,\mathrm{V}$, Figures 6.12b and 6.12d, is not localised to that strip. This is because only the two adjacent readout strips in the array were read out, and all other strips were not connected and were left at floating ground, due a limited number of readout connections in the DAQ system. As a result, all induced charge at positions beyond the readout strips was also collected due to the electric field strength, with the collection of induced charge decreasing with distance from the bias and readout electrodes within the readout strips. This induced charge could also be collected at lower bias voltages if the electric field strength were high enough, given that only a small fraction of such charge is collected at $U_b = -5\,\mathrm{V}$.

The response at $U_b = -40\,\mathrm{V}$, Figures 6.12b and 6.12d, can be compared to the response at $U_b = +40\,\mathrm{V}$, Figures 6.12e and 6.12f, where a significantly different response is observed. Although the response within the readout strips is mostly uniform, as is the case at $U_b = -40\,\mathrm{V}$, there is more charge collected from regions beyond the strips at $U_b = +40\,\mathrm{V}$. This effect is due to an asymmetry in the detector response at different bias polarities and also due to some "cross talk" between the two adjacent readout strips. The former is observed when comparing Figures 6.12b and 6.12e, where the metallisation pickup on the left hand side of the readout strip is noticeably different and the electrodes are more easily identifiable at $U_b = +40V$, likely indicating a weaker electric field. The latter effect is observed when comparing Figures 6.12e and 6.12f, where the signal observed in the top readout strip at approximately $x = -8.53\,\mathrm{mm}$ very closely matches the signal absent from the bottom readout strip at the exact same position in x.

A "shadow" of a gold wire bond is observed in Figures 6.12c and 6.12d due to the way in which the detector was read out. The wire bond is approximately 25 μm thick

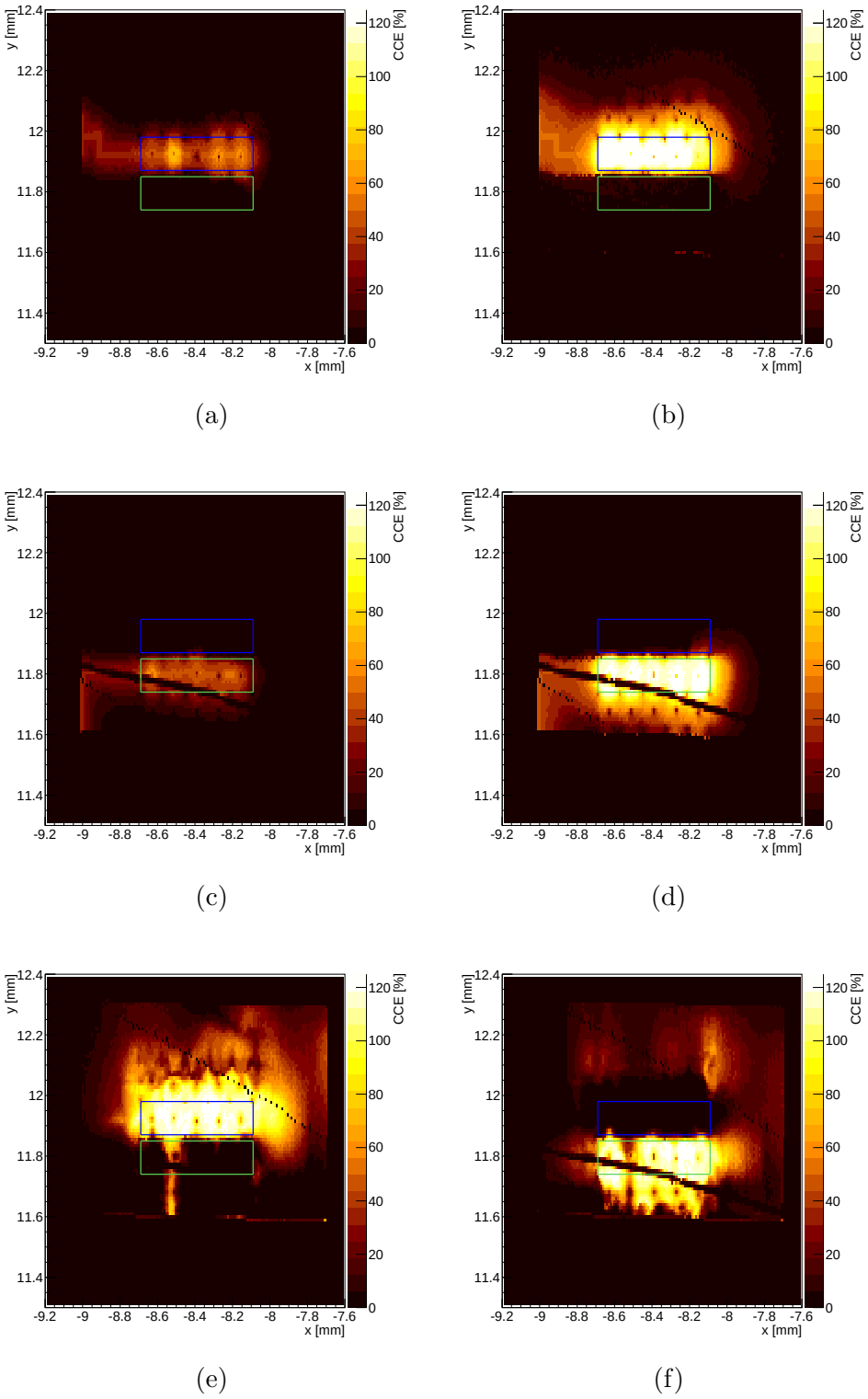

Figure 6.12: Response of Man-001 to photon beams for a range of bias voltages for array A. Two adjacent readout strips were probed with the photon beam. (a) Top readout strip, $U_b = -5\,\mathrm{V}$. (b) Top readout strip, $U_b = -40\,\mathrm{V}$. (c) Bottom readout strip, $U_b = -5\,\mathrm{V}$. (d) Bottom readout strip, $U_b = -40\,\mathrm{V}$. (e) Top readout strip, $U_b = +40\,\mathrm{V}$. (f) Bottom readout strip, $U_b = +40\,\mathrm{V}$. In each figure, the blue box denotes the top readout, while the green box denotes the bottom readout. Figures (a)-(d) are adapted from reference [73].

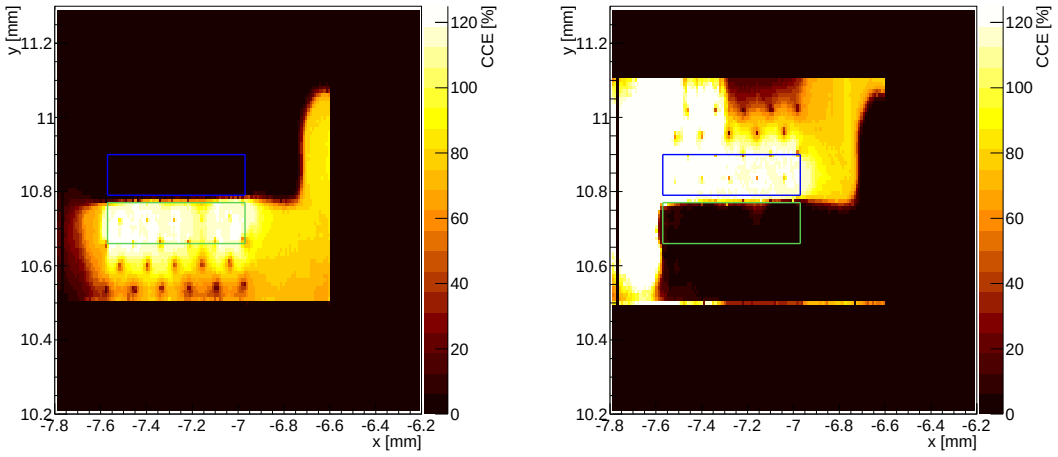

(a) (b)

Figure 6.13: Response of Man-001 to photon beams at $U_b = -40\,\mathrm{V}$ for array C. Two adjacent readout strips were probed with the photon beam. (a) Bottom readout strip. (b) Top readout strip. In each figure, the blue box denotes the top readout, while the green box denotes the bottom readout.

and attenuates the signal observed in this region by a factor of 2500 [96], as determined via the Beer-Lambert law, and explains why zero signal was observed.

The pickup due to metallisation is up to 30% at $U_b = 5\,\mathrm{V}$, as observed in Figures 6.12a and 6.12c, and is determined via the observation of signal in an area with graphitic electrodes. It is clear that the collection of the induced charge at this bias voltage is dominated by surface effects, such as the metallisation and surface currents, and little signal is observed otherwise. The metallisation pickup also increases with bias voltage where the pickup is up to 50%.

A comparison may also be made of the response of the readout strips in array A to that in array C, with the response at $U_b = -40\,\mathrm{V}$ shown in Figure 6.13. The response in this array is similar to array A in that it is mostly uniform and there is a noticeable level of signal pickup due to the metallisation. This means there is a negligible difference in the detector response from incident photons as a result of the different electrode properties, such as the electrical resistivity and electrode size, which were presented in the previous chapter. However, the metallisation pickup in array C seems higher than that in array A, as observed in the "hump" in the signal on the right hand edge of Figure 6.13a. This issue is more prevalent in Figure 6.13b on the left hand edge of the readout strip. The exact reason for this is not known,

though the effect due to the graphitic electrodes themselves may be ruled out, given that this effect is beyond the area in which the electrodes occupy.

6.2.3 Proton test beam (IBIC)

The proton microbeam at Ruder Boskovic Institute (IRB) at Zagreb [87] was used to study the detector response via ion beam induced current (IBIC), a complementary technique to XBIC. The setup itself is based on a Van-de-Graaff accelerator that produces a beam of 4 MeV protons, with a full-width half-maximum (FWHM) of O($\leq 2\,\mu$m). The data were recorded at $U_b = \pm 5\,\mathrm{V}$, $U_b = \pm 40\,\mathrm{V}$, and $U_b = \pm 60\,\mathrm{V}$, though only array A was tested during this beam time. The same readout strips on this array studied in the previous section were also tested during this beam time. Further details of the beam setup are discussed in reference [87].

It should be noted the DAQ system and calibration is similar to Ox-001, though the peak channel numbers differ by O(10%) rather than O(1%), resulting in an assigned uncertainty of 15% on these IBIC measurements. The x and y positions were also calibrated differently; each dimension was converted to a physical position and was then calibrated to match the positions recorded in the XBIC data. This was performed by eye where similar structures, such as the location of electrodes, were used as reference points.

The response of adjacent readout strips to protons as a function of position is shown in Figure 6.14, with the same readout line at $U_b = -5\,\mathrm{V}$ and $U_b = -40\,\mathrm{V}$ shown in Figures 6.14a and 6.14b, respectively. These readout strips are the same as those presented in Figure 6.12. These figures, and the other readout strip shown in Figures 6.14c and 6.14d, show the response of the strips at a higher bias voltage is slightly higher than the response at a lower bias voltage. The reason for the similarity of the response at different bias voltages is due to the difference in the absorption lengths of these particles inside the diamond substrate and the mechanism by which the charge is induced. For example, the absorption length of 15 keV photons in diamond is 3.56 mm [96], implying they typically pass through the detector. However, the absorption length of 4 MeV protons in diamond is O(80 μm) [27], implying they are typically stopped in the diamond bulk.

Other features identified from the response to a photon beam are also present. For

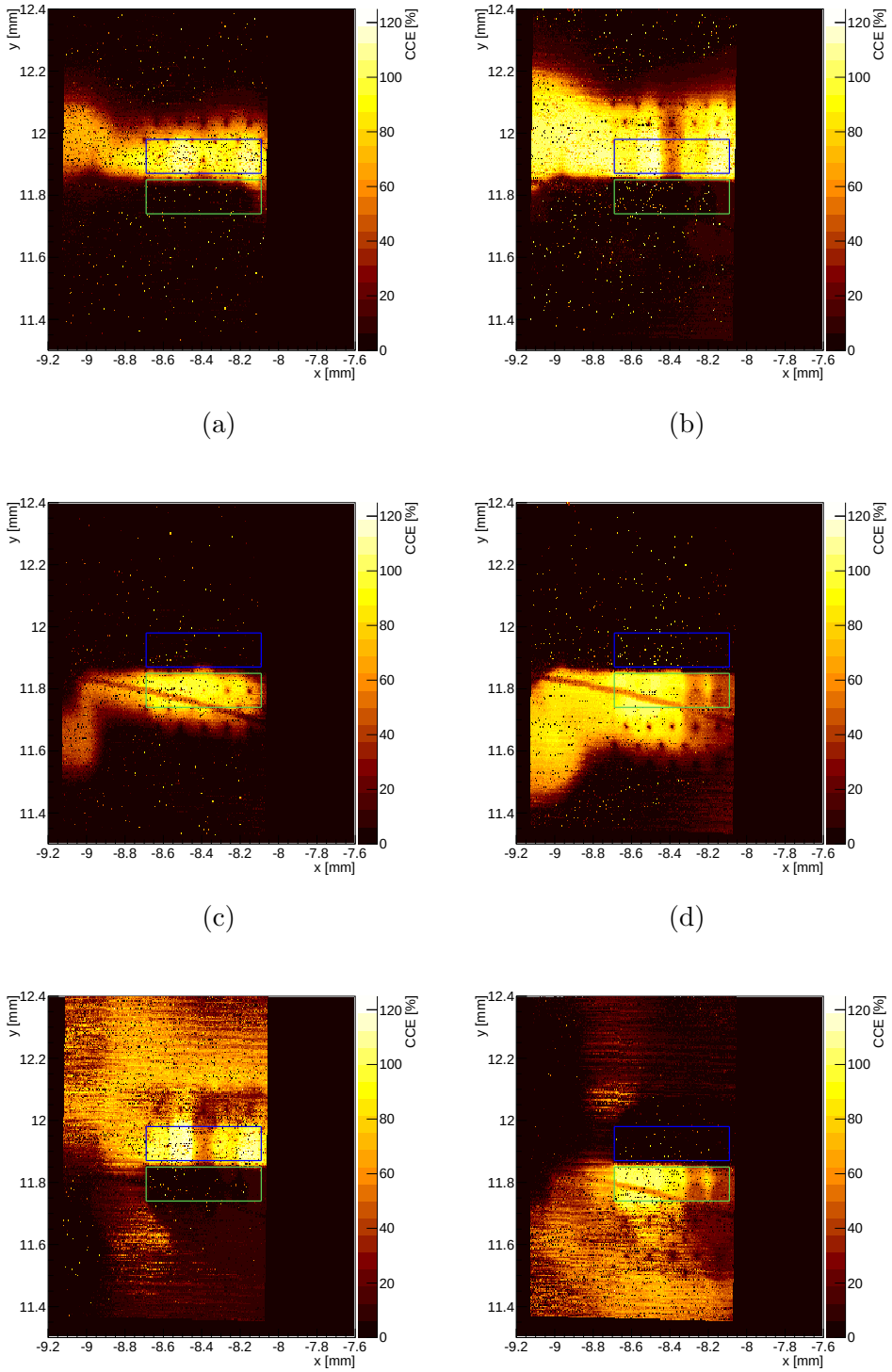

Figure 6.14: Response of Man-001 to a proton beam for a range of bias voltages for array A. Two adjacent readout strips were probed with the proton beam corresponding to the same readout strips shown in Figure 6.12. These figures have been translated to match the positions shown in Figure 6.12. (a) Top readout strip, $U_b = -5\,\mathrm{V}$. (b) Top readout strip, $U_b = -40\,\mathrm{V}$. (c) Bottom readout strip, $U_b = -5\,\mathrm{V}$. (d) Bottom readout strip, $U_b = -40\,\mathrm{V}$. (e) Top readout strip, $U_b = +40\,\mathrm{V}$. (f) Bottom readout strip, $U_b = +40\,\mathrm{V}$. In each figure, the blue box denotes the top readout, while the green box denotes the bottom readout. Figures (a)-(d) are adapted from reference [73].

example, the effect of the bond wire above the bottom readout strip can be seen, though it does not completely attenuate the incident protons. In this case, the absorption length of protons in the 25 μm gold bond wire is O(42 μm) [27], which indicates a significant fraction of protons pass through the bond wire. Similarly, the pickup due to metallisation also increases with bias voltage, though this signal pickup is significantly higher for protons compared to photons. This is likely due to the absorption length of the protons in diamond since the protons will be localised in the top surface of the diamond in closer proximity to the metallisation than photons. Additionally, the width of the region, that is, in y in these figures, in which charge is collected is of the same magnitude, O(200 μm), as for the XBIC data at $U_b = -40\,\mathrm{V}$, which again is due to the electric field strength.

Figures 6.14e and 6.14f show the response of the detector at $U_b = +40\,\mathrm{V}$, which significantly differs from the detector response at negative bias polarity, as was the case in the XBIC data. The readout strip in question is shown to have the highest charge collection efficiency (C.C.E.), but there is significantly more signal pickup in areas far beyond the readout strip. The exact reason for this is not known, though the most likely explanation is the pickup is due to surface current, given a similar, though less pronounced, effect is seen in the XBIC data. It is not unfeasible that some breakdown mechanism occurs in the device at or below $U_b = +40\,\mathrm{V}$, and the device breaks down at a much higher bias voltage in the negative polarity.

One way in which the two particle beams may be compared is to take a slice of the signals in one dimension, such as x, and compare the detector response for each particle type. Figure 6.15 shows that the shape of the response for each particle beam is largely similar. For example, Figure 6.15a shows the collection of charge increases at a similar rate around $y = 11.85\,\mathrm{mm}$, and the reduction in the charge collected occurs at similar positions, such as at $y = 11.92\,\mathrm{mm}$. This effect coincides with the location of the graphitic electrodes, and similar effects are also observed in Figure 6.15b. The difference in the height of the curves, the C.C.E., is purely due to the differences in ionisation profiles of the two particle beams. A comparison of these two overlay plots shows the charge sharing between the two readouts is consistent with the beam width for both particle beams. That is, no charge sharing is observed within the limits of the resolution of the beam width.

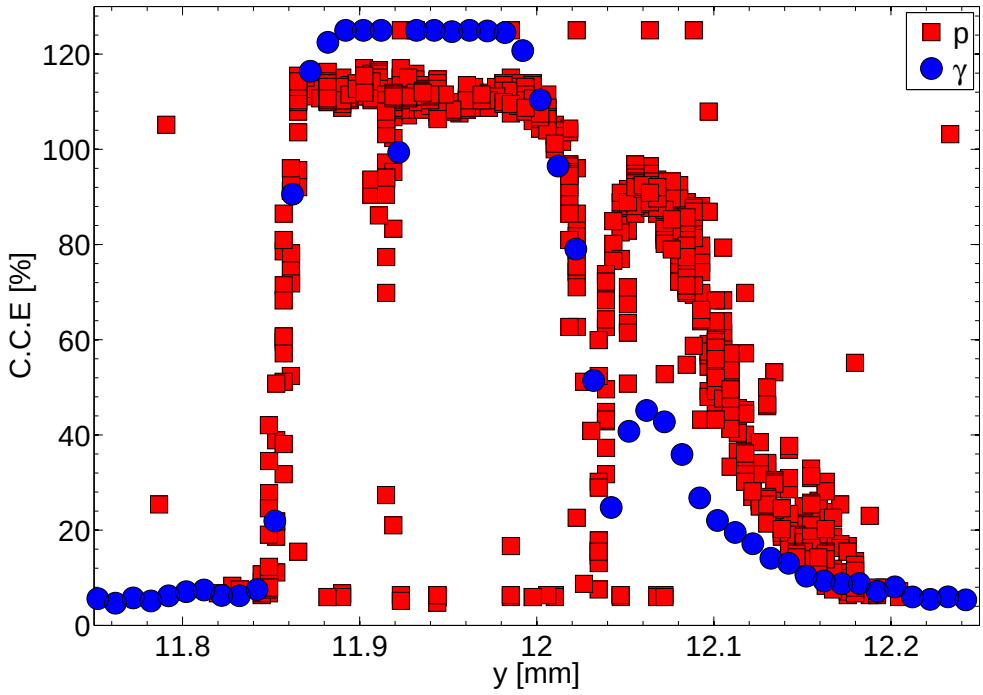

(a)

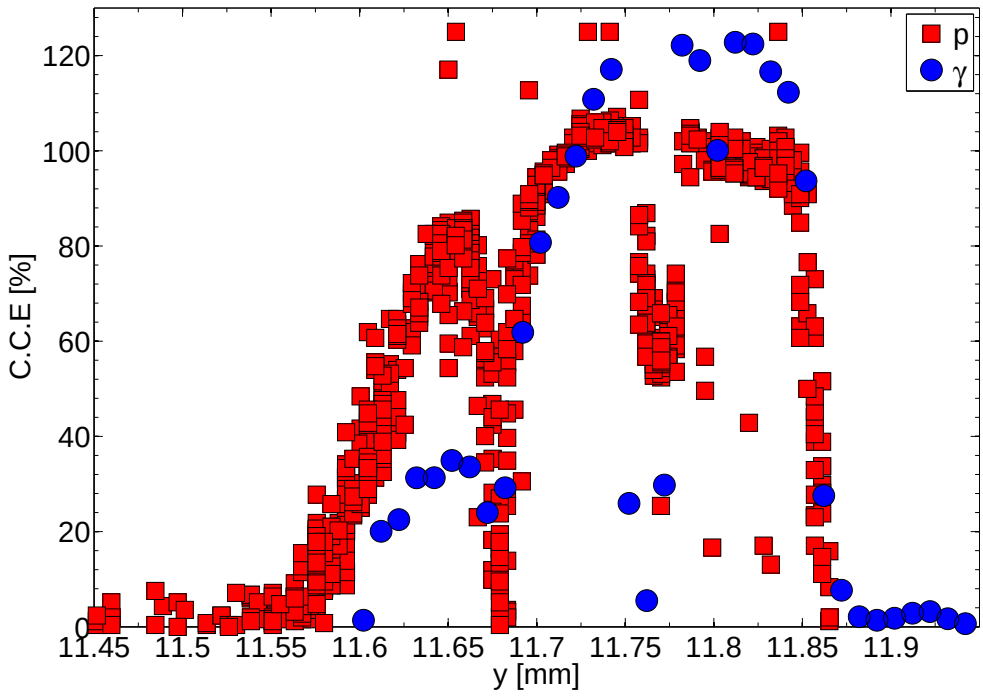

(b)

Figure 6.15: Response of Man-001 to a proton beam (red) and a photon beam (blue) at $U_b = -40\,\mathrm{V}$. The slice was taken at $x = -8.51$ (a) Top readout strip. (b) Bottom readout strip. Note that the charge collection efficiency is, in places, greater than 100%, though no evidence is seen for charge multiplication. The strip size in the y-direction is $120\,\mu\mathrm{m}$, with an expected electrode size of $\mathrm{O}(6\,\mu\mathrm{m})$. Both figures are adapted from reference [73].

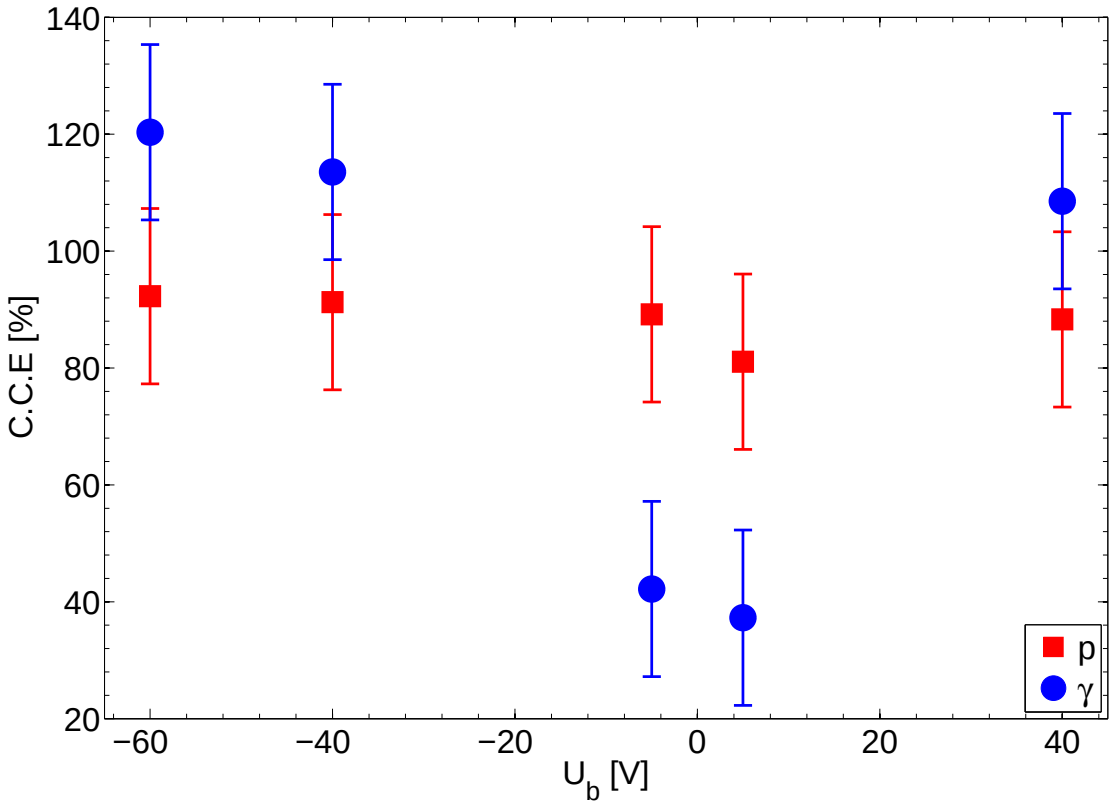

Figure 6.16: Charge collection efficiency of Man-001 as a function of bias voltage from incident protons (red) and photons (blue). Note that the charge collection efficiency is greater than 100%, though no evidence is seen for charge multiplication. Figure adapted from reference [73].

The average C.C.E. was calculated for each strip for each particle beam and is shown in Figure 6.16. The results of this figure have mostly been explained or observed previously. For example, the low C.C.E. for photons at $U_b = \pm 5\,\mathrm{V}$ is observable in the XBIC data, such as Figures 6.12a and 6.12c, and the limited improvement of the C.C.E. at higher bias voltages for protons is observable in the IBIC data, shown in a comparison of Figures 6.14a and 6.14b. The uncertainty of these measurements is set to the estimated calibration uncertainty in both particle beams, 15%. It is clear the results are inconsistent at $U_b = \pm 5\,\mathrm{V}$ for reasons outlined previously, though there is some degree of consistency at higher bias voltages. Although the XBIC data is significantly higher than 100% C.C.E., no evidence is observed in the plots already shown that illustrates charge multiplication, and the results are consistent with 100% C.C.E. to within 1.5σ.

6.2.4 Time-resolved IBIC (TRIBIC)

The TRIBIC data uses the same setup description described for Ox-001, with data taken at $U_b = \pm 60\,\mathrm{V}$ with protons incident on the readout side of the detector. The integrals are once again normalised to the IBIC data. The difference between Man-001 and Ox-001 is the lack of a high-frequency carrier board, which results in a strong sinusoidal component observed in the decay of the signal (see Figure 6.17). The TRIBIC setup and the printed circuit board were not optimised for high frequency, hence the high frequency ringing component. A Fourier transform was applied for each recorded waveform, where the modal frequency of 0.6467 GHz, a period of 1.5 ns, was taken as the ringing frequency.

A simple attempt was made to suppress the degree of ringing in the waveforms using this frequency. This was performed by applying an ad-hoc fit to the waveforms, given by Equation 6.3, where t_{offset} is the time at which the induced signal is recorded, t_{rise} is the time taken between zero signal and I_{max}, t_{decay} is the decay constant of the exponential, f is the ringing frequency, and ϕ is the phase. All of these parameters in the fit are allowed to vary, with the exception of the ringing frequency. Results of these fits at the same positions as the original data are shown in Figures 6.17b and 6.17d.

$$I(t) = \begin{cases} 0, & \text{for } \left[t \leq t_{\mathrm{offset}}\right] \\ I_{max}\frac{t - t_{\mathrm{offset}}}{t_{\mathrm{rise}}}, & \text{for } \left[t_{\mathrm{offset}} \leq t \leq t_{\mathrm{offset}} + t_{\mathrm{rise}}\right] \\ I_{max}\exp\left(-\dfrac{t - t_{\mathrm{offset}} - t_{\mathrm{rise}}}{t_{\mathrm{decay}}}\right) \times & \text{for } \left[t \geq t_{\mathrm{offset}} + t_{\mathrm{rise}}\right] \\ \cos\left(2\pi f(t - t_{\mathrm{offset}} - t_{\mathrm{rise}}) + \phi\right), & \end{cases} \tag{6.3}$$

A comparison of the original and "suppressed" traces show some degree of success with the suppression, given the reduction of the ringing component. However, "spikes" in the suppressed are observed in regions where the subtraction of this component was imperfect, which is readily observed in Figure 6.17b. This is attributed to the complexity of the fit, particularly the number of free parameters, along with the assumption made in the fits. The former implies a small chance of the fit failing and the best approximation before failing is taken. The latter may also result in the failure of the fit, given that several frequencies are required to more accurately reconstruct the data. Using just one frequency component, albeit the most dominant one, will

result in difficulty in reconstructing the fit. The difficulty of such a fit is also reflected in the $1\,\sigma$ contour in the waveforms, which is significantly wider in the suppressed data and indicates the calculation and subtraction of the ringing is imperfect.

The removal of the ringing component and the occurrence of these spikes also implies the overall amplitude slightly increases versus the original data. This implies the integral of the waveforms, which corresponds to the charge collected, is slightly larger in the suppressed data. This is observed when comparing Figures 6.17e and 6.17f, where in the latter the histogram is shifted to the right, that is, towards a higher C.C.E. The combination of this effect and the waveforms themselves led to the decision to analyse the original data over the suppressed data to avoid such unphysical artefacts. It is feasible that the ringing component could be removed more accurately by using more terms from the Fourier transform, though this would increase the time taken to fit to each waveform due to the higher number of parameters and fit complexity.

Figure 6.18 shows the measured amplitude, FWHM, and integral for $U_b = \pm 60\,\mathrm{V}$ for the original TRIBIC data. Despite the low quality traces, the amplitude plots, Figures 6.18a and 6.18b, indicate that the amplitude is highest near the electrodes, particularly the readout electrode (i.e. the centre of the cell). As such, the amplitude is lowest at the edges of the cell, that is, at points furthest from any given electrode. This result and similar results from the FWHM plots, Figures 6.18c and 6.18d, were previously demonstrated in Section 6.1.3. It should also be noted that there is less uniformity in the integral plots, Figures 6.18e and 6.18f, versus that presented in Section 6.1.3 due to the ringing issue.

Simulations of the waveforms were performed using the Synopsys TCAD package [90]. These simulations were performed by G. Forcolin and are discussed in more depth in reference [47]. Only 3D simulations were used for Man-001, and the signal frequency spectrum was not limited (see discussion in Section 6.1.3). The simulation parameters used for Man-001 remain the same as for Ox-001, despite the lower incident proton energy[7]. That is, the 3D simulations used charge densities of $5.88 \times 10^{-5}\,\mathrm{pC}\mu\mathrm{m}^{-1}$ and $4.24 \times 10^{-3}\,\mathrm{pC}\mu\mathrm{m}^{-1}$ at depths of $0 - 80\,\mu\mathrm{m}$ and $75 - 85\,\mu\mathrm{m}$, respectively, as an approximation of the Bragg peak.

[7]It has been shown that the difference between incident protons of energy 4 MeV and 4.5 MeV is negligible, hence the same simulation parameters. This is discussed further in reference [47].

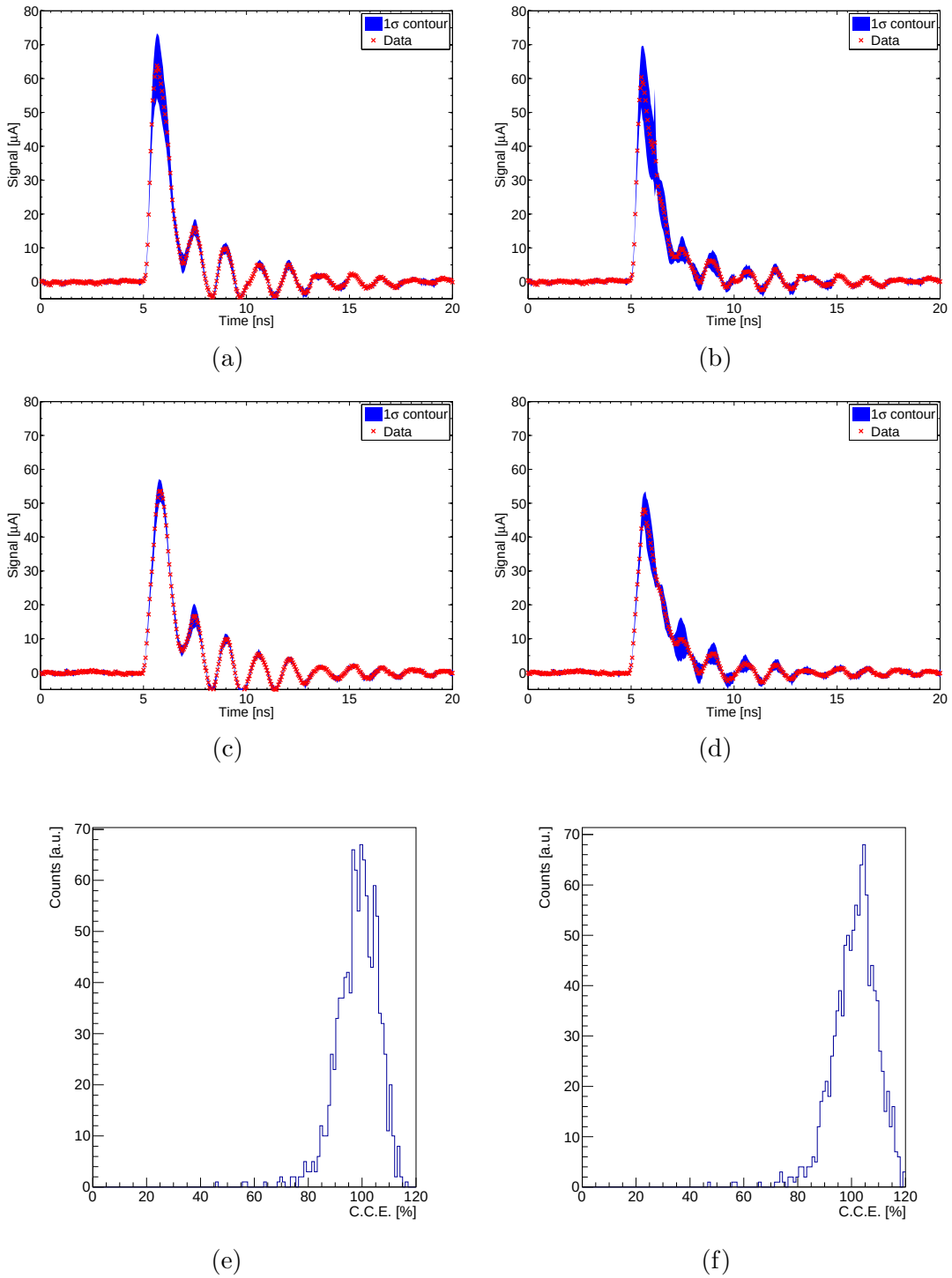

Figure 6.17: 1D TRIBIC waveforms for Man-001 showing the current as a function of time. The left images ((a), (c), and (e)) show the original waveforms, while the right images ((b), (d), and (f)) show the waveforms which have had the ringing component suppressed. The blue contours in Figures (a)-(d) result from averaging waveforms at a given location and its 4 nearest neighbours. The integral histograms ((e) and (f)) are normalised to the IBIC data.

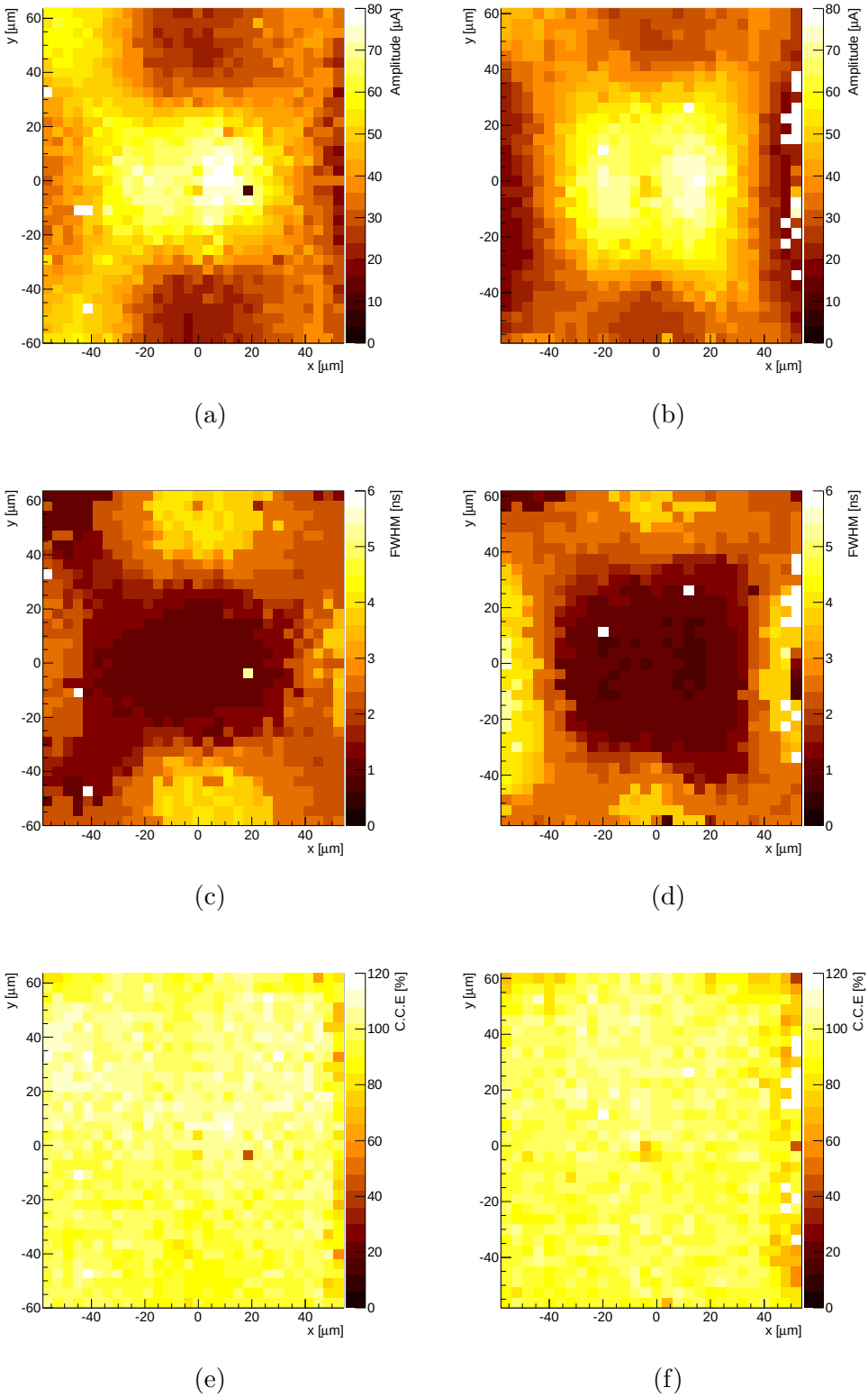

Figure 6.18: 2D TRIBIC plots for Man-001 showing the amplitude, FWHM, and integral of the TRIBIC pulses at two different bias polarities. (a) Amplitude plot, $U_b = +60\,\mathrm{V}$. (b) Amplitude plot, $U_b = -60\,\mathrm{V}$. (c) FWHM plot, $U_b = +60\,\mathrm{V}$. (d) FWHM plot, $U_b = -60\,\mathrm{V}$. (e) Integral plot, $U_b = +60\,\mathrm{V}$. (f) Integral plot, $U_b = -60\,\mathrm{V}$. The peak value in the integral plots is normalised to the IBIC data.

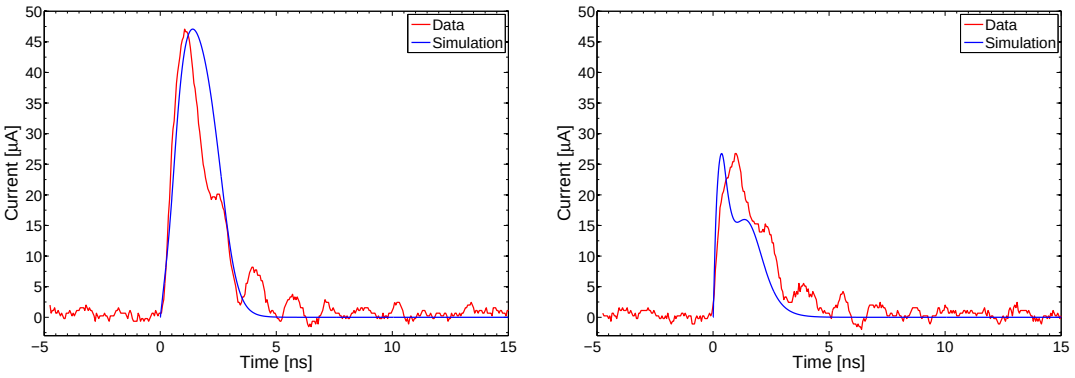

(a) (b)

Figure 6.19: 1D TRIBIC waveforms for Man-001 versus simulations. The data were taken at (a) the central point between two electrodes (30,30) and (b) near a bias electrode (54,54), with the coordinate system as defined in Figure 6.18. The bias voltage for each figure is +60 V, and the simulation data are normalised to the amplitude of the TRIBIC data.

A comparison of these simulations to the TRIBIC data are shown in Figure 6.19. Differences are observed between the two positions, in the high and low field regions close to and far from an electrode, respectively, in both the simulations and TRIBIC data. For example, data at the central point between two electrodes, Figure 6.19a, shows no substructure (aside from the ringing present in the TRIBIC data), while data near a bias electrode, Figure 6.19b, reveals definitive substructure in the simulation and in the TRIBIC data. Although the peak heights of the simulation and TRIBIC data are similar in Figure 6.19b, differing by O(0.1 μA), it is not clear whether this is a genuine signal or a ringing artefact. These plot not only highlight the difficulty in subtracting the ringing contribution from the TRIBIC data using the outlined method, but also the difficulty in achieving agreement between data and simulation likely due to the presence of the ringing in the experimental data.

6.2.5 Summary of Man-001

Man-001 was probed with photon and proton microbeams, the first 3D diamond detector to be probed with both beam sources, with a visible response observed from both beam sources. A large signal pickup due to metallisation was observed in both the XBIC and IBIC data. The response of the detector from these particle beams was mostly the same at high bias voltages, despite the difference in ionisation profiles

of the beam sources. The data quality was not optimal, due to the pickup from the metallisation and surface currents on the detector. The C.C.E. as a function of bias voltage for both the XBIC and IBIC data was determined, which was consistent with the expected ionisation profiles of these beams and no evidence for charge multiplication was observed. Similarly, the amount of charge sharing between the readout strips used was consistent with the FWHM of the beams, so no evidence for charge sharing was observed. TCT measurements were also taken on the detector using a proton beam source and showed results consistent with the expected electric field strength due to the 3D geometry. A ringing component was identified in these data due to a non-optimal readout setup, and an unsuccessful attempt was made to remove this ringing. The data were compared to simulation and shows qualitative agreement, though the presence of ringing in the data prevents any quantitative measurements, such as carrier lifetimes.

Chapter 7

Conclusions and Outlook

The work presented in the previous two chapters has shown that the use of a femtosecond laser in the fabrication of graphitic electrodes is a novel technique for the manufacture of 3D diamond detectors. The necessity of this work, specifically the importance of fabricating these electrodes, is driven by the requirement to overcome the material cost of diamond and thus make diamond detectors more competitive for potential large scale detectors. In particular, 3D diamond detectors are highly desired in high radiation environments, including high energy physics experiments, such as the Large Hadron Collider, and for use in cancer therapy as a dosimeter.

The optical setup used for the graphitisation process limits some of the characteristics of the electrodes important in 3D detectors, namely the electrode diameter and resistivity. These parameters need to be reduced to maximise the detector area, a key area to reduce the overall cost of 3D diamond detectors, and to reduce the collection time of the charge carriers, respectively. It has been shown that the use of an SLM improves these characteristics more than is feasible from conventional optics.

It has been demonstrated that an increase in the focal spot energy density increases the electrode diameter, which also increases the relative stress induced by the electrodes on the diamond itself. The use of an SLM improves the electrode yield, reduces the electrode diameter, and reduces the electrode resistivity, thus leading the way to 3D diamond detectors with a high cell density, that is, those with a smaller electrode separation. A simple method to deduce the graphitisation threshold has been shown, which could be used for future studies into graphite formation in diamond, particularly the difference in thresholds for both fabrication techniques.

Several characterisation methods were presented in this thesis to help verify the electrode fabrication process. Characterisation through the use of a pair of crossed polarisers reveals stress is induced in the diamond samples, which arise from either impurities and grain boundaries forming during the diamond fabrication process or from the presence of the graphitic electrodes. This technique has been used to identify partially formed electrodes, and thus potential "dead" areas if it were used as a diamond detector. It has also been used to identify, qualitatively, how the stress varies as a function of processing parameters to limited success. This is improved further by taking difference images of the sample before and after laser processing at the same position to account for stress induced by impurities and or grain boundaries, resulting in the stress induced by the electrodes only. It has been shown that the use of an SLM increases the stress induced by the electrodes due to a larger conversion rate of diamond to graphite at the focal point of the laser.

Characterisation via I-V curves has shown that there is a conversion of diamond to a conductive, graphite-like phase at the focal point of the laser. The resistance of the electrodes, as well as the non-linearity intercept, reduces as the beam energy increases, implying more conductive material forms at higher energies. In particular, the electrode material is more continuous at higher beam energies, whereby discontinuities in the electrode are assumed to be diamond. In conjunction with this, measurements from the I-V curves demonstrated that the use of an SLM is paramount in reducing the resistance of the electrodes, and the inclusion of SLMs for electrode fabrication is highly desirable.

Characterisation via SEM has identified the mechanism by which graphitic electrodes form within diamond. Excess material forms on the seed side with the chance of a small crater forming if the focal spot energy density is high enough, while a large crater forms on the exit side with a large "pop off" effect of both the surrounding area and the central electrode. This process is driven by a pressure build-up, and thus increasing induced stress, inside the diamond, whereby the electrode preferentially forms in the direction of beam incidence. SEM images have also shown the appearance of fringes for high quality optics, which arise from surface plasmon polaritons. These fringes appear to be related to the wavelength of the laser used for electrode fabrication, and their orientation is related to the polarisation of the laser. Further study

into these properties would likely yield a different fringe separation and orientation, which could alter the bulk parameters of the electrodes such as their resistivity.

Characterisation via Raman spectroscopy has revealed that the excess material formed on the seed side of the electrodes, identified through SEM images, is graphite, and measuring the ratio of diamond and graphite G peaks shows this ratio is generally lower on the seed side versus the exit side. Work performed by L. Graber [81] and work presented in this thesis both show agreement that a high beam power and fast translation speed provides the lowest diamond to graphite ratio, indicating more conductive material and thus a lower electrode resistivity. This work also proves that the maximum translation speed appears to scale with pulse repetition rate. A study into the processing parameters and the two fabrication techniques has shown that the use of an SLM is preferable for obtaining reliable measurements of the diamond to graphite ratio, and hints at the possibility of faster translation speeds with the use of an SLM only. This would increase the fabrication time of 3D diamond detectors and is, therefore, vital for their future viability.

Diamond detectors were also characterised through their response to particle beams. It has been shown that their response is intuitive and good agreement is observed for characterisation via both photon (XBIC) and proton (IBIC) beams, and this work demonstrates the first such comparison for 3D diamond detectors. An issue identified through this work is the signal pickup by the metallisation and surface current that account for a sizeable fraction of the charge collection efficiency of the detector. It is possible, though not shown in this work, to use an SLM to form graphitic channels in the diamond that function in a similar manner to the surface metallisation, but with a reduction of the surface current at the cost of fabrication time. The feasibility and effectiveness of this idea remains an area for future research. The data quality for this detector was limited due to no optimisation of carrier boards and the limitation of the electrode resistivity for this non-SLM fabricated device, which prevented high agreement of transient current technique (TCT) measurements with simulations.

The use of a SLM fabricated device drastically improved the quality of the data obtained from particle beams and allowed for further analysis. This resulted from an improvement to the electrode resistivity and the fabrication of a carrier board to filter high frequency noise. Square and hexagonal cell geometries were investigated and there

is no clear preference for either geometry in terms of the charge collection efficiency and cell uniformity. A significant difference was observed in the width of the charge sharing region, which indicates the potential for these geometries to be used in different environments. The previously mentioned improvements filtered out a high frequency ringing component in the TCT measurements and allowed for much greater agreement with simulations. The limitation in data from this SLM fabricated device comes from a lack of understanding of the simulations, and extraction of charge carrier properties was not possible. Further work into the simulations will yield insight into the charge carrier dynamics in 3D diamond detectors and deduction of the lifetimes of electrons and holes in diamond. TCT measurements were also taken on the bias side of the detector for the first time and reveals the signal is dominated by the RC time constant due to a much higher "observed" electrode resistance, smearing out variations in the signal at different XY positions. However, this is the first stage towards identifying the depth of induced charge in 3D diamond detectors. Regardless of the fabrication technique no charge multiplication was observed in 3D diamond detectors.

This work has identified areas of improvement and need of further research. For example, a much larger study into the effect of processing parameters and fabrication techniques on electrode formation is highly recommended since the study presented in this work is both systematically and statistically limited. This would also allow for the limits of electrode fabrication to be deduced for each processing parameter and fabrication technique, which would be found by using the characterisation techniques presented in this thesis. This study could also provide a starting point for some simulations of the electrode formation in the diamond bulk, which could help to explain why graphite is more prevalent on the seed side of the diamond. Another area of improvement would be the fabrication and characterisation of devices with much higher cell densities. Such a study is imperative to see if significant stress is induced within the diamond due to electrode proximity, identifiable through crossed polariser image characterisation, and to investigate the feasibility of reading out such a device. Characterisation of the device via particle beams would also be crucial for investigations into the width of the charge sharing region and whether this would limit the viability of the device.

In conclusion, this work has demonstrated that diamond detectors, while very much

still in their infancy versus silicon detectors, are a competitive alternative for the future of the LHC and other high luminosity experiments. However, there are many issues with diamond detectors that need to be addressed if they are to be used in the LHC, with the earliest opportunity coinciding with Phase 2 beginning in 2023. The use of the characterisation methods presented in this thesis, alongside the identification of the use of an SLM in laser processing, provide a basis to be built upon for further research into this field, and to make the insertion of 3D diamond detectors in the LHC not only possible, but also more likely.

Bibliography

[1] M. Robinson, *Symmetry and the Standard Model: Mathematics and Particle Physics*. Springer, 2011.

[2] The ATLAS Collaboration, "Observation of a new particle in the search for the Standard Model Higgs boson with the ATLAS detector at the LHC," *Physics Letters B*, vol. 716, pp. 1–29, 2012.

[3] P. W. Higgs, "Broken Symmetries and the Masses of Gauge Bosons," *Physical Review Letters*, vol. 13, pp. 508–509, 1964.

[4] F. Englert and R. Brout, "Broken Symmetry and the Mass of Gauge Vector Mesons," *Physical Review Letters*, vol. 13, pp. 321–323, 1964.

[5] G. Guralnik, C. R. Hagen, and T. W. B. Kibble, "Global Conservation Laws and Massless Particles," *Physical Review Letters*, vol. 13, pp. 585–587, 1964.

[6] S. I. Parker, C. J. Kenney, and J. Segal, "3D - a proposed new architecture for solid-state radiation detectors," *NIM Phys A*, vol. 395, pp. 328–343, 1997.

[7] C. Da Via and S. J. Watts, "The geometrical dependence of radiation hardness in planar and 3D silicon detectors," *NIM Phys A*, vol. 603, pp. 319–324, 2009.

[8] T. Schörner Sadenius, *The Large Hadron Collider: Harvest of Run 1*. Springer, 2015.

[9] F. Bordry. Presentation on the LHC schedule beyond LS1. Accessed 05-2017. [Online]. Available: https://lhc-commissioning.web.cern.ch/lhc-commissioning/schedule/LHC%20schedule%20beyond%20LS1%20MTP%202015_Freddy_June2015.pdf

[10] The CERN Collaboration. The HL-LHC Project. Accessed 07-2017. [Online]. Available: http://hilumilhc.web.cern.ch/about/hl-lhc-project

[11] The ATLAS Collaboration, "Letter of Intent for the Phase-II Upgrade of the ATLAS Experiment," *Geneva: CERN, LHC-I-023*, 2012.

[12] The CERN Collaboration. The FCC Project. Accessed 07-2017. [Online]. Available: https://fcc.web.cern.ch/Pages/Concepts.aspx

[13] M. I. Besana, F. Cerutti, A. Ferrari, W. Riegler, and V. Vlachoudis, "Characterisation of the Radiation Field in the FCC-HH Detector," in *Proceedings, 7th International Particle Accelerator Conference (IPAC 2016)*, K. S. Kim, I. S. Ko, K. R. Kim, and V. R. W. Schaa, Eds.

[14] B. Caylar, M. Tomasz, and P. Bergonzo, "Laser-processed three dimensional graphitic electrodes for diamond radiation detectors," *Applied Physics Letters*, vol. 103, 2013.

[15] S. Lagomarsino, M. Bellini, C. Corsi, F. Gorelli, G. Parrini, M. Santoro, and S. Sciortino, "Three-dimensional diamond detectors: Charge collection efficiency of graphitic electrodes," *Applied Physics Letters*, vol. 103, 2013.

[16] F. Bachmair, L. Bäni, P. Bergonzo, B. Caylar, G. Forcolin, I. Haughton, D. Hits, H. Kagan, R. Kass, L. Li, A. Oh, S. Phan, M. Pomorski, D. S. Smith, V. Tyzhnevyi, R. Wallny, and D. Whitehead, "A 3D diamond detector for particle tracking," *NIM Phys A*, vol. 786, pp. 97–104, 2015.

[17] S. Lagomarsino, M. Bellini, C. Corsi, V. Cindro, K. Kanxheri, A. Morozzi, D. Passeri, L. Servoli, C. J. Schmidt, and S. Sciortino, "Radiation hardness of three-dimensional polycrystalline diamond detectors," *Applied Physics Letters*, vol. 106, 2015.

[18] A. Oh, B. Caylar, M. Pomorski, and T. Wengler, "A novel detector with graphitic electrodes in CVD diamond," *Diamond and Related Materials*, vol. 38, pp. 9–13, 2013.

[19] E. Berdermann, K. Blasche, P. Moritz, H. Seltzer, B. Voss, and F. Zeytouni, "First applications of CVD-diamond detectors in heavy-ion experiments," *Nuclear Physics B*, vol. 78, pp. 533–539, 1999.

[20] G. Barr, R. Devenish, R. Walczak, and T. Weidberg, *Particle Physics in the LHC Era.* Oxford University Press, 2016.

[21] T. K. Gupta, *Radiation, Ionization, and Detection in Nuclear Medicine.* Springer, 2013.

[22] G. Schultz, G. Charpak, and F. Sauli, "Mobilities of positive ions in some gas mixtures used in proportional and drift chambers," *Physical Review Applied*, vol. 12, pp. 67–70, 1977.

[23] R. Baragiola, *Ionization of Solids by Heavy Particles.* Springer, 2012.

[24] The ATLAS Collaboration, "ATLAS detector and physics performance: Technical Design Report 1," *Geneva: CERN*, pp. 3–27, 1999.

[25] J. Beringer et al. (PDG). Passage of particles through matter. Accessed 07-2017. [Online]. Available: http://pdg.lbl.gov/2012/reviews/rpp2012-rev-passage-particles-matter.pdf

[26] W. R. Leo, *Techniques for Nuclear and Particle Physics Experiments: A How-to Approach.* Springer, 2012.

[27] M. J. Berger, J. S. Coursey, M. A. Zucker, and J. Chang. Stopping-power and range tables for electrons, protons, and helium ions. Accessed 04-2017. [Online]. Available: https://www.nist.gov/pml/stopping-power-range-tables-electrons-protons-and-helium-ions

[28] J. F. Ziegler. SRIM - The Stopping and Range of Ions on Matter. Accessed 07-2017. [Online]. Available: http://www.srim.org/

[29] W. Shockley, "Currents to Conductors Induced by a Moving Point Charge," *Journal of Applied Physics*, vol. 9, 635, 1938.

[30] S. Ramo, "Currents Induced by Electron Motion," in *Proceedings of the IRE, 27 (9).*

[31] H. Pernegger, S. Roe, and P. Weilhammer, "Charge-carrier properties in synthetic single-crystal diamond measured with the transient-current technique," *Journal of Applied Physics*, vol. 97, 2005.

[32] W. Primak, L. H. Fuchs, and P. P. Day, "Radiation Damage in Diamond and Silicon Carbide," *Physical Review 103*, vol. 1184, 1956.

[33] B. Campbell and A. Mainwood, "Radiation Damage of Diamond by Electron Gamma Irradiation," *Physica Status Solidi (A)*, vol. 181, pp. 99–107, 2000.

[34] A. V. Khomich, R. A. Khmelnitskii, X. J. Hu, A. A. Khomich, A. F. Popovich, I. I. Vlasov, V. A. Dravin, Y. G. Chen, A. E. Karkin, and V. G. Ralchenko, "Radiation Damage Effects on Optical, Electrical, and Thermophysical Properties of CVD Diamond Films," *Journal of Applied Spectroscopy*, vol. 80, pp. 707–714, 2013.

[35] B. Alessandro, S. Antinori, R. Bala, G. Batigne, S. Beolè, E. Biolcati, N. Bock Garcia, E. Bruna, P. Cerello, S. Coli, Y. Corrales Morales, F. Costa, E. Crescio, P. De Remigis, S. Di Liberto, D. Falchieri, G. Feofilov, W. Ferrarese, E. Gandolfi, C. Garcia, L. Gaudichet, G. Giraudo, P. Giubellino, T. J. Humanic, S. Igolkin, M. Idzik, S. K. Kiprich, A. Kisiel, A. Kolozhvari, I. Kotov, J. Kral, S. Kushpil, V. Kushpil, R. Lea, M. A. Lisa, M. I. Martinez, A. Marzari Chiesa, M. Masera, M. Masetti, G. Mazza, M. A. Mazzoni F Meddi, L. M. Montano Zetina, M. Monteno, B. S. Nilsen, D. Nouais, F. Padilla Cabal, V. Petráček, M. G. Poghosyan, F. Prino, L. Ramello, A. Rashevsky, L. Riccati, A. Rivetti, S. Senyukov, M. Siciliano, M. Sitta, M. A. Subieta Vasquez, M. Sumbera, L. Toscano, F. Tosello, D. Truesdale, G. M. Urciuoli, A. Vacchi, S. Vallero, A. Werbrouck, G. Zampa, and G. Zinovjev, "Operation and calibration of the Silicon Drift Detectors of the ALICE experiment during the 2008 cosmic ray data taking period," *Journal of Instrumentation*, vol. 5, p. P04004, 2010.

[36] C. Da Via. Silicon sensors go 3D. Accessed 01-2017. [Online]. Available: http://cerncourier.com/cws/article/cern/49691

[37] B. Caylar. Fabrication, Characterization of a 3D Diamond Detector. Unpublished Talk from the 13th Vienna Conference on Istrumentation, 2013, Accessed 08-2017. [Online]. Available: http://slideplayer.com/slide/10694787/

[38] K. Kanxheri, L. Servoli, A. Oh, F. Munoz Sanchez, G. T. Forcolin, S. A. Murphy, A. Aitkenhead, C. J. Moore, A. Morozzi, D. Passeri, M. Bellini, C. Corsi, S. Lagomarsino, and S. Sciortino, "Evaluation of a 3D diamond detector for medical radiation dosimetry," *Journal of Instrumentation*, vol. 12, 2017.

[39] C. Bauer, I. Baumann, C. Colledani, J. Conway, P. Delpierre, F. Djama, W. Dulinski, A. Fallou, K. K. Gan, R. S. Gilmore, E. Grigoriev, G. Hallewell, S. Han, T. Hessing, K. Honschied, J. Hrubec, D. Husson, R. James, H. Kagan, D. Kania, R. Kass, K. T. Knöpfle, M. Krammer, T. J. Llewellyn, P. F. Manfredi, D. Meier, L. S. Pani, H. Pernegger, M. Pernicka, V. Re, S. Roe, D. Roff, A. Rudge, M. Schaeffer, M. Schieber, S. Schnetzer, S. Somalwar, V. Speziali, R. Stone, R. J. Tapper, R. Tesarek, W. Trischuk, R. Turchetta, G. B. Thomson, R. Wagner, P. Weilhammer, C. White, H. J. Ziock, and M. Zoeller, "Recent results from the RD42 diamond detector collaboration," *NIM Phys A*, vol. 383, pp. 64–74, 1996.

[40] NSM. Properties of semiconductor materials. Accessed 01-2017. [Online]. Available: http://www.ioffe.ru/SVA/NSM/Semicond/

[41] H. Spieler, *Semiconductor Detector Systems*. OUP Oxford, 2005.

[42] M. Červ, "The ATLAS Diamond Beam Monitor," *Journal of Instrumentation*, vol. 9, 2014.

[43] D. M. Schaefer, "The ATLAS Diamond Beam Monitor: Luminosity detector at the LHC," *NIM Phys A*, vol. 824, pp. 459–461, 2016.

[44] N. Venturi, "Diamond Pixel Detectors and 3D Diamond Devices," *Journal of Instrumentation*, vol. 11, 2016.

[45] Element Six Ltd. The Element Six CVD Diamond Handbook. Accessed 07-2017. [Online]. Available: https://e6cvd.com/media/wysiwyg/pdf/E6_CVD_Diamond_Handbook_A5_v10X.pdf

[46] IIa Technologies Ltd. IIa Diamond Properties. Accessed 03-2017. [Online]. Available: http://2atechnologies.com/2a-diamond-properties/

[47] G. T. Forcolin, "Development and Simulation of 3D Diamond Detectors," 2017, Unpublished Doctoral Thesis.

[48] T. Behnke, P. Huntemeyer, A. Oh, J. Steuerer, A. Wagner, and W. Zeuner, "The charge-collection properties of CVD diamond," *NIM Phys A*, vol. 414, pp. 340–356, 1998.

[49] L. Schäfer, A. Bluhm, M. Paul, A. Oh, A. Wagner, and W. Zeuner, "Development of chemical vapour deposited diamond films for particle detector applications," *Diamond and Related Materials*, vol. 7, 1998.

[50] J. Isberg, J. Hammersberg, H. Bernhoff, D. J. Twitchen, and A. J. Whitehead, "Charge collection distance measurements in single and polycrystalline CVD diamond," *Diamond and Related Materials*, vol. 13, 2004.

[51] S. Franssila, *Introduction to Microfabrication*. John Wiley and Sons, 2010.

[52] H. O. Jeschke, M. E. Garcia, and K. H. Bennemann, "Microscopic analysis of the laser-induced femtosecond graphitization of diamond," *Phys Rev B*, vol. 60, 1999.

[53] T. V. Kononenko, M. S. Komlenok, V. P. Pashinin, S. M. Pimenov, V. I. Konov, M. Neff, V. Romano, and W. Lüthy, "Femtosecond laser microstructuring in the bulk of diamond," *Diamond and Related Materials*, vol. 18, pp. 196–199, 2009.

[54] Coherent Inc. Coherent Inc. Vitesse Seed Laser. Accessed 10-2016. [Online]. Available: https://www.coherent.com/products/?1439/Vitesse

[55] C. B. Hitz, J. J. Ewing, and J. Hecht, *Introduction to Laser Technology*. John Wiley and Sons, 2012.

[56] D. Strickland and G. Mourou, "Compression of amplified chirped optical pulses," *Optics Communications*, vol. 56, pp. 219–221, 1985.

[57] Coherent Inc. Coherent Inc. SDG Data Sheet. Accessed 10-2016. [Online]. Available: http://www.coherent.com/downloads/ACF86A.pdf#page=1

[58] Coherent Inc. Coherent Inc. Evolution Data Sheet. Accessed 10-2016. [Online]. Available: https://www.coherent.com/downloads/Evolution_DS_0612RevD_2.pdf

[59] G. R. Hays, "Development of broad spectrum technologies for high energy chirped pulse amplification," Ph.D. dissertation, The University of Texas at Austin, 2007.

[60] J. Asmussen and D. Reinhard, *Diamond Films Handbook*. CRC Press, 2002.

[61] D. A. B. Miller, D. S. Chemla, T. C. Damen, T. H. Wood, C. A. Burrus, A. C. Gossard, and W. Wiegmann, "The Quantum Well Self-Electrooptic Effect Device: Optoelectronic Bistablity and Oscillation, and Self-Linearized Modulation," *IEEE Journal of Quantum Electronics*, vol. QE-21, pp. 1462–1476, 1985.

[62] H. H. Arsenault and Y. Sheng, *An Introduction to Optics in Computers*. SPIE Press, 1992.

[63] Hamamatsu Photonics K K. Hamamatsu Phase Spatial Light Modulator Data Sheet. Accessed 11-2016. [Online]. Available: https://www.hamamatsu.com/resources/pdf/ssd/e12_handbook_lcos_slm.pdf

[64] B. Sun, P. S. Salter, and M. J. Booth, "High conductivity micro-wires in diamond following arbitrary paths," *Applied Physics Letters*, vol. 105, 2014.

[65] T. Kurihara and Y. Takaki, "Improving viewing region of 4f optical system for holographic displays," *Optics Express*, vol. 19, pp. 17 621–17 631, 2011.

[66] Swamp Optics LLC. FROG beam profiler data sheet. Accessed 02-2018. [Online]. Available: http://www.swampoptics.com/assets/brochure-near-ir-grenouilles-2015-08.pdf

[67] kLayout. kLayout Documentation. Accessed 01-2017. [Online]. Available: http://www.klayout.de/doc.html

[68] H. M. Pinto, R. Jones, J. P. Goss, and P. R. Briddon, "Point and extended defects in chemical vapour deposited diamond," *Journal of Physics Conference Series*, vol. 281, 2011.

[69] L. Vandevenne. Lodepng image reading program. Accessed 02-2017. [Online]. Available: http://lodev.org/lodepng/

[70] International Telecommunications Union. Luminance standard BT.709. Accessed 02-2017. [Online]. Available: https://www.itu.int/rec/R-REC-BT.709-6-201506-I/en

[71] L. S. P. Glano, *Growth of CVD Diamond for Electronic Applications.* Springer, 2013, pp. 71–72.

[72] S. Reich and C. Thomsen, "Raman spectroscopy of graphite," *Philosophical Transactions of the Royal Society A*, vol. 362, pp. 2271–2288, 2004.

[73] G. T. Forcolin, V. Grilj, B. Hamilton, L. Li, M. McGowan, S. A. Murphy, A. Oh, N. Skukan, D. Whitehead, and A. Zadoroshnyj, "Study of a 3D diamond detector with photon and proton micro-beams," *Diamond and Related Materials*, vol. 65, pp. 75–82, 2016.

[74] J. Gaudin, N. Medvedev, J. Chalupský, T. Burian, S. Dastjani Farahani, V. Hájková, M. Harmand, H. O. Jeschke, L. Juha, M. Jurek, D. Klinger, J. Krzywinski, R. A. Loch, S. Moeller, M. Nagasono, C. Ozkan, K. Saksl, H. Sinn, R. Sobierajski, P. Sovák, S. Toleikis, K. Tiedtke, M. Toufarová, T. Tschentscher, V. Vorlíček, L. Vyšín, H. Wabnitz, and B. Ziaja, "Photon energy dependence of graphitization threshold for diamond irradiated with an intense XUV FEL pulse," *Physical Review B*, vol. 88, 2013.

[75] Horiba Ltd. LabRAM HR Evolution Raman Spectrometer. Accessed 03-2017. [Online]. Available: http://www.horiba.com/uk/scientific/products/raman-spectroscopy/raman-spectrometers/raman-microscopes/hr-evolution/labram-hr-evolution-17309

[76] Mathworks Inc. MATLAB (r2017a). Accessed 08-2017. [Online]. Available: https://in.mathworks.com/products/matlab.html

[77] Mathworks Inc. Curve Fitting Toolbox (r2017a). Accessed 03-2017. [Online]. Available: https://uk.mathworks.com/products/curvefitting.html

[78] Textronix Inc. Keithley sourcemeter data sheet. Accessed 03-2017. [Online]. Available: http://www.keithley.com/products/software/?path=2410/Documents#4

[79] The Engineering ToolBox. Resistivity and Conductivity - Temperature Coefficients for Common Materials. Accessed 03-2017. [Online]. Available: http://www.engineeringtoolbox.com/resistivity-conductivity-d_418.html

[80] H. O. Pierson, *Handbook of Carbon, Graphite, Diamonds and Fullerenes: Processing, Properties and Applications*. William Andrew, 2012.

[81] L. Graber, "Radiation Hard 3D Diamond Sensors for Vertex Detectors at HL-LHC," Ph.D. dissertation, The University of Goettingen, 2016.

[82] M. J. Booth, G. T. Forcolin, V. Grilj, B. Hamilton, I. Haughton, M. McGowan, S. A. Murphy, A. Oh, P. S. Salter, I. Sudić, and N. Skukan, "Study of cubic and hexagonal cell geometries of a 3D diamond detector with a proton micro-beam," *Diamond and Related Materials*, vol. 77, pp. 137–145, 2017.

[83] I. Haughton, A. Oh, and S. A. Murphy, "Study of the Resistivity of Graphitic Electrodes in 3D Diamond Detectors," Private Communication, Publication in Preparation.

[84] P. Calvani, A. Bellucci, M. Girolami, S. Orlando, V. Valentini, R. Polini, A. Mezzetti, F. Di Fonzo, and D. M. Trucchi, "Infrared absorption of fs-laser textured CVD diamond," *Applied Physics A*, vol. 121, 2016.

[85] T. J.-Y. Derrien, T. E. Itina, R. Torres, T. Sarnet, and M. Sentis, "Possible surface plasmon polariton excitation under femtosecond laser irradiation of silicon," *Journal of Applied Physics*, vol. 114, 2014.

[86] J. Bonse and J. Krüger, "Pulse number dependence of laser-induced periodic surface structures for femtosecond laser irradiation of silicon," *Journal of Applied Physics*, vol. 108, 2010.

[87] M. Jaksic, I. B. Radovic, M. Bogovac, V. Desnica, S. Fazinic, M. Karlusic, Z. Medunic, H. Muto, Z. Pastuovic, Z. Siketic, N. Skukan, and T. Tadic, "New capabilities of the Zagreb ion microbeam system," *NIM Physics B*, vol. 260, pp. 114–118, 2007.

[88] Cividec Instrumentation. C2-HV Broadband Amplifier Data Sheet. Accessed 04-2017. [Online]. Available: https://cividec.at/files/15_pdf.pdf

[89] LeCroy Corporation. WaveMaster-8500 data sheet. Accessed 04-2017. [Online]. Available: http://teledynelecroy.com/japan/pdf/wm8000a_series_ds.pdf

[90] Synopsys Inc. Synopsys TCAD. Accessed 04-2017. [Online]. Available: http://www.synopsys.com/home.aspx/

[91] S. M. Sze, *Semiconductor devices physics and technology.* John Wiley and Sons, 1985.

[92] A. Oh, T. Wengler, M. Ahmed, C. Da Via, and S. Watts, "A study of the charge collection properties of polycrystalline CVD diamond with synchrotron radiation," *Diamond and Related Materials*, vol. 20, pp. 398–402, 2011.

[93] K. J. Sawhney, I. P. Dolbnya, M. K. Tiwari, L. Alianelli, S. M. Scott, G. M. Preece, U. K. Pederson, and R. D. Walton, "A test beamline on diamond light source," *AIP Conference Proceedings*, vol. 1234, 2010.

[94] Tektronix Inc. Keithley 428 current amplifier data sheet. Accessed 04-2017. [Online]. Available: http://www.tek.com/sites/tek.com/files/media/media/resources/428-PROG.pdf

[95] J. W. Robinson, *Atomic Spectroscopy, Second Edition.* CRC Press, 1996.

[96] J. H. Hubbell and S. M. Seltzer. X-ray mass attenuation coefficients for elemental media. Accessed 04-2017. [Online]. Available: http://nist.gov/pml/data/xraycoef/

[97] The Engineering ToolBox. Densities of Solids. Accessed 06-2017. [Online]. Available: http://www.engineeringtoolbox.com/density-solids-d_1265.html